Improving the Speed and Accuracy of ab initio Calculations of the Electronic Structure of Metal Complexes

Von der Fakultät Chemie der Universität Stuttgart zur Erlangung der Würde eines Doktors der Naturwissenschaften (Dr. rer. nat.) genehmigte Abhandlung

vorgelegt von

Philipp Paul Hallmen

aus Stuttgart

Hauptberichter:	Prof. Dr. Joris van Slageren
Mitberichter:	Prof. Dr. Andreas Köhn
Prüfungsvorsitzender:	Prof. Dr. Johannes Kästner

Tag der mündlichen Prüfung: 13.12.2019

Institut für Physikalische Chemie der Universität Stuttgart

2019

Erklärung über die Eigenständigkeit der Dissertation

Ich versichere, dass ich die vorliegende Arbeit mit dem Titel

Improving the Speed and Accuracy of ab initio Calculations of the Electronic Structure of Metal Complexes

selbstständig verfasst und keine anderen als die angegebenen Quellen und Hilfsmittel benutzt habe. Aus fremden Quellen entnommene Passagen und Gedanken sind als solche kenntlich gemacht.

Declaration of Authorship

I hereby certify that the dissertation entitled

Improving the Speed and Accuracy of ab initio Calculations of the Electronic Structure of Metal Complexes

is entirely my own work except where otherwise indicated. Passages and ideas from other sources have been clearly indicated.

Name/Name: Philipp Paul Hallmen

Unterschrift/Signed:

Datum/Date:

With special thanks to

Prof. Dr. Joris Van Slageren for giving me the opportunity to join his group and to work on this fascinating topic. I really appreciate that I had the possibility to follow my own research ideas and that I always got support for new ideas. I learned a lot about many different topics in this versatile group and really enjoyed the frequent scientific discussions. The broad spectrum of science which was offered to me in this group was really a pleasure for me and I want to thank everyone in the group who accompanied me during my PhD (Michal Kern, Samuel Lenz, Heiko Bamberger, Dennis Schäfter, David Hunger, Mario Winkler, Dr. Dominik Bloos, Dr. Mauro Perfetti, Dr. Oleksii Laguta, Dr. Peng Zhang, Dr.-Ing. Petr Neugebauer). Thanks for this great time, not only for the "scientific time", but also for the "fun time", the great working atmosphere and for all the new friends I made there.

Prof. Dr. Hermann Stoll for supervising me and sharing his incredible knowledge with me and always supporting me in times where I did not see any solution for a problem and for answering so many questions.

Prof. Dr. Guntram Rauhut for supervising me, his support and for many fruitful scientific discussions with his whole group (Benjamin Ziegler, Sebastian Erfort, Tina Mathea, Taras Petrenko) and for nice bowling evenings.

Prof. Dr. Andreas Köhn and Prof. Dr. Johannes Kästner for kindly agreeing to act as examiners for this thesis.

Dr. Christoph Köppl for facilitating the beginning of my PhD thesis by always kindly answering my questions, introducing me to the Molpro source code and helping me in many programming issues.

Dr. Alexander Mitrushchenkov for all his great support regarding the MRCI and spin-orbit-code and for always answering all of my frequent questions and for all his valuable help during my PhD thesis.

Prof. Dr. Hans-Joachim Werner for all his programming help, especially regarding the implementation of SINGLE_ANISO and the LDF-MOS-CAHF code into Molpro.

Dr. Daniel Kats for helping me with the PNO-CASPT2 program and answering all of my questions.

Prof. Dr. Liviu Ungur for collaborating with us to implement SINGLE_ANISO into Molpro.

Dr. Mauro Perfetti for helping me to produce the files for the point charge embedding of the investigated compounds and for all the great scientific discussions.

Samuel Lenz for helping me to project my ab initio results onto pseudospin Hamiltonians and to simulate experimental spectra and for all the valuable scientific discussions.

David Kreplin for answering all my questions about the MCSCF program.

Dr. Stefan Jagiella for his help concerning computers and software.

The “cooking group” (Dr.-Ing. Petr Neugebauer, Dr. Oleksii Laguta, Dr. Mauro Perfetti, Marek Tuček, Jakub Hrubý, Martin Schneider) for the great, funny and of course delicious lunch times we had together.

My parents, my family and my friends for being there for me, supporting me and always believing in me.

Publications within the framework of this thesis

1. P. P. Hallmen, C. Köppl, G. Rauhut, H. Stoll, and J. van Slageren, “Fast and reliable ab initio calculation of crystal field splittings in lanthanide complexes”, *J. Chem. Phys.* **147**, 164101 (2017).

2. P. Zhang, M. Perfetti, M. Kern, P. P. Hallmen, L. Ungur, S. Lenz, M. R. Ringenberg, W. Frey, H. Stoll, G. Rauhut, and J. van Slageren, “Exchange coupling and single molecule magnetism in redox-active tetraoxolene-bridged dilanthanide complexes”, *Chem. Sci.* **9**, 1221–1230 (2018).

3. P. P. Hallmen, G. Rauhut, H. Stoll, A. O. Mitrushchenkov, and J. van Slageren, “Crystal Field Splittings in Lanthanide Complexes: Inclusion of Correlation Effects beyond Second Order Perturbation Theory”, *J. Chem. Theory. Comput.* **14**, 3998–4009 (2018).

4. L. C. J. Pereira, J. T. Coutinho, M. Perfetti, J. J. Baldoví, M. A. Antunes, P. Hallmen, H. Bamberger, I. Crassee, M. Orlita, M. Almeida, and J. van Slageren, “Spectroscopic Determination of the Electronic Structure of a Uranium Single-Ion Magnet,” *Chem. Eur. J.* **25**, 1758–1766 (2018).

5. S. Lenz, H. Bamberger, P. P. Hallmen, Y. Thiebes, S. Otto, K. Heinze, and J. van Slageren, “Chromium(III)-based potential molecular quantum bits with long coherence times,” *Phys. Chem. Chem. Phys.* **21**, 6976–6983 (2019).

6. P. P. Hallmen, H.-J. Werner, D. Kats, S. Lenz, G. Rauhut, H. Stoll, and J. van Slageren, “Toward fast and accurate ab initio calculation of magnetic exchange in polynuclear lanthanide complexes,” *Phys. Chem. Chem. Phys.* **21,** 9769–9778 (2019).

7. U. Albold, H. Bamberger, P. P. Hallmen, J. van Slageren, and B. Sarkar, “Strong exchange couplings drastically slow down magnetization relaxation in an air-stable cobalt(II)-radical single-molecule magnet,” *Angew. Chem. Int. Ed.* (2019), DOI: 10.1002/anie.201904645.

Table of Contents

Abbreviations

AO	Atomic orbital
CAHF	Configuration-averaged Hartree-Fock
CAS	Complete active space
CASCI	Complete active space configuration interaction
CASPT2	Complete active space perturbation theory of second order
CASSCF	Complete active space self-consistent field
CF	Crystal-field
CFP	Crystal-field parameter
CI	Configuration interaction
CPU	Central processing unit
DFT	Density functional theory
DKH	Douglas-Kroll-Hess
DMRG	Density matrix renormalization group
EPR	Electron paramagnetic resonance
FCI	Full configuration interaction
FCIQMC	Full configuration interaction quantum Monte Carlo
FIC	Fully internally contracted
FIR	Far-infrared
HF	Hartree-Fock
HFEPR	High-field electron paramagnetic resonance
ICC	Internally contracted configuration
icMRCI	Internally contracted multireference configuration interaction
KD	Kramers doublet
LCAO	Linear combination of atomic orbitals
LDF-CAHF	Local density-fitted configuration-averaged Hartree-Fock

LDF-HF	Local density-fitted Hartree-Fock
LDF-MOS-CAHF	Local density-fitted multiple-open-shell configuration-averaged Hartree-Fock
LMO	Localized molecular orbital
MCD	Magnetic circular dichroism
MCSCF	Multi-configurational self-consistent field
MO	Molecular orbital
MQB	Molecular quantum bit
MRCC	Multireference coupled cluster
MRCI	Multireference configuration interaction
MRPT	Multireference perturbation theory
MS	Multi-state
NEVPT2	N-Electron valence state perturbation theory of second order
PNO-CASPT2	Pair-natural-orbital complete active space perturbation theory of second order
PP	Pseudopotential
qlp-icMRCI	Quasi-local projected multireference configuration interaction
QTM	Quantum tunnelling of magnetization
RASCI	Restricted active space configuration interaction
RAM	Random access memory
RHF	Restricted Hartree-Fock
ROHF	Restricted open-shell Hartree-Fock
SA-CASSCF	State-averaged complete active space self-consistent field
SIM	Single-ion magnet
SI-SO	State interaction with spin-orbit coupling
SMM	Single-molecule magnet

SO	Spin-orbit
SQUID	Superconducting quantum interference device
UHF	Unrestricted Hartree-Fock
VO	Valence-only
ZFS	Zero-field splitting

Zusammenfassung

Die Anfänge des Forschungsfeldes der Einzelmolekülmagnete gehen auf das Jahr 1993 zurück, als magnetische Hysterese rein molekularen Ursprungs im Mangan-Komplex $[Mn_{12}O_{12}(OAc)_{16}(H_2O)_4]$ ("$Mn_{12}ac$") beobachtet wurde[1,2]. Einzelmolekülmagnete sind Komplexe, welche aus von Liganden umgebenen Übergangsmetall-, Lanthanoid- oder Actinoidionen bestehen, die nach Abschalten eines äußeren Magnetfelds eine langsame Relaxation der Magnetisierung aufweisen, d.h. für eine gewisse Zeit magnetisiert bleiben. Diese magnetische Bistabilität lässt sich durch eine effektive Energiebarriere für die Umkehrung des magnetischen Moments erklären. Aufgrund ihrer einzigartigen (Quanten-) Eigenschaften und den daraus folgenden potentiellen Anwendungen im Bereich der Ultrahochdichtedatenspeicherung, Spintronik und Quantencomputer[3–6] haben diese Moleküle in den letzten Jahren besondere Aufmerksamkeit erregt. Trivalente Lanthanoidionen haben sich hinsichtlich der Höhe der effektiven Energiebarriere für die magnetische Relaxation und der *Blockierungstemperatur* (*BT,* engl.: *blocking temperature*), d.h. der Temperatur unterhalb derer keine Relaxation (auf einer bestimmten Zeitskala) mehr stattfindet, gegenüber den Übergangsmetallionen als überlegen herausgestellt[7–9]. Außergewöhnlich hohe BTs von bis zu 80 K wurden in Dysprosoceniumderivaten beobachtet[10,11]. Außerdem wurde die potentielle Anwendung von lanthanoidbasierten Systemen in Spintronik-Bauelementen von verschiedenen Gruppen erfolgreich demonstriert[12–15]. Die rationale Verbesserung und Weiterentwicklung dieser Materialien hinsichtlich ihrer potentiellen Anwendung in Bauteilen erfordert ein detailliertes Verständnis der Zusammenhänge zwischen den magnetischen Eigenschaften auf der einen Seite und der elektronischen und geometrischen Struktur auf der anderen Seite. Für lanthanoidbasierte Einzelmolekülmagnete sind die elektronische Struktur und damit die Eigenschaften im Wesentlichen durch die tiefliegenden Kristallfeldzustände bestimmt. Diese Kristallfeldzustände können als Spin-Bahn-Multiplette des Gesamtdrehimpulses J betrachtet werden, welche durch das von den Liganden erzeugte Kristallfeld aufgespalten sind. Der Gesamtdrehimpuls hat seinen Ursprung in den ungepaarten 4f-Elektronen der Verbindungen und die starke Spin-Bahn-Kopplung in den Lanthanoidionen macht ihren Magnetismus stark anisotrop. Die Größe und Ausrichtung der magnetischen Anisotropie wird durch die Natur und die Anordnung der Liganden um das Lanthanoidion bestimmt. Um ein rationales Design

von verbesserten Ln(III)-Komplexen zu ermöglichen, ist eine Kombination von Experimenten und ab initio Rechnungen unerlässlich.

Zurzeit werden ab-initio-Elektronenstrukturrechnungen von Lanthanoidkomplexen meistens mit der (*state-averaged*) *complete active space self-consistent field and state interaction with spin-orbit coupling* Methode ((*SA*-)*CASSCF/SI-SO*)[3,16] durchgeführt. Diese Methode liefert Energien und Wellenfunktionen, welche dann wiederrum zur Berechnung verschiedenster Eigenschaften, z.B. Kristallfeldparameter und *g*-Tensoren, verwendet werden können und wurde im letzten Jahrzehnt erfolgreich auf viele Einzelmolekülmagnete angewandt[3,11,17–26]. Die Methode ist jedoch rechentechnisch sehr aufwändig und systematische Studien großer Moleküle mit großen Basissätzen erfordern sehr lange Rechenzeiten. Aus diesem Grund werden Rechnungen für große Systeme normalerweise in Hochleistungsrechenzentren durchgeführt. Ein weiterer Nachteil der CASSCF/SI-SO-Methode ist, dass sie die sogenannte *dynamische Elektronenkorrelation* vernachlässigt, was zu unzureichender Genauigkeit der Rechnungen im Vergleich mit dem Experiment führen kann. Die *multi-state complete active space perturbation theory of second order* (*CASPT2*)-Methode[27–30] kann verwendet werden, um die Genauigkeit der CASSCF/SI-SO-Rechnungen durch Berücksichtigung dynamischer Korrelation zu erhöhen. Diese Methode weist jedoch oft Probleme auf, wenn der minimale aktive Raum gewählt wird (z.B. *intruder state problems, „overshooting effect“*)[28,31,32] oder ist für große Moleküle und große aktive Räume aufgrund des hohen Rechenaufwands nicht durchführbar. Die *multi-state multireference configuration interaction* (*MRCI*)-Methode[33–36] berücksichtigt die dynamische Elektronen-korrelation auf variationelle Art und Weise und leidet nicht unter den für multi-state CASPT2 typischen Problemen. Jedoch ist diese Methode aufgrund des enormen Rechenaufwandes nicht einmal für kleine Lanthanoidkomplexe durchführbar, besonders wenn die Berechnung einer hohen Anzahl von Zuständen erforderlich ist. Das dritte Problem der konventionellen CASSCF/SI-SO-Methode ist ihre Anwendbarkeit auf mehrkernige Lanthanoidkomplexe. Der aktive Raum wird für mehrkernige Systeme, insbesondere für die Berechnung der Austauschwechselwirkung zwischen Lanthanoidionen, sehr schnell sehr groß, was die CASSCF/SI-SO Berechnungen extrem aufwändig, wenn nicht sogar unmöglich macht. Außerdem ist es notwendig für die Berechnung von Austauschkopplungen zwischen Lanthanoidionen dynamische Korrelation in den Rechnungen zu berücksichtigen, was

Methoden wie CASPT2 oder MRCI erfordert, welche rechentechnisch sogar noch aufwändiger sind.

Aus diesen Gründen war das Ziel dieser Arbeit die Verbesserung der Geschwindigkeit und der Genauigkeit konventionell angewandter Methoden für die ab initio Berechnung der elektronischen Struktur von lanthanoidbasierten Einzelmolekülmagneten und weiterhin die Ermöglichung der effizienten und genauen Berechnung von (Austauschkopplungen in) mehrkernigen Lanthanoidkomplexen. Außerdem sollten die entwickelten Methoden auf übergangsmetall- und actinoidbasierte Verbindungen angewendet werden, um die Anwendbarkeit der Methoden auf diese Systeme zu erforschen. Die neu entwickelten Methodologien sollen dabei helfen, die Möglichkeiten der Forschung und Entwicklung im Bereich dieser Verbindungen zu verbessern und letztlich dazu führen, die Eigenschaften dieser Materialien im Hinblick auf deren praktische Anwendung weiterzuentwickeln.

Im ersten Teil der Arbeit wurde die *local density-fitted configuration-averaged Hartree-Fock* (*LDF-CAHF*) Methode[37] entwickelt, welche eine Alternative zu der rechen- und zeitaufwändigen Orbitaloptimierung der SA-CASSCF Methode darstellt. Die Methode bestimmt die zustandsgemittelten SA-CASSCF-äquivalenten Orbitale durch das Lösen von *restricted open-shell Hartree-Fock-(ROHF-)*-ähnlichen Gleichungen und nutzt dabei lokale Dichtefitting-Näherungen, um die Rechnungen zu beschleunigen. Dabei wurde für das getestete Benchmark-System $Er[N(SiMe_3)_2]_3$[37–39] eine bis zu 26-fach kürzere Rechenzeit gegenüber der SA-CASSCF Methode erreicht. Durch die nahezu lineare Skalierung der Methode mit der Molekülgröße (für die Orbitaloptimierung) wird dieser Beschleunigungsfaktor für größere Systeme noch weiter ansteigen und durch die effiziente Parallelisierung der Methode kann die Rechenzeit noch weiter reduziert werden, indem man mehr CPU-Kerne gleichzeitig für die Rechnungen verwendet. Die Genauigkeit der Energien bei der Verwendung der LDF-CAHF-Orbitale bleibt dabei gleich wie die für SA-CASSCF. Um die Anwendbarkeit der Methode auf verschiedenste Systeme zu demonstrieren, wurde sie auf einen Dysprosium- und einen Terbiumkomplex ($[(HBpz_3)_2Ln(\mu\text{-}CA)Ln(HBpz_3)_2]\cdot 2CH_2Cl_2$ (Ln=Dy,Tb; $HBpz_3^-$=Hydrotris (pyrazol-1-yl)borat, CA^{2-}=Chloranilat))[40] und einen Urankomplex ($[U^{III}\{SiMe_2NPh\}_3\text{-}tacn)(OPPh_3)]$ (tacn=1,4,7,-Triazacyclononan))[41] angewendet. Während die Resultate für den Dy- und Tb-Komplex gut mit den experimentellen Messungen übereinstimmten, war die Situation für den Urankomplex komplizierter. Im Falle des

Urankomplexes wurden die LDF-CAHF Orbitale als Startnäherung für eine nachfolgende SA-CASSCF Rechnung mit einem größeren aktiven Raum verwendet. Dabei konnte gezeigt werden, dass die LDF-CAHF Methode effizient im Zusammenspiel mit anderen Methoden angewendet werden kann. Allerdings waren die Ergebnisse für den Urankomplex selbst mit vergrößertem aktiven Raum in schlechterer Übereinstimmung mit den Experimenten als für die Lanthanoidkomplexe, was zeigt, dass für dieses System zusätzlich Methoden verwendet werden sollten, die dynamische Korrelation mit berücksichtigen. Als nächstes wurde die LDF-CAHF Methode auf Übergangsmetall-verbindungen angewendet. Dabei wurde einerseits das Energiespektrum eines einkernigen Chromkomplexes ($[Cr(ddpd)_2](BF_4)_3$ (ddpd=*N,N'*-Dimethyl-*N,N'*-dipyridin-2,6-diamin))[42] bestimmt und andererseits die Austauschkopplung in einem zweikernigen radikal-verbrückten Kobaltkomplex ($(K\text{-}18\text{-}c\text{-}6)_3[\{(H_2L_B^{2-})Co^{II}\}_2(\mu\text{-}L_B^{3\bullet-})]$ (H_4L_B=1,2,4,5-Tetrakis (methansulfonamido)benzol))[43] berechnet. Im Falle des Chromkomplexes wurden die LDF-CAHF Orbitale als Startnäherung für eine darauf aufbauende SA-CASSCF-Rechnung mit einem weiteren Satz von metallzentrierten d-Orbitalen im aktiven Raum (*double shell effect*) verwendet, wobei die geschlossenschaligen Orbitale aus der LDF-CAHF Rechnung eingefroren und nicht weiter optimiert wurden. Anschließend wurde dynamische Korrelation mittels der *complete active space perturbation theory of second order using pair natural orbitals* (*PNO-CASPT2*) Methode berücksichtigt. Die Resultate, insbesondere die Nullfeldaufspaltung des Grund-(Spin-)Multipletts, waren dabei in guter Übereinstimmung mit den experimentellen Befunden, was die Anwendbarkeit der LDF-CAHF Methode (im Zusammenspiel mit anderen Methoden) auf Übergangsmetallverbindungen demonstriert. Bei der Anwendung der Methode auf den zweikernigen radikal-verbrückten Kobaltkomplex wurde die Methode der diamagnetischen Substitution verwendet, d.h. ein Kobaltion wurde durch ein diamagnetisches Zinkion ersetzt und der verbrückende Ligand wurde im ersten Schritt der Rechnung zu seiner geschlossenschaligen Form reduziert. Dies war nötig, weil die LDF-CAHF Methode ansonsten „Hochenergiezustände“ in die Optimierung der zustandsgemittelten Orbitale mit einbeziehen würde, bei denen mehrere Elektronen zwischen den Kobaltionen und dem Radikal-Liganden und den Kobaltionen transferiert werden, was zu Orbitalen führen würde, welche für die Beschreibung der energetisch tiefliegenden Zustände des Moleküls ungeeignet sind (eine Erweiterung der LDF-CAHF Methode wurde im späteren Verlauf dieser Arbeit entwickelt, um dieses Problem zu lösen). Die LDF-CAHF Methode wurde in diesem Fall

erneut dafür verwendet (mit den fünf d-Orbitalen des nicht-substituierten Kobalts als aktiver Raum), geeignete Startorbitale für eine darauf aufbauende SA-CASSCF-Rechnung zu bestimmen, in welcher der Ligand erneut zu seiner radikalischen Form oxidiert wurde. In dieser SA-CASSCF-Rechnung wurde der aktive Raum um zwei π- und zwei π^*-Orbitale des Liganden erweitert und die (verbleibenden) geschlossenschaligen Orbitale aus der LDF-CAHF Rechnung wurden unverändert eingefroren und nicht weiter optimiert. Im letzten Schritt wurde schließlich dynamische Korrelation mittels CASPT2 berücksichtigt. Die Projektion der ab initio Ergebnisse auf einen Pseudospin-Hamiltonoperator, welcher einen isotropen Austauschkopplungsterm für die Wechselwirkung zwischen dem Kobaltion und dem Radikal-Liganden enthält (und Nullfeldaufspaltungs- und Zeeman-Wechselwirkungsterme), lieferte eine antiferromagnetische Kopplung, was in Übereinstimmung mit den experimentellen Befunden ist. Der anhand der ab initio Rechnungen bestimmte Wert des Nullfeldaufspaltungsterms stimmt dabei sehr gut mit dem experimentellen Wert überein (ab initio D_{Co} = –110 cm^{-1}; experimentell D_{Co} = –115 cm^{-1}). Allerdings ist die aus den ab initio Rechnungen bestimmte Austauschkopplungskonstante (J_{Co-Rad} =+174 cm^{-1}) weniger als halb so groß wie der experimentell bestimmte Wert (J_{Co-Rad} =+440 cm^{-1}). Dies lässt sich einerseits darauf zurückführen, dass die dynamische Korrelation und die Kristallumgebung des Moleküls nicht ausreichend berücksichtigt wurden und andererseits vor allem darauf, dass ein Kobaltion durch ein Zinkion ersetzt wurde. Bei starken Austauschkopplungen in dieser Größenordnung ist die diamagnetische Substitution eines Kobalts eine sehr grobe Näherung, weil die (starke) Kopplung des einen Kobalts zum Radikal-Liganden die Kopplung des anderen Kobalts zum selben Liganden signifikant beeinflussen könnte. Um dieses Problem zu umgehen, müsste man das gesamte Molekül (ohne diamagnetische Substitution) berechnen, was aufgrund des großen benötigten aktiven Raumes und der vielen zu berechnenden Zustände (welche zur Berechnung der Spin-Bahn-Kopplung benötigt werden) eine große Herausforderung darstellt.

Zusammenfassend lässt sich sagen, dass die LDF-CAHF Methode zur effizienten Berechnung von Kristallfeldaufspaltungen in Lanthanoidkomplexen angewendet werden kann, mit der gleichen Genauigkeit, jedoch deutlich geringerem Rechenaufwand als die konventionelle SA-CASSCF Methode. Aus diesem Grund wäre die Anwendung der Methode besonders interessant in Gebieten, in denen die schnelle Berechnung vieler unterschiedlicher

molekularer Geometrien notwendig ist, beispielsweise in der Berechnung von Spin-Phonon-Kopplungen oder in der Entwicklung von Blaupausen für molekulare Nanomagnete, wobei viele verschiedene Kandidaten/Strukturen getestet werden müssen. Außerdem könnte die Methode aufgrund ihrer hohen Geschwindigkeit für räumlich ausgedehnte Systeme in Untersuchungen der Wechselwirkung von molekularen Nanomagneten mit (geschlossenschaligen) Oberflächen angewendet werden, wobei ein großer endlicher Ausschnitt der Oberfläche zur Berechnung herangezogen werden kann. Die LDF-CAHF Methode kann außerdem zur Berechnung von Actinoid- und Übergangsmetallverbindungen verwendet werden. Dabei sollte die Methode jedoch in Kombination mit anderen Methoden verwendet werden, welche statische und dynamische Korrelation berücksichtigen, um genaue Resultate zu erhalten. Beispielsweise kann die Methode dazu verwendet werden, effizient sehr genaue Startorbitale für eine nachfolgende SA-CASSCF-Rechnung mit vergrößertem aktiven Raum und anschließende CASPT2 und MRCI Rechnungen zu berechnen. Dabei können bei der SA-CASSCF-Rechnung mit vergrößertem aktiven Raum die (verbleibenden) geschlossenschaligen Orbitale aus der LDF-CAHF-Rechnung übernommen und eingefroren werden und nur die aktiven Orbitale optimiert werden. Dies führt zu einer sehr großen Zeitersparnis gegenüber einer SA-CASSCF-Rechnung ohne vorherige LDF-CAHF-Rechnung (d.h. mit der vollen Optimierung aller Orbitale).

Im zweiten Teil der Arbeit wurde die Genauigkeit konventioneller Berechnungen der Kristallfeldaufspaltung in Lanthanoidkomplexen über das CASPT2-Level hinaus erhöht, indem MRCI-Rechnungen für diese Systeme ermöglicht wurden. Der Konfigurationsraum ist für die MRCI-Methode (durch die Einfachanregungen) größer als der für CASPT2 (bei gleichem aktiven Raum) und die dynamische Korrelation wird zudem variationell behandelt. Die Ermöglichung der MRCI-Rechnungen wurde durch die Entwicklung der *quasi-local projected internally contracted MRCI* (*qlp-icMRCI*) Methode[44] erreicht. Konventionelle multi-state icMRCI-Rechnungen von Lanthanoidkomplexen sind normalerweise aufgrund der enorm großen erforderlichen *central processing unit* (*CPU*) Zeiten und des großen Arbeitsspeicherbedarfs nicht durchführbar. Diese hohen Anforderungen an Rechenkapazität ergeben sich aufgrund der (normalerweise) großen Anzahl an geschlossenschaligen Orbitalen, welche korreliert werden müssen, und aufgrund der hohen Anzahl an Zuständen, welche gleichzeitig berechnet werden müssen. Die qlp-icMRCI-Methode umgeht diese

Probleme, indem sie die Anzahl an korrelierten geschlossenschaligen Orbitalen reduziert, wobei sie diese lokalisiert und nur die Untermenge an lokalen Orbitalen korreliert, welche am oder nahe zum zentralen Lanthanoidion liegen, und indem sie eine Projektionsoperatortechnik verwendet, welche die gewünschten Zustände nacheinander statt gleichzeitig berechnet. Die Methode wurde auf den Einzelionmagneten $\{C(NH_2)_3\}_5[Er(CO_3)_4]\cdot 11H_2O$[44,45] angewendet. Die resultierenden Energien lagen näher an den experimentellen Werten (bestimmt durch Ferninfrarotspektroskopie) und die Rechenzeit war deutlich kürzer als für die entsprechenden multi-state CASPT2-Rechnungen des Systems. Eine Anwendung der Methode auf Actinoid- und Übergangsmetallverbindungen wäre interessant für die Zukunft. Außerdem wäre es wünschenswert, die lokalen Näherungen auf der virtuellen Orbitalraum zu erweitern, um eine vollständig lokale icMRCI-Methode zu erhalten, wobei man zusätzlich noch lokale Dichtefitting-Näherungen einbauen könnte, um die Rechnungen weiter zu beschleunigen.

Der dritte und letzte Teil der Arbeit befasste sich mit der schnellen und genauen Berechnung von anisotropen Austauschwechselwirkungen in mehrkernigen Lanthanoidkomplexen. Aufgrund der großen aktiven Räume, der hohen erforderlichen Anzahl an zu berechnenden Zuständen und der Notwendigkeit, dynamische Korrelation in den Rechnungen zu berücksichtigen, handelt es sich dabei um eine sehr schwieriges Problem. Um dieses zu lösen, wurde die LDF-CAHF-Methode auf Systeme mit mehr als einer Gruppe an offenschaligen Orbitalen (z.B. an verschiedenen Metallatomen) erweitert. Dies führte zur *LDF-MOS-CAHF*-Methode (*MOS: multiple open-shells*), welche mit der linear-skalierenden *many-state PNO-CASPT2*-Methode kombiniert wurde, um effizient dynamische Korrelation in der Berechnung mehrkerniger Systeme zu berücksichtigen[46]. Die neue Methode wurde auf den asymmetrischen zweikernigen Komplex $[hqH_2][Yb_2(hq)_4(NO_3)_3]\cdot MeOH$ (hqH=8-hydroxyquinoline) angewendet, zu welchem ausführliche experimentelle Studien existieren[47]. Unsere ab initio Rechnungen bestätigten die Existenz einer signifikanten Superaustauschwechselwirkung zwischen den beiden Yb^{3+}-Ionen und die Resultate wurden auf einen Pseudospin-Hamiltonoperator mit anisotroper Austauschwechselwirkung projiziert. Die experimentellen Elektronenspinresonanzspektren konnten vernünftig mit diesem Hamiltonoperator reproduziert werden. Für die Zukunft wäre es interessant diese Methode auf Systeme mit mehr als zwei offenschaligen Ionen oder auf radikal-verbrückte

Verbindungen anzuwenden. Außerdem wäre die Anwendung auf mehrkernige Übergangsmetallkomplexe interessant. Darüber hinaus wäre die Kombination der LDF-MOS-CAHF-Methode mit anderen (Korrelations-)Methoden für Systeme mit großen aktiven Räumen, z.B. der Dichtematrixrenormierungsgruppe (*density matrix renormalization group, DMRG*) oder Quanten-Monte-Carlo Methoden (*full configuration interaction quantum Monte Carlo, FCIQMC*), ein interessantes Forschungsfeld.

Zusammenfassend lässt sich sagen, dass in dieser Arbeit neue Methoden zur schnellen und genauen ab initio Berechnung des Energiespektrums und der (magnetischen und spektroskopischen) Eigenschaften von ein- und mehrkernigen Metallkomplexen entwickelt wurden. Die Methoden wurden auf bereits bekannte und auch neue Systeme angewendet und konnten sowohl die Geschwindigkeit, als auch die Genauigkeit von konventionellen Rechnungen erhöhen, insbesondere für große Systeme. Außerdem wurden die neuen Methoden erfolgreich mit bereits existierenden Ansätzen kombiniert. Es konnte gezeigt werden, dass keine universelle Methode für alle Problemstellungen existiert, sondern dass eine sinnvolle Kombination verschiedener Methoden und eine sorgfältige Voranalyse der untersuchten Systeme notwendig ist, um die Rechenzeitanforderungen für Simulationen zu minimieren und um eine hohe Genauigkeit zu erreichen, insbesondere für große Systeme. Aufgrund der steigenden Rechenleistung moderner Computer und der effizienten Näherungen in quantenchemischen Rechnungen ist zu erwarten, dass ab initio Methoden ein unverzichtbares Werkzeug in der rationalen Weiterentwicklung von Metallkomplexen für die praktische Anwendung und in der Ergänzung experimenteller Untersuchungen werden.

1. Introduction

The beginning of the research field of single molecule magnets (SMMs) can be dated back to 1993, where magnetic hysteresis of purely molecular origin was observed in the manganese cluster $[Mn_{12}O_{12}(OAc)_{16}(H_2O)_4]$ ("$Mn_{12}ac$")[1,2]. Single molecule magnets are complexes of transition metal, lanthanide, or actinide ions surrounded by ligands, which show slow relaxation of the magnetization after having switched off an external magnetic field, i.e. have the ability to show long-living spin polarized states. This magnetic bistability can be explained by an effective energy barrier for the reversal of the magnetic moment. Due to their unique (quantum) properties, these molecules have gained special interest during the last years because of their potential practical applications in ultrahigh-density magnetic data storage, spintronic devices and quantum computers[3–6]. Regarding the height of the effective energy barrier towards magnetic relaxation, as well as the magnetization blocking temperature, molecules containing trivalent lanthanide ions proved to be superior to transition metal based systems[7–9]. Extraordinarily high blocking temperatures of up to 80K have recently been observed in dysprosocenium derivatives[10,11]. Furthermore, the potential use of lanthanide based systems in spintronic devices was successfully demonstrated by different groups[12–15]. The rational improvement of these materials regarding their potential application in devices requires a detailed understanding of the correlation between the magnetic properties and the electronic and geometric structure. For lanthanide SMMs, the electronic structure and therefore the properties are essentially determined by their low-lying crystal-field (CF) levels. These can be regarded as spin-orbit multiplets of the total angular momentum J, which are split by the crystal field generated by the surrounding ligands of the complex. The total angular momentum is rooted in the unpaired 4f-electrons of the compounds and the strong spin-orbit coupling in these complexes makes the magnetism strongly anisotropic. The magnitude and direction of the anisotropy is determined by the nature and arrangement of the ligands surrounding the lanthanide ions. In order to enable rational design of improved Ln(III) complexes, a combined use of experiment and ab initio calculations is necessary.

Conventionally, ab initio electronic structure calculations of lanthanide complexes are performed employing the *CASSCF/SI-SO (complete active space self-consistent field and state interaction with spin-orbit coupling)* method[3,16]. This method provides energy levels and

wave functions, which can then be used to calculate various properties, e.g. crystal-field parameters and *g*-tensors, and was successfully applied to many SMM systems during the past decade[3,11,17–26]. However, this method is computationally very demanding and systematic studies of large molecules with large basis sets are very-time consuming. Therefore, calculations for large systems are normally performed on high performance computing clusters. Moreover, the CASSCF/SI-SO method neglects so-called *dynamical correlation*, which can lead to insufficient accuracy compared to the experiment. The *multi-state complete active space perturbation theory of second order (CASPT2)* method[27–30] can be employed to increase the accuracy of the CASSCF/SI-SO calculations by including dynamical correlation. However, this method often suffers from problems if the minimal active space is chosen (e.g., intruder state problems, "overshooting effect")[28,31,32] or is not feasible for large molecules or large active spaces. The *multi-state multireference configuration interaction (MRCI)* method[33–36] is a method to variationally include dynamical correlation into calculations and does not suffer from the standard problems of multi-state CASPT2. However, this method is not feasible even for small lanthanide complexes, in particular if the calculation of many states/roots is required. The third problem of the conventional CASSCF/SI-SO approach is that it cannot be easily applied to polynuclear lanthanide complexes. For polynuclear systems, especially for the calculation of exchange couplings between the lanthanide ions, the active space becomes rapidly very large, which renders the CASSCF calculations extremely demanding or even impossible. Moreover, for the calculation of exchange couplings between lanthanide ions it is necessary to include dynamical correlation by methods such as CASPT2 or MRCI, which are computationally even more demanding.

Therefore, the main goal of this thesis is the improvement of the speed and accuracy of conventional methods used for the ab initio calculation of lanthanide single molecule magnets, as well as enabling the fast and accurate calculation of (exchange couplings in) polynuclear lanthanide complexes. Furthermore, the developed methods will be applied to transition metal and actinide based compounds, in order to investigate their applicability to these systems. The new methodologies will help to guide the research to improve ab initio calculations of metal complexes and will serve to rationally improve the properties of these materials for device applications.

2. Molecular ab initio calculations

This chapter gives an introduction to the basics of ab initio quantum chemistry and to the methods used for the calculation/simulation of single molecule magnets. We start with the description of non-relativistic quantum chemistry in section 2.1. However, for the molecules studied in this thesis, relativistic effects are very important. Therefore, the basic concepts of relativistic quantum chemistry and the most important relativistic Hamiltonians used in will be introduced in section 2.2. Section 2.3 deals with wave-function-based methods for electronic structure calculations. It starts with an introduction to the Hartree-Fock method and (local) density-fitting approximations to speed up the calculations and then gives a brief overview about the subsequent multireference (correlation) methods eymployed in this thesis. In the end, we will briefly outline the projection of the ab initio results onto pseudospin Hamiltonians, which is important for the comparison with experiments.

2.1. Non-relativistic quantum chemistry

This chapter deals with the fundamentals of non-relativistic quantum chemistry. A brief overview of the basic theory is given. For a more detailed description, the interested reader is referred to the literature that this chapter is based on[48–52].

2.1.1. The molecular Schrödinger equation

In order to interpret results of experiments on existing compounds or to predict the properties of new compounds, *ab initio* calculations are an important tool. These calculations allow the investigation of structure-property-relations solely based on fundamental constants and without additional information from the experiment. Due to the increasing computational power over the last decades, these quantum chemical calculations have been used to guide research in many fields, i.e. organic chemistry, inorganic chemistry, medical chemistry or physical chemistry with great and increasing success. For example, they can be used to predict spectra of compounds, analyse reaction pathways and for the prediction of electric and magnetic properties. The main goal of ab initio quantum chemistry is the efficient numerical solution of the *time-independent molecular Schrödinger equation*

$$\widehat{H}_{\mathrm{mol}}\Psi_k^{\mathrm{mol}}(\mathbf{x},\mathbf{R}) = E_k^{\mathrm{mol}}\Psi_k^{\mathrm{mol}}(\mathbf{x},\mathbf{R}). \tag{2.1}$$

Here, $\widehat{H}_{\mathrm{mol}}$ is the molecular Hamiltonian describing the kinetic energies and interactions of all particles, i.e. all electrons and nuclei, in the molecule. The wave functions $\Psi_k^{\mathrm{mol}}(\mathbf{x}, \mathbf{R})$ and the corresponding energies E_k^{mol} of quantum state k are obtained by solving this equation. The wave functions depend on the electronic coordinates $\mathbf{x}$ and the nuclear coordinates $\mathbf{R}$ and can be used to calculate any (time-independent) property of the molecule. In the following, we will assume that there are N electrons and M nuclei and label the electrons with the index i and the nuclei by the index K. The vector $\mathbf{x}$ contains the spatial coordinates $\mathbf{r}_i = (x_i, y_i, z_i)$ of each electron as well as its spin coordinate s_i, which can be summarized to a spatial-spin-coordinate $\mathbf{x}_i$ defined as

$$\mathbf{x}_i = (\mathbf{r}_i, s_i). \tag{2.2}$$

$\mathbf{x}$ is then given as

$$\mathbf{x} = (\mathbf{x}_1, \mathbf{x}_2, \mathbf{x}_3, \dots, \mathbf{x}_N). \tag{2.3}$$

The vector $\mathbf{R}$ containing the nuclear coordinates $\mathbf{R}_K = (X_K, Y_K, Z_K)$ is defined as

$$\mathbf{R} = (\mathbf{R}_1, \mathbf{R}_2, \mathbf{R}_3, \dots, \mathbf{R}_M). \tag{2.4}$$

The non-relativistic molecular Hamiltonian $\widehat{H}_{\mathrm{mol}}$ is given by

$$\widehat{H}_{\mathrm{mol}} = -\sum_{K=1}^{M} \frac{\hbar^2}{2M_K} \nabla_K^2 - \sum_{i=1}^{N} \frac{\hbar^2}{2m_e} \nabla_i^2 - \sum_{K=1}^{M} \sum_{i=1}^{N} \frac{e^2 Z_K}{4\pi\epsilon_0 r_{Ki}} + \sum_{i>j}^{N} \frac{e^2}{4\pi\epsilon_0 r_{ij}} + \sum_{K>L}^{M} \frac{e^2 Z_K Z_L}{4\pi\epsilon_0 R_{KL}} \tag{2.5}$$

where $\hbar$ is the reduced Planck constant, e is the elementary charge, Z_K and M_K are the atomic numbers and atomic masses, m_e is the electron mass and ϵ_0 the dielectric constant of vacuum. r_{Ki} is the distance between nucleus K and electron i, r_{ij} is the distance between electron i and electron j and R_{KL} represents the distance between nucleus K and nucleus L. The first two summations represent the kinetic energy of the nuclei and electrons, respectively, the third term the Coulomb interaction between the nuclei and electrons, the

fourth term the Coulomb interaction between the electrons and the last term is the nuclear repulsion energy. In atomic units, in which $e \equiv 1$, $\hbar \equiv 1, m_e \equiv 1$ and $4\pi\epsilon_0 \equiv 1$, the molecular Hamiltonian can be written as

$$\hat{H}_{\mathrm{mol}} = -\sum_{K=1}^{M} \frac{1}{2M_K} \nabla_K^2 - \frac{1}{2}\sum_{i=1}^{N} \nabla_i^2 - \sum_{K=1}^{M}\sum_{i=1}^{N} \frac{Z_K}{r_{Ki}} + \sum_{i>j}^{N} \frac{1}{r_{ij}} + \sum_{K>L}^{M} \frac{Z_K Z_L}{R_{KL}}. \tag{2.6}$$

For further discussions, it is convenient to split this Hamiltonian into three parts

$$\hat{H}_{\mathrm{mol}} = \hat{T}_{\mathrm{nuc}} + \hat{H}_{\mathrm{el}} + E_{\mathrm{nuc}} \tag{2.7}$$

with

$$\hat{T}_{\mathrm{nuc}} = -\sum_{K=1}^{M} \frac{1}{2M_K} \nabla_K^2, \tag{2.8}$$

$$\hat{H}_{\mathrm{el}} = -\frac{1}{2}\sum_{i=1}^{N} \nabla_i^2 - \sum_{K=1}^{M}\sum_{i=1}^{N} \frac{Z_K}{r_{Ki}} + \sum_{i>j}^{N} \frac{1}{r_{ij}}, \tag{2.9}$$

$$E_{\mathrm{nuc}} = \sum_{K>L}^{M} \frac{Z_K Z_L}{R_{KL}}. \tag{2.10}$$

$\hat{T}_{\mathrm{nuc}}$ is the operator for the kinetic energy of the nuclei and E_{nuc} is the nuclear repulsion energy. The remaining operator $\hat{H}_{\mathrm{el}}$ is called the electronic Hamiltonian and can be written as

$$\hat{H}_{\mathrm{el}} = \sum_{i=1}^{N} \hat{h}(i) + \sum_{i>j}^{N} \hat{g}(i,j) \tag{2.11}$$

where the one-electron operator $\hat{h}(i)$ is given as

$$\hat{h}(i) = -\frac{1}{2}\nabla_i^2 - \sum_{K=1}^{M} \frac{Z_K}{r_{Ki}} \tag{2.12}$$

and the two-electron operator $\hat{g}(i,j)$ as

$$\hat{g}(i,j) = \frac{1}{r_{ij}}. \tag{2.13}$$

We furthermore define the electronic Hamiltonian including the nuclear repulsion energy as

$$\widehat{H} = \widehat{H}_{\mathrm{el}} + E_{\mathrm{nuc}}. \tag{2.14}$$

The non-relativistic molecular Hamiltonian is spin-free, i.e. it does not contain the spin of the electrons (or nuclei). This is an approximation, which does not hold for heavier elements, for example lanthanides, where relativistic effects become more important. We will discuss relativistic effects in the next chapter. In this non-relativistic description, the Hamiltonian commutes with the total N-electron spin operators $\hat{S}^2$ and $\hat{S}_z$:

$$\left[\widehat{H}_{\mathrm{mol}}, \hat{S}^2\right] = 0, \qquad \left[\widehat{H}_{\mathrm{mol}}, \hat{S}_z\right] = 0, \qquad \left[\hat{S}^2, \hat{S}_z\right] = 0. \tag{2.15}$$

This implies that the total wave function of the molecule should be a simultaneous eigenfunction of all three operators:

$$\widehat{H}_{\mathrm{mol}} \Psi_k^{\mathrm{mol}}(\mathbf{x}, \mathbf{R}) = E_k^{\mathrm{mol}} \Psi_k^{\mathrm{mol}}(\mathbf{x}, \mathbf{R}) \tag{2.16}$$

$$\hat{S}^2 \Psi_k^{\mathrm{mol}}(\mathbf{x}, \mathbf{R}) = S(S+1) \Psi_k^{\mathrm{mol}}(\mathbf{x}, \mathbf{R}) \tag{2.17}$$

$$\hat{S}_z \Psi_k^{\mathrm{mol}}(\mathbf{x}, \mathbf{R}) = M_S \Psi_k^{\mathrm{mol}}(\mathbf{x}, \mathbf{R}). \tag{2.18}$$

2.1.2. The Born-Oppenheimer approximation

The molecular Schrödinger equation is a very complicated eigenvalue equation and cannot be solved exactly. Therefore approximations have to be introduced to allow its solution, without significantly affecting the accuracy. The most fundamental simplification is the Born-Oppenheimer (BO) approximation[53]. This approximation allows the separation of the electronic and nuclear motions. It is based on the fact that the nuclei are much heavier than the electrons and therefore move much more slowly, which implies that the electronic motion instantly adapts to the nuclear movements.

First, let us assume the Schrödinger equation for fixed nuclear positions, i.e. in the absence of nuclear motion. In this case, the operator for the nuclear kinetic energy, $\hat{T}_{\mathrm{nuc}}$, is neglected. The nuclear coordinates enter as constant parameters $\overline{\mathbf{R}}$ into the Schrödinger equation, which yields the *electronic Schrödinger equation*

$$\hat{H}\Psi_n^{(\mathrm{el})}(\mathbf{x},\overline{\mathbf{R}}) = E_n(\overline{\mathbf{R}})\Psi_n^{(\mathrm{el})}(\mathbf{x},\overline{\mathbf{R}}). \tag{2.19}$$

$\Psi_n^{(\mathrm{el})}(\mathbf{x},\overline{\mathbf{R}})$ are the *electronic wavefunctions* and they depend parametrically on the nuclear coordinates. The same holds for the electronic eigenvalues $E_n(\overline{\mathbf{R}})$. The quantum number n specifies the *electronic state*.

To obtain $E_n(\overline{\mathbf{R}})$, one has to solve the electronic Schrödinger position for each nuclear position $\overline{\mathbf{R}}$. Since $\hat{H}$ is invariant with respect to rotations and translations of the whole molecule, $E_n(\overline{\mathbf{R}})$ only depends on $3M-6$ ($3M-5$ for linear molecules) internal coordinates, i.e. bond angles and bond lengths. In practice, the electronic Schrödinger equation is solved on a grid of nuclear coordinates $\overline{\mathbf{R}}$ to obtain $E_n(\overline{\mathbf{R}})$ for each grid point and then the energies are interpolated between these grid points. The resulting function $E_n(\mathbf{R})$ is then a continuous function of the nuclear coordinates $\mathbf{R}$ and called *potential energy surface* (PES) for the electronic state n.

Up to this point, no nuclear motions were involved. However, the electronic wave functions $\Psi_n^{(\mathrm{el})}(\mathbf{x},\mathbf{R}) \equiv \Psi_n(\mathbf{x},\mathbf{R})$ form a complete basis in the space of electronic coordinates $\mathbf{x}$, because they are eigenfunctions of the Hermitian operator $\hat{H}$. Therefore, the total molecular wave function can be expanded in this basis for each choice of the nuclear coordinates $\mathbf{R}$:

$$\Psi_k^{\mathrm{mol}}(\mathbf{x},\mathbf{R}) = \sum_m \Psi_m(\mathbf{x},\mathbf{R})\, \chi_{mk}\,(\mathbf{R}) \tag{2.20}$$

where the expansion coefficients $\chi_{mk}(\mathbf{R})$ depend only on the nuclear coordinates.

Inserting this *ansatz* into the molecular Schrödinger equation, multiplying from the left by $\Psi_n^*(\mathbf{x},\mathbf{R})$, integrating over all electronic coordinates and neglecting all terms containing derivatives of $\Psi_m(\mathbf{x},\mathbf{R})$ with respect to $\mathbf{R}$, which is the mathematical foundation of the Born-Oppenheimer approximation, yields the *Schrödinger equation for nuclear motion* for the electronic state n

$$\left[\hat{T}_{\mathrm{nuc}} + E_n(\mathbf{R})\right]\chi_{nk}(\mathbf{R}) = E_{nk}^{\mathrm{mol}}\chi_{nk}(\mathbf{R}) \tag{2.21}$$

where $\chi_{nk}(\mathbf{R})$ are the nuclear wavefunctions.

It should be noted that the index for the total state k originally included all electronic and nuclear states. In the Born-Oppenheimer approximation, the molecular states are defined by two quantum numbers n, for the electronic state, and k, for the eigenstates of the Schrödinger equation for the nuclear motion corresponding to vibrations and rotations. The quantum number k can approximately be further separated into quantum number v, for vibration, and the quantum numbers J, K for rotation. There can be further quantum numbers if also the nuclear spin is taken into account. The molecular energies in this case are then denoted as $E_{nk}^{\mathrm{mol}} = E_{n,v,J,K,\ldots}^{\mathrm{mol}}$. The Schrödinger equation for the nuclear motion shows that $E_n(\mathbf{R})$ can be considered as an effective potential, in which the nuclei move. The total molecular wave function in the Born-Oppenheimer approximation $\Psi_{nk}^{\mathrm{mol}}(\mathbf{x},\mathbf{R})$ is given as a simple product of the electronic wavefunction $\Psi_n(\mathbf{x},\mathbf{R})$ and the nuclear wavefunction $\chi_{nk}(\mathbf{R})$

$$\Psi_{nk}^{\mathrm{mol}}(\mathbf{x},\mathbf{R}) = \Psi_n(\mathbf{x},\mathbf{R})\chi_{nk}(\mathbf{R}). \tag{2.22}$$

2.1.3. Representations of many-electron wavefunctions

2.1.3.1. Spin orbitals

First, we will discuss the representation of one-electron functions by spin-orbitals. In general, the spin-dependent eigenfunctions $\psi_i^{\sigma}(\mathbf{x})$ of a one-electron operator such as $\hat{h}$ can be written as a product of a spatial function $\phi_i(\mathbf{r})$ and a spin function $\sigma(s)$, which is either $\alpha(s)$ (corresponding to $m_s = +1/2$) or $\beta(s)$ (corresponding to $m_s = -1/2$):

$$\psi_i^{\alpha}(\mathbf{x}) = \phi_i(\mathbf{r})\alpha(s) \tag{2.23}$$

$$\psi_i^{\beta}(\mathbf{x}) = \phi_i(\mathbf{r})\beta(s) \tag{2.24}$$

$\psi_i^{\sigma}(\mathbf{x})$ are called *spin orbitals* and the spatial functions $\phi_i(\mathbf{r})$ *orbitals*. The spin functions $\alpha(s)$ and $\beta(s)$ are orthonormal, which can be written in Bra-Ket-notation (where $\alpha(s) \equiv |\alpha\rangle$, $\beta(s) \equiv |\beta\rangle$) as :

$$\langle\alpha|\alpha\rangle = \int \alpha^*(s)\alpha(s)\mathrm{d}s = 1 \tag{2.25}$$

$$\langle\beta|\beta\rangle = \int \beta^*(s)\beta(s)\mathrm{d}s = 1 \tag{2.26}$$

$$\langle\alpha|\beta\rangle = \int \alpha^*(s)\beta(s)\mathrm{d}s = 0 \tag{2.27}$$

These spin orbitals can be used to construct many-electron wave functions.

2.1.3.2. Slater-determinants and Slater-Condon rules

In quantum theory, all fundamental particles can be either classified as *fermions*, having a half-integer spin, or *bosons*, having an integer spin. The total wave function of a system must obey the *Pauli-principle*, which states that the wave function must be symmetric with respect to the exchange of two identical bosons and antisymmetric with respect to the exchange of two identical fermions. Electrons, having a spin of $S = 1/2$, are fermions and therefore the total wave function must be antisymmetric with respect to the exchange of the space-spin coordinates of any pair of electrons, e.g.

$$\Psi(\mathbf{x}_1, \mathbf{x}_2, \mathbf{x}_3, \dots, \mathbf{x}_N) = -\Psi(\mathbf{x}_1, \mathbf{x}_3, \mathbf{x}_2, \dots, \mathbf{x}_N) \tag{2.28}$$

In quantum chemistry, the building blocks of antisymmetric many-electron wave functions are *Slater determinants*, which are antisymmetrized products of (usually orthonormal) spin-orbitals taken from a *one-electron basis* $\{\psi_k(\mathbf{x}_i)\}$. From now on, we will always assume we are dealing with orthonormal spin-orbitals. In this case, a normalized N-electron Slater determinant $\Phi \equiv \Phi_{klm\dots r}(\mathbf{x}_1, \mathbf{x}_2, \mathbf{x}_3, \dots, \mathbf{x}_N)$ can be written as

$$\Phi_{klm\dots r}(\mathbf{x}_1, \mathbf{x}_2, \mathbf{x}_3, \dots, \mathbf{x}_N) = \frac{1}{\sqrt{N!}} \begin{vmatrix} \psi_k(\mathbf{x}_1) & \psi_l(\mathbf{x}_1) & \psi_m(\mathbf{x}_1) & \cdots & \psi_r(\mathbf{x}_1) \\ \psi_k(\mathbf{x}_2) & \psi_l(\mathbf{x}_2) & \psi_m(\mathbf{x}_2) & \cdots & \psi_r(\mathbf{x}_2) \\ \psi_k(\mathbf{x}_3) & \psi_l(\mathbf{x}_3) & \psi_m(\mathbf{x}_3) & \cdots & \psi_r(\mathbf{x}_3) \\ \vdots & \vdots & \vdots & \vdots & \vdots \\ \psi_k(\mathbf{x}_N) & \psi_l(\mathbf{x}_N) & \psi_m(\mathbf{x}_N) & \dots & \psi_r(\mathbf{x}_N) \end{vmatrix}. \tag{2.29}$$

Slater-determinants are written in more compact notation as

$$\Phi_{klm\dots r}(\mathbf{x}_1, \mathbf{x}_2, \mathbf{x}_3, \dots, \mathbf{x}_N) = \|\psi_k(\mathbf{x}_1)\psi_l(\mathbf{x}_2)\psi_m(\mathbf{x}_3)\dots\psi_r(\mathbf{x}_N)\| \tag{2.30}$$

It can be immediately seen that a Slater determinant fulfils the Pauli-principle, since the exchange of two electrons means the exchange of two rows of the determinants, which changes its sign. Furthermore, Slater determinants fulfil the requirement of indistinguishability of electrons, because one can never say which electron is in a particular orbital or at a particular position. Moreover, each spin-orbital can be occupied by only one electron, because a Slater determinant vanishes if two columns are identical. The distribution of N electrons in N different spin-orbitals is called *electron configuration*. In the *Hartree-Fock (HF) method*, which will be discussed later, the wave function *ansatz* is a single

Slater determinant and the (optimum) spin-orbitals are obtained by iteratively solving the *Hartree-Fock equations* for a certain electron configuration.

Let us assume we have a set $\{\psi_k(\mathbf{x}_i)\}$ of M spin-orbitals and N electrons. Then, the number of determinants N_{det} which can be constructed by distributing N electrons over M spin-orbitals is given by

$$N_{\mathrm{det}} = \frac{M!}{N!\,(M-N)!}. \tag{2.31}$$

This number grows very rapidly with the number of electrons and spin-orbitals, which is an important reason for the large time requirements for ab initio calculations for large molecules, as we will see later.

In general, any N-electron wave function can then be written as a linear combination of all possible Slater-determinants (which form an N-electron basis spanning an N-electron space):

$$\Psi(\mathbf{x}_1, \mathbf{x}_2, \mathbf{x}_3, \dots, \mathbf{x}_N) = \sum_I c_I \Phi_I(\mathbf{x}_1, \mathbf{x}_2, \mathbf{x}_3, \dots, \mathbf{x}_N) \tag{2.32}$$

The coefficients c_I of this expansion can be determined in different ways, for example by the variational method, which is based on the Rayleigh-Ritz principle. The Rayleigh-Ritz principle states that the energy expectation value is an upper bound to the exact energy, which means that the expansion coefficients can be determined by minimizing the energy expectation value with respect to them. The wave function *ansatz* (2.32) in combination with the variational method to determine the coefficients c_I is called *configuration interaction* (CI) and in case of a full configuration expansion (using all possible determinants constructed from the distribution of N electrons over all M spin-orbitals from $\{\psi_k(\mathbf{x}_i)\}$) *full configuration interaction* (FCI). This procedure yields the best possible, i.e. lowest, energy and wave function for a given one-electron basis set $\{\psi_k(\mathbf{x}_i)\}$. Minimization of the CI coefficients with the constraint that the wave function is normalized and assuming an orthonormal set of Slater determinants lead to a matrix eigenvalue equation

$$\mathbf{HC} = \mathbf{CE}. \tag{2.33}$$

$\mathbf{H}$ is called *Hamiltonian matrix* with the matrix elements

$$\begin{aligned} H_{IJ} &= \langle \Phi_I | \hat{H} | \Phi_J \rangle \\ &= \int \mathrm{d}\,\mathbf{x}_1 \int \mathrm{d}\mathbf{x}_2 \ldots \int \mathrm{d}\mathbf{x}_N \, \Phi_I^*(\mathbf{x}_1, \mathbf{x}_2, \mathbf{x}_3, \ldots, \mathbf{x}_N) \hat{H} \Phi_J(\mathbf{x}_1, \mathbf{x}_2, \mathbf{x}_3, \ldots, \mathbf{x}_N). \end{aligned} \tag{2.34}$$

$\mathbf{C}$ is the coefficient matrix containing the n-th eigenvector of $\mathbf{H}$ with eigenvalue E_n in column n and $\mathbf{E}$ is a diagonal matrix containing the energy eigenvalues on its diagonal

$$\mathbf{E} = \begin{pmatrix} E_1 & 0 & 0 & \cdots \\ 0 & E_2 & 0 & \cdots \\ 0 & 0 & E_3 & \cdots \\ \vdots & \vdots & \vdots & \ddots \end{pmatrix}. \tag{2.35}$$

The matrix elements H_{IJ} can be calculated using the *Slater-Condon rules*. We define a *reference determinant* in which, for simplicity, the first N spin-orbitals of $\{\psi_k(\mathbf{x}_i)\}$ are occupied

$$\Phi = \left\| \psi_1(\mathbf{x}_1)\psi_2(\mathbf{x}_2) \ldots \psi_i(\mathbf{x}_i) \ldots \psi_j(\mathbf{x}_j) \ldots \psi_k(\mathbf{x}_k) \ldots \psi_N(\mathbf{x}_N) \right\|. \tag{2.36}$$

We can then define “excited” determinants as

$$\Phi_i^a = \left\| \psi_1(\mathbf{x}_1)\psi_2(\mathbf{x}_2) \ldots \psi_a(\mathbf{x}_i) \ldots \psi_j(\mathbf{x}_j) \ldots \psi_k(\mathbf{x}_k) \ldots \psi_N(\mathbf{x}_N) \right\|, \tag{2.37}$$

$$\Phi_{ij}^{ab} = \left\| \psi_1(\mathbf{x}_1)\psi_2(\mathbf{x}_2) \ldots \psi_a(\mathbf{x}_i) \ldots \psi_b(\mathbf{x}_j) \ldots \psi_k(\mathbf{x}_k) \ldots \psi_N(\mathbf{x}_N) \right\|, \tag{2.38}$$

$$\Phi_{ijk}^{abc} = \left\| \psi_1(\mathbf{x}_1)\psi_2(\mathbf{x}_2) \ldots \psi_a(\mathbf{x}_i) \ldots \psi_b(\mathbf{x}_j) \ldots \psi_c(\mathbf{x}_k) \ldots \psi_N(\mathbf{x}_N) \right\|, \tag{2.39}$$

…

where Φ_i^a, Φ_{ij}^{ab},… are called singly,doubly,… excited determinants.

The Slater-Condon rules for the matrix elements of the Hamiltonian matrix in atomic units read

$$\langle\Phi|\widehat{H}_{\mathrm{el}}|\Phi\rangle = \sum_{i}^{\mathrm{occ}}\langle\psi_i|\hat{h}|\psi_i\rangle + \frac{1}{2}\sum_{i,j}^{\mathrm{occ}}\left[\left\langle\psi_i\psi_j\left|\frac{1}{r_{12}}\right|\psi_i\psi_j\right\rangle - \left\langle\psi_i\psi_j\left|\frac{1}{r_{12}}\right|\psi_j\psi_i\right\rangle\right] \tag{2.40}$$

$$\langle\Phi_i^a|\widehat{H}_{\mathrm{el}}|\Phi\rangle = \langle\psi_a|\hat{h}|\psi_i\rangle + \sum_{j}^{\mathrm{occ}}\left[\left\langle\psi_a\psi_j\left|\frac{1}{r_{12}}\right|\psi_i\psi_j\right\rangle - \left\langle\psi_a\psi_j\left|\frac{1}{r_{12}}\right|\psi_j\psi_i\right\rangle\right] \tag{2.41}$$

$$\langle\Phi_{ij}^{ab}|\widehat{H}_{\mathrm{el}}|\Phi\rangle = \left\langle\psi_a\psi_b\left|\frac{1}{r_{12}}\right|\psi_i\psi_j\right\rangle - \left\langle\psi_a\psi_b\left|\frac{1}{r_{12}}\right|\psi_j\psi_i\right\rangle \tag{2.42}$$

$$\langle\Phi_{ijk}^{abc}|\widehat{H}_{\mathrm{el}}|\Phi\rangle = 0 \tag{2.43}$$

where the summations run over all spin-orbitals that are occupied in Φ and the matrix elements vanish if two determinants differ by more than two spin-orbitals. The electrons are indistinguishable due to the Pauli-principle and therefore the integrations in all one-electron integrals $\langle\psi_r(\mathbf{x}_1)|\hat{h}(\mathbf{r}_1)|\psi_s(\mathbf{x}_1)\rangle$ and the integrations in all two-electron integrals $\left\langle\psi_r(\mathbf{x}_1)\psi_s(\mathbf{x}_2)\left|\frac{1}{r_{12}}\right|\psi_t(\mathbf{x}_1)\psi_u(\mathbf{x}_2)\right\rangle$ run over the electron coordinates with label 1 and 2, since the value of the integrals is independent of the labelling of the coordinates.

2.2. Relativistic effects

This chapter covers the basic concepts of relativistic quantum chemistry. For a more detailed explanation of special relativity and derivations, the interested reader is referred to the literature used for the formulation of this chapter[54].

2.2.1. Dirac equation for a free electron

For heavier elements, the non-relativistic Schrödinger equation is not sufficient for an accurate calculation of energies. Due to the larger nuclear charge, the electrons move faster and their speed attains a significant fraction of the speed of light c. Therefore, a quantum theory is required which takes into account the principles of special relativity. In special relativity, the equations of motion have to be *covariant*, i.e. they should keep their basic form, under *Lorentz transformations*. The non-relativistic Schrödinger equation is not covariant under Lorentz transformations, therefore a new equation is needed. In 1928, Dirac proposed a new quantum mechanical equation for the freely moving electron which fulfils the requirement for Lorentz-covariance, the *time-dependent Dirac equation* (in SI units)

$$\mathrm{i}\hbar\frac{\partial}{\partial t}\Psi = \left[\frac{\hbar c}{\mathrm{i}}\vec{\alpha}\nabla + \beta m_e c^2\right]\Psi \equiv H^D\Psi. \tag{2.44}$$

The vector $\vec{\alpha} = (\alpha^1, \alpha^2, \alpha^3)$ contains three 4×4 matrices given by

$$\alpha^1 = \begin{pmatrix} 0 & 0 & 0 & 1 \\ 0 & 0 & 1 & 0 \\ 0 & 1 & 0 & 0 \\ 1 & 0 & 0 & 0 \end{pmatrix}, \alpha^2 = \begin{pmatrix} 0 & 0 & 0 & -\mathrm{i} \\ 0 & 0 & \mathrm{i} & 0 \\ 0 & -\mathrm{i} & 0 & 0 \\ \mathrm{i} & 0 & 0 & 0 \end{pmatrix}, \alpha^3 = \begin{pmatrix} 0 & 0 & 1 & 0 \\ 0 & 0 & 0 & -1 \\ 1 & 0 & 0 & 0 \\ 0 & -1 & 0 & 0 \end{pmatrix} \tag{2.45}$$

and the matrix β given by

$$\beta = \begin{pmatrix} 1 & 0 & 0 & 0 \\ 0 & 1 & 0 & 0 \\ 0 & 0 & -1 & 0 \\ 0 & 0 & 0 & -1 \end{pmatrix}. \tag{2.46}$$

With the three Pauli spin matrices $\vec{\sigma} = (\sigma_1, \sigma_2, \sigma_3)$ given by

$$\sigma_1 = \begin{pmatrix} 0 & 1 \\ 1 & 0 \end{pmatrix}, \qquad \sigma_2 = \begin{pmatrix} 0 & -\mathrm{i} \\ \mathrm{i} & 0 \end{pmatrix}, \qquad \sigma_3 = \begin{pmatrix} 1 & 0 \\ 0 & -1 \end{pmatrix}, \tag{2.47}$$

the α^i and β matrices can be written in compact form as

$$\alpha^i = \begin{pmatrix} 0 & \sigma_i \\ \sigma_i & 0 \end{pmatrix}, \quad \beta = \begin{pmatrix} \mathbf{1}_2 & 0 \\ 0 & -\mathbf{1}_2 \end{pmatrix}, \tag{2.48}$$

where $\mathbf{1}_2$ is the 2×2 unit matrix.

The space and time variables of the electron in the time-dependent Dirac equation are well separated, therefore one can use the *ansatz*

$$\Psi(t, \vec{r}) = \exp\left(-\frac{\mathrm{i}Et}{\hbar}\right)\Psi(\vec{r}), \tag{2.49}$$

which, after insertion into the time-dependent Dirac equation, leads to the *time-independent Dirac equation* for $\Psi(\vec{r})$**:**

$$\left[\frac{\hbar c}{\mathrm{i}}\vec{\alpha}\nabla + \beta m_e c^2\right]\Psi(\vec{r}) = E\Psi(\vec{r}) \tag{2.50}$$

The wave function Ψ contains four components and is called a 4-spinor or simply a spinor. Because of the block structure of the α^i and β matrices the spinor is often split into an upper 2-spinor Ψ^L and a lower 2-spinor Ψ^S. Ψ^L is called *large component* of the 4-spinor and Ψ^S *small component*:

$$\Psi = \begin{pmatrix} \Psi_1 \\ \Psi_2 \\ \Psi_3 \\ \Psi_4 \end{pmatrix} = \begin{pmatrix} \Psi^L \\ \Psi^S \end{pmatrix}. \tag{2.51}$$

The Dirac equation for the freely moving particle has four solutions, which can be divided into two classes. The first class contains two eigensolutions corresponding to a spin-$1/2$ particle with positive energy and the second class to a spin-$1/2$ particle with negative energy. The first class describes the electron while the second class describes its antiparticle, the *positron* (which has opposite charge). For electronic solutions the relation $\Psi^L > \Psi^S$

holds (provided that the kinetic energy is small compared to the rest energy $m_e c^2$), which explains the names *large* and *small* component. It should be noted that in *quantum field theory*, the fundamental (many-particle) Hamiltonian of the theory is constructed using the principles of *second quantization* and the states with negative energy are reinterpreted as positronic states with positive energy, due to so called *normal ordering*. However, an introduction into quantum field theory is beyond the scope of this chapter and the interested reader is referred to the literature[54,55]. The (positive and negative) energy eigenvalues of the freely moving particle fulfil the energy-momentum relation of special relativity

$$E = \pm\sqrt{c^2\vec{p}^2 + m_e^2 c^4}, \tag{2.52}$$

where $\vec{p}$ is the momentum of the particle (electron or positron).

2.2.2. Molecular many-electron theory based on the Dirac equation

A strictly Lorentz covariant description of molecules and the electromagnetic interactions within them is given by *quantum electrodynamics (QED)*. In this quantum field theory, the electron-positron field and the photon field (quantized electromagnetic field) are treated on equal footing, including their mutual interactions. However, the second quantized Hamiltonian of QED[54], $\widehat{H}_{QED}$, is rather complicated and contains many degrees of freedom which are not relevant for many applications of chemical interest. In order to simplify the calculations, a first quantized quasi-relativistic many-particle Hamiltonian is desirable, which can be derived from $\widehat{H}_{QED}$. An example of such a Hamiltonian is given by the *Dirac-Coulomb-Breit (DCB)* many-electron Hamiltonian $\widehat{H}_{DCB}$, which reads

$$\widehat{H}_{DCB} = \sum_{i}^{N} \hat{h}^D(i) + \sum_{i<j}^{N} \hat{g}_{DCB}(i,j), \tag{2.53}$$

where the *Dirac Hamiltonian* is given by (in SI units)

$$\hat{h}^D(i) = c\vec{\alpha}_i \left(\hat{\vec{p}}_i - \frac{e}{c}\vec{A}_{\text{ext}}\right) + (\beta_i - 1)m_e c^2 + \hat{V}_{\text{nuc}}(i), \tag{2.54}$$

with the three-dimensional momentum operator $\hat{\vec{p}}_i = \frac{\hbar}{\mathrm{i}}\nabla_i$ and the (three-dimensional) external vector potential $\vec{A}_{\mathrm{ext}}$ related to the external magnetic field $\vec{B}_{\mathrm{ext}}$ by $\vec{B}_{\mathrm{ext}} = \nabla \times \vec{A}_{\mathrm{ext}}$and $\vec{A}_{\mathrm{ext}} = 0$ if no external magnetic field is present. In the following, we will set $\vec{A}_{\mathrm{ext}} = 0$ in $\hat{h}^D$, unless otherwise noted. The term $\hat{V}_{\mathrm{nuc}}(i) = -\sum_{K=1}^{M}\sum_{i=1}^{N}\frac{Z_K e}{4\pi\epsilon_0 r_{Ki}}$ describes the Coulomb interaction of the electrons with the nuclei. Note that the energy scale of this operator is shifted by $-Nm_e c^2$ (compared with the sum of one-particle Dirac-operators H^D from equation (2.44)), i.e. the rest energy of all electrons. The mutual electron-electron interaction is described by

$$\hat{g}_{DCB}(i,j) = \sum_{i>j}^{N}\frac{e^2}{4\pi\epsilon_0 r_{ij}} + B_\omega(i,j), \tag{2.55}$$

i.e. it is composed out of the Coulomb interaction and the *frequency-dependent Breit interaction* $B_\omega(i,j)$ which accounts for retardation effects and magnetic contributions of the electron-electron interaction mediated by *virtual photons* (with angular frequency ω) and is a correction term for the (Lorentz non-covariant) *instantaneous* Coulomb interaction. If the frequency-dependent Breit interaction is neglected (i.e. $B_\omega(i,j) = 0$), one arrives at the Dirac-Coulomb Hamiltonian $\widehat{H}_{DC}$, which is often sufficient for chemical applications (except for the calculation of spin-orbit splittings). The total molecular wave function can now be again expanded in terms of Slater-determinants, which contain 4-spinors now instead of spin-orbitals. However, much more integrals and significantly larger basis sets are needed for these four-component relativistic calculations and often yield them unfeasible for molecular applications. Moreover, in quantum chemistry, one is only interested in the electronic solutions, not the positronic ones. For the electronic eigenstates of the Dirac-Coulomb(-Breit) Hamiltonian, the lower components Ψ^S of the 4-spinors are small (if the nuclear charge is not too large, which is only the case for super heavy elements ($Z \geq 104$)). We therefore seek to eliminate the small component. This can, e.g., be done by *elimination techniques*, where the small component is eliminated by implicitly including it in an equation for the large component. However, elimination techniques yield energy-dependent operators[56]. A more elegant solution is the use of *transformation techniques*. One of them is the Douglas-Kroll-Hess transformation, which will be discussed in the next section.

2.2.3. Douglas-Kroll-Hess theory

This chapter describes the basic concepts of Douglas-Kroll-Hess theory. For a more detailed description including specific mathematical details, the interested reader is referred to the literature which was used for the preparation of this chapter[54,56]. We will use atomic units throughout this chapter.

The occurrence of states with negative energies - associated with positrons - is a conceptual problem of the four-component description presented in the last section. These states have no physical meaning, due to a number of reasons: First, the Dirac-Coulomb(-Breit) Hamiltonian presented in the last section is a first-quantized Hamiltonian, which does not allow for particle creation processes (e.g. the creation of electron-positron pairs) and keeps the number of particles constant. To account for these particle creation processes, one would need the fully Lorentz-covariant second-quantized QED Hamiltonian[54]. Furthermore, the full second-quantized QED Hamiltonian assigns positive energies to positrons, in contrast to the first-quantized Dirac-Coulomb(-Breit) Hamiltonian, which gives negative energies to the positronic states. The third reason is that molecular calculations usually employ local Gaussian-type basis functions, which cannot adequately describe the negative-energy states, because they represent unbound continuum states. This is due to the fact that the electron-nucleus potential $\hat{V}_{\mathrm{nuc}}(i)$ is only attractive for electronic bound states, due to the negative charge of the electron. Therefore, the positronic states are only troublesome artefacts in four-component relativistic quantum chemical calculations.

It would be elegant to replace the four-component formulation by an approach of the same accuracy, but without the appearance of negative-energy states. Such an approach is given by *transformation techniques*, such as the Douglas-Kroll-Hess (DKH) transformation discussed in this chapter. This method aims at a block-diagonalization of the Dirac Hamiltonian

$$\hat{h}^D_{\mathrm{bd}} = U\hat{h}^D U^\dagger = \begin{pmatrix} h_+ & 0 \\ 0 & h_- \end{pmatrix} \tag{2.56}$$

to obtain an 2×2 upper block Hamiltonian h_+ (sometimes called a *no-pair* operator) of reduced dimension which can be used for the relativistic description of electrons only. The

negative energy states are then described by the lower block h_-, which is simply neglected. The transformation can in principle be also applied to many-electron operators (such as $\hat{g}_{DCB}(i,j)$), but for simplicity, we will only discuss the application to the one-electron Dirac Hamiltonian in external field $\hat{h}^D$.

The transformation U is a unitary transformation in order to preserve the spectrum of the Hamiltonian and the orthonormality of the states. Applying U to the four-component wave function Ψ yields the transformed wave function ϕ,

$$\phi = U\begin{pmatrix}\Psi^L\\ \Psi^S\end{pmatrix} = \begin{pmatrix}U_{LL}\Psi^L + U_{LS}\Psi^S\\ U_{SL}\Psi^L + U_{SS}\Psi^S\end{pmatrix} = \begin{pmatrix}\phi^L\\ \phi^S\end{pmatrix}, \tag{2.57}$$

with $\phi^S = \mathbf{0}$ for electronic solutions. The eigenvalue equation for a relativistic electron then reduces to a 2-component form:

$$h_+\phi^L = E_+\phi^L \tag{2.53}$$

The 2×2 Hamiltonian h_+ can be further split into a one-component spin-free Hamiltonian and a two-component spin-dependent Hamiltonian. In many applications only the spin-free operator is used to account for *scalar relativistic effects* by modifying only the one-electron integrals $\langle\psi_r|\hat{h}|\psi_s\rangle$.

The matrix U can be formally given in closed-form, but the elements of U can only be obtained by iteratively solving a complicated equation. Therefore it is useful to split U into a sequence of unitary transformations in order to block-diagonalize $\hat{h}^D$ in a stepwise fashion:

$$U = \cdots U_4U_3U_2U_1U_0 \tag{2.58}$$

$$\hat{h}^D_{\mathrm{bd}} = \cdots U_4U_3U_2U_1U_0\hat{h}^D U_0^\dagger U_1^\dagger U_2^\dagger U_3^\dagger U_4^\dagger \cdots = \begin{pmatrix}h_+ & 0\\ 0 & h_-\end{pmatrix} \tag{2.59}$$

The requirement for each unitary transformation U_i is to reduce the (block-)off-diagonal or *odd* terms order by order. The formal expansion parameter of the Douglas-Kroll-Hess transformation is the external potential $\hat{V}_{\mathrm{nuc}}$, which allows identifying the order k of the

expansion, by relating it to the block-diagonal or *even* operators $\mathcal{E}_k$. To obtain the full block-diagonal Hamiltonian $\hat{h}_{\mathrm{bd}}^{D}$, all these even operators have to be summed up,

$$\hat{h}_{\mathrm{bd}}^{D} = \sum_{k=0}^{\infty} \mathcal{E}_k. \tag{2.60}$$

The partially transformed Hamiltonian $\hat{h}_{\mathrm{pt}}^{D}$ which is obtained after the m-th unitary transformation is given by

$$\hat{h}_{\mathrm{pt}}^{D} = \sum_{k=0}^{2m+1} \mathcal{E}_k + \sum_{k=2m+2}^{\infty} \mathcal{E}_k^{(m+1)} + \sum_{k=m+1}^{\infty} \mathcal{O}_k^{(m+1)}, \tag{2.61}$$

where each unitary transformation produces two orders k of the expansion parameter $\hat{V}_{\mathrm{nuc}}$. There are still odd operators $\mathcal{O}_k$ left which have to be eliminated by subsequent unitary transformations, which can only be fulfilled if the magnitude of $\mathcal{O}_k$ decreases for increasing k. Moreover, we require that the lowest $2m+1$ even terms $\mathcal{E}_k$ remain untouched by the subsequent unitary transformations and only the higher-order even terms $\mathcal{E}_k^{(m+1)}$ for $k \geq 2m+2$ are affected by the following unitary transformations. This requirement is necessary for the method to be systematically improvable by adding higher-order terms without changing the already existent low-order terms. In order to fulfil this requirement, each unitary matrix U_m has to be expanded into a power series

$$U_m = \sum_{j=0}^{\infty} a_{m,j} W_m^j = \mathbf{1} + \sum_{j=1}^{\infty} a_{m,j} W_m^j, \tag{2.62}$$

where each term of the series can be uniquely assigned to the order $k = m \times j$ with respect to the expansion parameter $\hat{V}_{\mathrm{nuc}}$ and with $a_{m,0} = 1$. This is the most general way for a parametrization of a unitary matrix with W_m being the parameter, which can be chosen arbitrarily as long as it fulfils the requirement to be anti-hermitian,

$$W_m^{\dagger} = -W_m, \tag{2.63}$$

in order to fulfil $U^\dagger U = \mathbf{1}$. This most general parametrization of the unitary matrices is called *generalized* DKH transformation. Due to the identity operator $\mathbf{1}$, the low-order even terms $\mathcal{E}_k$ with $k \leq 2m+1$ remain unchanged. The order of the term W_m^j is $m \times j$, therefore the product with an even term $\mathcal{E}_k$ is of order $k + (m \times j)$. This number is always larger than $2m+1$ for even products. It may be lower for odd products, but then the lower-order term will be eliminated in this or in a subsequent transformation step. Thus, the mentioned higher-order even operators remain unchanged in the following unitary transformation steps, while the lower-order odd operators get eliminated step-by-step. Therefore we have already obtained the final form of the even terms at an early stage of the DKH transformation and can simply neglect the remaining odd terms. It can be shown[54] that the step-by-step elimination of the odd terms $\mathcal{O}_k$ requires W_m to fulfil

$$[W_m, \mathcal{E}_0] - \frac{a_{m,0}}{a_{m,1}} \mathcal{O}_m^{(m)} = 0. \tag{2.64}$$

In order to derive the DKH Hamiltonian, the first transformation U_0 *must* be carried out as free-particle Foldy-Wouthuysen transformation[57,58]

$$U_0 \hat{h}^D U_0^\dagger = \mathcal{E}_0 + \mathcal{E}_1 + \mathcal{O}_1 \tag{2.65}$$

with

$$\mathcal{E}_0 = \beta E_p - c^2, \tag{2.66}$$

$$\mathcal{E}_1 = A_p \big(V + R_p V R_p\big) A_p, \tag{2.67}$$

$$\mathcal{O}_1 = \beta A_p \big[R_p, V\big] A_p, \tag{2.68}$$

where

$$E_p = \sqrt{c^2 \hat{\vec{p}}^2 + c^4}, \tag{2.69}$$

$$A_p = \sqrt{\frac{E_p + c^2}{2E_p}}, \tag{2.70}$$

$$R_p = \frac{c\vec{\alpha} \cdot \hat{\vec{p}}}{E_p + c^2}. \tag{2.71}$$

All following unitary transformations can then be carried out in an automated manner based on equation (2.64), which makes the calculation of DKH Hamiltonians of arbitrary order feasible.

The DKH Hamiltonian of order n is given by

$$\hat{h}_{DKH,n} = \sum_{k=0}^{n} \mathcal{E}_k. \tag{2.72}$$

Note that the lower right block of the Hamiltonian (responsible for the negative-energy states) is never calculated in practical calculations. Only the upper left block responsible for the description of electronic states is selectively calculated. For this purpose, the even terms of the transformation are collected and represented as commutators, which are then expanded and calculated employing proper commutation and anti-commutation rules for β and $\vec{\alpha}$ and exploiting the relation $\beta^2 = \mathbf{1}$. The interested reader is referred to the literature for more details[54,56,59]. The remaining 2×2 Hamiltonian can be further split into a spin-free (scalar-relativistic) and spin-dependent part by applying Dirac's relation[60].

For numerical quantum chemical calculations, where finite basis sets are employed, the $\hat{\vec{p}}^2$-containing terms in the DKH transformed Hamiltonian are calculated by applying a procedure invented by Hess[61]. In this approach, the primitive basis set is transformed to a basis in which the matrix representation of $\hat{\vec{p}}^2$ is diagonal. This basis is obtained by the diagonalization of the matrix representation of the non-relativistic kinetic energy operator

$\hat{\vec{p}}^2/(2m_e)$, which is anyway calculated in all quantum chemistry program packages. After transformation to this basis, where all $\hat{\vec{p}}^2$-containing terms have a diagonal representation, all even terms can be calculated and added using standard matrix operations. In the end, the obtained matrix representation of the DKH Hamiltonian can be transformed back to the initial basis by employing the inverse transformation.

Note that there are other ways for parametrizing the unitary matrices U_m (beside the most general parametrization presented above), for example the exponential parametrization $U_m = e^{W_m}$. All parametrizations can be expanded in a Taylor series and only differ in the resulting expansion coefficients. There is a dependence of the truncated Douglas-Kroll-Hess Hamiltonian on the parametrization for orders in the external potential of higher than four, but this dependence is very small.

Applying the DKH transformation to the Dirac-Coulomb-Breit Hamiltonian[62] , separating the spin $\hat{\vec{s}}_i = \frac{\hbar}{2}\vec{\sigma}_i$ by using Dirac's relation and keeping only the lowest (0th) order terms yields the *Douglas-Kroll-Hess spin-orbit (DKH SO) operator*

$$\hat{H}_{DKH}^{SO} = \sum_i \hat{h}_{1,DKH}^{SO}(i) + \sum_{i \neq j} \hat{h}_{2,DKH}^{SO}(i,j). \tag{2.73}$$

This operator is closely related to the Breit-Pauli (BP) SO-operator. The relation for the one-electron terms is given by

$$\hat{h}_{1,DKH}^{SO}(i) = B_{p_i} \hat{h}_{1,BP}^{SO}(i) B_{p_i}, \tag{2.74}$$

with

$$\hat{h}_{1,BP}^{SO}(i) = \sum_{K=1}^{M} \frac{Z_K}{2c^2} \hat{\vec{s}}_i \cdot \left(\frac{\vec{r}_{iK}}{r_{iK}^3} \times \hat{\vec{p}}_i \right) \tag{2.75}$$

and the kinematic factor

$$B_{p_i} = \frac{2c^2 A_{p_i}}{E_{p_i} + c^2}, \tag{2.76}$$

where E_{p_i} and A_{p_i} have been defined in equations (2.69) and (2.70).

The two-electron terms of the DKH SO operator are given by

$$\begin{aligned}\hat{h}_{2,DKH}^{SO}(i,j) = &-\frac{1}{2c^2} B_{p_i} A_{p_j} \hat{\vec{s}}_i \cdot \left(\frac{\vec{r}_{ij}}{r_{ij}^3} \times \hat{\vec{p}}_i\right) B_{p_i} A_{p_j} \\ &-\frac{1}{2c^2} B_{p_j} A_{p_i} 2\hat{\vec{s}}_j \cdot \left(\frac{\vec{r}_{ij}}{r_{ij}^3} \times \hat{\vec{p}}_i\right) B_{p_i} A_{p_j},\end{aligned} \tag{2.77}$$

and are also closely related to the two-electron terms of the BP SO operator

$$\hat{h}_{2,BP}^{SO}(i,j) = -\frac{1}{2c^2} \left(\hat{\vec{s}}_i + 2\hat{\vec{s}}_j\right) \cdot \left(\frac{\vec{r}_{ij}}{r_{ij}^3} \times \hat{\vec{p}}_i\right). \tag{2.78}$$

For low momenta, $A_{p_i} \to 1$ and $B_{p_i} \to 1$ and the DKH SO operator reduces to the BP SO operator. The kinematic factors A_{p_i} and B_{p_i} render the DKH SO operator variationally stable, in contrast to the BP SO operator. The latter should therefore only be used in low-order perturbation theory after a scalar-relativistic DKH all-electron calculation.

2.2.4. Pseudopotentials

A different way to cope with relativistic effects in an efficient way is the use of pseudopotentials (PPs)[54,62]. The direct impact of relativistic effects is mainly on the nucleus-near regions of both the core and valence orbitals. However, the core orbitals are often not affected very much in chemical reactions or in spectroscopic excitations of the valence shell. Therefore, it would be elegant to replace the core electrons by an effective potential, in order to reduce the computational requirements and absorb the direct and indirect impact of the relativistic effects on the valence orbitals into this effective potential.

2.2.4.1. Generalized Phillips-Kleinman equation

Let us assume there is an effective one-electron Hamiltonian $\widehat{H}_{\text{eff}}$ with an upper energy eigenfunction, called the valence (v) eigenfunction $|\varphi_v\rangle$ and several lower energy eigenfunctions, called core (c) eigenfunctions $|\varphi_c\rangle$

$$\widehat{H}_{\text{eff}}\,|\varphi_a\rangle = \varepsilon_a|\varphi_a\rangle\,, a\ \in \{c, v\}, \tag{2.79}$$

where we assume orthonormal eigenfunctions.

It is possible to show[62] that one can derive a nonlocal, energy-dependent effective one-electron operator, called the generalized Phillips-Kleinman (GPK) pseudopotential $\hat{V}^{GPK}$, which, when added to $\widehat{H}_{\text{eff}}$, yields an effective valence-only Hamiltonian with a so-called pseudovalence orbital $|\varphi_p\rangle$ as (lowest) eigenfunction with the eigenvalue ε_v

$$\left(\widehat{H}_{\text{eff}} + \hat{V}^{GPK}\right)|\varphi_p\rangle = \varepsilon_v|\varphi_p\rangle, \tag{2.80}$$

with

$$\hat{V}^{GPK} = -\widehat{H}_{\text{eff}}\hat{P}_c - \hat{P}_c\widehat{H}_{\text{eff}} + \hat{P}_c\widehat{H}_{\text{eff}}\hat{P}_c + \varepsilon_v\hat{P}_c \tag{2.81}$$

and the projection operator

$$\hat{P}_c = \sum_c |\varphi_c\rangle\langle\varphi_c|. \tag{2.82}$$

It can moreover be shown[62] that the functions $|\varphi_c\rangle$ do not necessarily have to be eigenfunctions of $\widehat{H}_{\text{eff}}$, and only $|\varphi_v\rangle$ is required to be one . The GPK Hamiltonian implicitly ensures valence-core orthogonality and therefore one can variationally optimize $|\varphi_p\rangle$ to obtain ε_v without the danger to collapse to core energy levels. Moreover, it is possible to construct a pseudovalence orbital $|\varphi_p\rangle$ with a smooth and nodeless radial structure and therefore low basis set requirements due to the implicit valence-core orthogonality conditions in the GPK Hamiltonian. The basic result of the GPK formalism is that it is in principle possible to find a potential can be added to a Hamiltonian that only acts on the valence electrons to allow for a variational solution of the Schrödinger equation without the problem of variational collapse to core-like solutions.

However, neither the pseudovalence orbitals nor the corresponding pseudopotential are unique. There are two ways to eliminate this non-uniqueness. The *energy-consistent PP* approach chooses a potential with physically reasonable analytical form and optimizes the

free parameters to fit all electron ab initio reference data, for example the energy spectrum obtained by solving the so-called *Dirac-Hartree-Fock equations* numerically for the corresponding atom[62]. In the *shape-consistent PP* approach one constructs some appropriately smooth (in the core region) pseudovalence orbital $|\varphi_p\rangle$ by some prescription and then generates the corresponding potential.

2.2.4.2. Analytical form of pseudopotentials

The molecular electronic *valence-only (VO)* Hamiltonian $\widehat{H}_{\mathrm{v}}$ (for nonrelativistic, scalar-relativistic or quasi-relativistic PPs) for n_v valence electrons and M cores (including 0-electron cores, i.e. nuclei) can be written as (in atomic units)

$$\widehat{H}_{\mathrm{v}} = -\frac{1}{2}\sum_{i=1}^{n_v}\nabla_i^2 + \sum_{i>j}^{n_v}\frac{1}{r_{ij}} + \sum_{K=1}^{M}\sum_{i=1}^{n_v}\left[-\frac{Q_K}{r_{Ki}} + \Delta V_{cv}^K(i)\right] + V_{cpp} + V_{cc}, \tag{2.83}$$

where the index i labels refers to electrons and the index K to cores/nuclei. The subscripts c and v again refer to core and valence. Q_K is the charge of the core K (obtained by subtracting the number of core electrons from the nuclear charge) and $\Delta V_{cv}^K(i)$ describes the core-valence interaction (beyond point-charge interaction) and is parametrized by pseudopotentials. V_{cc} describes the repulsion of all cores and nuclei and V_{cpp} is the core-polarization potential which accounts for the mutual polarization of the cores or the polarization of the cores by nuclei and valence electrons. Both V_{cc} and V_{cpp} can be parametrized according to different models[62]. We will focus on parametrization of $\Delta V_{cv}^K(i)$ in the following.

It turns out that the analytical form of pseudopotentials requires not only a (local) dependence on the electron-core/-nucleus distance r_{Ki}, but also on the angular momentum quantum number l, especially for atoms with valence orbitals of various angular symmetries[63–65]. This is already implied by the GPK Hamiltonian, when core orbitals with different l quantum numbers are present.

The so-called semilocal PP ansatz $\Delta V_{cv}^K(i) \cong \Delta V_{PP}^K(i)$ for a core K takes this into account and can be written as

$$\Delta V_{PP}^{K}(i) = \sum_{l=0}^{\infty} V_l^K(r_{Ki}) \hat{P}_l^K(i), \tag{2.84}$$

where $\hat{P}_l^K(i)$ is the angular momentum projection operator based on spherical harmonics $|lm, K\rangle$ with respect to core K

$$\hat{P}_l^K(i) = \sum_{m=-l}^{m=l} |lm, K\rangle\langle lm, K|. \tag{2.85}$$

We define $(L-1)$ as the largest angular momentum quantum number used by the core orbitals on centre K. The pseudopotential terms $V_l^K(r_{Ki})$ differ only slightly (from each other) for $l \geq L$[66], i.e.

$$V_l^K(r_{Ki}) \cong V_L^K(r_{Ki}) \text{ for } l \geq L, \tag{2.86}$$

therefore we can rewrite the pseudopotential $\Delta V_{PP}^K(i)$ using the closure property of the projection operators as[66]

$$\Delta V_{PP}^{K}(i) = V_L^K(r_{Ki}) + \sum_{l=0}^{L-1} [V_l^K(r_{Ki}) - V_L^K(r_{Ki})] \hat{P}_l^K(i). \tag{2.87}$$

This semilocal form of the pseudopotential can be used for nonrelativistic and scalar-relativistic pseudopotentials, i.e. pseudopotentials that do not include spin-orbit coupling. In order to include the spin-orbit interaction into the pseudopotential, some modifications are necessary. The orbitals resulting from nonrelativistic atomic Hartree-Fock calculations are degenerate if they belong to a shell with the same main quantum number n and the same angular momentum quantum number l. However, at the relativistic Dirac-Hartree-Fock (DHF) level, this degeneracy is lifted and depends on a further quantum number j, the quantum number of the *total angular momentum* of the orbital/spinor. This requires a semilocal pseudopotential with a lj-dependence

$$\Delta V_{PP}^{K}(i) = \sum_{l=0}^{\infty} \sum_{j=|l-1/2|}^{l+1/2} V_{lj}^{K}(r_{Ki}) \hat{P}_{lj}^{K}(i), \tag{2.88}$$

and projection operators constructed using spinor spherical harmonics

$$\hat{P}_{lj}^{K}(i) = \sum_{m=-j}^{m=j} |ljm, K\rangle\langle ljm, K|. \tag{2.89}$$

As for the nonrelativistic case, $\Delta V_{PP}^{K}(i)$ can again be approximately written as

$$\Delta V_{PP}^{K}(i) = V_{LJ}^{K}(r_{Ki}) + \sum_{l=0}^{L-1} \sum_{j=|l-1/2|}^{l+1/2} \left[V_{lj}^{K}(r_{Ki}) - V_{LJ}^{K}(r_{Ki})\right] \hat{P}_{lj}^{K}(i). \tag{2.90}$$

This term can be rewritten as the sum of a spin-free averaged (av) and a spin-dependent spin-orbit (so) term[67]

$$\Delta V_{PP}^{K}(i) = \Delta V_{PP,av}^{K}(i) + \Delta V_{PP,so}^{K}(i). \tag{2.91}$$

The spin-free term $\Delta V_{PP,av}^{K}(i)$ is a scalar-relativistic pseudopotential and corresponds to $\Delta V_{PP}^{K}(i)$ of equation (2.82) if the difference between $V_{LJ}^{K}(r_{Ki})$ and $V_{L}^{K}(r_{Ki})$ is neglected[62].

The spin-dependent spin-orbit term is given by

$$\Delta V_{PP,so}^{K}(i) = \sum_{l=0}^{L-1} \frac{\Delta V_{l}^{K}(r_{Ki})}{2l+1} \left[l \hat{P}_{l,l+1/2}^{K}(i) - (l+1) \hat{P}_{l,|l-1/2|}^{K}(i)\right], \tag{2.92}$$

with

$$\Delta V_{l}^{K}(r_{Ki}) = V_{l,l+1/2}^{K}(r_{Ki}) - V_{l,|l-1/2|}^{K}(r_{Ki}). \tag{2.93}$$

The spin-orbit pseudopotential can be written in a simpler form which is especially suited for SO configuration interaction (CI) calculations performed after a scalar-relativistic Hartree-

Fock, complete active space self-consistent field (CASSCF) or multi-reference configuration interaction (MRCI) calculation:

$$\Delta V_{PP,so}^{K}(i) = \sum_{l=0}^{L-1} \frac{2\Delta V_l^K(r_{Ki})}{2l+1} \hat{P}_l^K(i) \hat{\vec{l}}_{Ki} \hat{\vec{s}}_i \hat{P}_l^K(i), \tag{2.94}$$

where

$$\hat{P}_l^K(i) = \sum_j \hat{P}_{lj}^K(i) = P_{l,|l-1/2|}^K(i) + \hat{P}_{l,l+1/2}^K(i). \tag{2.95}$$

The terms $\hat{\vec{l}}_{Ki} = \hat{\vec{r}}_{Ki} \times \hat{\vec{p}}_i$ and $\hat{\vec{s}}_i$ represent the operators of orbital angular momentum with respect to core K and spin. Note that it is always recommended to use the same PP core in both the scalar-relativistic and subsequent SO-calculation, since the use of different cores can lead to non-negligible errors in the results.

The radial pseudopotentials $V_l^K(r_{Ki}) - V_L^K(r_{Ki})$, $V_L^K(r_{Ki})$, $V_{lj}^K(r_{Ki}) - V_{LJ}^K(r_{Ki})$ and $V_{LJ}^K(r_{Ki})$ are usually represented by linear combinations of radial Gaussian functions multiplied by powers of the electron-core distance

$$V_a^K(r_{\lambda i}) = \sum_k A_{ka}^K r_{Ki}^{n_{ka}} e^{-\alpha_{ka}^K r_{Ki}^2}, a = l, L, lj, LJ \tag{2.96}$$

where the free parameters are determined by fitting them to all-electron ab initio reference data from, e.g., atomic four-component relativistic Dirac-Hartree-Fock calculations (solved on a grid to account for basis set incompleteness effects). The choice of Gaussian basis functions for the expansion of radial pseudopotentials was made mainly because of computational convenience, because it facilitates the evaluation of the matrix elements of the pseudopotential operators. Usually, the powers n_{ka} of the electron-core distance are restricted to the values -2, -1 and 0 (and must be ≥ -2 to avoid divergencies), because this proved to be sufficient for the description of the behaviour of ΔV_{PP}^K at the origin (i.e., close to the nucleus).

2.3. Wave-function-based methods for electronic structure calculations

The preceding chapters dealt with the construction of the molecular (relativistic) electronic Hamiltonian. However, the question remains how the molecular Schrödinger equation (employing the discussed Hamiltonian) is solved numerically using a computer. For this purpose, different methods have been developed, which differ in the wave function *ansatz* and/or the solution of the resulting equations. We will mainly introduce so-called *multireference methods* because these methods are required for electronic structure calculations of lanthanide, actinide and transition metal complexes. The basis for most of these methods is the *Hartree-Fock method*, which we will discuss in the next chapter. In the following, we will work with atomic units unless otherwise noted.

2.3.1. Hartree-Fock theory

This chapter covers the most important aspects of Hartree-Fock theory required for the methods used and developed in this thesis. For a more detailed description, the interested reader is referred to the literature used for the preparation of this chapter[48–50,52]. The *ansatz* for the wave function in the Hartree-Fock method is a single Slater determinant. The orbitals contained in the determinant are then optimized variationally to minimize the energy expectation value, with the additional constraint to remain orthonormal. The energy expectation value E_{HF} for a single Slater determinant can be written (applying the Slater-Condon rules) as

$$E_{HF} = \sum_{i}^{\mathrm{occ}} \langle \psi_i | \hat{h} | \psi_i \rangle + \frac{1}{2} \sum_{i,j}^{\mathrm{occ}} \left[\left\langle \psi_i \psi_j \middle| \frac{1}{r_{12}} \middle| \psi_i \psi_j \right\rangle - \left\langle \psi_i \psi_j \middle| \frac{1}{r_{12}} \middle| \psi_j \psi_i \right\rangle \right] + E_{\mathrm{nuc}} \qquad (2.97)$$

We did not make any assumptions about the individual spins and the spatial parts of the spin-orbitals yet. In Hartree-Fock theory, one can distinguish between different versions of the method, depending on the occupation and form of the spin-orbitals. We will discuss two of them, namely *closed-shell Hartree-Fock* and *spin-restricted open-shell Hartree-Fock (ROHF)*. In practical calculations, the orbitals are expanded in terms of so-called *atomic orbitals* (even though they do not need to represent the true atomic orbitals), which is called

linear combination of atomic orbitals (LCAO) approximation. We will introduce this approximation in the next section.

2.3.1.1. The LCAO approximation

In the LCAO approximation, the orthogonal molecular orbitals $|r\rangle \equiv |\phi_r(\mathbf{r})\rangle$ are expanded in terms of non-orthogonal basis functions $|\mu\rangle \equiv |\chi_\mu(\mathbf{r})\rangle$

$$|r\rangle = \sum_{\mu=1}^{N_{AO}} |\mu\rangle\, C_{\mu r}, \tag{2.98}$$

with the so-called molecular orbital (MO) coefficients $C_{\mu r}$.

The basis functions $|\mu\rangle$ are ususally atom-centered and their radial part is given by (linear combinations of) Gaussians. With N_{AO} linearly independent basis functions, N_{AO} orthogonal (molecular) orbitals can be formed, therefore $\mathbf{C}$ is a square matrix. The MOs are always restricted to be orthonormal, i.e.

$$\langle r|s\rangle = \sum_{\mu,\nu} C_{\mu r}\langle\mu|\nu\rangle C_{\nu s} = [\mathbf{C}^\dagger\mathbf{S}\mathbf{C}]_{rs} = \delta_{rs}, \tag{2.99}$$

with the *AO overlap matrix* $S_{\mu\nu} = \langle\mu|\nu\rangle$. With the unit matrix $\mathbf{1}$ this can be written as

$$\mathbf{C}^\dagger\mathbf{S}\mathbf{C} = \mathbf{1}. \tag{2.100}$$

2.3.1.2. Closed-shell Hartree-Fock

In closed-shell Hartree-Fock (simply denoted as HF), the number of α-spin-orbitals N_α equals the number of β-spin-orbitals N_β, i.e. $N_\alpha = N_\beta$, and the spatial parts are assumed to be identical for each pair of α- and β-spin. In other words, each spatial orbital ϕ_i is occupied by one α-spin electron and one β-spin electron. These orbitals are denoted as *closed-shell* orbitals. Applying this assumption for the energy expectation value and integrating over the spin-coordinates (using the orthonormality of the spin functions) yields

$$E_{HF} = 2\sum_{i}^{\text{closed}} \langle \phi_i | \hat{h} | \phi_i \rangle + \sum_{i,j}^{\text{closed}} \left[2 \left\langle \phi_i \phi_j \middle| \frac{1}{r_{12}} \middle| \phi_i \phi_j \right\rangle - \left\langle \phi_i \phi_j \middle| \frac{1}{r_{12}} \middle| \phi_j \phi_i \right\rangle \right] + E_{\text{nuc}} \tag{2.101}$$

In the following, we will use the so-called "chemical" or "Mulliken" notation for the 2-electron integrals, defined by (assuming real orbitals)

$$(ij|kl) \equiv \left\langle \phi_i \phi_k \middle| \frac{1}{r_{12}} \middle| \phi_j \phi_l \right\rangle = \int \mathrm{d}\mathbf{r}_1 \int \mathrm{d}\mathbf{r}_2 \, \phi_i(\mathbf{r}_1) \phi_j(\mathbf{r}_1) \frac{1}{r_{12}} \phi_k(\mathbf{r}_2) \phi_l(\mathbf{r}_2). \tag{2.102}$$

Using this notation, the closed-shell HF energy takes the compact form

$$E_{HF} = 2\sum_{i}^{\text{closed}} \langle i | \hat{h} | i \rangle + \sum_{i,j}^{\text{closed}} [2(ii|jj) - (ij|ji)] + E_{\text{nuc}}. \tag{2.103}$$

In the following, we will use the indices i, j, k, l, m, n for occupied (closed-shell and *active/open-shell*) orbitals, the indices a, b, c, d for unoccupied (so-called *virtual*) orbitals and the indices p, q, r, s, t, u for any sort of orbitals, but in most cases for open-shell or active orbitals, which will be introduced later. For the AO basis functions we will use the indices μ, ν, ρ, σ.

2.3.1.2.1. The closed-shell Hartree-Fock equations in the LCAO approximation

Inserting the LCAO expansion for the orbitals into the HF energy functional yields

$$E_{HF} = \sum_{\mu,\nu} D_{\mu\nu} \left\{ H_{\mu\nu} + \frac{1}{2} G_{\mu\nu} \right\} + E_{\text{nuc}} = \text{tr}\left[\mathbf{D} \cdot \left(\mathbf{H} + \frac{1}{2} \mathbf{G} \right) \right], \tag{2.104}$$

with the one-electron integrals $H_{\mu\nu} = \langle \mu | \hat{h} | \nu \rangle$ in the AO basis and the *density matrix* $\mathbf{D}$ and the *electron interaction matrix* $\mathbf{G}$ (both in the AO basis) defined by

$$D_{\mu\nu} = 2\sum_{i=1}^{\mathrm{occ}} C_{\mu i} C_{\nu i} = 2\left[\mathbf{C}_{\mathrm{o}}\mathbf{C}_{\mathrm{o}}^{\dagger}\right]_{\mu\nu}, \tag{2.105}$$

$$G_{\mu\nu} = \sum_{\rho,\sigma} D_{\rho\sigma}\left[(\mu\nu|\rho\sigma) - \frac{1}{2}(\mu\rho|\sigma\nu)\right], \tag{2.106}$$

where $\mathbf{C}_{\mathrm{o}}$ is the rectangular $N_{AO} \times N_{\mathrm{o}}$ block of $\mathbf{C}$ which describes the N_{o} occupied/closed-shell orbitals.

The next step is the constrained minimization of E_{HF} with respect to the orbitals, i.e. the MO coefficients $\mathbf{C}_{\mathrm{o}}$, with the orthonormality constraint $\langle i|j\rangle = \delta_{ij}$. This can be achieved by the unconstrained minimization of the Lagrange functional

$$L = E_{HF} - 2\sum_{i,j} e_{ij}\left([\mathbf{C}^{\dagger}\mathbf{S}\mathbf{C}]_{ij} - \delta_{ij}\right), \tag{2.107}$$

with the symmetric $N_{\mathrm{o}} \times N_{\mathrm{o}}$ Lagrange multiplier matrix e_{ij}. In order to minimize this functional we have to calculate the derivatives of L with respect to the MO coefficients and set them zero, i.e.

$$\left(\frac{\partial L}{\partial C_{\mu i}}\right) = 0 \quad \forall\, \mu, i. \tag{2.108}$$

This (after some calculation) finally yields the variational conditions, which can be summarized in the *Hartree-Fock-Roothaan equations*

$$\mathbf{F}\mathbf{C}_{\mathrm{o}} = \mathbf{S}\mathbf{C}_{\mathrm{o}}\mathbf{e}, \tag{2.109}$$

with the symmetric and Hermitian *Fock matrix* defined by

$$\mathbf{F} = \mathbf{H} + \mathbf{G}. \tag{2.110}$$

The Fock matrix can be further split to

$$F_{\mu\nu} = H_{\mu\nu} + 2J_{\mu\nu} - K_{\mu\nu}, \tag{2.110}$$

with the *Coulomb matrix* $J_{\mu\nu}$ and the *exchange matrix* $K_{\mu\nu}$ given by

$$J_{\mu\nu} = \frac{1}{2}\sum_{\rho,\sigma} D_{\rho\sigma}(\mu\nu|\rho\sigma), \tag{2.111}$$

$$K_{\mu\nu} = \frac{1}{2}\sum_{\rho,\sigma} D_{\rho\sigma}(\mu\rho|\sigma\nu). \tag{2.112}$$

Multiplication of the Hartree-Fock-Roothaan equations from the left with $\mathbf{C}^\dagger$ and exploiting $[\mathbf{C}^\dagger\mathbf{S}\mathbf{C}]_{rs} = \delta_{rs}$ yields (with i, j occupied and a virtual):

$$[\mathbf{C}^\dagger\mathbf{F}\mathbf{C}]_{ij} = e_{ij}, \tag{2.113}$$

$$[\mathbf{C}^\dagger\mathbf{F}\mathbf{C}]_{ai} = 0. \tag{2.114}$$

The first equation does not uniquely fix the Lagrange multipliers, and it is valid for any set of occupied orbitals related by unitary transformations. This results from the fact that the density matrix is invariant with respect to any unitary transformation among the occupied orbitals $\bar{\mathbf{C}}_\mathrm{o} = \mathbf{C}_\mathrm{o}\mathbf{U}$ with an arbitrary $N_\mathrm{o} \times N_\mathrm{o}$ unitary matrix $\mathbf{U}$ ($\mathbf{U}^\dagger\mathbf{U} = \mathbf{1}$). Therefore the Fock matrix and the energy are also invariant with respect to unitary transformations among the occupied orbitals. This can also be understood from the fact that the wave function, i.e. the Hartree-Fock Slater determinant, is invariant (except for a global phase factor) with respect to unitary transformations among the occupied orbitals, since linear combinations of rows or columns of a determinant do not change its value. We therefore have the freedom to choose different sets of Lagrange multipliers, related by the unitary matrix $\mathbf{U}$

$$[\bar{\mathbf{C}}^\dagger\mathbf{F}\bar{\mathbf{C}}]_{ij} = [\mathbf{U}^\dagger\mathbf{e}\mathbf{U}]_{ij} = [\bar{\mathbf{e}}]_{ij}. \tag{2.115}$$

This allows us to choose $\mathbf{U}$ to diagonalize $\mathbf{e}$, i.e.

$$[\mathbf{U}^{\dagger}\mathbf{e}\mathbf{U}]_{ij} = \epsilon_i \delta_{ij}. \tag{2.116}$$

In this case, the eigenvalues ϵ_i of the Lagrange multiplier matrix are denoted as *orbital energies* and the corresponding orbitals

$$|\bar{i}\rangle = \sum_{\mu} |\mu\rangle \bar{C}_{\mu i} \tag{2.117}$$

are called *canonical orbitals*.

This unitary transformation only defines a unique choice of the occupied orbitals, but it does not affect the energy and therefore does not help us to minimize E_{HF}. The variational conditions to minimize the energy are therefore only represented by the requirement for the optimized orbitals that the matrix elements $f_{ai} = [\mathbf{C}^{\dagger}\mathbf{F}\mathbf{C}]_{ai} = 0$ for all a, i. These are the *Brillouin conditions*. However, these conditions do not tell us how to actually find the optimized orbitals. This is discussed in the next section.

2.3.1.2.2. Iterative solution of the Hartree-Fock-Roothaan equations

The matrix $\mathbf{F}$ represents the Fock matrix in the AO basis. The Fock matrix in the MO basis is defined by

$$\mathbf{f} = \mathbf{C}^{\dagger}\mathbf{F}\mathbf{C}. \tag{2.118}$$

In the following we will use the convention that quantities in the MO and AO bases are represented by matrices in lower and upper case, respectively. We already figured out that the occupied-occupied block of $\mathbf{f}$ can be diagonalized to yield canonical occupied orbitals. Furthermore, the occupied-virtual blocks $f_{ai} = f_{ia}$ must vanish for the optimized orbitals. Since any unitary transformation among the virtual orbitals has no effect on the Fock matrix, the energy and the wave function (because it does not contain the virtual orbitals), we can choose a unitary transformation to diagonalize the virtual-virtual block f_{ab} to obtain canonical virtual orbitals. Summarizing these conditions means that the whole Fock matrix in the MO basis should be diagonal, i.e.

$$f_{rs} = \epsilon_r \delta_{rs}. \tag{2.119}$$

This allows us to extend the Hartree-Fock-Roothaan equations to include also the virtual orbitals and leads to the generalized matrix eigenvalue equation

$$\mathbf{FC} = \mathbf{SC}\bar{\mathbf{e}}, \tag{2.120}$$

with $\bar{e}_{rs} = \epsilon_r \delta_{rs}$.

In the beginning of the Hartree-Fock algorithm, we compute $\mathbf{f}$ with non-optimized orbitals $\mathbf{C}$ constructed by some reasonable *initial guess* and it will not be diagonal. In the next step, we can diagonalize it

$$[\mathbf{U}^{\dagger}\mathbf{f}\mathbf{U}]_{rs} = \epsilon_r \delta_{rs}, \tag{2.121}$$

to get new MO coefficients

$$\bar{\mathbf{C}} = \mathbf{CU}, \tag{2.122}$$

where $\mathbf{U}$ is now an $N_{\mathrm{AO}} \times N_{\mathrm{AO}}$ matrix.

This transformation mixes occupied and virtual orbitals and therefore changes $\mathbf{D}$, $\mathbf{F}$ and E_{HF}. The new occupied orbitals $\bar{\mathbf{C}}_{\mathrm{o}}$ are then used to recompute $\mathbf{D}$, $\mathbf{F}$ and the energy and the process is repeated until $\mathbf{f}$ is diagonal and $\mathbf{U} = \mathbf{1}$, which is called *self-consistent* solution. The whole procedure is called *Hartree-Fock self-consistent field (HF-SCF)* method. It is not guaranteed that this algorithm converges, but if a reasonably good starting guess for $\mathbf{D}$ is used, for example constructed from atomic densities[68,69], it often does. Moreover, convergence can be stabilized and accelerated by interpolation techniques, such as the DIIS (direct inversion of the iterative subspace) method[70,71].

2.3.1.3. Spin-restricted open-shell Hartree-Fock (ROHF)

In Hartree-Fock theory of *open-shell* systems, one or several spatial orbitals are only singly occupied. Therefore many different spin states are possible, depending on the distribution of the electron spins among the singly occupied orbitals. These states can be classified by the

total spin quantum numbers S and M_S. States with $S = 0, 1/2, 1$ or $3/2$ are called singlet, doublet, triplet or quartet states, respectively, in view of their M_S degeneracies. Without external magnetic fields, all states with different M_S quantum numbers corresponding to the same S are degenerate and we can choose the ones which are simplest to describe. For most of the M_S states with $S > 0$ more than one Slater determinant is required for their description. Only the *high-spin* states with the highest possible M_S value ($M_S = S$), i.e. where all open-shell orbitals are occupied by α-spin electrons, can be represented by a single determinant. We will only consider the high-spin cases in this chapter.

If we have a molecule with $N = N_\alpha + N_\beta$ (and $N_\alpha > N_\beta$), M_S for the high-spin case can be calculated by (in atomic units)

$$M_S = \frac{1}{2}(N_\alpha - N_\beta). \tag{2.123}$$

Different choices are possible for the spatial orbitals. The most general choice is to allow different spatial orbitals for α-spin and β-spin electrons, which is called *spin-unrestricted* Hartree-Fock (UHF). However, this can lead to *spin contaminated* or *symmetry broken* wave functions, i.e. wave functions which are not eigenfunctions of $\hat{S}^2$ (but still eigenfunctions of $\hat{S}_z$), if the spatial parts for the α- and β-spin-orbitals are different. This is a problem, especially in subsequent electron correlation treatments. An alternative choice, which avoids spin contamination, is to impose that the first N_β orbitals are doubly occupied, i.e. have the same spatial parts for α-spin and β-spin electrons, as for the closed-shell case. This is called *spin-restricted open-shell* Hartree-Fock (ROHF). We will discuss this method in the following.

In the ROHF case there are N_β doubly occupied closed-shell orbitals and $(N_\alpha - N_\beta)$ open-shell orbitals occupied with α-spin electrons. The energy functional for this case, after integration over the spin-coordinates, can be written as

$$\begin{aligned} E_{ROHF} = 2 \sum_{i}^{\text{closed}} \langle \phi_i | \hat{h} | \phi_i \rangle + \sum_{t}^{\text{open}} \langle \phi_t | \hat{h} | \phi_t \rangle \\ + \sum_{i}^{\text{occ}} \sum_{j}^{\text{closed}} \left[2(\phi_i \phi_i | \phi_j \phi_j) - (\phi_i \phi_j | \phi_j \phi_i) \right] \\ + \frac{1}{2} \sum_{t,u}^{\text{open}} \left[(\phi_t \phi_t | \phi_u \phi_u) - (\phi_t \phi_u | \phi_u \phi_t) \right] + E_{\text{nuc}}, \end{aligned} \tag{2.124}$$

with $\text{occ} = \text{closed} + \text{open}$.

In the LCAO approximation, this can be rewritten as

$$E_{ROHF} = \frac{1}{2} \text{tr}[\mathbf{D}(\mathbf{H} + \mathbf{F}^c)] + \frac{1}{2} \text{tr}[\mathbf{D}^o \mathbf{F}^o] + E_{\text{nuc}}, \tag{2.125}$$

with the total density $\mathbf{D}$, the open-shell density $\mathbf{D}^o$, the "total" Fock matrix $\mathbf{F}^c$ and the open-shell Fock matrix $\mathbf{F}^o$ given by

$$D_{\mu\nu} = 2 \sum_{i}^{\text{closed}} C_{\mu i} C_{\nu i} + \sum_{t}^{\text{open}} C_{\mu t} C_{\nu t}, \tag{2.126}$$

$$D^o_{\mu\nu} = \sum_{t}^{\text{open}} C_{\mu t} C_{\nu t}, \tag{2.127}$$

$$F^c_{\mu\nu} = H_{\mu\nu} + \sum_{\rho,\sigma} D_{\rho\sigma} \left[(\mu\nu|\rho\sigma) - \frac{1}{2} (\mu\rho|\sigma\nu) \right], \tag{2.128}$$

$$F^o_{\mu\nu} = -\frac{1}{2} \sum_{\rho,\sigma} D^o_{\rho\sigma} (\mu\rho|\sigma\nu). \tag{2.129}$$

The energy functional is invariant with respect to unitary transformations within the closed-shell subspace and within the open-shell subspace. However, it depends on orbital rotations between both subspaces. The Lagrangian for the constrained minimization of E_{ROHF} with inter- and intershell orthonormality conditions can be written as

$$L = E_{ROHF} - 2\sum_{i}^{\text{closed}} \epsilon_i \left[\langle i|i\rangle - 1\right] - \sum_{t}^{\text{open}} \epsilon_t[\langle t|t\rangle - 1] - 2\sum_{i}^{\text{closed}}\sum_{t}^{\text{open}} \epsilon_{ti}\langle t|i\rangle. \quad (2.130)$$

Here, we have assumed that the closed- and open-shell orbitals are canonical (the matrices of the Lagrangian multipliers are assumed to be diagonal). Taking the derivatives of this Lagragian with respect to the MO coefficients and setting them zero leads to the variational conditions. Defining the Fock matrices in the MO basis,

$$\mathbf{f}^c = \mathbf{C}^\dagger \mathbf{F}^c \mathbf{C}, \quad (2.131)$$

$$\mathbf{f}^o = \mathbf{C}^\dagger \mathbf{F}^o \mathbf{C}, \quad (2.132)$$

the variational conditions can be summarized in one single matrix eigenvalue equation as

$$\bar{\mathbf{f}} = \begin{pmatrix} \mathbf{f}^c & \mathbf{f}^c - \mathbf{f}^o & \mathbf{f}^c \\ \mathbf{f}^c - \mathbf{f}^o & \mathbf{f}^c + \mathbf{f}^o & \mathbf{f}^c + \mathbf{f}^o \\ \mathbf{f}^c & \mathbf{f}^c + \mathbf{f}^o & \mathbf{f}^c + \mathbf{f}^o \end{pmatrix} = \begin{pmatrix} \mathbf{e}^c & \mathbf{0} & \mathbf{0} \\ \mathbf{0} & \mathbf{e}^o & \mathbf{0} \\ \mathbf{0} & \mathbf{0} & \mathbf{e}^v \end{pmatrix}. \quad (2.133)$$

Here, the rows and columns 1-3 represent the closed, active and virtual subspaces and $\mathbf{e}^c$, $\mathbf{e}^o$ and $\mathbf{e}^v$ are diagonal Lagrangian multiplier matrices. $\bar{\mathbf{f}}$ can be seen as an effective Fock matrix, which is built and diagonalized in each SCF iteration

$$\mathbf{U}^\dagger \bar{\mathbf{f}}\, \mathbf{U} = \mathbf{e}. \quad (2.134)$$

This defines the improved MO-coefficients $\tilde{\mathbf{C}}$ as

$$\tilde{\mathbf{C}} = \mathbf{C}\mathbf{U}. \quad (2.135)$$

In the next iteration, the updated MO-coefficients are obtained by setting $\mathbf{C} = \tilde{\mathbf{C}}$ and this process is repeated until self-consistency.

There are some degrees of freedom left in the eigenvalue equation. For example, it is possible to shift the diagonal elements of the closed-closed, open-open or virtual-virtual block by some arbitrary value without changing the resulting energy and orbitals. This is called *level shift*. Level shifts can be used to account for potential convergence problems, e.g. in cases where orbitals are continuously rotated between the closed and open-shells. This can be inhibited by energetically separating the closed- and open-shell by level shifts. However, if the level shift is chosen too large, convergence might be very slow. The reasonable choice of the magnitude of the level shift strongly depends on the specific system under consideration.

2.3.1.4. Density-fitting

One of the computationally most expensive and difficult steps in molecular ab initio calculations is the computation, storage and the readout (from disk) of the two-electron integrals (assuming real orbitals)

$$(pq|rs) = \int \mathrm{d}\mathbf{r}_1 \int \mathrm{d}\mathbf{r}_2 \, \phi_p(\mathbf{r}_1)\phi_q(\mathbf{r}_1)\frac{1}{r_{12}}\phi_r(\mathbf{r}_2)\phi_s(\mathbf{r}_2). \tag{2.136}$$

Density-fitting is a method to approximate the two-electron integrals. We will mainly follow the presentation of Werner, Manby and Knowles[72] and the lecture notes of Sherrill[73].

Defining the generalized one-electron densities

$$\rho_{pq}(\mathbf{r}) = \phi_p(\mathbf{r})\phi_q(\mathbf{r}), \tag{2.137}$$

$$\rho_{rs}(\mathbf{r}) = \phi_r(\mathbf{r})\phi_s(\mathbf{r}), \tag{2.138}$$

we can rewrite the two-electron integrals as

$$(pq|rs) = \int \mathrm{d}\mathbf{r}_1 \int \mathrm{d}\mathbf{r}_2 \, \rho_{pq}(\mathbf{r}_1)\frac{1}{r_{12}}\rho_{rs}(\mathbf{r}_2). \tag{2.139}$$

In density-fitting, the one-electron densities are approximated as

$$\bar{\rho}_{pq}(\mathbf{r}) = \sum_{A}^{N_{fit}} d_A^{pq} \chi_A(\mathbf{r}), \tag{2.140}$$

with so-called *fitting basis functions* $\chi_A(\mathbf{r})$ and *fitting coefficients* d_A^{pq}. The fitting coefficients can be obtained by minimizing an appropriate functional, for example the positive definite functional[74,75]

$$\Delta_{pq} = \int \mathrm{d}\mathbf{r}_1 \int \mathrm{d}\mathbf{r}_2 \frac{\left[\rho_{pq}(\mathbf{r}_1) - \bar{\rho}_{pq}(\mathbf{r}_1)\right]\left[\rho_{pq}(\mathbf{r}_2) - \bar{\rho}_{pq}(\mathbf{r}_2)\right]}{r_{12}}, \tag{2.141}$$

which minimized the error in the electric field. Minimization of this functional leads to

$$d_B^{pq} = \sum_{A}^{N_{fit}} (pq|A)[\mathbf{J}^{-1}]_{AB}, \tag{2.142}$$

with

$$J_{AB} = \int \mathrm{d}\mathbf{r}_1 \int \mathrm{d}\mathbf{r}_2 \frac{\chi_A(\mathbf{r}_1)\chi_B(\mathbf{r}_2)}{r_{12}}, \tag{2.143}$$

$$(pq|A) = \int \mathrm{d}\mathbf{r}_1 \int \mathrm{d}\mathbf{r}_2 \frac{\phi_p(\mathbf{r}_1)\phi_q(\mathbf{r}_1)\chi_A(\mathbf{r}_2)}{r_{12}}. \tag{2.144}$$

This leads to an expression for the two-electron integrals

$$(pq|rs) = \sum_{A,B}^{N_{fit}} (pq|A)[\mathbf{J}^{-1}]_{AB}\,(B|rs). \tag{2.145}$$

The four-index integrals therefore have been replaced by a sum of products of three-index integrals. The three-index integrals in the MO basis $(pq|A)$ are obtained by a two-step transformation of the three-index integrals $(\mu\nu|A)$ in the AO basis. All of the operations above, i.e. transformation for the three-index integrals, the calculation of the fitting

coefficients and the final integral assembly step only require simple matrix multiplications and can therefore be performed very efficiently on modern computers.

The auxiliary basis set (=fitting basis) in density fitting is usually composed of (atom-centered) Gaussian basis functions and about 3-4 times the size of the standard AO basis. There are different types of density fitting basis sets optimized for different types of densities being fit, e.g. for Coulomb and exchange integrals in Hartree-Fock theory (so-called *JK-fit* basis sets)[76], or basis sets optimized for the use together with correlation-consistent AO basis sets for density fitted *(dynamical) correlation methods*, such as *Møller-Plesset perturbation theory of second order (MP2)*[77].

A very important advantage of density fitting is the reduction of storage requirements, since the number of three-index integrals (used to construct the four-index integrals) is much smaller than the number of four-index integrals. Therefore, the three-index integrals are more likely to fit in memory. If the three-index integrals do not fit in memory, the time requirements to write them to disk and read them from disk are still much less than for the four-index integrals. Even though the four-index integrals have to be constructed out of the three-index integrals, this procedure is usually much faster than reading the four-index integrals from disk.

2.3.1.5. Local density-fitted Hartree-Fock

Density-fitting techniques can be combined with local approximations, i.e. approximations which neglect interaction integrals/terms for spatially distant orbitals. This results in local density-fitting (LDF) techniques, which can be applied in dynamical correlation methods, such as local MP2[72], or to speed up density-fitted Hartree-Fock (DF-HF) calculations, which is called local density-fitted Hartree-Fock (LDF-HF)[69,78]. We will discuss the basic concepts of the LDF-HF method as implemented in Molpro[69,79,80] in this section and use the closed-shell case as example. For more details, the interested reader is referred to the literature on which this section is based[37,69].

The most expensive part of a conventional closed-shell Hartree-Fock program is the calculation of the exchange matrix in the AO basis

$$K_{\mu\nu} = \frac{1}{2}\sum_{\rho,\sigma} D_{\rho\sigma}(\mu\rho|\sigma\nu), \tag{2.146}$$

with the density matrix

$$D_{\mu\nu} = 2\sum_{i=1}^{\mathrm{occ}} C_{\mu i}C_{\nu i}. \tag{2.147}$$

In the LDF approximation, the sparsity of the MO coefficients in a localized molecular orbital (LMO) basis can be exploited to calculate the exchange matrix efficiently as a sum of contributions of individual LMOs, without using the density matrix. LMOs can be obtained by a unitary transformation among the canonical MOs (with certain requirements, for example to maximize the spatial distance of the centres of charge). The implementation in Molpro uses intrinsic bond orbitals (IBOs)[81] as LMOs.

Different orbital-specific subsets, also called *domains*, of LMOs, AO basis functions and fitting basis functions are defined in the LDF approximation. These domains are denoted as $[i]_{LMO}$, $[i]_{AO}$ and $[i]_{fit}$. Due to their localized nature, the size of these domains is asymptotically independent of the molecular size. The criteria for the construction of these domains have been investigated and optimized by Köppl and Werner[69] and the exchange matrix is then calculated by summing up the contributions of different LMOs,

$$K_{\mu\nu} \approx \sum_{i}\sum_{\bar{B}\in[i]_{fit}} (\bar{B}|\mu i)(\bar{B}|\nu i)\,, \qquad \mu,\nu \in [i]_{AO} \tag{2.148}$$

and the integrals $(\bar{B}|\mu\nu)$ are calculated by solving the linear equation

$$(A|\mu i) = \sum_{\bar{A}\in[i]_{fit}} G_{AB}(\bar{B}|\mu i)\,, \qquad A,B \in [i]_{fit}, \mu \in [i]_{AO}. \tag{2.149}$$

The half-transformed integrals $(A|\mu i)$ obtained by

$$(A|\mu i) = \sum_{\nu\in[i]_{LMO}} (A|\mu\nu)C_{\nu i}\,, \qquad A \in [i]_{fit}, \mu \in [i]_{AO} \tag{2.150}$$

with the MO coefficients $C_{\nu i}$ in LMO basis.

The triangular matrices G_{AB} are calculated separately for each fitting domain by performing a Cholesky decomposition of the Coulomb metric J_{AB} according to

$$J_{AB} = \int \mathrm{d}\mathbf{r}_1 \int \mathrm{d}\mathbf{r}_2 \frac{\chi_A(\mathbf{r}_1)\chi_B(\mathbf{r}_2)}{r_{12}} = [\mathbf{G}\mathbf{G}^\dagger]_{AB}, \tag{2.151}$$

where $\chi(\mathbf{r})$ again denotes fitting basis functions.

All summations are restricted to domains and all types of domains are asymptotically independent of the molecular size. Therefore, the required computational effort becomes independent of the molecular size for each LMO, which leads to a linear scaling of the methodology in the number of LMOs. In contrast to the exchange matrix, the Coulomb matrix is calculated using the density matrix and standard density fitting, because it was demonstrated that the use of LDF approximations for the Coulomb part leads to much larger errors in the energy[69,75,76,78,82–84]. However, this conventional approach does not significantly slow down the calculation, because the steps needed for the calculation of the Coulomb matrix are very fast. The LDF approximations lead to a significant reduction of the required storage space/memory and central processing unit (CPU) time. The errors in the final energy (compared to the exact DF-HF energy) are in the sub-μH range[69].

2.3.2. Multireference methods

The Hartree-Fock method has certain limitations[52]. The wave function *ansatz* of a single Slater determinant in Hartree-Fock theory is an approximation which often accounts for approximately 99 % of the total (exact) energy. The remaining 1 % to the total energy is called *correlation energy* E_{corr}, which is the difference of the exact energy and the Hartree-Fock energy and which is always negative, due to the variational principle:

$$E_{corr} = E_{exact} - E_{HF} \leq 0. \tag{2.152}$$

The correlation energy is in the same order of magnitude as chemical energy differences and therefore it is very important and needs to be accounted for in ab initio calculations to obtain quantitative predictions. The Hartree-Fock method is a so-called *mean-field theory* or

independent particle model in which each electron moves in an *average* field generated by the other electrons. It only includes the so-called *Fermi correlation*, i.e. the effect that two electrons with the same spin cannot be at the same position, which results from the Pauli principle. However, also electrons with different spins avoid each other when they their spatial distance becomes small[52]. This *short-range* contribution to the correlation energy is called *dynamical correlation* and not accounted for by Hartree-Fock theory. Dynamical correlation is described by including many Slater determinants with small (compared to the *leading* Hartree-Fock configuration) contributions into the wave function, which are built by exciting electrons from occupied orbitals into (unoccupied) virtual orbitals. In many cases, the Hartree-Fock method yields a qualitatively correct description of the system and the Hartree-Fock wave function can be used as a zeroth-order approximation for a more sophisticated theoretical description including electron correlation. If the Hartree-Fock method even fails to give qualitatively correct results, this is called a *multireference case*, where more than one Slater-determinant is required to obtain a reasonable zeroth-order description. The lanthanide, actinide and transition metal based open-shell systems described in this work also fall into this category. Multireference cases will be described in this chapter.

Bond dissociation processes constitute one example of a multireference case: In the dissociation limit for a homonuclear diatomic molecule, the two electrons contributing to the bond should be located at different nuclei and the probability for finding them both at the same nucleus should be zero. This long-range correlation effect is called *static correlation* and can only be described correctly, if several (leading) Slater determinants contribute equally to the zeroth-order wave function ansatz. In general, static correlation becomes important for systems with many (quasi-)degenerate orbitals, e.g. systems containing (one or more) open-shell transition metal or f-element ions. The analogue to the Hartree-Fock method for multireference cases is the *multiconfiguration self-consistent field (MCSCF)* method. The wave function ansatz in MCSCF in composed of several Slater determinants and both the orbitals contained in these determinants and the expansion coefficients of the Slater determinants (CI coefficients) are optimized simultaneously. The MCSCF method describes mainly static electron correlation effects and only a small amount of dynamical electron correlation, because usually not many virtual orbitals are included in

the wave function ansatz. However, the MCSCF wave function can be used as zeroth-order approximation for subsequent multireference correlation methods, such as multireference perturbation theory (MRPT) or multireference configuration interaction (MRCI). The basic concepts of the MCSCF method and of the MRPT and MRCI methods will be described in this chapter.

2.3.2.1. Multiconfiguration self-consistent field theory

This section covers the basic concepts of MCSCF theory. It is based on the presentation of second-order direct MCSCF method by Werner, Meyer and Knowles[85–89] as implemented in Molpro[80], because this quantum chemistry program package is used for the calculations in this work. It should be noted that there are also first-order MCSCF methods[90,91]. For more details, the interested reader is referred to the literature used for the preparation of this chapter[85].

The MCSCF wave function can be expanded in terms of Slater determinants or alternatively *configuration state functions (CSFs)*. CSFs are (spin) symmetry adapted linear combinations of Slater determinants which are eigenfunctions of the spin-operators $\hat{S}_z$ and $\hat{S}^2$. We will present the expansion in terms of CSFs. Given a set of orthonormal CSFs $\{\Phi_I\}$, the normalized MCSCF wave function Ψ_{MCSCF} can be written as

$$\Psi_{MCSCF} = \sum_I c_I \, \Phi_I, \tag{2.153}$$

with

$$\langle \Phi_I | \Phi_J \rangle = \delta_{IJ}, \tag{2.154}$$

and

$$\sum_I c_I^2 = 1. \tag{2.155}$$

The orthonormal molecular orbitals $\{\phi_i\}$ used to construct the (Slater-determinants and subsequently) CSFs contained in the MCSCF wave function are called *internal* orbitals. Internal orbitals, which are (strictly) doubly occupied in all CSFs, are called closed-shell or *inactive* orbitals. Internal orbitals, which are not closed-shell orbitals, are denoted as *active*

orbitals. They define the *active space* in the MCSCF method. For a transition metal complex, the active space is often chosen to contain the d-orbitals of the corresponding transition metal ion, for a lanthanide or actinide complex, the active space usually includes the f-orbitals of the metal ion. If the MCSCF wave function contains all possible CSFs which can be constructed by distributing n *active electrons* among m active orbitals, this is called *complete active space self-consistent field (CASSCF)* and the complete active space is denoted as CAS(n,m). If the number of CSFs in the MCSCF wave function is reduced by certain restrictions for their construction, the method is denoted as restricted active space self-consistent field (RASSCF)[92–94]. The complementary orbital space to the internal orbitals, i.e. the space of orbitals not occupied in any CSF contained in the MCSCF wave function, is called *external* (or virtual) orbital space. In this chapter, we will label the internal orbitals by the indices $i, j, k, l, m, n, \ldots$, the external orbitals by $a, b, c, d, \ldots$ and any sort of orbitals by $p, q, r, s, t, u, \ldots$.

The molecular orbitals $\{\phi_r\}$ are again (as in Hartree-Fock) constructed employing the LCAO approximation

$$|r\rangle = \sum_{\mu=1}^{N_{AO}} |\mu\rangle\, C_{\mu r}. \tag{2.156}$$

The energy expectation value $E^{(0)}$ for the MCSCF wave function can be written in the form[85]

$$\begin{aligned} E^{(0)} &= \langle \Psi_{MCSCF} | \hat{H}_{\mathrm{el}} | \Psi_{MCSCF} \rangle \\ &= \sum_{IJ} c_I c_J \left(\sum_{ij} h_{ij} \gamma_{ij}^{IJ} + \frac{1}{2} \sum_{ijkl} (ij|kl) \Gamma_{ij,kl}^{IJ} \right) = \sum_{IJ} c_I c_J \, H_{IJ}, \end{aligned} \tag{2.157}$$

with the one-electron integrals h_{ij} and two-electron integrals $(ij|kl)$ in the MO basis and the coupling coefficients

$$\gamma_{ij}^{IJ} = \langle \Phi_I | \hat{E}_{ij} | \Phi_J \rangle, \tag{2.158}$$

$$\Gamma_{ij,kl}^{IJ} = \langle \Phi_I | \hat{E}_{ij,kl} | \Phi_J \rangle. \tag{2.159}$$

$\hat{E}_{ij}$ and $\hat{E}_{ij,kl}$ are spin-summed excitation operators defined by

$$\hat{E}_{ij} = \hat{a}_i^{\alpha\dagger}\hat{a}_j^{\alpha} + \hat{a}_i^{\beta\dagger}\hat{a}_j^{\beta}, \tag{2.160}$$

$$\hat{E}_{ij,kl} = \hat{a}_k^{\alpha\dagger}\hat{E}_{ij}\hat{a}_l^{\alpha} + \hat{a}_k^{\beta\dagger}\hat{E}_{ij}\hat{a}_l^{\beta}, \tag{2.161}$$

with the usual annihilation and creation operators $\hat{a}_i^{\alpha}$ and $\hat{a}_i^{\beta\dagger}$ in second quantization for electrons with α and β spin, respectively[48,52]. These operators must fulfil certain anticommutation relations to satisfy the Pauli exclusion principle, namely

$$\left[\hat{a}_i^{\rho}, \hat{a}_j^{\sigma}\right]_+ = 0, \tag{2.162}$$

$$\left[\hat{a}_i^{\rho\dagger}, \hat{a}_j^{\sigma\dagger}\right]_+ = 0, \tag{2.163}$$

$$\left[\hat{a}_i^{\rho\dagger}, \hat{a}_j^{\sigma}\right]_+ = \delta_{ij}\delta_{\rho\sigma}, \text{ with } \rho, \sigma \in \{\alpha, \beta\}, \tag{2.164}$$

where $+$ denotes the *anticommutator*. A more detailed description of second quantization can be found in the literature[48].

The coupling coefficients and CI coefficients c_I can be used to calculate the first- and second order density matrices

$$(\mathbf{d})_{rs} = \sum_{IJ} c_I c_J \gamma_{rs}^{IJ}, \tag{2.165}$$

$$\Gamma_{rs,tu} = \sum_{IJ} c_I c_J \Gamma_{rs,tu}^{IJ}. \tag{2.166}$$

Futhermore, we define symmetrized density matrices to simplify later expressions,

$$(\mathbf{P}^{kl})_{rs} = \frac{1}{2}\left(\Gamma_{rs,kl} + \Gamma_{sr,kl}\right), \tag{2.167}$$

$$(\mathbf{Q}^{kl})_{rs} = \frac{1}{2}\left(\Gamma_{rk,sl} + \Gamma_{kr,sl}\right), \tag{2.168}$$

as well as generalized Coulomb and exchange matrices

$$(\mathbf{J}^{kl})_{rs} = (rs|kl), \tag{2.169}$$

$$(\mathbf{K}^{kl})_{rs} = (rk|ls). \tag{2.170}$$

With these definitions and expressions, the energy expectation value can now be written in a simple form:

$$E^{(0)} = \mathrm{tr}(\mathbf{hd}) + \frac{1}{2}\sum_{kl} \mathrm{tr}(\mathbf{J}^{kl}\mathbf{P}^{lk}). \tag{2.171}$$

In the MCSCF method, the energy expectation value is minimized with respect to the CI coefficients and MO coefficients with the constraint that the molecular orbitals stay orthonormal. The energy expectation value is a fourth-order function of the molecular orbitals and therefore its direct minimization is very complicated and not practicable. An iterative procedure is required which minimizes an approximate energy functional in each iteration.

The orbital changes are described by a unitary transformation

$$|\tilde{i}\rangle = \sum_{r} |r\rangle\, U_{ri}, \tag{2.172}$$

or written in matrix form,

$$\tilde{\mathbf{C}} = \mathbf{CU}. \tag{2.173}$$

The unitary transformation matrix can be parametrized by a matrix exponential

$$\mathbf{U} = \exp(\mathbf{R}) = \mathbf{1} + \mathbf{R} + \frac{1}{2}\mathbf{R}\mathbf{R} + \cdots, \tag{2.174}$$

with an antisymmetric matrix $\mathbf{R} = -\mathbf{R}^{\dagger}$. The elements $\{R_{ri}, r > i\}$ form a set of independent variational parameters.

One possibility to minimize the energy is to use a Newton-Raphson approach, such as the augmented Hessian method[85], to optimize the energy with respect to the CI coefficients and the variables R_{ri}. In this approach, the energy is expanded up to second order in the changes of the CI coefficients $\{\Delta c_I\}$ and the variables R_{ri} and resulting functional is minimized, which leads to new orbitals and a new CI vector and this process is repeated until convergence is achieved. However, because the energy is a fourth-order function of the orbitals, a very expensive integral transformation is needed after each iteration. This makes the approach rather slow, if many iteration steps are required, i.e. if the starting guess is not very close to the solution. Therefore, a different approach is used in the Molpro implementation employed in this thesis, described below.

The energy expectation value is a function of the CI coefficients (via the density matrices) and the orbital changes

$$|\Delta i\rangle = |\tilde{i}\rangle - |i\rangle = \sum_r |r\rangle\, T_{ri}, \tag{2.175}$$

with

$$\mathbf{T} = \mathbf{U} - \mathbf{1} = \mathbf{R} + \frac{1}{2}\mathbf{R}\mathbf{R} + \cdots. \tag{2.176}$$

The exact energy is a fourth-order function of the orbital changes, which is denoted as $E_{MCSCF} = E^{(4)}(\mathbf{T})$, and it is of infinite order in $\mathbf{R}$. However, the energy can be approximated as a second-order function $E^{(2)}(\mathbf{T})$ of the orbital changes by truncating the expansion to second order in $\mathbf{T}$. This second-order expansion can be seen as “model energy”, which is of second order in $\mathbf{T}$, but still of infinite order in $\mathbf{R}$, and often a good approximation to the exact energy. Using the definitions

$$\mathbf{A} = \mathbf{hd} + \sum_{kl} \mathbf{J}^{kl}\mathbf{P}^{lk}, \tag{2.177}$$

$$\mathbf{B} = \mathbf{hUd} + \sum_{kl} (\mathbf{J}^{kl}\mathbf{UP}^{lk} + 2\mathbf{K}^{kl}\mathbf{TQ}^{lk}), \tag{2.178}$$

$$\mathbf{G}^{ij} = \mathbf{h}d_{ij} + \sum_{kl} \left(\mathbf{J}^{kl}P_{ij}^{kl} + 2\mathbf{K}^{kl}Q_{ij}^{kl}\right), \tag{2.179}$$

the second-order energy can be written in the compact form

$$E^{(2)}(\mathbf{T}) = E^{(0)} + 2\mathrm{tr}(\mathbf{T}^{\dagger}\mathbf{A}) + \sum_{ij} \left(\mathbf{T}^{\dagger}\mathbf{G}^{ij}\mathbf{T}\right)_{ij} = E^{(0)} + \mathrm{tr}[\mathbf{T}^{\dagger}(\mathbf{A} + \mathbf{B})]. \tag{2.180}$$

Minimization of this energy functional with respect to the orbital changes can be performed with a Newton-Raphson approach, for which a gradient and Hessian (i.e. the first and second derivatives with respect to the orbital changes) have to be calculated. To do so, we investigate the change of $E^{(2)}(\mathbf{T})$ at a certain point $\mathbf{T} = \mathbf{T}(\mathbf{R})$ for small variations of $\mathbf{T}$. This small change can be described mathematically by multiplying $\mathbf{U}$ with a second unitary transformation $\mathbf{U}(\Delta\mathbf{R})$, which results in

$$\mathbf{U}(\mathbf{R}, \Delta\mathbf{R}) = \mathbf{U}(\mathbf{R})\mathbf{U}(\Delta\mathbf{R}) = \mathbf{U} + \mathbf{U}\left(\Delta\mathbf{R} + \frac{1}{2}\Delta\mathbf{R}\Delta\mathbf{R} + \cdots\right). \tag{2.181}$$

$\mathbf{U}(\mathbf{R}, \Delta\mathbf{R})$ is then inserted into the second-order energy and the first and second derivative of the resulting expression with respect to $\Delta\mathbf{R}$ at $\Delta\mathbf{R} = 0$ are calculated to obtain the gradient and Hessian[85], respectively. Setting the gradient to zero results in the variational conditions for the orbitals

$$\mathbf{U}^{\dagger}\mathbf{B} - \mathbf{B}^{\dagger}\mathbf{U} = \mathbf{0}. \tag{2.182}$$

The orbitals are then optimized with a Newton-Raphson approach until the variational conditions are fulfilled.

However, the second-order energy is a function of both the orbital changes and CI coefficients, i.e. $E^{(2)}(\mathbf{T},\mathbf{c})$, and has to be optimized with respect to both sets of variables. To make the dependence on the CI coefficients clearer, the second-order energy can be rewritten in the form

$$E^{(2)}(\mathbf{T},\mathbf{c}) = \frac{\mathbf{c}^\dagger \mathbf{H}^{(2)} \mathbf{c}}{\mathbf{c}^\dagger \mathbf{c}}, \tag{2.183}$$

with the second-order Hamiltonian matrix defined as

$$H_{IJ}^{(2)} = \sum_{ij} (\mathbf{U}^\dagger \mathbf{h} \mathbf{U})_{ij} \gamma_{ij}^{IJ} + \frac{1}{2} \sum_{ijkl} (ij|kl)^{(2)} \Gamma_{ij,kl}^{IJ}. \tag{2.184}$$

The second-order Hamiltonian matrix is an approximation to the exact Hamiltonian matrix, because it contains second-order approximations to the exact two-electron integrals as a function of the orbital changes, i.e. $\mathbf{T}$, which are given by

$$\begin{aligned}(ij|kl)^{(2)} = &-(ij|kl) + (\mathbf{U}^\dagger \mathbf{J}^{kl} \mathbf{U})_{ij} + \left(\mathbf{U}^\dagger \mathbf{J}^{ij} \mathbf{U}\right)_{kl} \\ &+\left(1+\tau_{ij}\right)(1+\tau_{kl})\left(\mathbf{T}^\dagger \mathbf{K}^{ik} \mathbf{T}\right)_{jl},\end{aligned} \tag{2.185}$$

where the operator τ_{ij} permutes the indices i and j. The minimization of the second-order energy (2.183) with respect to the CI coefficients results in the eigenvalue equation

$$\mathbf{H}^{(2)} \mathbf{c} = E^{(2)} \mathbf{c}, \tag{2.186}$$

which is solved employing direct CI methods, such as the Davidson algorithm[85]. The orbitals and the CI coefficients are optimized in alternating optimizations until both coupled non-linear equations (2.182) and (2.186) are fulfilled simultaneously for the same $\mathbf{T}$ and $\mathbf{c}$. The alternating optimization procedures are called *micro-iterations*. After convergence, an exact (fourth-order) integral transformation of the two-electron integrals is performed and the process is repeated again, which is called a *macro-iteration*. It should be noted, that in the micro-iterations, the internal orbital rotations are preoptimized first, to avoid convergence problems. In this process, a Newton-Raphson optimization of the exact energy with respect to internal orbital rotations only is performed, with full (i.e. exact fourth-order) two-electron

integral transformations. This is feasible because of the small number of internal orbitals compared to the large number of external orbitals. Details on this preoptimization can be found in the literature[85].

The MCSCF method can also be applied to excited states by using a multi-state direct CI procedure to calculate several roots of the CI matrix and use the eigenvector corresponding to the excited state of interest to calculate the first- and second-order density matrices. However, this can lead to problems for calculations of excited states in a given symmetry. During the optimization of the excited state, the orbitals can become worse for the ground state (or the lower excited states) and this can lead to the so-called "root-flipping problem"[85], where two states exchange their order. In this situation, the excited state to be calculated does not correspond to the chosen root of the CI matrix anymore and this leads to oscillations in the convergence behaviour.

To avoid these convergence problems, *state-averaged (SA)* MCSCF calculations can be performed. In these calculations, the average energy of all states up to the excited state of interest is optimized and a single set of molecular orbitals is obtained which is a compromise for all states. This is achieved by replacing the first- and second-order density matrices by their state-averaged analogues

$$(\mathbf{d})_{ij} = \sum_n W_n \sum_{IJ} c_I^n c_J^n \gamma_{rs}^{IJ}, \tag{2.187}$$

$$\Gamma_{rs,tu} = \sum_n W_n \sum_{IJ} c_I^n c_J^n \Gamma_{rs,tu}^{IJ}, \tag{2.188}$$

where $\mathbf{c}^n$ and W_n are the CI vector and an arbitrary weight factor for state n, respectively.

The SA-MCSCF procedure is very useful in the field of molecular magnetism, i.e. for calculations of transition metal, lanthanide and actinide complexes. For these systems, SA-CASSCF calculations are performed and often all possible roots of all possible spin-manifolds are included in the averaging with equal weights. The resulting SA-CASSCF wave functions are then used to build the spin-orbit matrix (using a suitable SO-operator), which is finally diagonalized. This method is denoted as *CASSCF/SI-SO (CASSCF and state interaction with*

spin-orbit coupling)[3,95] or CASSCF/RASSI-SO[94]. The obtained eigenvectors of the spin-orbit matrix can be used to calculate properties such as crystal field parameters or g-tensors. As mentioned earlier, the CASSCF method mainly covers static correlation effects but only a small amount of dynamical correlation (unless very large active spaces are used). However, dynamical correlation effects can be very important, e.g. for the description of superexchange mechanisms between open-shell ions or for the accurate prediction of crystal-field splittings. In order to include dynamical correlation into calculations, it is necessary to include CSFs with occupied virtual/external orbitals into the wave function *ansatz*. For this, multireference correlation methods based on a MCSCF wave function as zeroth-order approximation can be employed. We will present two of these methods in the next sections, namely complete active space perturbation theory of second order (CASPT2) and multireference configuration interaction (MRCI), because these methods are used for the calculations in this thesis.

2.3.2.2. Complete active space perturbation theory of second order

CASPT2 is a perturbational method to include dynamical correlation into calculations by including CSFs with occupied virtual/external orbitals into the wave function ansatz. It uses the MCSCF wave function as zeroth order approximation (reference function). In this chapter, the basic concepts of single-state (SS-) (based on a single reference function) and multi-state (MS-) (based on several reference functions) CASPT2 theory are explained. Moreover, the PNO-CASPT2 method is introduced, which exploits local approximations to speed up calculations. For more details and further versions of the CASPT2 method, the interested reader is referred to the literature on which this chapter is based[27,29,96,97].

2.3.2.2.1. Single-state CASPT2

In methods employing perturbation theory, the full (molecular electronic) Hamiltonian $\widehat{H}$ of the system is split into a zeroth-order part $\widehat{H}_0$ and the perturbation $\hat{V}$. This can be written as

$$\widehat{H} = \widehat{H}_0 + \hat{V}. \tag{2.189}$$

Moreover, the Hilbert space is partitioned into a reference space P and a secondary space Q, which together form a complete basis, i.e.

$$P + Q = 1. \tag{2.190}$$

For single-state CASPT2, the reference space is chosen as a CASSCF or CASCI (complete active space configuration interaction) reference state $|\alpha\rangle$, which is an eigenfunction of $\widehat{H}_0$, i.e.

$$P = |\alpha\rangle\langle\alpha|, \tag{2.191}$$

and

$$\widehat{H}_0|\alpha\rangle = E_0^\alpha|\alpha\rangle. \tag{2.192}$$

Furthermore, a *wave-operator* Ω^α is introduced, which produces the exact state of interest $|\Psi\rangle$, when it operates on the zeroth-order state $|\alpha\rangle$:

$$\Omega^\alpha|\alpha\rangle = |\Psi\rangle. \tag{2.193}$$

This wave operator is obtained by solving the Bloch equation[27]

$$\left(E_0^\alpha - \widehat{H}_0\right)\Omega^\alpha|\alpha\rangle = Q\hat{V}\Omega^\alpha|\alpha\rangle - Q\Omega^\alpha|\alpha\rangle\langle\alpha|\hat{V}\Omega^\alpha|\alpha\rangle, \tag{2.194}$$

where intermediate normalization is used, i.e. $\langle\alpha|\Psi\rangle = 1$.

Performing a perturbative order-by-order expansion for the wave operator, the equation for the first-order wave operator Ω_1^α, which is completely determined by $\widehat{H}_0$ and $|\alpha\rangle$, reads

$$\left(E_0^\alpha - \widehat{H}_0\right)\Omega_1^\alpha|\alpha\rangle = Q\widehat{H}|\alpha\rangle, \tag{2.195}$$

and the energy up to second order E_{2nd}^α is given by

$$E_{2nd}^\alpha = E_{1st}^\alpha + \langle\alpha|\widehat{H}\Omega_1^\alpha|\alpha\rangle. \tag{2.196}$$

In single-state CASPT2, the zeroth-order Hamiltonian $\widehat{H}_0^\alpha$ for (CASCI or CASSCF) reference state $|\alpha\rangle$ is given by

$$\hat{H}_0^\alpha = |\alpha\rangle\langle\alpha|\hat{F}^\alpha|\alpha\rangle\langle\alpha| + \sum_k |k\rangle\langle k|\hat{F}^\alpha|k\rangle\langle k| + Q_{sd}^\alpha \hat{F}^\alpha Q_{sd}^\alpha + Q_{tq\ldots}^\alpha \hat{F}^\alpha Q_{tq\ldots}^\alpha . \quad (2.197)$$

Here, the sum over k runs over all states within the CAS which are orthogonal to $|\alpha\rangle$. The subspace Q_{sd}^α is composed of *internally contracted* states $|pqrs;\alpha\rangle$ (which are nonorthogonal and linearly dependent) that are generated by applying double excitation operators (2.160) to $|\alpha\rangle$, i.e.

$$|pqrs;\alpha\rangle = \hat{E}_{pq}\hat{E}_{rs}|\alpha\rangle, \quad (2.198)$$

where internally contracted states, in which p, q, r and s are all active orbital indices, are not part of Q_{sd}^α. The subspace $Q_{tq\ldots}^\alpha$ includes all higher-order (higher than double) excitations. The configuration space, in which the wave function is expanded, does not necessarily need to be composed of internally contracted configurations. It is also possible to use configurations which are generated by applying the excitation operators to the individual CSFs used to build the reference state, i.e. *uncontracted configurations*, or a mixture of internally contracted and uncontracted configurations. It depends on the specific implementation, which configuration space is used. In the conventional CASPT2 method implemented in Molpro[28,30,80], only the doubly external configurations, i.e. the configurations in which two electrons are excited from the internal to the external orbital space, are internally contracted. The PNO-CASPT2 method[29] implemented in Molpro employs a fully internally contracted configuration space. Both methods are used in this thesis.

$\hat{F}^\alpha$ is a generalized one-body Hartree-Fock operator which is usually non-diagonal and depends on the one-particle density matrix of $|\alpha\rangle$. Its form is often chosen in a way that it is equivalent to the Møller-Plesset Hamiltonian[98] in the limiting case of a closed-shell reference function. This form is given by

$$\hat{F} = \sum_{pq} f_{pq}\hat{E}_{pq}, \quad (2.199)$$

where f_{pq} are the spin-summed expectation values of the operators

$$\hat{F}_{pq\sigma} = \hat{a}_{p\sigma}\left[\hat{H}, \hat{a}^{\dagger}_{q\sigma}\right] - \hat{a}^{\dagger}_{p\sigma}\left[\hat{H}, \hat{a}_{q\sigma}\right]. \tag{2.200}$$

Using certain mathematical identities[27], the first-order equation for the wave operator can be rewritten as

$$\left(E_0^{\alpha} - \hat{F}^{\alpha}\right)\Omega_1^{\alpha}|\alpha\rangle = Q_{sd}^{\alpha}\hat{H}|\alpha\rangle. \tag{2.201}$$

Therefore, the operator Ω_1^{α} only projects into Q_{sd}^{α} (when acting on $|\alpha\rangle$).

Equation (2.201), can be iteratively solved to obtain Ω_1^{α} using states which span the Q_{sd}^{α} space. The linear dependence of the $|pqrs;\alpha\rangle$ states is removed by transforming them to an orthonormalized form first. This is achieved by diagonalizing their overlap matrix and deleting the eigenvectors which correspond to zero (or almost zero) eigenvalues.

2.3.2.2.2. Multi-state CASPT2

There are cases in which the CASSCF wave function is not a good reference state for the perturbation calculation, for example at avoided crossings, i.e. if two or more (excited) states lie very close in energy. In these cases, a strong mixing between the reference state and external-space CASCI states (and therefore also indirectly between the reference states) can occur. The single-state CASPT2 method cannot account for this mixing. A remedy for this problem is given by the multi-state CASPT2 method[27], which is presented is this section. The equations for multi-state CASPT2 are derived in a similar way as for single-state CASPT2, therefore several steps in the derivation are skipped. For more details about the exact derivation, the interested reader is referred to the literature used for the preparation of this chapter[27].

The multi-state CASPT2 method is based on a multidimensional reference space P, which consists of d state-averaged CASSCF or CASCI states

$$P = \sum_{\alpha=1}^{d} |\alpha\rangle\langle\alpha|. \tag{2.202}$$

All quantities occurring in single-state CASPT2 are generalized for this multidimensional reference space. The zeroth-order Hamiltonians are chosen to be identical to the ones used for the single-state version. The generalized wave operator for multi-state CASPT2 Ω^P generates the exact states of interest $|\psi_p\rangle$ when acting on the so-called *model states* $|\psi_p^0\rangle$ (where $p = 1,2 \dots, d$), which are the projections of the exact states of interest into the P space. These model states $|\psi_p^0\rangle$ are linear combinations of the reference states $|\alpha\rangle$. It can be shown that the model states are eigenfunctions of an effective Hamiltonian $\hat{H}^{eff}$,

$$\hat{H}^{eff}|\psi_p^0\rangle = E_p|\psi_p^0\rangle \quad (p = 1,2, \dots, d), \tag{2.203}$$

where E_p is the exact energy of energy of $|\psi_p\rangle$, i.e.

$$\hat{H}|\psi_p\rangle = E_p|\psi_p\rangle \qquad (p = 1,2, \dots, d). \tag{2.204}$$

The effective Hamiltonian is given by

$$\hat{H}^{eff} = P\hat{H}\Omega^P P, \tag{2.205}$$

and the wave operator Ω^P can be expanded order-by-order, i.e.

$$\Omega^P = 1 + \Omega_1^P + \Omega_2^P + \cdots. \tag{2.206}$$

It can be shown[27] that the first-order multireference wave operator Ω_1^P is simply a linear combination of single-state wave operators

$$\Omega_1^P = \sum_{\alpha=1}^{d} \Omega_1^\alpha |\alpha\rangle\langle\alpha|. \tag{2.207}$$

Therefore the effective Hamiltonian up to second order $\hat{H}_{2nd}^{eff}$ is given by

$$\hat{H}_{2nd}^{eff} = P\hat{H}P + P\hat{H}\Omega_1^P P. \tag{2.208}$$

The single-reference CASPT2 energies E_{2nd}^α are the diagonal elements of this operator, i.e.

$$\langle\alpha|\widehat{H}_{2nd}^{eff}|\alpha\rangle = E_{2nd}^{\alpha} \qquad (\alpha = 1,2,\dots,d), \tag{2.209}$$

and the off-diagonal elements are given by

$$\langle\beta|\widehat{H}_{2nd}^{eff}|\alpha\rangle = \langle\beta|\widehat{H}\Omega_1^P|\alpha\rangle \quad (\alpha,\beta = 1,2,\dots,d). \tag{2.210}$$

The multi-state CASPT2 method presented here therefore consists of d independent single-state CASPT2 calculations and a subsequent *mixing* step, which consists of building and diagonalizing the effective Hamiltonian $\widehat{H}_{2nd}^{eff}$. The diagonal elements of $\widehat{H}_{2nd}^{eff}$ are calculated as in the single-state version and the non-diagonal elements are generated by scalar products between vectors which are calculated by the single-state CASPT2 method. This makes this multi-state version of CASPT2 not much more time consuming than d independent single-state CASPT2 calculations.

The multi-state CASPT2 version described in this section is denoted as a *single-reference multi-state (SR-MS)* CASPT2 method, because the configuration basis for each state is generated only from its own reference function. It should be noted that the approximative second-order mixing can lead to problems for SR-MS-CASPT2 calculations. For example, in calculations of free lanthanide ions or lanthanide complexes, the second-order mixing can lead to symmetry breakings and artificial splittings of states which are physically degenerate. This can be a problem, if one is interested in the accurate calculation of small energy differences. In these cases it is recommended to neglect the state mixing step in the end.

There are numerous ways to choose the zeroth-order Hamiltonian and the configuration basis. For example, there are also multi-state CASPT2 formulations in which the first-order wavefunction is expanded in terms of the union of internally contracted basis functions generated from all reference functions, which guarantees invariance of the theory with respect to unitary rotations of the reference functions. This is denoted as *multireference multi-state (MR-MS-)* CASPT2. Moreover, it is possible to employ state-averaged Fock operators for CASPT2. If equal weights are used for all reference states included in the Fock operator, it is invariant with respect to rotations among the reference functions. The extended multi-state (XMS) CASPT2 implemented in Molpro[97] is one of the MR-MS-CASPT2 methods which works with the union of the internally contracted configurations generated

from all reference functions and applies a unitary transformation to the reference states already before solving the CASPT2 equations. For more details on this method, the interested reader is referred to the literature[97].

2.3.2.2.3. Local CASPT2 using pair natural orbitals

The number of *internally contracted configurations* (*ICCs*, defined by equation (2.198)) strongly increases with the number of closed-shell and active orbitals. Therefore, conventional CASPT2 calculations for large molecules/complexes are very demanding and often computationally not feasible. A solution for this problem is given by local multireference correlation methods, such as the *local CASPT2 method using pair natural orbitals (PNO-CASPT2)*[29]. This method is briefly described in this section. Since the underlying theory is quite extensive, only the basic principles of the theory are explained. For more details and equations, the interest reader is referred to the literature used for the preparation of this section[29].

The PNO-CASPT2 method implemented in Molpro uses a fully internally contracted configuration space for the expansion of the first-order wave function. As for conventional CASPT2, the ICCs are generated by applying double excitation operators to the reference function as a whole, i.e.

$$|rmsn;\alpha\rangle \equiv |\Phi_{mn}^{rs};\alpha\rangle = \hat{E}_{rm,sn}|\alpha\rangle, \tag{2.211}$$

where the orbital indices m, n run over all occupied/correlated orbitals and r, s over all active and virtual orbitals. The first-order wave function (for reference state $|\alpha\rangle$) in CASPT2 (generated by the first-order wave operator) is expanded in terms of these ICCs as

$$\left|\Psi_{\alpha}^{(1)}\right\rangle = \Omega_1^{\alpha}|\alpha\rangle = \frac{1}{2}\sum_{mn}\sum_{rs}|\Phi_{mn}^{rs};\alpha\rangle\, T_{rs}^{mn}, \tag{2.212}$$

where the factors T_{rs}^{mn} are called *pair amplitudes*.

In order to achieve linear scaling of the computation time and required memory with molecular size, local approximations are used. For this purpose, the occupied (inactive and active) orbitals are localized and the local virtual space for each electron pair (excited from

the occupied orbitals m, n) is spanned by a domain of local *pair-natural orbitals (PNOs)*[99–101]. The domains are constructed in a two-step procedure: First, projected atomic orbitals (PAOs)[102] are generated by projecting out the occupied orbitals from the atomic orbitals. These PAOs are used to calculate a non-iterative approximation for the pair amplitudes, which are then used to generate PNOs, which leads to a strong reduction of the domain sizes. The specific size of the domains can be regulated by certain thresholds. Therefore, the number of ICCs is reduced by only keeping ICCs which are constructed by excitations from local inactive and active orbitals to spatially close local virtual orbitals. Moreover, the small energy contributions of spatially distant pairs m, n are calculated by simple *multipole approximations*. A further speedup is achieved by using parallel local density fitting techniques for the transformation and evaluation of the two-electron integrals[103].

Recently, a multi-state version of the method (MS-PNO-CASPT2) was implemented[104], which is equivalent to the non-local SR-MS-CASPT2 method described above. This method enables the application of the PNO-CASPT2 method in the field of single molecule magnets, which requires the calculations of a large number of excited states.

2.3.2.3. Multireference configuration interaction

The *multireference configuration interaction (MRCI)* method can account for dynamical electron correlation effects in multireference cases in a variational, i.e. non-perturbative, way. It is an extension of the conventional CI method for MCSCF (instead of Hartree-Fock) wave functions as zeroth-order approximation. This chapter gives a short overview of the method. For more details, the interested reader is referred to literature used to write this chapter[33–35,44,105].

In the *uncontracted* MRCI method, the correlated wave function $|\Psi_{MRCI}\rangle$ is constructed from a subset of CSFs which are generated by applying single and double excitations to each reference configuration, i.e.

$$|\Psi_{MRCI}\rangle = \sum_{I} C^{I}|\Phi_{I}\rangle + \sum_{S,a} C_{a}^{S}|\Phi_{S}^{a}\rangle + \sum_{P,ab} C_{ab}^{P}|\Phi_{P}^{ab}\rangle. \tag{2.213}$$

Here, the index I refers to the internal space, the index S refers to the singles space, i.e. to the space of CSFs containing one electron in some external orbital and the index P to the pair space which consists of all CSFs with two electrons in external orbitals.

This ansatz is inserted into the molecular electronic Schrödinger equation which is then solved variationally by direct CI methods. To reduce the number of variational parameters, internal contraction can be employed, which results in the internally contracted MRCI (icMRCI) method. However, the use of ICCs leads to various difficulties due to nonorthogonality, linear dependencies (as for CASPT2) and the necessity of calculating high-order reduced density matrices[105]. Therefore, the implementation of icMRCI by Werner and Knowles[33] in Molpro[80] uses a mixed excitation basis consisting of ICCs and CSFs, where only the doubly external CSFs are replaced by doubly external ICCs $|\Phi_{mn}^{ab}\rangle$ (as for the conventional CASPT2 method implemented in Molpro). The wave function ansatz for this case[105] is

$$|\Psi_{icMRCI}\rangle = \sum_{R} C^{R}|\Phi_{R}\rangle + \sum_{I} C^{I}|\Phi_{I}\rangle + \sum_{S,a} C_{a}^{S}|\Phi_{S}^{a}\rangle + \frac{1}{2}\sum_{mn,ab} C_{ab}^{mn}|\Phi_{mn}^{ab}\rangle. \qquad (2.214)$$

where $|\Phi_{R}\rangle$ are the internal CSFs which are contained in the reference space and $|\Phi_{I}\rangle$ are the internal CSFs not contained in the reference space.

The icMRCI method can also be used for the calculation of several excited states. In conventional *multi-state icMRCI (MS-icMRCI)* calculations one typically employs an ICC basis which is the union of all contracted configurations generated from separate reference functions for each state up to and including the highest state of interest. This is a severe problem if a large number of states needs to be calculated, for example in calculations of crystal-field splittings in lanthanide complexes. In these calculations, the number of ICCs is extremely large due to the large number of required states and also due to the typically large number of closed-shell orbitals. Therefore, multi-state icMRCI of crystal-field splittings in lanthanide complexes are usually not feasible and one is restricted to CASPT2 calculations.

2.3.3. Projection of ab initio wave functions onto a pseudospin

This chapter gives a short introduction to the pseudospin formalism and the projection of ab initio wave functions onto a pseudospin. For more details, the interested reader is referred to the literature on which this chapter is based[18,106].

For the interpretation of experiments, e.g. spectra, one typically employs so-called *pseudospin Hamiltonians* which are used to simulate the specific experiment. The free parameters in these pseudospin Hamiltonians are then fit to optimally reproduce the experiment. Important quantities, such as g-tensors, zero-field splitting tensors, crystal-field parameters (CFPs) and exchange coupling tensors/constants can be obtained by this approach. In general, the pseudospin $\tilde{S}$ does not necessarily have to correspond to a physical quantity, but in the limiting cases of weak or moderate spin-orbit coupling (e.g. transition metal complexes) and strong spin-orbit coupling (e.g. lanthanide or actinide complexes) it approximately corresponds to the (physical) spin S or the total angular momentum J, respectively.

If one wants to obtain pseudospin Hamiltonian parameters directly from ab initio calculations, a one-to-one mapping of the (often lowest) $N = 2\tilde{S} + 1$ ab initio wave functions (including spin-orbit coupling) $|\Psi_i\rangle$, $i = 1, \dots, N$ of interest onto pseudospin eigenfunctions $\left|\tilde{S}M\right\rangle$, $M = -\tilde{S}, \dots, \tilde{S}$ is necessary. The dimension of the pseudospin is therefore given by $\tilde{S} = (N-1)/2$. The mapping can be achieved by the requirement that the Hamiltonian of interest should yield the same eigenvalues in the basis of ab initio wave functions and in the basis of pseudospin eigenfunctions.

In general, there are different procedures for the calculation of pseudospin Hamiltonian parameters using the results from ab initio calculations. We will briefly introduce the procedures used in the program SINGLE_ANISO[18], which was used for the calculations in this thesis.

As an example, the Zeeman Hamiltonian $\widehat{H}_{Zee}$ for the interaction of a molecule, e.g. a transition metal or lanthanide/actinide complex, with an external magnetic field $\vec{B}$ can be considered. For an ab initio calculation, this Hamiltonian is given as

$$\hat{H}_{Zee} = -\vec{\hat{\mu}}\vec{B}, \tag{2.215}$$

where the *total magnetic moment* operator $\vec{\hat{\mu}}$ is given as

$$\vec{\hat{\mu}} = -\mu_B \left(g_e \vec{\hat{S}} + \vec{\hat{L}} \right), \tag{2.216}$$

with the Bohr magneton μ_B, the free electron spin g-factor g_e and the total spin operator $\vec{\hat{S}}$ and the total angular momentum operator $\vec{\hat{L}}$.

Now let us consider the simplest example of a pseudospin $\tilde{S} = 1/2$, which corresponds to a Kramers doublet. According to the Kramers theorem, this doublet is always degenerate without an applied magnetic field, i.e. there is no zero-field splitting. The two ab initio wave functions corresponding to the Kramers doublet are denoted as Ψ_1 and Ψ_2. In order to calculate the g-tensor and its eigenvectors (corresponding to the *main magnetic axes*), the Zeeman Hamiltonian (2.215) is written in the basis (Ψ_1, Ψ_2) and diagonalized for an arbitrary orientation of the magnetic field $\vec{B} = (\xi_x, \xi_y, \xi_z)B$ (with $\xi_x^2 + \xi_y^2 + \xi_z^2 = 1$), which yields the analytical eigenvalues

$$E_{Zee} = -\lambda B, \qquad \lambda_{\pm} = \pm \left(\sum_{\alpha\beta \in \{x,y,z\}} \xi_\alpha A_{\alpha\beta} \xi_\beta \right)^{1/2} \tag{2.217}$$

where the tensor $\bar{\bar{A}}$ for an $N = 2\tilde{S} + 1$ dimensional basis is given as

$$A_{\alpha\beta} = \frac{1}{2} \mathrm{tr}\{\mu_\alpha \mu_\beta\} = \frac{1}{2} \sum_{i=1}^{N} \sum_{j=1}^{N} (\mu_\alpha)_{ij} (\mu_\beta)_{ji}, \tag{2.218}$$

and $N = 2$ for the Kramers doublet in the present case. μ_α and μ_β denote the components of the total magnetic moment operator.

The tensor $\bar{\bar{A}}$ can be diagonalized with a rotation $\bar{\bar{R}}_r$ of the real space coordinate system x, y, z to its principal axes X, Y, Z, i.e.

$$\bar{\bar{R}}_r^{-1}\bar{\bar{A}}\bar{\bar{R}}_r = \tilde{\bar{\bar{A}}}_{diag} = \mathrm{diag}\left(\tilde{A}_{XX}, \tilde{A}_{YY}, \tilde{A}_{ZZ}\right). \tag{2.219}$$

The Zeeman splitting has extremal values for the magnetic field applied along the principal axes. Therefore, these axes are the main magnetic axes of the complex.

The description of the Zeeman splitting of a Kramers doublet using the pseudospin formalism employs the Hamiltonian

$$H_{Zee} = \mu_B \vec{B}\bar{\bar{g}}\vec{\tilde{S}}, \tag{2.220}$$

where $\bar{\bar{g}}$ is the g-tensor of the system and the pseudospin operator $\vec{\tilde{S}}$ contains the three Pauli spin matrices multiplied by $1/2$ (and in SI-units also multiplied by $\hbar$) as components for the case of a pseudospin $\tilde{S} = 1/2$.

Diagonalization of the pseudospin Hamiltonian yields the analytical eigenvalues (in atomic units)

$$E_{Zee} = -\lambda B, \qquad \lambda_{\pm} = \pm\frac{\mu_B}{2}\left(\sum_{\alpha\beta\in\{x,y,z\}} \xi_\alpha G_{\alpha\beta}\xi_\beta\right)^{1/2}, \tag{2.221}$$

with the Abragam-Bleaney tensor[107] $G_{\alpha\beta}$ defined by

$$\bar{\bar{G}} = \bar{\bar{g}}\bar{\bar{g}}^T. \tag{2.222}$$

Comparing equation (2.221) with equation (2.217) yields the relation

$$\frac{\mu_B^2}{4}\bar{\bar{G}} = \bar{\bar{A}}. \tag{2.223}$$

Both $\bar{\bar{G}}$ and $\bar{\bar{A}}$ can be brought simultaneously to diagonal form by the rotation $\bar{\bar{R}}_r$ of the real space coordinate system to the main magnetic axes, which yields for the main components g_i of the g-tensor the expression

$$g_i = \pm\frac{2}{\mu_B}\sqrt{\tilde{A}_{ii}}, \quad i = X, Y, Z, \tag{2.224}$$

which can therefore completely be determined from ab initio calculations, apart from their sign. Only the sign of the product of all three main values can be obtained from the results of the quantum chemical calculations[18]. The g-tensor in the initial coordinate system can be calculated from the main values by an inverse rotation.

The only quantities necessary for a projection of ab initio results onto a pseudospin $\tilde{S} = 1/2$ are therefore the matrix elements of the total magnetic moment in the basis of ab intio wave functions, which can be calculated from the matrix elements of the total spin operator and the matrix elements of the total angular momentum operator $(\mu_\alpha)_{ij}$. Note that there is an origin dependence of the matrix elements of the total angular momentum operator. The most reasonable choice of the origin for mononuclear complexes is usually the transition metal/lanthanide/actinide ion of the complex. For higher pseudospins, the zero-field splitting Hamiltonian $\widehat{H}_{ZFS}$ is also required, for which one also needs the (zero-field) energy eigenvalues E_i obtained by ab initio calculations. Analytical projections can be done for the pseudospins $\tilde{S} = 1/2$ and $\tilde{S} = 1$. For pseudospins $\tilde{S} \geq 3/2$, approximate projections are possible, which also only require $(\mu_\alpha)_{ij}$ and E_i. The zero-field splitting Hamiltonian (and also the Zeeman Hamiltonian) can be decomposed into irreducible tensor operators (ITOs)[18] and the projection of the ab initio results onto this operator allows the extraction of crystal-field parameters of complexes. In the case of lanthanide or actinide complexes, the ab initio results are projected onto a pseudospin of the dimension of the ground J-multiplet of the lanthanide or actinide ion. It should be noted that the values of the crystal-field parameters depend on the chosen quantization axis. In many cases, this quantization axis is chosen as the main magnetic axis Z of the ground (pseudo) doublet or as the main rotational symmetry axis of the complex. Note that the crystal-field parameters, especially the ones which must be numerically zero in certain symmetries, slightly depend on the local approximations employed in ab initio methods. The thresholds for the local approximations should be tightened if one aims for an accurate determination of those parameters. For more details on these projections for higher pseudospins, the interested reader is referred to the literature[18].

3. Results

The main objective of this thesis was the improvement of the methods used for ab initio calculations of lanthanide based single-molecule magnets. During the process of research, the developed methods were also applied to transition metal and actinide complexes. The title of this thesis therefore includes metal complexes in general. However, since the main focus was originally lying on lanthanide complexes, most parts of the thesis are discussed from the perspective of improving and subsequently applying methods used for the ab initio calculations of lanthanide based systems.

Conventional ab initio calculations of lanthanide based single-molecule magnets employ the CASSCF/SI-SO approach[3,16,31,94,106]. This method is able to provide relevant quantities of lanthanide complexes, e.g. the orientation of the principal magnetic axes, g-tensors and crystal-field parameters, which was successfully demonstrated during the last decade[3,18–26,108]. The CASSCF calculations are usually performed as state-averaged calculations (SA-CASSCF), i.e. one common set of orbitals is determined for all states. Due to the relatively small orbital relaxation between the states of the $4f^n$ space, this approach works quite well. However, this method has different shortcomings.

The first problem is that the method is computationally very demanding for large molecules and large basis sets and the calculations have to be performed on high performance computing clusters. This is in particular due to the demanding orbital optimization in the CASSCF approach and the coupled optimization of both the CI coefficients *and* the orbitals. Therefore, the investigations are most often restricted to single-point calculations at the experimental geometry obtained from X-ray crystallography. This can lead to problems, for example because of the positions of the positions of the hydrogen atoms, which are usually inserted at idealized positions during the crystallographic refinement. However, it was demonstrated[22] that these positions can be crucial for the crystal-field splitting. Moreover, the calculation of dynamic effects on the crystal-field splitting, i.e. spin-phonon coupling, requires property calculations at many different geometries, obtained by, for example, elongation along some normal coordinate. For large molecules and basis sets, this is usually not feasible because of the enormous required computational effort. Furthermore, the development of blueprints for the design of single-molecule magnets requires the *in silico*

variation of different ligands groups and the investigation of the resulting influence on the crystal-field splitting. However, the required time for CASSCF calculations of large molecules is too large for an effective *screening* of many different chemical modifications of a single-molecule magnet. The first aim of this thesis was therefore to increase the speed of the CASSCF/SI-SO method (Chapter 3.1).

The second shortcoming of the CASSCF/SI-SO method is its accuracy. The methods neglects dynamical correlation which often leads to an underestimation of the crystal-field splitting [31,109]. The inclusion of dynamical correlation is computationally extremely demanding and is therefore usually only accounted for by multireference perturbation theory, e.g. CASPT2. However, the CASPT2 method often overestimates the energy of the high-lying crystal field states ("overshooting effect")[31] if the minimal active space is chosen or is not feasible for large active spaces and large molecules. Moreover, it can suffer from the well-known problems of perturbation theory, such as *intruder state problems*[28,32]. Variational multi-state MRCI calculations, which do not suffer from these problems, are usually not feasible, even for small lanthanide complexes, especially if the calculation of many states/roots is required. This is due to the enormous time and central processing unit (CPU) requirements for these calculations. The second aim of this thesis was therefore to enable the efficient inclusion of dynamical correlation beyond perturbation theory in calculations of crystal-field splitting in lanthanide complexes (Chapter 3.2).

The third problem of the CASSCF/SI-SO method is the calculation of polynuclear complexes and the calculation of magnetic exchange in those systems, especially for lanthanide complexes. The development of polynuclear complexes that involve strong exchange couplings is a promising approach to achieve magnetic bistability in those systems[110]. Moreover, magnetic (exchange) interactions between lanthanide ions have been suggested as building blocks for multiqubit gates in quantum information processing/quantum computers[6,47]. However, the calculation of exchange couplings in polynuclear lanthanide complexes beyond density-functional-theory (DFT) is extremely challenging, because the active space and therefore the number of CSFs and required states quickly becomes very large. This renders the CASSCF calculations very demanding. Furthermore, the calculation of exchange couplings between the lanthanide ions often requires the inclusion of dynamical correlation. For this, multireference correlation methods such as CASPT2 and MRCI are

needed, which are computationally even more demanding than the CASSCF method. Recently, ab initio calculations of the magnetic coupling in $Ce_2(COT)_2$ (COT=1,3,5-cyclooctatetraenide) including dynamical correlation were presented[111,112], which employed the variational difference dedicated configuration interaction (DDCI) method and MRCI, including only single excitations in the wave function ansatz (this method was called MRCI+CIS by the authors). However, the resulting configuration space for the DDCI (DDCIn, n=2,3) and MRCI+CIS calculations was smaller than the configuration space for CASPT2 assuming the same active space. Furthermore, the MRCI+CIS approach does not contain double excitations and therefore neglects two-electron correlation, which are very important for the description of dynamical correlation. The authors moreover employed symmetry[111] to decrease the computation time and render the calculations feasible. However, this is not possible in most cases, since the majority of complexes of interest corresponds to the point group C_1. The third aim of this thesis was therefore to enable the fast and accurate calculation of magnetic exchange in polynuclear (lanthanide) complexes including dynamical correlation (Chapter 3.3).

In the following, the methods developed within this thesis to solve the described problems and their application to different complexes are presented.

3.1. Increasing the speed of conventional calculations

In the following, the local density-fitted configuration-averaged Hartree-Fock (LDF-CAHF) method developed within this thesis is presented. First, the conventional approach for ab initio calculations in the molecular nanomagnetism community, the CASSCF/SI-SO method, is briefly summarized. Subsequently, the configuration-averaged Hartree-Fock (CAHF) method is introduced and the equivalency of the orbitals obtained by state-averaged CASSCF and CAHF is explained. Finally, the LDF-CAHF method is presented, which results from a combination of the techniques of local-density fitting with CAHF. The method is then applied to different complexes to assess its performance. Parts of this chapter, in particular the presentation of the LDF-CAHF method and its application to various complexes, have already been published, see *J. Chem. Phys.* **147** (16), 164101 (2017)[37] (presentation of the LDF-CAHF method) and *Chem. Sci.* **9** (5), 1221–1230 (2018)[40], *Chem. Eur. J.* **25**, 1758-1766 (2019)[41], *Phys. Chem. Chem. Phys.* **21** (13), 6976-6983 (2019)[42], *Angew. Chem. Int. Ed.*, DOI: 10.1002/anie.201904645 (2019)[43] (application to different complexes), and have been used for the formulation/text of this thesis. In the publication presenting the LDF-CAHF method[37], Dr. Christoph Köppl helped to implement the method into Molpro. Moreover, Dr. Liviu Ungur helped to implement the SINGLE_ANISO[18] module into Molpro.

3.1.1. CASSCF/SI-SO

In the case of lanthanide complexes, the active space in the CASSCF method is most often chosen to consist of the seven $4f$-orbitals of the lanthanide ion. Pseudopotentials or the (second order) Douglas-Kroll-Hess operator[113] are employed in the one-electron part of the Hamiltonian to account for scalar-relativistic effects. The optimized CASSCF wave functions are then used to build the spin-orbit matrix using a suitable SO-operator such as the no-pair Douglas-Kroll-Hess, the Breit-Pauli, or a pseudopotential SO-operator[94,95,114,115]. The spin-orbit matrix is finally diagonalized, yielding the crystal-field energy levels. The obtained eigenvectors can be used to calculate different properties, such as g-tensors or crystal-field parameters, usually after projection onto a pseudospin with the dimension of the Russell-Saunders ground multiplet. The best description of spin-orbit coupling is achieved if all possible CASSCF states (roots) of all spin-manifolds are used to build the SO-matrix.

In principle, the orbitals could be optimized individually for different roots and different spin-manifolds. However, this would require an enormous computational effort and the CASSCF wave functions would no longer be orthogonal, which leads to further difficulties in the SO-coupling (SOC) step. This problem can be overcome by determining one set of orbitals which is as good as possible for all different roots of all different spin-manifolds at the same time. This is achieved by state-averaged CASSCF (SA-CASSCF), where the average energy of the roots of interest is optimized. SA-CASSCF is the standard method used in the field of lanthanide containing molecular nanomagnets. Normally, all possible states of all possible spin-manifolds are included in the averaging process with identical weights. It is important to note that the orbital optimization is decoupled from the CI diagonalization step in this case. The reason for this is that the minimization of the average energy of all possible roots for a given CSF basis with respect to orbital rotations is equivalent to the minimization of the trace of the CI matrix. This trace is invariant under unitary transformations, i.e. CI diagonalization steps, and therefore no alternating orbital and CI coefficient steps are necessary. Instead, one can simply first determine the optimized orbitals by minimizing the trace of the CI matrix and then perform one CI diagonalization to obtain the final energies and wave functions. Configuration-averaged Hartree-Fock is a method for the orbital optimization in this procedure.

3.1.2. CAHF/CASCI/SI-SO

Configurational averaging in the general case was described by McWeeny several decades ago[51,116] and the idea was recently implemented for the $4f$-case by Soncini and co-workers[117]. This section reviews some of the most important aspects of the methodology. Given a system with a closed and an open shell, we call the number of spatial orbitals in the closed shell (inactive orbitals) n_c and the number of spatial orbitals in the open shell (active orbitals) n_o. The number of active electrons, i.e., electrons in the open shell, is denoted as n_A. The (fractional) occupation numbers of the closed and open shell are $a_1 = 2$ and $a_2 = n_A/n_o$, respectively. The energy functional of an SA-CASSCF calculation, averaging over all possible roots of all spin-manifolds taking into account the M_S-degeneracy of the corresponding spin-manifolds by a weighting factor, can be rewritten as

$$E_{av}^{all\ S/M_S} = a_1 \sum_{i}^{n_c} h_i + \frac{{a_1}^2}{2} \sum_{i,j}^{n_o} \left(J_{ij} - \frac{1}{2} K_{ij} \right) + a_1 a_2 \sum_{i}^{n_c} \sum_{t}^{n_o} \left(J_{it} - \frac{1}{2} K_{it} \right) + a_2 \sum_{t}^{n_o} h_t + a_2 \frac{(n_A - 1)}{(2n_o - 1)} \sum_{t,u}^{n_o} \left(J_{tu} - \frac{1}{2} K_{tu} \right) + E_{nuc}, \quad (3.1)$$

where h_r are the one-electron integrals (in MO basis) and J_{rs} and K_{rs} are the Coulomb and exchange integrals (in MO basis). The indices i, j run over the closed-shell orbitals and the indices t, u over the active orbitals.

The constrained minimization of this functional with respect to the orthonormality condition for the orbitals yields a Hartree-Fock-like equation which can be iteratively solved until self-consistency is achieved. The converged orbitals can then be used in a subsequent CASCI step to yield the actual wave functions which are mathematically equivalent to the wave functions from a SA-CASSCF calculation over all roots of all spin-manifolds with weighting factors considering the M_S-degeneracy of each spin-state. These wave functions are then used to build up the spin-orbit matrix, which is subsequently diagonalized to obtain the final energies and SO-coupled wave functions. The resulting energies and eigenvectors of the spin-orbit matrix can then be used to calculate different properties and simulate experiments. This simplified approach scales as a standard open-shell Hartree-Fock calculation with respect to the system size and moreover enables the treatment of a large number of active/open orbitals. Consequently, this approach allows for fast and stable ab initio calculations of large systems. As the orbital optimization in CASSCF is quite involved and moreover coupled to the optimization of the CI coefficients, this method is significantly faster than SA-CASSCF for large molecules. Note that special attention has to be paid for polynuclear systems, i.e., systems with more than one lanthanide ion, as these possess several open shells. In order to avoid the inclusion of states with very high energy (e.g., states where all electrons in the active space are at one lanthanide) in the averaging, the theory has to be modified[51], which is done by an extension of LDF-CAHF, denoted as LDF-MOS-CAHF (MOS: multiple-open-shell), in this thesis (Chapter 3.3).

3.1.3. Combining CAHF with local density-fitting

3.1.3.1. Local density-fitted configuration-averaged Hartree-Fock

In the following, the LDF-CAHF method developed in this thesis is presented. The aim was to combine the high speed and efficiency of the LDF-HF method described in the theory section with the configurational averaging required for simulation of, e.g. lanthanide containing molecular nanomagnets. The first step to achieve this is to rewrite the energy functional (3.1) for the configurational averaging over all spin-manifolds in a form which is similar to the form of the open-shell LDF-HF equations implemented in Molpro. This form is different from the form of Soncini and co-workers[117] and, using the LCAO approximation, given by

$$E_{av}^{all\ S/M_S} = \frac{1}{2}\mathrm{tr}[\mathbf{D}(\mathbf{H}+\mathbf{F}^c)] + \frac{1}{2}\mathrm{tr}[\mathbf{D}^o\mathbf{F}^o] + E_{nuc}, \tag{3.2}$$

with the density and Fock matrices

$$D_{\mu\nu} = 2\sum_{i}^{n_c} C_{\mu i}\, C_{\nu i} + a_2 \sum_{t}^{n_o} C_{\mu t}\, C_{\nu t}, \tag{3.3}$$

$$D^o_{\mu\nu} = a_2 \sum_{t}^{n_o} C_{\mu t}\, C_{\nu t}, \tag{3.4}$$

$$F^c_{\mu\nu} = H_{\mu\nu} + \sum_{\rho\sigma} D_{\rho\sigma}\left[(\mu\nu|\rho\sigma) - \frac{1}{2}(\mu\rho|\nu\sigma)\right], \tag{3.5}$$

$$F^o_{\mu\nu} = \left(\frac{2(n_A-1)}{a_2(2n_o-1)} - 1\right)\sum_{\rho\sigma} D^o_{\rho\sigma}\left[(\mu\nu|\rho\sigma) - \frac{1}{2}(\mu\rho|\nu\sigma)\right]. \tag{3.6}$$

The last two equations can be split into expressions with separate Coulomb and exchange parts for the closed and active/open parts

$$F^c_{\mu\nu} = H_{\mu\nu} + 2J^c_{\mu\nu} - K^c_{\mu\nu}, \tag{3.7}$$

$$F_{\mu\nu}^{o} = 2J_{\mu\nu}^{o} - K_{\mu\nu}^{o}. \tag{3.8}$$

Here, the Coulomb part is calculated using the scaled density matrices and conventional density fitting techniques and the more expensive exchange part is calculated by employing the LDF approximations presented above, where the additional scaling factors are included to ensure consistency with equations (3.3)-(3.6)

$$K_{\mu\nu}^{c} \approx \sum_{i}^{n_c}\left[\sum_{\bar{B}\in[i]_{fit}} (\bar{B}|\mu i)(\bar{B}|\nu i)\right] + \frac{a_2}{2}\sum_{t}^{n_o}\left[\sum_{\bar{C}\in[t]_{fit}} (\bar{C}|\mu t)(\bar{C}|\nu t)\right], \tag{3.9}$$

$$K_{\mu\nu}^{o} \approx \left(\frac{(n_A-1)}{(2n_o-1)} - \frac{a_2}{2}\right)\sum_{t}^{n_o}\left[\sum_{\bar{C}\in[t]_{fit}} (\bar{C}|\mu t)(\bar{C}|\nu t)\right]. \tag{3.10}$$

The indices i,t run over LMOs obtained by localization within the closed/active space only. Consequently, we have two sets of LMOs in these equations, one for the space of closed orbitals and one for the space of active orbitals and also corresponding LMO, AO and fitting domains for both spaces. The calculation of the exchange part using LDF approximations is the crucial factor enabling the high speed of the LDF-CAHF method.

Having defined the calculation of the energy functional we can proceed as in standard restricted open shell Hartree-Fock (ROHF) theory with its constrained minimization with respect to the MO-coefficients. The Lagrangian L for the constrained minimization of this functional can be written as

$$L = E_{av}^{all\ S/M_S} - 2\sum_{i}^{n_c}\epsilon_i\left[\langle i|i\rangle - 1\right] - \sum_{t}^{n_o}\epsilon_t[\langle t|t\rangle - 1] - 2\sum_{i}^{n_c}\sum_{t}^{n_o}\epsilon_{ti}\langle t|i\rangle. \tag{3.11}$$

Here, we have assumed that the closed- and open-shell orbitals are canonical (the matrices of the Lagrangian multipliers are assumed to be diagonal).

Taking the derivatives with respect to the MO-coefficients leads to

$$\left(\frac{\partial L}{\partial C_{\mu i}}\right) = 4[\mathbf{F}^{c}\mathbf{C}]_{\mu i} - 4[\mathbf{SC}]_{\mu i}\epsilon_i - 2\sum_{t}^{n_o}[\mathbf{SC}]_{\mu t}\epsilon_{ti}, \tag{3.12}$$

$$\left(\frac{\partial L}{\partial C_{\mu t}}\right) = 2a_2[(\mathbf{F}^c + \mathbf{F}^o)\mathbf{C}]_{\mu t} - 2[\mathbf{SC}]_{\mu t}\epsilon_t - 2\sum_i^{n_c}[\mathbf{SC}]_{\mu i}\epsilon_{ti}. \tag{3.13}$$

Setting these derivatives to zero, the variational conditions become

$$2[\mathbf{F}^c\mathbf{C}]_{\mu i} = 2[\mathbf{SC}]_{\mu i}\epsilon_i + \sum_t^{n_o}[\mathbf{SC}]_{\mu t}\epsilon_{ti}, \tag{3.14}$$

$$a_2[(\mathbf{F}^c + \mathbf{F}^o)\mathbf{C}]_{\mu t} = [\mathbf{SC}]_{\mu t}\epsilon_t + \sum_i^{n_c}[\mathbf{SC}]_{\mu i}\epsilon_{ti}. \tag{3.15}$$

The Fock matrices in the MO basis are defined as

$$\mathbf{f}^c = \mathbf{C}^\dagger\mathbf{F}^c\mathbf{C}\,, \tag{3.16}$$

$$\mathbf{f}^o = \mathbf{C}^\dagger\mathbf{F}^o\mathbf{C}\,. \tag{3.17}$$

The variational conditions are now multiplied from the left with $\mathbf{C}^\dagger$ and become

$$f_{ij}^c = \epsilon_i\delta_{ij}, \tag{3.18}$$

$$2f_{ti}^c = \epsilon_{ti}, \tag{3.19}$$

$$f_{ai}^c = 0, \tag{3.20}$$

$$a_2(\mathbf{f}^c + \mathbf{f}^o)_{it} = \epsilon_{ti}, \tag{3.21}$$

$$a_2(\mathbf{f}^c + \mathbf{f}^o)_{tu} = \epsilon_t\delta_{tu}, \tag{3.22}$$

$$a_2(\mathbf{f}^c + \mathbf{f}^o)_{at} = 0. \tag{3.23}$$

The indices a, b refer to virtual orbitals. Equating the two expressions for ϵ_{ti} and exploiting that the matrices $\mathbf{f}^c$and $\mathbf{f}^o$ are symmetric yields

$$((2-a_2)\mathbf{f}^c - a_2\mathbf{f}^o)_{it} = 0. \tag{3.24}$$

Furthermore, canonical virtual orbitals can be defined by imposing the condition

$$(\mathbf{f}^c + \mathbf{f}^o)_{ab} = \epsilon_a \delta_{ab}. \tag{3.25}$$

This set of variational conditions can be summarized in one single matrix equation as

$$\bar{\mathbf{f}} = \begin{pmatrix} \mathbf{f}^c & (2-a_2)\mathbf{f}^c - a_2\mathbf{f}^o & \mathbf{f}^c \\ (2-a_2)\mathbf{f}^c - a_2\mathbf{f}^o & a_2(\mathbf{f}^c + \mathbf{f}^o) & a_2(\mathbf{f}^c + \mathbf{f}^o) \\ \mathbf{f}^c & a_2(\mathbf{f}^c + \mathbf{f}^o) & \mathbf{f}^c + \mathbf{f}^o \end{pmatrix} = \begin{pmatrix} \mathbf{e}^c & \mathbf{0} & \mathbf{0} \\ \mathbf{0} & \mathbf{e}^o & \mathbf{0} \\ \mathbf{0} & \mathbf{0} & \mathbf{e}^v \end{pmatrix}. \tag{3.26}$$

Here, the rows and columns 1-3 represent the closed, active and virtual subspaces and $\mathbf{e}^c$, $\mathbf{e}^o$ and $\mathbf{e}^v$ are diagonal Lagrangian multiplier matrices. There are some degrees of freedom left. For instance, the factor a_2 in the active-active and active-virtual blocks can be set to 1, which only affects convergence but does not change the solution of the equation. In order to stay as close as possible to the standard ROHF equations, this factor is replaced by 1 in the implementation for the corresponding matrix blocks, yielding

$$\bar{\mathbf{f}} = \begin{pmatrix} \mathbf{f}^c & (2-a_2)\mathbf{f}^c - a_2\mathbf{f}^o & \mathbf{f}^c \\ (2-a_2)\mathbf{f}^c - a_2\mathbf{f}^o & \mathbf{f}^c + \mathbf{f}^o & \mathbf{f}^c + \mathbf{f}^o \\ \mathbf{f}^c & \mathbf{f}^c + \mathbf{f}^o & \mathbf{f}^c + \mathbf{f}^o \end{pmatrix} = \begin{pmatrix} \tilde{\mathbf{e}}^c & \mathbf{0} & \mathbf{0} \\ \mathbf{0} & \tilde{\mathbf{e}}^o & \mathbf{0} \\ \mathbf{0} & \mathbf{0} & \tilde{\mathbf{e}}^v \end{pmatrix}. \tag{3.27}$$

$\bar{\mathbf{f}}$ can be seen as an effective Fock matrix, which is built and diagonalized in each SCF iteration in the LDF-CAHF code

$$\mathbf{U}^\dagger \bar{\mathbf{f}}\, \mathbf{U} = \mathbf{e}. \tag{3.28}$$

This defines the improved MO-coefficients $\tilde{\mathbf{C}}$ as

$$\tilde{\mathbf{C}} = \mathbf{C}\mathbf{U}. \tag{3.29}$$

In the next iteration, the updated MO-coefficients are obtained by setting $\mathbf{C} = \tilde{\mathbf{C}}$ and this process is repeated until self-consistency in order to obtain the optimized averaged orbitals. These orbitals can be subsequently used for a CASCI step to obtain the wave functions which are equivalent to those obtained by the SA-CASSCF method and which can also be used as a reference for methods which also include dynamical correlation, e.g. CASPT2 or MRCI.

3.1.3.2. Initial guess

As the systems of interest have a complicated electronic structure and many different local minima are possible in the variational procedure, a good starting guess (and often also level-shifts and the DIIS method) is necessary to allow convergence to the right solution with, e.g., the f-orbitals in the active space. The default starting guess in Molpro, constructed by atomic densities, is not sufficient for that. Therefore we used a different strategy which consists of merging the orbitals from independent calculations of the ligand and the metal ion using the MERGE directive of Molpro. To be more precise, in a first step the orbitals of the ligand are obtained by a LDF-HF calculation with a point charge at the position of the paramagnetic ion simulating its electrostatic influence on the ligand orbitals. Of course this approach neglects the Pauli repulsion of the electrons but is, in our experience, the best approach to obtain fast convergence. In a second step the configuration averaged orbitals of the free ion are calculated using LDF-CAHF. The occupied and active orbitals of both systems are then symmetrically orthogonalized to obtain a good starting guess that fulfills the orthogonality criterion. In the next step the virtual orbitals of both the ligand and free ion are added to this set of starting orbitals. In order to make them orthogonal to the occupied/active orbitals without changing those, a Gram-Schmidt orthogonalization is performed at the end within the virtual space only. The resulting orthogonalized set of merged closed, active and virtual orbitals is then used as starting guess for the LDF-CAHF calculation of the whole system. Attention has to be paid when diffuse functions, i.e. augmented basis sets, are used for the ligands directly coordinating to the central ion. In these cases the point charge at the position of the paramagnetic ion might lead to an artificial accumulation of electron density at this ion because of the lacking Pauli repulsion. This artifact could lead to convergence to a wrong state with a higher absolute energy than that of the desired state if the starting guess is constructed out of these orbitals. Therefore, it may be beneficial to perform the ligand calculation without point charges if augmented basis sets are used for the first coordination

sphere of the ion, which possibly increases the number of necessary iterations but avoids the convergence to a wrong state. The whole strategy can be easily generalized to polynuclear systems by performing a LDF-CAHF calculation for all free ions at once, optionally with negative point charges at the positions of the formally charged ligand atoms, and the standard ligand calculation with point charges at the positions of the positively charged ions. This is possible, because increasing the active space does not require significantly more computational effort as the method still scales as a standard open-shell Hartree Fock calculation with respect to the number of open-shell orbitals. In contrast, such calculations are not easily performed within the SA-CASSCF formalism. Nevertheless, as already mentioned above, the theory has to be slightly modified in order to avoid the inclusion of high energy states in the averaging and this modification for systems containing more than one open shell is presented in Chapter 3.3.

Because the LDF-CAHF and the standard LDF-HF method are used to construct the starting guess, it is obtained in a fast and robust way also for large molecules. Note that all this can be done in one input stream and does not require any programming.

3.1.4. Benchmark applications of LDF-CAHF

In the following, the application of the developed LDF-CAHF method to certain systems is presented to assess the performance of the method.

3.1.4.1. Computational details

This section covers the technical details of the calculations of the systems investigated in this work, the free Er(III) and Dy(III) ions, $Er[N(SiMe_3)_2]_3$, Er(trensal) (H_3trensal = 2,2',2''-tris(salicylideneimino)trimethylamine) and $(NBu_4)^+[Er(Pc)_2]^-$ (H_2Pc = phthalocyanine). All calculations were carried out with the Molpro[80] suite of ab initio programs. For the all-electron SA-CASSCF calculations of the molecule $Er[N(SiMe_3)_2]_3$, the ANO-RCC[118] basis set reduced to triple-zeta ([8s][7p][4d][3f][2g][1h]) quality was used for the lanthanide. Scalar relativistic effects were accounted for by the second order Douglas-Kroll-Hess transformation, and the Breit-Pauli operator was used for the SO-coupling step. The LDF-CAHF calculations were always performed using the 28 electron pseudopotential/effective core potential (ECP) ECP28MWB[114] for the lanthanide due to the lack of an auxiliary density fitting basis set optimized for the ANO-RCC AO basis. The same ECP was used for the

pseudopotential SA-CASSCF calculations. In case of all pseudopotential calculations the def2-DZVPP/def2-TZVPP[119] basis sets were employed. In addition, for the LDF-CAHF calculations the corresponding def2-DZVPP/def2-TZVPP-JKFIT[119] auxiliary basis sets for the density fitting and an appropriate ECP-SO operator[114] were used for the SO-coupling step. For the remaining elements, cc-pVDZ/cc-pVTZ[120–122] basis sets were used and the corresponding cc-pVDZ/cc-pVTZ-JKFIT[76] auxiliary basis sets in case density fitting was employed. In case of $Er[N(SiMe_3)_2]_3$ and $[Er(Pc)_2]^-$, a minimal basis (MINAO[81]) was used for hydrogen, as no significant effect of these atoms on the crystal field splitting is expected for the molecules considered. The active space was always chosen to be CAS(11,7) for Er(III) (and the corresponding erbium containing complexes) and CAS(9,7) for Dy(III). In case of the molecular calculations, the weighting factors in the SA-CASSCF calculation were chosen the same for each spin-manifold. For the SA-CASSCF calculations of the free Er(III) ion, the quartets were given a weighting factor of 2 and the doublets a weighting factor of 1. In case of the SA-CASSCF calculations of the free Dy(III) ion, the sextets, quartets and doublets were given a weighting factor of, respectively, 3, 2, and 1. Moreover, the SA-CASSCF calculations of the free ions employed density fitting (DF-SA-CASSCF) to obtain more comparable results with LDF-CAHF. For none of the other SA-CASSCF calculations density fitting approximations were used. In case of the calculation of $(NBu_4)^+[Er(Pc)_2]^-$, only the $[Er(Pc)_2]^-$ anion was explicitly treated quantum-chemically, the effects of the counterion and the surrounding crystal were described by putting a +1-point charge at the crystallographic position[25] of the central N of the $(NBu_4)^+$ cation and a −1-point charge at the position of the central Er of all $[Er(Pc)_2]^-$ anions beside the one treated quantum-chemically for all ions within 1 crystallographic shell of unit cells in all directions of the crystal. The specific details for the different systems are displayed in Table 3.1.1. For $Er[N(SiMe_3)_2]_3$, different basis sets were employed. To distinguish these basis sets, they are listed in Table 3.1.2 and numbered from 1 to 4. While basis 1 and 2 correspond to all-electron calculations, basis 3 and 4 are the basis sets used for the pseudopotential calculations. The all-electron SA-CASSCF calculations were performed using basis 1 and 2, but calculations without freezing any orbitals were only possible (because of hardware limitations) for the calculations employing basis 1. Moreover, for basis 2, the SA-CASSCF calculation could be converged, but due to the hardware limitation, no subsequent SO-calculation was possible, therefore, no CF splitting pattern is available for this basis. If any orbitals were frozen in the SA-CASSCF calculations for

$Er[N(SiMe_3)_2]_3$, they were generated by merging (see section “Initial Guess”) the orbitals from a closed shell HF calculation of the ligand with the orbitals from a SA-CASSCF calculation of the free ion including 35 quartet states in the averaging. The number of frozen orbitals was chosen in a way that for C and N the 1s orbitals were frozen, the 1s, 2s and 2p-orbitals for Si and for Er all orbitals except of 4f and higher shells.

Table 3.1.1. Specific computational details for the different systems.

	Free ions	$Er[N(SiMe_3)_2]_3$	Er(trensal)	$[Er(Pc)_2]^-$
Processor	Quad-Core AMD Opteron™ Processor 2382	Quad-Core AMD Opteron™ Processor 2382	Quad-Core AMD Opteron™ Processor 2382	AMD Opteron™ Processor 6140
Number of CPU cores used	1	2	4	8
Basis set	def2-TZVPP	See Table 3.1.2	Er: def2-TZVPP N,O: cc-pVTZ C,H: cc-pVDZ	Er: def2-TZVPP N: cc-pVTZ C: cc-pVDZ H: MINAO
Auxiliary basis set	def2-TZVPP/ JKFIT	JKFIT basis sets corresponding to basis in Table 3.1.2	Er: def2-TZVPP/ JKFIT N,O: cc-pVTZ/JKFIT C,H: cc-pVDZ/JKFIT	Er: def2-TZVPP/ JKFIT N: cc-pVTZ/JKFIT C,H: cc-pVDZ/JKFIT
Pseudopotenial/all-electron calculation?	Pseudopotential	Pseudopotential + all-electron	Pseudopotential	Pseudopotential
Pseudopotential for Er/Dy	ECP28MWB	ECP28MWB	ECP28MWB	ECP28MWB
Structure	-	Crystallographic[a]	Crystallographic[b] (T=122K)	Crystallographic[c]
Quartets/doublets in SO-mixing for Er	35/112	35/20	35/112	35/112
Sextets/quartets/doublets in SO-mixing for Dy	21/224/490	-	-	-
Energy convergence threshold (Hartree)	10^{-9}	10^{-9}	10^{-7}	10^{-7}
Number of atoms	1	82	62	113
Number of electrons	Dy(III): 63 Er(III): 65	335	309	569

[a] From reference [39]

[b] From reference [123]

[c] From reference [25]

Table 3.1.2. Different basis sets used for the calculation of $Er[N(SiMe_3)_2]_3$. The ANO-RCC basis sets were contracted to [8s7p4d3f2g1h] (=TZ).

	Basis 1	Basis 2	Basis 3	Basis 4
Er	ANO-RCC (TZ)	ANO-RCC (TZ)	def2-TZVPP	def2-TZVPP
N	cc-pVTZ	cc-pVTZ	cc-pVDZ	cc-pVTZ
Si	cc-pVTZ	cc-pVTZ	cc-pVDZ	cc-pVTZ
C	cc-pVDZ	cc-pVTZ	cc-pVDZ	cc-pVTZ
H	MINAO	MINAO	MINAO	MINAO
ECP Er	-	-	ECP28MWB	ECP28MWB

3.1.4.2. Results

In this section, the performance of the developed method is discussed. In section 3.1.4.2.1, a comparison with all-electron and pseudopotential SA-CASSCF calculations will be given in order to demonstrate the equivalency of the two methods. Moreover, the influence of the local approximations on the crystal field splitting will be briefly presented. Section 3.1.4.2.2 presents applications and timings for a large molecule in order to demonstrate the computational speed for these systems and therefore the advantages of the method compared to conventional CASSCF.

3.1.4.2.1. CASSCF benchmarks

3.1.4.2.1.1. Free lanthanide ions

To investigate the equivalence of the LDF-CAHF orbitals with the orbitals obtained by SA-CASSCF, benchmark calculations for free Er(III) and Dy(III) ions were performed. The spin-orbit energies for different multiplets of the total angular momentum J obtained by diagonalizing the SO-matrix in the basis of SA-CASSCF/ CAHF-CASCI wave functions were numerically identical and are displayed in Table 3.1.3. This clearly shows the equivalence of both approaches for an averaging over all roots of all spin-manifolds and also all M_S-values.

Table 3.1.3. Spin-orbit energies of different J-multiplets for Er^{3+}/Dy^{3+} for LDF-CAHF and DF-SA-CASSCF. Energies are given in cm^{-1}.

J	LDF-CAHF Er	DF-SA-CASSCF Er	LDF-CAHF Dy	DF-SA-CASSCF Dy
15/2	0.00	0.00	0.00	0.00
13/2	6348.67	6348.67	3193.82	3193.82
11/2	10363.32	10363.32	5525.16	5525.16
9/2	13207.87	13207.87	7331.69	7331.69

3.1.4.2.1.2. $Er[N(SiMe_3)_2]_3$

$Er[N(SiMe_3)_2]_3$[38,39] (Figure 3.1.1) was chosen as a benchmark system for our method because its low lying energy level structure is well-known from experiment[38] and also because it is a relatively small molecule.

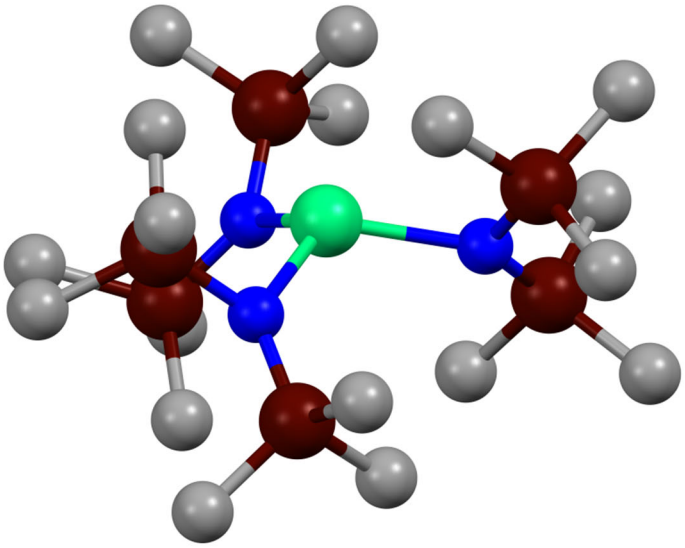

Figure 3.1.1. Crystal structure of $Er[N(SiMe_3)_2]_3$. Scheme: Er: green, N: blue, Si: black, C: gray. H atoms are omitted for clarity.

In order to save computation time, all quartets (35), but only 20 doublets were included in the state averaging/CASCI and SO-coupling step. In order to justify this procedure, the deviations from the calculation including all possible roots (i.e. 35 quartets and 112 doublets) were investigated with LDF-CAHF employing basis 3. The results are displayed in Table 3.1.4.

Table 3.1.4. Influence of the inclusion of low-spin states (quartets/doublets) on the crystal-field splitting for $Er[N(SiMe_3)_2]_3$. Energies are given in cm^{-1}. Basis set number refers to Table 3.1.1.

Method/Basis	Doublet	35/20	35/112
LDF-CAHF	1	0	0
Basis 3	2	107	109
	3	191	197
	4	262	272
	5	321	335
	6	424	439
	7	481	496
	8	518	533

The energies have a maximum deviation from each other of only about 15 cm^{-1} but almost a constant relative error of 3-4 % which is within the error range of typical CASSCF calculations of lanthanide complexes. This indicates that it is sufficient to use only 20 doublet states for the state-averaging/CASCI and SO-coupling step. Next, the effect of the local density fitting applied in LDF-CAHF on the crystal field splitting was investigated by comparing the calculations employing local density fitting (including local approximations) with the calculations using standard density fitting (no local approximations included). The results are displayed in Table 3.1.5.

Table 3.1.5. Local approximations (left) vs. no local approximations (right) for $Er[N(SiMe_3)_2]_3$. Energies are given in cm^{-1}. Basis set number refers to Table 3.1.2. No local approximations means the use of full LMO, AO and fitting domains[69].

Method/Basis	Doublet	Local approx.	No local approx.
LDF-CAHF	1	0.00	0.00
Basis 3	2	107.53	107.56
	3	191.11	191.20
	4	262.11	262.21
	5	320.74	320.83
	6	424.35	424.43
	7	480.97	481.06
	8	517.94	518.03

The crystal-field splittings determined with the use of local approximations differ at most by 0.1 cm^{-1} from the results obtained without using local approximations, which validates the LDF-CAHF method.

LDF-CAHF calculations, pseudopotential SA-CASSCF and all-electron SA-CASSCF calculations with different basis sets and different numbers of frozen orbitals were performed in order to

investigate their timings and their accuracy compared to the experiment and assess the influence of the basis set size, the use of a pseudopotential and the freezing of orbitals in calculations of crystal field splittings. In order to distinguish them, the different calculations performed are numbered from 1 to 4 in case of SA-CASSCF and from 1 to 2 in case of LDF-CAHF. The computational details and the CPU timings are displayed in Table 3.1.6.

Table 3.1.6. Different calculations of $Er[N(SiMe_3)_2]_3$ performed in this work and their CPU-timings[a].

Method	Pseudopotential?	Number of frozen orbitals	Number of non-frozen electrons	Basis (see Table 3.1.2)	Number of basis functions	CPU time CASSCF/ LDF-CAHF+CASCI
LDF-CAHF 1	Yes	0	307	3	561	9.3 h
SA-CASSCF 1	Yes	0	307	3	561	29.0 h
LDF-CAHF 2	Yes	0	307	4	993	14.6 h
SA-CASSCF 2	Yes	0	307	4	993	381.4 h
SA-CASSCF 3	No	74	187	1	699	35.2 h
SA-CASSCF 4	No	74	187	2	987	205.6 h
SA-CASSCF 5	No	0	335	1	699	134.5 h

[a] Note that all calculations were performed in a parallelized fashion on 2 CPU cores (see Table 3.1.1).

The most comparable calculations are LDF-CAHF 1 and 2 and SA-CASSCF 1 and 2 because they both use a pseudopotential, the same basis and no orbitals are frozen. One can clearly see that LDF-CAHF 1 is faster than SA-CASSCF 1 by a factor of more than 3. This factor is increased to more than 26 when the basis set size increases to basis 4, i.e. comparing LDF-CAHF 2 and SA-CASSCF 2. An increase of the basis in LDF-CAHF by ~80%, i.e. going from LDF-CAHF 1 to LDF-CAHF 2, leads to an increase of computation time of only ~60% while the computation time for SA-CASSCF is increased by over 1200% going from SA-CASSCF 1 to SA-CASSCF 2. This further underlines the high efficiency of the LDF-CAHF method. To further investigate the dependence of the computation time for SA-CASSCF on the basis set size, SA-CASSCF 3 and SA-CASSCF 4 are compared. Going from SA-CASSCF 3 to 4 means an increase of 40 % of the basis set size, whereas the computation time increases by 480 %, even though

the time demanding SA-CASSCF 2 and 3 calculations freeze 74 orbitals which are not relaxed during the microiterations, in order to save computation time. This can lead to errors and should be avoided. If these 74 orbitals are also relaxed, i.e. going from SA-CASSCF 3 to SA-CASSCF 5, increases the computation time by a factor of approximately 3.8. LDF-CAHF always relaxes all orbitals and is still very fast. The calculation LDF-CAHF 2 is the calculation with the largest number of basis functions of all calculations performed in this work and still faster than SA-CASSCF 1, which is the SA-CASSCF calculation with the lowest number of basis functions, by a factor of 2. Note that none of the calculations performed in this work include dynamical correlation. If such methods (like CASPT2 and MRCI) are used in a subsequent step, it is necessary to go to larger basis sets (at least VTZ), as the convergence of the correlation energy with respect to the basis set size is slower than for Hartree-Fock. This also favours the use of the LDF-CAHF method.

In order to compare the energies obtained by LDF-CAHF with those calculated with SA-CASSCF and to estimate their deviation from experiment, the crystal field splitting patterns of the ground multiplet are listed in Table 3.1.7 for both ab initio methods (all except of SA-CASSCF 4, because of hardware limitation in the SO-calculation) as well as the values obtained by luminescence and the corresponding values fitted to the splitting pattern using a CF-Hamiltonian for C_{3v} symmetry[38]. Moreover, the root mean square deviations (RMSD) of the calculated and fitted values to the experimental ones are presented.

Table 3.1.7. Crystal-field splitting pattern for SA-CASSCF (S.-C.) and LDF-CAHF (L.-C.), as well as the experimental values obtained by luminescence (Exp. CF energy) and the energy levels fitted to the experiment using a CF Hamiltonian for C_{3v} symmetry (CF fit energy) for $Er[N(SiMe_3)_2]_3$. Energies are given in cm^{-1}.

Doublet	L.-C. 1	S.-C. 1	L.-C. 2	S.-C. 2	S.-C. 3	S.-C. 5	CF fit energy	Exp. CF energy
1	0	0	0	0	0	0	0	0
2	108	112	108	112	131	111	111	110
3	191	199	192	200	207	195	173	190
4	262	273	263	274	244	267	228	245
5	321	333	321	333	261	330	280	327
6	424	440	425	441	475	440	450	455
7	481	498	481	497	478	503	495	-
8	518	536	517	535	483	543	528	-
RMSD Exp.	16	15	16	15	33	12	24	0

Both LDF-CAHF calculations are very close to the experiment and their RMSD to the experimental values is smaller than the RMSD of the crystal-field fit to the experiment.

Increasing the basis set size, i.e. going from LDF-CAHF 1 to LDF-CAHF 2 leads to no significant improvement. Nevertheless, as mentioned above, this might not be true for subsequent treatments of dynamical correlation to improve accuracy. In this case, the influence of the basis set size is usually much larger. The results and the RMSD to the experiment of LDF-CAHF 1 and 2 and SA-CASSCF 1 and 2, which are the most comparable calculations, are very similar (they are not identical because the SA-CASSCF calculations give all spin manifolds the same weighting factor). This shows that both approaches have similar accuracies, while LDF-CAHF is significantly faster. SA-CASSCF 3, the all-electron calculation with a larger basis set size, yields worse results compared to the experimental values, which might be attributed to the 74 frozen orbitals in combination with the unbalanced basis, i.e. giving the atoms closer to the lanthanide a larger basis than the more distant atoms. Although this calculation yields worse results, it is 2.4 times slower than LDF-CAHF 2, even though LDF-CAHF 2 employs a basis which is 1.4 times larger. In SA-CASSCF 5, the remaining 74 orbitals are relaxed, which lowers the RMSD compared to the experiment and makes it similar to the RMSD of SA-CASSCF 1 and 2 and LDF-CAHF 1 and 2, but significantly increases the computation time. It is generally not predictable what influence the freezing of a large number of ligand orbitals generated by merging (see section “Initial Guess”) has on the CF-splitting, especially if unbalanced basis sets are used, therefore orbital-freezing should be avoided. We will investigate a second example, namely Er(trensal), to assess if the excellent agreement between LDF-CAHF and experiment is coincidental.

3.1.4.2.1.3. Er(trensal)

We chose the molecule Er(trensal)[123] (Figure 3.1.2) as a second benchmark system to test the performance of our method because many experimental studies are available for this system[123–126].

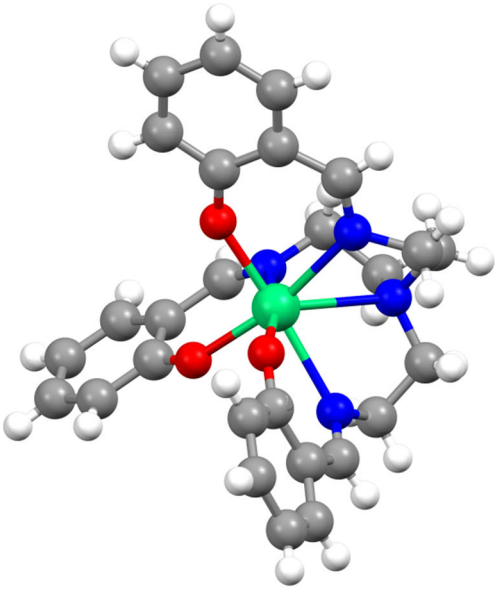

Figure 3.1.2. Crystal structure of Er(trensal). Scheme: Er: green, O: red, N: blue, C: gray, H: white.

We compared our LDF-CAHF calculations with all-electron SA-CASSCF calculations for the structure at T=122K (without point charge embedding) with a basis set quality comparable to ours from previous work of Pedersen et al.[123] (our basis employs polarization functions for all atoms while in the work of Pedersen et al. some elements are described with a basis without polarization functions). The literature SA-CASSCF calculation was carried out using the quantum chemistry software package Molcas[127]. Furthermore, we compared our results with experimental data obtained by absorption spectroscopy by Flanagan et al.[124]. The results and timings for our method are shown in Table 3.1.8.

Table 3.1.8. Comparison of the CF splitting pattern obtained by LDF-CAHF with those obtained by SA-CASSCF and experiment for Er(trensal). Energies are given in cm^{-1}.

Doublet	LDF-CAHF	SA-CASSCF[a]	Observed[b]
1	0	0	0
2	67	67	54
3	94	100	102
4	101	104	110
5	178	199	299
6	383	428	568
7	417	465	610
8	441	491	642
RMSD to observed energies	135	103	0
Number of basis functions LDF-CAHF	828		
Number of electrons in LDF-CAHF	281		
CPU time LDF-CAHF+CASCI	2.2 h		

[a] From reference [123]

[b] From reference [124]

The agreement of our LDF-CAHF method with the SA-CASSCF calculations of Pedersen et al. is good and the deviations can be explained by the fact that their calculations were all-electron calculations while ours were pseudopotential calculations. Besides that, they used a different spin-orbit operator, a basis set of slightly different quality and their orbitals are obtained from an SA-CASSCF calculation giving all spin-manifolds the same weighting factor. The deviation of both ab initio calculations from the experiment is remarkably small for the lowest four Kramers doublets and becomes larger for the higher lying states which might be attributed to the missing inclusion of dynamical correlation. Altogether, the agreement with the experiment is good, but not as good as for $Er[N(SiMe_3)_2]_3$. Hence, the accuracy of LDF-CAHF is similar (for this molecule, the results for the lowest four Kramers doublets are very similar for both methods and SA-CASSCF is 20-30 % closer to the experiment for the Kramers doublets 5-8) to the accuracy of SA-CASSCF and the method is therefore a good alternative to the conventional SA-CASSCF approach.

3.1.4.2.2. Application to a large molecule: $(NBu_4)^+[Er(Pc)_2]^-$

In order to demonstrate the applicability of the LDF-CAHF method to large systems using large basis sets, we performed calculations of the $[Er(Pc)_2]^-$-molecule[25] (Figure 3.1.3), because it is quite large and there are already SA-CASSCF calculations and experimental studies have been reported by Marx et al.[25].

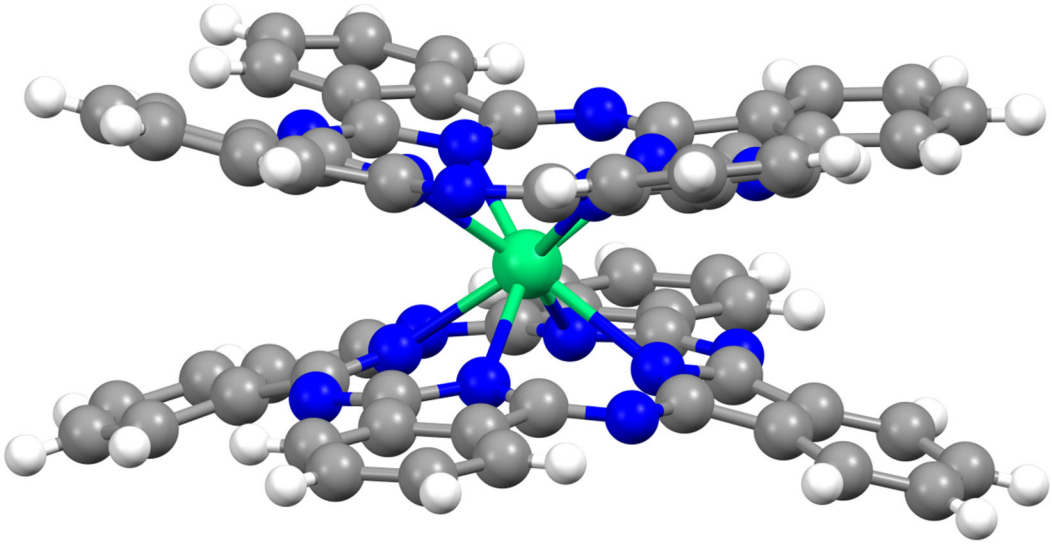

Figure 3.1.3. Crystal structure of $[Er(Pc)_2]^-$. Scheme: Er: green, N: blue, C: gray, H: white.

The number of basis functions and number of electrons is almost twice that of the previous example. In the previous work by Marx et al., the SA-CASSCF calculations were carried out using Molcas[127]. They determined the excitation energy from the ground doublet to the first excited doublet to be at 74 cm^{-1} by far-infrared spectroscopy in this work. Table 3.1.9 shows the LDF-CAHF results and timings, the SA-CASSCF results and the experimentally determined energy of the first excited doublet.

Table 3.1.9. Comparison of the CF splitting pattern obtained by LDF-CAHF with those obtained by SA-CASSCF and the energy of the first excited doublet from experiment for $[Er(Pc)_2]^-$. Energies are given in cm^{-1}.

Doublet	LDF-CAHF	SA-CASSCF[a]	Observed[a]
1	0	0	0
2	53	59	74
3	137	151	-
4	180	199	-
5	211	229	-
6	226	249	-
7	232	258	-
8	257	286	-
Number of basis functions in LDF-CAHF	1513		
Number of electrons in LDF-CAHF	569		
CPU time for LDF-CAHF+CASCI	14 h		

[a] From reference [25]

Again, the energies obtained by LDF-CAHF and SA-CASSCF coincide well and their deviation from the experiment is quite similar. The reasons that they do not fully coincide can be

found in the facts, that the SA-CASSCF calculations were all-electron calculations (while the LDF-CAHF calculations use a pseudopotential for erbium), they employed a different basis set than we did and the point charge embedding of the SA-CASSCF calculations was more sophisticated, because they used the Mulliken charges of all atoms as point charge model and embedded the molecule in five crystallographic shells of unit cells. Moreover, also in this case, the LDF-CAHF orbitals are obtained in a way that corresponds to an SA-CASSCF calculation giving the spin-quartets a weighting factor of 2 and the spin-doublets a weighting factor of 1, while the SA-CASSCF calculations in Table 3.1.7 employ the same weighting factor for all spin-manifolds. The timings show the very high speed of the LDF-CAHF method, as it is possible to calculate a large molecule like $[Er(Pc)_2]^-$ using a large basis set in about half a day without the use of a high performance compute cluster. The accuracy is similar to CASSCF, but it is much more convenient, especially for very large systems and/or basis sets, to use LDF-CAHF, because of the low-order scaling. The remaining deviation from the experiment can be attributed to the missing consideration of dynamical correlation, but once the averaged orbitals are obtained by LDF-CAHF, subsequent correlation methods like CASPT2 or MRCI can be employed to improve the results.

3.1.5. Further applications of LDF-CAHF

In the following, further applications of the presented LDF-CAHF method to various systems, also including actinide and transition metal systems, will be presented. Note that these results have already been published[40–43].

3.1.5.1. Application to tetraoxolene bridged lanthanide single molecule magnets

Parts of this section have already been published in *Chem. Sci.* **9** (5), 1221–1230 (2018)[40] and have been used for the text/formulation of this thesis. The ab initio investigations in this publication were performed by me.

The development of exchange coupled polynuclear lanthanide clusters with radical bridges is seen as one of the most efficient routes to a high-performance SMM since the discovery that quantum tunnelling of the magnetic moment is strongly suppressed in N_2^{3-}-radical-bridged lanthanide SMMs compared to single ion systems[110,128,129]. In the publication mentioned

above[40], a family of tetraoxolene bridged lanthanide dimers, $[(HBpz_3)_2Ln(\mu\text{-}CA)Ln(HBpz_3)_2]\cdot 2CH_2Cl_2$ (**1Ln**, Ln=Dy, Tb, Gd, Y, $HBpz_3^-$ =hydrotris(pyrazol-1-yl)borate, CA^{2-} =chloranilate) was synthesized. Chemical reduction by cobaltocene enabled the isolation of radical bridged species, $[(HBpz_3)_2Ln(\mu\text{-}CA^{\cdot})Ln(HBpz_3)_2]^{-}\cdot[CoCp_2]^{+}$ (**2Ln**, Ln=Dy, Tb, Gd, Y). Magnetic measurements revealed strong magnetic couplings between the radical and the lanthanide ions, promoting the appearance of SMM behaviour in zero applied field. Furthermore the magnetic coupling was studied by means of high-frequency electron paramagnetic resonance (HFEPR) spectroscopy, which gave more accurate information on the magnetism than magnetic measurements.

In that work, the LDF-CAHF methodology was applied to the species **1Dy** and **1Tb** (Figure 3.1.4), the species with a non-radical ligand (i.e. the species before reduction), to obtain information about the local ground and excited states of the systems. Therefore, the calculations were performed using the method of diamagnetic substitution, i.e. one lanthanide was replaced by diamagnetic Y^{3+}.

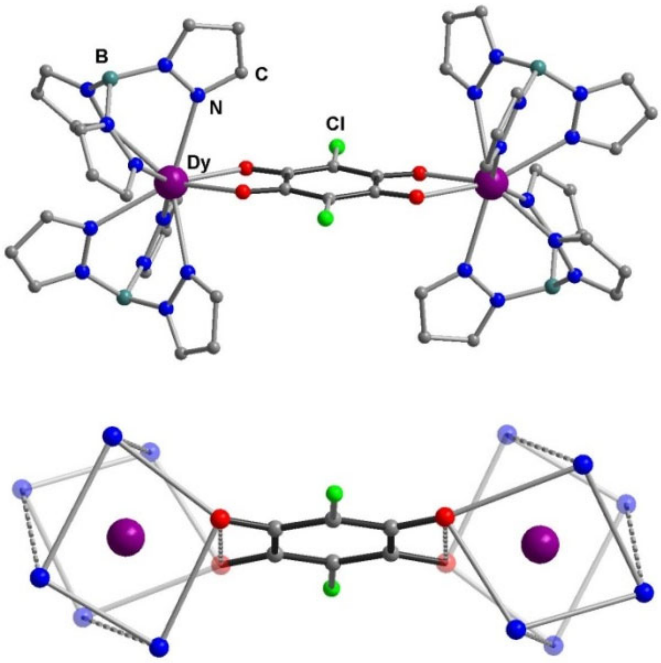

Figure 3.1.4. Top: Crystal structure of compounds with lattice solvent molecules and hydrogen atoms omitted for clarity with Ln=Dy as example. Color code: Dy purple, O red, N blue, C grey, Cl blue. Bottom: Depiction of molecular structure, omitting the noncoordinating atoms of the ancillary ligands, highlighting the coordination polyhedral around the lanthanide ions. Figure reproduced from *Chem. Sci.* **9** (5), 1221–1230 (2018)[40] (Figure 1) with permission from The Royal Society of Chemistry.

3.1.5.1.1. Computational details

Multi-configurational ab initio calculations were performed for **1Tb** and **1Dy**, replacing one of the two Tb^{3+}/ Dy^{3+} by diamagnetic Y^{3+}. The calculations were carried out with the Molpro[79,80] suite of ab initio programs using the measured crystal structure. The (state-averaged) orbitals were obtained by employing the LDF-CAHF method[37,69]. The active space included 8 electrons of Tb^{III}/9 electrons of Dy^{III} in seven 4f-type orbitals. The 28 electron pseudopotential/effective core potential (ECP) ECP28MWB[114,130] was used for Tb/Dy and Y. The basis set employed for Tb/Dy and Y was def2-TZVPP[119] and the auxiliary basis set for density fitting def2-TZVPP-JKFIT[119]. The elements O and N were described by the cc-pVTZ[120–122] basis set and the corresponding auxiliary basis set for these elements was cc-pVTZ-JKFIT[76]. For the remaining elements except H, the cc-pVDZ[120–122] basis set and the corresponding cc-pVDZ-JKFIT[76] basis set for density fitting were used. The hydrogen atoms were described by a minimal basis (MINAO)[81] and the auxiliary basis set cc-pVDZ-JKFIT[76] was employed for density fitting. In the spin-orbit coupling step the ECP-SO operator corresponding to ECP28MWB was employed[114]. The orbitals resulting from the LDF-CAHF calculation are equivalent to the orbitals of a state-averaged CASSCF calculation averaging over all possible roots, i.e. 7 septets, 140 quintets, 588 triplets and 490 singlets for **1Tb** and 21 sextets, 224 quartets and 490 doublets for **1Dy**, taking into account the M_S-degeneracy of the corresponding spin-manifold by a weighting factor, i.e. a weighting factor of 7 for the septets, 5 for the quintets, 3 for the triplets and 1 for the singlets (**1Tb**) and moreover 3 for the sextets, 2 for the quartets and 1 for the doublets (**1Dy**). The state-averaged orbitals were used in a subsequent CASCI step to obtain the multi-configurational spin-free wave functions. In the following SO-coupling step, a limited number of roots was mixed, i. e., all septets (7), all quintets (140), 294 triplets and 292 singlets for **1Tb** and 21 sextets, 128 quartets and 130 doublets for **1Dy**, respectively. On the basis of the resulting spin-orbit multiplets, the g_Z-value of the lowest pseudo-doublet and its direction for **1Tb** and the g-tensor for the ground Kramers doublet of **1Dy**, as well as the composition of the wave functions in terms of m_j-microstates for both compounds were calculated using the SINGLE_ANISO[18] program. The ab initio results were projected on the $^6H_{15/2}$ (**1Dy**) and $^7F_6$ (**1Tb**) ground multiplet, respectively. The quantization axis was chosen as the main magnetic axis Z of the ground Kramers doublet/lowest pseudo-doublet.

3.1.5.1.2. Results and discussion

Table 3.1.10 shows the crystal field (CF) energies for **1Dy**/**1Tb** as well as the g_Z-value for the ground Kramers doublet/lowest pseudo-doublet and Figure 3.1.5 shows the orientation of the main magnetic axes corresponding to g_Z.

Table 3.1.10. Kramers doublets/crystal-field states of **1Dy** and **1Tb** and the main values of their g-tensors. Energies are given in cm^{-1}.

Kramers doublet	**1Dy**	CF state	**1Tb**
1	0.00	1	0.00
2	84.50	2	2.52
3	122.86	3	52.96
4	142.04	4	70.95
5	172.31	5	107.49
6	221.75	6	158.53
7	259.23	7	183.42
8	498.05	8	256.73
		9	261.98
		10	373.72
		11	374.73
		12	412.97
		13	413.97
$\boldsymbol{g_X}$	0.029	g_X	0
$\boldsymbol{g_Y}$	0.036	g_Y	0
$\boldsymbol{g_Z}$	19.76	g_Z	17.26

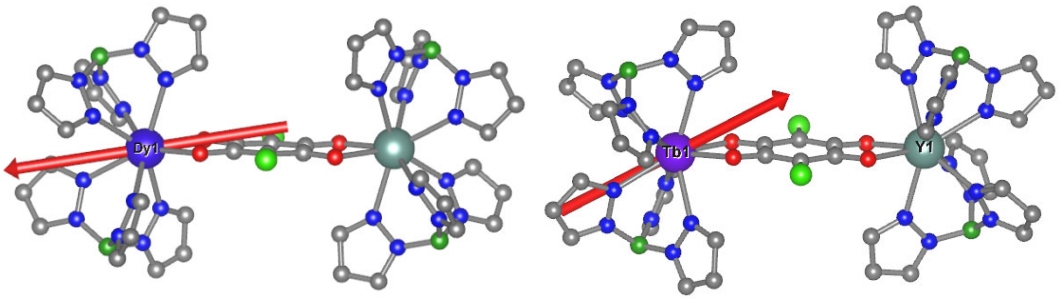

Figure 3.1.5. The calculated orientation of the local g_Z axes of ground (Kramers/pseudo) doublets on Dy^{III} and Tb^{III} ions for **1Dy** and **1Tb**. Figure reproduced from *Chem. Sci.* **9** (5), 1221–1230 (2018)[40] (Figure S19) with permission from The Royal Society of Chemistry.

Table 3.1.11 and 3.1.12 show the wave functions composition in terms of m_j-states for the two lowest CF states for **1Tb** and **1Dy**, respectively.

Table 3.1.11. Projection of the total moment on the quantization axis for the ground Kramers doublet of **1Dy**.

CF state	Energy [cm^{-1}]	Projection of the total moment on quantization axis
1	0.00	80.8%|-15/2>+0%|-13/2>+0.6%|-11/2>+0.7%|-9/2>+0.3%|-7/2>+0.1%|-5/2>+0%|-3/2> +0.1%|-1/2>+17%|15/2 >+0%|13/2>+0.1%|11/2>+0.1%|9/2>+0.1%|7/2>+0%|5/2> +0%|3/2 >+0%|1/2>
2	0.00	17%|-15/2 >+0%|-13/2>+0.1%|-11/2>+0.1%|-9/2>+0.1%|-7/2>+0%|-5/2>+0%|-3/2> +0%|1/2>+80.8%|15/2>+0%|13/2>+0.6%|11/2>+0.7%|9/2>+0.3%|7/2>+0.1%|5/2> +0%|3/2>+0.1%|1/2>

Table 3.1.12. Projection of the total moment on the quantization axis for the lowest pseudo-doublet of **1Tb**.

CF state	Energy [cm^{-1}]	Projection of the total moment on quantization axis
1	0.00	45.3%|-6 >+2.7%|-4>+0.2%|-3>+1.3%|-2>+0.1%|-1>+0.8%|0> +45.3%|6 >+2.7%|4>+0.2%|3>+1.3%|2>+0.1%|1>
2	2.52	47.9%|-6 >+1.7%|-4>+0.1%|-3>+0.3%|-2> +47.9%|6 >+1.7%|4>+0.1%|3>+0.3%|2>

The g_Z values of ground doublet states are indicative of easy-axis anisotropy for Dy (19.76) and Tb (17.26), approaching values expected for a m_j= ±15/2 and ±6 ground state, respectively. The local easy axes point toward the CA^{2-} ligand (Figure 3.1.5), which exhibits shorter bond distances i.e. stronger crystal field interactions to lanthanide centers than $HBpz_3^-$ ligands. The angle between the g_Z orientation and the vector connecting two lanthanide centers is smaller in **1Dy** (9°) than in **1Tb** (31°). More importantly, non-negligible transverse components of the g-tensor (g_X= 0.029 , g_Y= 0.036) are found in the ground Kramers doublet of 1Dy, which leads to the strong quantum tunneling of magnetization as a result of mixed microstates (Table 3.1.11). As a non-Kramers ion, the ground pseudo-doublet of **1Tb** can be split in a low-symmetry crystal field and we find a large intrinsic tunneling gap of 2.5 cm^{-1} (Table 3.1.10), which is in good agreement with the experimental value (1.5 cm^{-1}) obtained from high-field electron paramagnetic resonance (HF-EPR) measurements[40]. This is consistent with the absence of SMM behavior in zero field for **1Tb**. Furthermore, the total splitting for the ground multiplets of the Dy^{III} and Tb^{III} ions is below 500 cm^{-1}, indicating a weak crystal field environment. For **1Dy**, the first excited doublet is on 84 cm^{-1} (120 K), which is much higher than the effective energy barrier for relaxation U_{eff} obtained from ac susceptibility measurements[40], suggesting the inefficiency of the Orbach process here.

The LDF-CAHF+CASCI/SI-SO method is able to provide reliable insights into the electronic structure of the investigated systems and is in good agreement with the experimental studies. However, it cannot be applied to the full complexes (without diamagnetic

substitution), with and without radical bridges, due to the *high-energy states* mentioned in section 3.1.2 which would be included in the averaging and yield inappropriate orbitals for the low-lying states of the molecules. A remedy for this problem is presented later in the thesis (Chapter 3.3).

3.1.5.2. Application to [U^{III}{$SiMe_2NPh$}$_3$-tacn)($OPPh_3$)]

Part of this section have already been published in *Chem. Eur. J.* **25**, 1758-1766 (2019)[41] and have been used for the text/formulation of this thesis. The ab initio investigations in this publication were performed by me.

Actinides are an interesting alternative to lanthanides for designing single molecule magnets, because they possess stronger spin-orbit coupling and ligand field interactions and therefore potentially larger magnetic anisotropies. Moreover, actinide containing SMMs can have much stronger exchange interactions with neighbouring spin centres (e.g. transition metals)[131–134], which can efficiently suppress under barrier tunnelling processes. This is due to the increased covalency of metal-ligand interactions which arises because of the larger radial extensions of the 5f-orbitals compared to the 4f-orbitals[4,135]. However, due to the abovementioned reasons, ab initio calculations of actinide containing systems are very challenging. They need to accurately account for the stronger relativistic effects, often larger active spaces are required for the multireference calculations due to the increased covalency of metal-ligand interactions and the contributions of dynamical correlation are usually larger than for lanthanides.

The LDF-CAHF methodology was applied to the uranium single-ion magnet [U^{III}{$SiMe_2NPh$}$_3$-tacn)($OPPh_3$)] (Figure 3.1.6, tacn=1,4,7,-triazacyclononane) to learn more about its electronic structure and assess the applicability of the method to actinide containing systems. The results were compared with the experimental findings[41] .

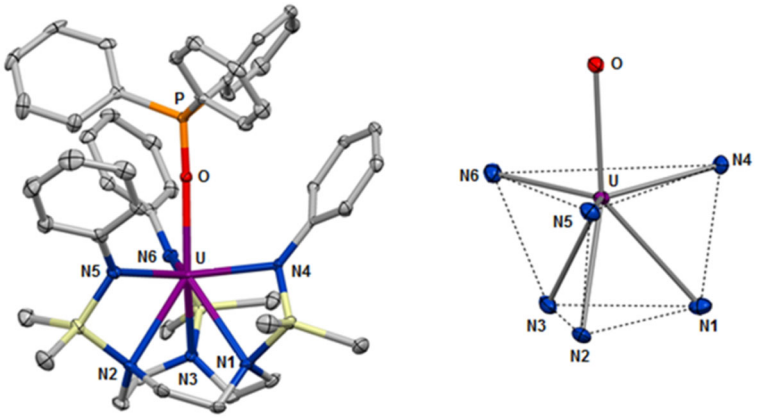

Figure 3.1.6. Molecular structure and coordination geometry of compound $[U^{III}(\{SiMe_2NPh\}_3\text{-tacn})(OPPh_3)]\cdot 2C_7H_8$ (ellipsoids displayed at a probability level of 50%). Hydrogen atoms and solvent molecules are not shown for clarity. Figure reproduced from *Chem. Eur. J.* **25**, 1758-1766 (2019)[41] (Figure 1) with permission from *John Wiley and Sons*.

3.1.5.2.1. Computational details

Multi-configurational LDF-CAHF+CASCI/SI-SO[37,69] (local-density-fitted configuration-averaged Hartree-Fock + complete active space configuration interaction followed by state-interaction through spin-orbit coupling) ab initio calculations were performed for the compound $U^{III}[\{SiMe_2NPh\}_3\text{-tacn})(OPPh_3)]$. The calculations were carried out with the Molpro[79,80] suite of ab initio programs using the measured crystal structure and the also the structure symmetrized to C_3 symmetry[41]. The active space included 3 electrons of U^{III} in seven 5f-type orbitals (CAS(3,7)). The 60 electron pseudopotential/effective core potential (ECP) ECP60MDF[136] was used for U for the scalar-relativistic part of the calculation and the corresponding ECP60MDF-spin-orbit (SO) operator for the SO-coupling step. The basis set employed for U was the basis which is optimized for the corresponding ECP and the auxiliary basis set for density fitting was manually constructed as an even-tempered basis set whose details are given in Table 3.1.13. For density-fitted state-averaged (SA) complete active space self-consistent field (CASSCF) calculations, this auxiliary basis set reproduces the SO-energies of non-density-fitted SA-CASSCF calculations to an agreement of better than 0.01 cm^{-1}. The elements N, O, P and Si in the close vicinity of uranium were described by a cc-pVTZ[120–122] basis set and the corresponding auxiliary basis set for these elements was cc-pVTZ-JKFIT[76]. For the remaining elements, the cc-pVDZ[120–122] basis set, and the corresponding cc-pVDZ-JKFIT[76] basis set for density fitting was used. The state-averaged orbitals resulting from the LDF-CAHF calculation were used in a subsequent CASCI step to obtain the multi-configurational spin-free wave functions. In the following SO-coupling step, all possible

roots, i.e. 35 quartets and 112 doublets, were mixed. Furthermore, SA-CASSCF calculations with a larger active space were performed, where the LDF-CAHF orbitals were used as initial guess and all closed-shell orbitals were kept frozen on LDF-CAHF level of theory and the state averaging (and the SO-coupling step) still included 35 quartet and 112 doublet states. The active space in these calculations was extended by another set of (more diffuse) metal based f-orbitals (to account for the *double shell effect*, i.e. adding more spatial flexibility to the active electrons in the CASSCF calculation) and d-orbitals (CAS(3,19)). On the basis of the resulting spin-orbit multiplets, the g-tensor of the lowest Kramers doublet, as well as the composition of the wave functions in terms of m_j-microstates of the ground J=9/2 multiplet, were calculated using the SINGLE_ANISO[18] program.

Table 3.1.13. Details of the construction of the even-tempered auxiliary basis set for uranium.

Type	Number of primitives	Ratio of successive exponents	Geometric mean of exponents
s	41	1.5	33.253
p	33	1.5	6.568
d	27	1.5	5.839
f	22	1.5	2.825
g	17	1.5	7.689
h	17	1.5	6.407
i	17	1.5	6.407

3.1.5.2.2. Results and discussion

For aiding the crystal-field fit of the experimental excitation energies (see below), the investigated compound was symmetrized to C_3, and analogous calculations starting from this idealized structure were performed. Moreover, the active space was extended to CAS(3,19) (see section 3.1.5.2.1) to assess the influence of its size on the results, which will be discussed later. Table 3.1.14 shows the calculated of the five lowest Kramers doublets for both the real (for CAS(3,7) and CAS(3,19)) and C_3-symmetrized geometry (for CAS(3,7)) and their comparison with the collective crystal field fit (using the semi-empirical CONDON[137] program) to data from HF-EPR spectroscopy, magnetic circular dichroism (MCD) spectroscopy, as well as magnetic susceptibility and magnetization data[41]. In this fitting procedure, a crystal field Hamiltonian with idealized C_3-symmetry was used and the crystal field parameters obtained from ab initio calculations of the C_3-symmetrized geometry were

used as initial guess[41]. Furthermore, Figure 3.1.7 shows the energy levels up to 12000 cm^{-1} for the real structure and the active space CAS(3,7).

Table 3.1.14. Lowest energy levels for U^{III}[{$SiMe_2NPh$}$_3$-tacn)($OPPh_3$)] calculated by LDF-CAHF+CASCI/SI-SO (small active space) and LDF-CAHF/SA-CASSCF/SI-SO (large active space) calculations using the atomic coordinates from the experimental crystal structure or those from the C_3-symmetrized structure, as well as the energy level scheme derived from the phenomenological fit (CONDON)[41]. Energies are given in cm^{-1}.

Kramers doublet	ab initio crystal struct. CAS(3,7)	ab initio C_3-symmetrized CAS(3,7)	ab initio crystal struct. CAS(3,19)	Phenom. Fit (CONDON)
1	0	0	0	0
2	146.87	184.17	65.4	142
3	223.71	239.14	87.38	337
4	750.71	783.56	702.89	1185
5	865.13	871.65	844.03	1246

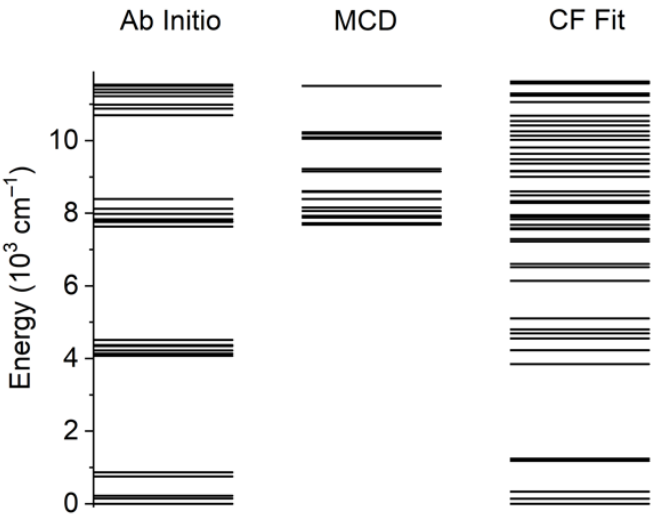

Figure 3.1.7. Experimental and calculated (CAS(3,7)) energy-level diagrams for U^{III}[{$SiMe_2NPh$}$_3$-tacn)($OPPh_3$)] (real structure) up to 12000 cm^{-1} (CF=crystal field). Figure reproduced from *Chem. Eur. J.* **25**, 1758-1766 (2019)[41] (Figure S5) with permission from *John Wiley and Sons*.

Figure 3.1.7 clearly reveals groups of states that can be assigned to the Russell-Saunders multiplets ^4I_J (J = 9/2 to 15/2 in order of increasing energy). Note that in view of the large spin-orbit coupling and substantial covalency, J is not necessarily a good quantum number. The results for the real structure and C_3-symmetry are qualitatively very similar. Projection of the two lowest states calculated for the real structure (CAS(3,7)) onto a pseudo-spin 1/2 yields the following principal g-tensor components for this Kramers doublet: g_1 = 3.546, g_2 = 2.638 and g_3 = 0.802. These values are in reasonable agreement with the values

obtained from HF-EPR spectroscopy (and g_1 matches exactly). Table 3.1.15 shows the g-values obtained by different methods (ab initio and experimental).

Table 3.1.15. Ab initio calculated g-tensor values for regular and expanded active spaces for the real structure and comparison with the ones calculated by CONDON and the experimental values[41].

	g_1	g_2	g_3
ab initio CAS(3,7)	3.546	2.638	0.802
ab initio CAS(3,19)	4.017	2.225	0.795
Crystal field analysis*	2.725	2.725	1.679
HF-EPR	3.54(5)	2.042(4)	1.66(5)

*Due to the assumed C_3 ideal symmetry, g_1 = g_2 in the crystal field analysis.

The g-values suggest a considerably mixed ground doublet of the lowest multiplet. Indeed, projection of the lowest 10 ab initio states onto a 9/2 pseudospin by means of the SINGLE_ANISO program allows expressing the composition of the Kramers doublets in terms of m_j functions, which is shown in Table 3.1.16 for the real structure and the active space CAS(3,7). The quantization axis is chosen as the main magnetic axis corresponding to g_3 (of the ground Kramers doublet).

Table 3.1.16. Composition of the lowest two Kramers doublets as calculated by LDF-CAHF+CASCI/SI-SO for the real structure and the active space chosen as CAS(3,7). The main magnetic axis corresponding to g_3 (of the ground Kramers doublet) is chosen as quantization axis. KD=Kramers doubet.

m_j level	KD1	KD2
|±9/2>	0.40%	43.70%
|±7/2>	9.30%	1.50%
|±5/2>	9.10%	0.50%
|±3/2>	1.00%	52.40%
|±1/2>	80.30%	1.90%

The ab initio results suggest that the ground Kramers doublet is largely composed by the |±1/2> m_j wave function, with smaller contributions of |±7/2> and | ±5/2>. The first excited Kramers doublet is calculated to lie at 147 cm^{-1} above the ground doublet, and essentially consisting of a 50/50 mixture of |±9/2> and |±3/2>. According to the phenomenological CONDON fit[41], the ground state is determined mainly by |±7/2> (62%) and | ±5/2> (35%), with a very small contribution of |±1/2> (3%). This description is compatible with the observed SMM behaviour. Compared with the ab initio results in Table 3.1.16 for the ground state (KD1), they coincide in the m_j components that are involved, but the composition is markedly different. This is not surprising as in the fit the g_3 value determined by EPR (1.66(5)) was included, which is almost twice the value of the one predicted by ab initio calculations (0.802), evidencing the presence of larger contributions of higher m_j

microstates in the ground state. This sum of different contributions to the ground state wave function may be attributed to the competition between both the equatorial amino and amido groups with the apical oxygen atom of the $OPPh_3$ group. According to the phenomenological description, the inclusion of the apical group may be the key for stabilizing a ground state composed mainly by higher m_j microstates, but not necessarily sufficient to achieve *easy axis* instead of *easy plane*. The effect of this apical group seems to be underestimated by the ab initio calculations, yielding a dominant effect of the equatorial amino and amido groups.

The phenomenological description results in an overall ligand-field splitting of the ground multiplet J = 9/2 of about 1246 cm^{-1}. Consequently, this is about a 40% larger than the total ligand-field splitting determined by ab initio calculations (865 and 872 cm^{-1} for the real and C_3-symmetrized structures, respectively, and CAS(3,7)). In contrast, the first excited Kramers doublet is located at about 142 cm^{-1}, very close to the one predicted using the real structure (147 cm^{-1}) and compatible with the experimental data[41]. On the other hand, the first excited multiplet (J = 11/2) is calculated to be placed at 3847 cm^{-1}, which is in good agreement with the ab initio value of 4075 cm^{-1} for the real structure. However, this picture clearly differs for the upper part of the energy level diagram: from the CF fit, a large number of energy levels are obtained (Figure 3.1.7) that are not all observed in the MCD experiment. More details can be found in the corresponding publication[41]. Interestingly, the CF fit also suggests a continuous series of energy levels, in agreement with MCD, but in contrast to the ab initio calculations.

In order to assess the influence of the size of the active space on the results, it was expanded to include 3 electrons in 19 orbitals, where the latter were selected to include a further set of f-orbitals (double shell effect) and d-orbitals. The corresponding LDF-CAHF/SA-CASSCF/SI-SO calculations (see section 3.1.5.2.1) resulted in a slight decrease in the gap between the third and fourth multiplets (below and above 10000 cm^{-1}), which is shown in Figure 3.1.8.

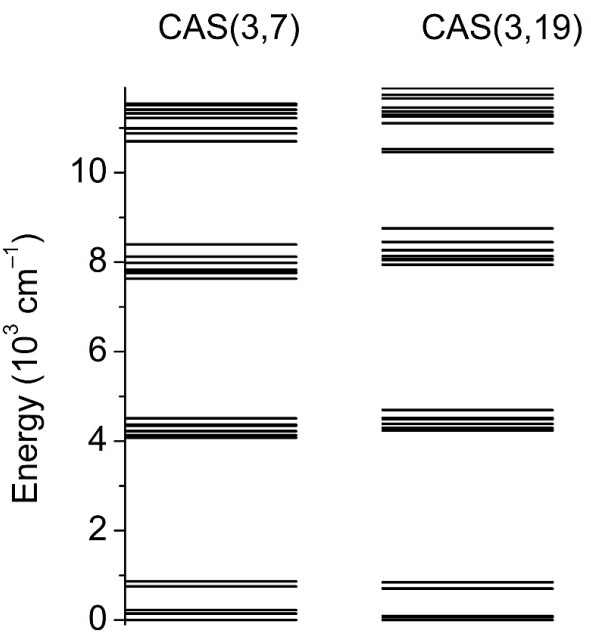

Figure 3.1.8. Influence of the size of the active space on the calculated energy levels. Figure reproduced from *Chem. Eur. J.* **25**, 1758-1766 (2019)[41] (Figure S6) with permission from *John Wiley and Sons*.

It also gave slightly different *g*-values for the ground Kramers doublet (Table 3.1.15). Interestingly, the first two excited KDs of the ground multiplets are calculated at much lower energies than in the original calculation (Table 3.1.14), but the total crystal field splitting of the ground multiplet remains essentially constant. These results indicate that the ab initio calculations are not yet at their optimum, and that further effects should be taken into account. These include even larger active spaces and dynamical correlation at CASPT2 or MRCI level. These effects also need to be included to treat the apical ligand field generated by the $OPPh_3$ group properly. However, such calculations rapidly exceed current capabilities, especially for such large active spaces.

3.1.5.3. Application to the chromium complex $[Cr(ddpd)_2](BF_4)_3$ (ddpd=*N,N'*-dimethyl-*N,N'*-dipyridine-2,6-diamine)

Part of this have already been published in *Phys. Chem. Chem. Phys.* **21** (13), 6976-6983 (2019)[42] and have been used for the text/formulation of this thesis. The ab initio investigations in this publication were performed by me.

Quantum computing is expected to enable calculations/simulations which are currently not feasible even on modern supercomputers and could therefore generate numerous possibilities for research and development in various areas. The basic building blocks of a

quantum computer are *quantum bits*, which are systems that can be put into coherent superposition states of their discrete levels. Molecular nanomagnets can potentially be used as *molecular quantum bits (MQBs)*, which are especially attractive, because they can be tailored by chemical synthesis and placed with atomic precision[138,139]. The majority of MQBs consists of transition metal complexes. For example, mononuclear chromium(III) complexes have been shown to be promising MQBs. Their advantage is the presence of four levels that can be used to generate coherent superposition states[140].In order to be able to understand and rationally improve these transition metal based MQBs, ab initio calculations can be employed. However, there are certain differences to lanthanide based systems. The spatial extension of the d-orbitals of transition metal ions is larger than for the 4f-orbitals of lanthanides, which increases the covalency of the interactions with the ligands. This often renders a simple active space consisting of the five d-orbitals of a transition metal ion insufficient for a quantitatively correct description. The larger spatial extension and increased covalency often requires the inclusion of a further set of more diffuse metal centred d-orbitals into the active space, which gives a larger spatial flexibility to the active (d-)electrons and is called *double shell effect*. The natural orbital occupation numbers (which are a measure for the contribution to the wave function) of the d-orbitals corresponding to the diffuse set are typically small compared to the natural orbital occupation numbers of the original set of (less diffuse) d-orbitals. However, this double shell effect cannot be properly accounted for in (LDF-)CAHF calculations, because increasing the active space by this more diffuse set of d-orbitals in a (LDF-)CAHF calculation would lead to the inclusion of *high-energy states* (see section 3.1.2), i.e. states, where the diffuse d-orbitals have large contributions to the wave function, into the state-averaging. This would yield state-averaged orbitals which are inappropriate for the description of the energetically low-lying molecular states of interest. Nevertheless, it is possible to construct a very accurate initial guess with the LDF-CAHF methodology for the subsequent SA-CASSCF calculation which in turn can account for the double shell effect. Moreover, the closed-shell orbitals are often robust against changes of the active orbitals caused by the double shell effect, i.e. the closed-shell orbitals can be kept frozen at the LDF-CAHF level of theory in the subsequent SA-CASSCF calculation. This strategy significantly improves the speed of convergence and hence strongly decreases the computation time for SA-CASSCF. In this section, we investigate the accuracy of the ab initio results obtained by this strategy of combining LDF-CAHF with SA-CASSCF (and

other subsequent correlation methods) by comparing them with experimental findings, in order to assess the applicability of the LDF-CAHF method for transition metal based systems.

In our abovementioned publication[42], the complex $[Cr(ddpd)_2](BF_4)_3$ (Figure 3.1.9, ddpd=*N,N'*-dimethyl-*N,N'*-dipyridine-2,6-diamine)[141–146] was investigated in a combined experimental and theoretical approach to assess its applicability as optically addressable MQB. The LDF-CAHF methodology was applied to the compound (in combination with SA-CASSCF and PNO-CASPT2) to complement the experimental studies and to investigate the applicability of the methodology for transition metal based systems. Figure 3.1.9 shows the molecular structure of the complex and its energy level diagram determined by MCD and HF-EPR spectroscopy and ab initio calculations, which will be discussed below.

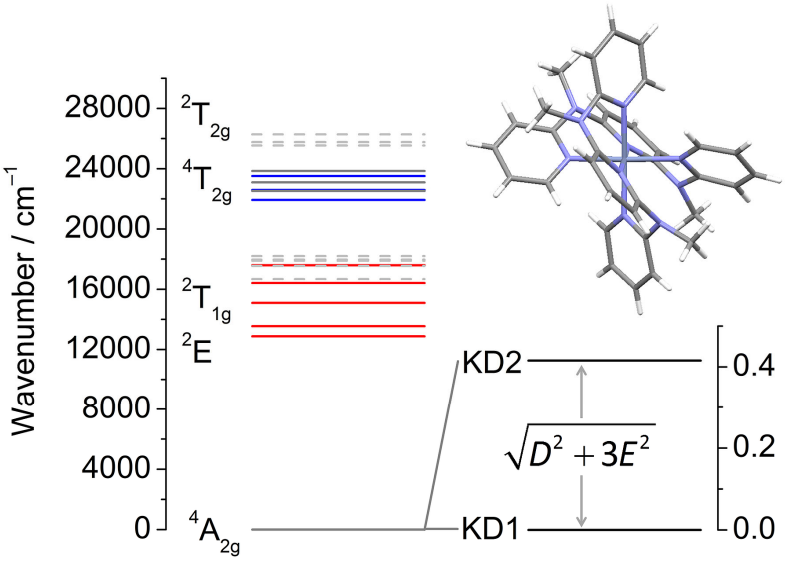

Figure 3.1.9. Molecular structure and energy level diagram of $[Cr(ddpd)_2](BF_4)_3$. The energies of the terms (here denoted in O_h symmetry) were determined by magnetic circular dichroism (MCD) spectroscopy (red: doublet states; blue: quartet states) and ab initio calculations (grey dotted: doublet states; grey solid: quartet states). The right hand side displays the zero-field splitting of the $^4A_{2g}$ ground term into two Kramers doublets (KD1, KD2) where the energy gap is a function of *D*- and *E*-parameters determined by high-frequency electron paramagnetic resonance (HF-EPR) spectroscopy. Figure reproduced from *Phys. Chem. Chem. Phys.* **21** (13), 6976-6983 (2019)[42] (Figure 1) with permission from The Royal Society of Chemistry.

3.1.5.3.1. Computational details

Multi-configurational LDF-CAHF/SA-CASSCF/PNO-CASPT2/SI-SO[29,37,69,86] ab initio calculations were performed for $[Cr(ddpd)_2]^{3+}$. The calculations were carried out with the Molpro[79,80] suite of ab initio programs using the measured crystal structure of $[Cr(ddpd)_2](BF_4)_3$[141–146].

Only the molecular cation was included in the calculations. The active space for LDF-CAHF included 3 electrons of Cr^{III} in five 3d-type orbitals (CAS(3,5)). The LDF-CAHF orbitals were used as initial guess for a subsequent SA-CASSCF calculation including a further set of five more diffuse d-orbitals (double shell effect, CAS(3,10)) into the calculation, while the closed-shell orbitals were kept frozen on LDF-CAHF level of theory. 10 quartet and 40 doublet states were calculated in these calculations. The SA-CASSCF wave functions were used as reference for multi-state PNO-CASPT2[29] calculations. The spin-orbit matrix was built and diagonalized in the basis of the 10 quartet and 40 doublet roots obtained by SA-CASSCF. The multi-state PNO-CASPT2 energies (without state mixing) were used to replace the diagonal elements of the spin-orbit matrix to correct them by inclusion of dynamical correlation. The Breit-Pauli SO-operator was used, employing the atomic mean field integral (AMFI) approximation, for the SO-coupling step[95,115]. On the basis of the resulting spin-orbit multiplets, the g-tensor corresponding to the lowest four states (the lowest quartet) was calculated using the SINGLE_ANISO[18] program. The basis set employed for Cr was def2-TZVPP[147] and the corresponding def2-TZVPP-JKFIT/MP2FIT[148,149] basis set was used for the density fitting in LDF-CAHF/PNO-CASPT2. The directly coordinating N atoms in the close vicinity of Cr were described by a cc-pVTZ[120–122] basis set and the corresponding auxiliary basis set for them were cc-pVTZ-JKFIT[76] and cc-pVTZ-MP2FIT[150]. For the remaining elements, the cc-pVDZ[120–122] basis set and the corresponding cc-pVDZ-JKFIT[76] and cc-pVDZ-MP2FIT[150] basis sets for density fitting were used. Only for H a minimal basis[81] (MINAO) was employed, but still the cc-pVDZ-JKFIT/MP2FIT[76,150] basis sets for density fitting.

3.1.5.3.2. Results and discussion

The chromium(III) ion in octahedral complexes has three unpaired electrons which leads to an electronic spin of S = 3/2. The zero-field splitting (ZFS) splits this quartet into two Kramers doublets, often with a large rhombicity[151]. The latter is important, because it allows to use arbitrary combinations of the spin microstates for qubit operations[140]. Therefore the understanding of factors governing ZFS is important to develop novel chromium(III) MQBs.

In order to determine the ZFS with HF-EPR spectroscopy, the HF-EPR spectra in our abovementioned publication were fitted[42] employing the pseudospin (S = 3/2) Hamiltonian

$$\widehat{H} = \mu_B \vec{B} \bar{\bar{g}} \hat{\vec{S}} + D\hat{S}_z^2 + E\left(\hat{S}_x^2 - \hat{S}_y^2\right), \tag{3.30}$$

where $\bar{\bar{g}}$ defines the Zeeman interaction and D and E the ZFS. The spectra could be satisfactorily simulated with the following ZFS parameters: D =+0.18 cm^{-1}, E= –0.06 cm^{-1}, $g_{//}$ = 1.98, $g_{\perp}$ = 1.99. Thus, the ZFS of this system is completely rhombic, i.e. $|E/D|$ = 1/3.

To validate these ZFS pseudospin Hamiltonian values, we have carried out ab initio calculations on $[Cr(ddpd)_2]^{3+}$ (see section 3.1.5.2.1). Projection of the lowest four states onto a S = 3/2 pseudospin allowed the extraction of pseudospin Hamiltonian parameters D =+0.13 cm^{-1} and E =–0.042 cm^{-1}, which are thus slightly smaller than what is found experimentally, but accurately reproduce the large rhombicity ($|E/D| \approx$ 1/3). The ab initio calculations also yielded the energies of the electronic states, as depicted in Figure 3.1.9 as dotted (doublet states) or solid (quartet states) grey lines. The components of the first excited $^4T_{2g}$ (O_h) state were calculated at 22523, 23092 and 23847 cm^{-1}. SA-CASSCF(7,12)-FIC-NEVPT2 calculations on DFT optimized geometries[144] found these states at slightly higher energies of 23027, 23303 and 24320 cm^{-1}. The first two excited spin-doublet states (^2E_g and $^2T_{1g}$) were calculated at 16670, 17545, 17891, 17966 and 18202 cm^{-1}. Because currently the calculation of spin densities is not implemented, we cannot conclusively attribute these energies to specific doublet states.

To validate the theoretical results, the experimental determination of the dd excitation energies by means of MCD spectroscopy was carried out in our publication[42]. In this work, the MCD spectrum was deconvoluted as a sum of Gaussian peaks giving three components at wavenumbers of 21976, 22530 and 23071 cm^{-1}, which are assigned to excitations to the three components of the $^4T_{2g}$ (O_h) state. In addition, a number of much weaker peaks are observed at 12874, 13546, and 16529 cm^{-1} that are attributed to spin-forbidden excitations to the ^2E_g (two components) and the $^2T_{1g}$ states. Interestingly, the quartet states energies agree very well with those found from ab initio calculations (see Figure 3.1.9), whilst the doublet states agree less well. A better agreement of the doublet state energies was achieved in the previous work mentioned above[144], by performing geometry optimisation in combination with an increase in the active space, leading to energies of 14745, 15602 and 15708 cm^{-1} ($^2T_{1g}$) and 15329 and 15888 cm^{-1} (^2E).

These results show that the LDF-CAHF methodology can be successfully applied to transition metal containing systems, especially in combination with other methods, such as (SA-) CASSCF and (PNO-)CASPT2. The orbitals efficiently generated by LDF-CAHF can be used as a very good starting point for a more sophisticated description of the electronic structure using subsequent correlation methods.

3.1.5.4. Application to a dinuclear radical-bridged cobalt complex

Parts of this chapter have already been published in *Angew. Chem. Int. Ed.*, DOI: 10.1002/anie.201904645 (2019)[43] and have been used for the text/formulation of this thesis. The ab initio investigations in this publication were performed by me.

Currently, the best performing mononuclear single-molecule magnets with true magnetic bistability are dysprosocenium[10,11,17] and low-coordinate transition metal ions[152,153], whereas an example of the latter is given by four-coordinate cobalt(II) complexes[154]. Large energy barriers have been reported for four-coordinate cobalt(II) complexes. However, no true bistability, which is indicated by substantial coercivity in the magnetic hysteresis curve without zero-field step, has been reported yet. Under-barrier relaxation processes, such as the Raman process or quantum tunneling of the magnetization[129], are the main reasons for the lack of coercivity. These under-barrier relaxation processes are expected to be suppressed in strongly exchange coupled multi-spin systems. A good example of these systems are radical bridged dinuclear lanthanide complexes[110,128,155]. However, due to the small spatial extension of the 4f-orbitals, truly strong exchange couplings are challenging to achieve for lanthanides. Such very strong couplings are required, because weak or moderate exchange couplings will lead to exchange coupled multiplets below the energy levels arising from the single-ion anisotropy. These multiplets can function as intermediate states in an Orbach relaxation process, which effectively decreases the energy barrier. In contrast, very strong exchange couplings can be achieved in transition metal-radical systems, where coupling strengths of hundreds of cm^{-1} have been reported[156,157]. The rational improvement of polynuclear radical-bridged transition metal complexes requires an understanding of their electronic structure. However, SA-CASSCF calculations of these systems are extremely challenging, due to the large required active space, the numerous roots needed for the SO-coupling step and often the large numbers of closed-shell orbitals to be optimized.

Moreover, the accurate determination of exchange couplings requires the inclusion of dynamical correlation by even more demanding methods such as CASPT2 and MRCI. The application of the (LDF-)CAHF methodology to these systems, with an active space consisting out of the d-orbitals of each transition metal ion and the orbitals corresponding to the radical-bridge, again leads to the problems of high-energy states included in the averaging, i.e. states where electrons are transferred between the different open-shell metal ions and between the metal ions and the radical-bridge (a remedy for this problem is presented in Chapter 3.3). This leads to orbitals which are inappropriate for the description of the low-lying molecular states of interest. However, the LDF-CAHF calculations can be used to prepare a sophisticated initial guess for the active orbitals of the systems and to determine the closed-shell orbitals, which are then kept frozen on LDF-CAHF level of theory in the subsequent correlated (SA-CASSCF, CASPT2, MRCI,…) calculations. In this section, we want to follow this strategy and use the LDF-CAHF method to generate a sophisticated initial orbital guess for subsequent SA-CASSCF and CASPT2 calculations of a polynuclear radical-bridged cobalt complex, in order to significantly reduce the time requirements for these calculations. Then, we want to assess the accuracy of the obtained ab initio results compared to experimental findings.

We set out to use the $[Co^{II}(L_A^{2-})_2]^{2-}$ (H_2L_A is 1,2-bis(methanesulfonamido)benzene) complex (**1**) as an inspiration in a multispin metal-radical complex (Figure 3.1.10). It was recently shown[154] that this complex possesses a D value in excess of 100 cm^{-1}, separating the two Kramers doublets of the $S = 3/2$ by more than 200 cm^{-1}. In our abovementioned publication[43] (on which this section is based), we presented the synthesis as well as theoretical and magnetic investigations of the air- and moisture-stable radical-bridged system $(K\text{-}18\text{-}c\text{-}6)_3[\{(H_2L_B^{2-})Co^{II}\}_2(\mu\text{-}L_B^{3\bullet-})]$ (**2**, H_4L_B = 1,2,4,5-tetrakis(methanesulfonamido) benzene). In particular, we showed that in this strongly coupled multispin system, Raman relaxation has been strongly suppressed leading to a slowing down of the magnetization by up to 350 times compared to the mononuclear building block .

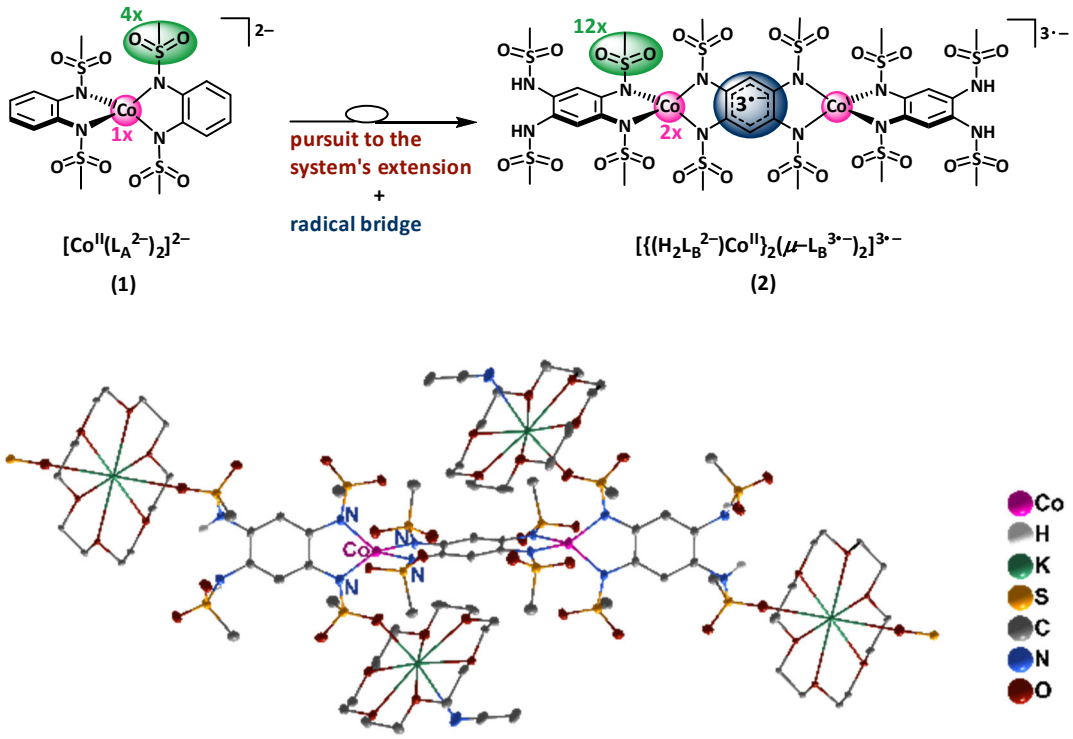

Figure 3.1.10. Single crystal ORTEP view of **2** in the polymeric chain of the crystal. Ellipsoids of **2**/K-18-c-3 shown at 50%/20% probability level. H atoms (except for NH groups) omitted for clarity. Figure reproduced from *Angew. Chem. Int. Ed.*, DOI: 10.1002/anie.201904645 (2019)[43] (Figure 1).

Complex **2** crystallizes with four 18-crown-6 encased potassium counterions, two located on either side of the molecule and two are shared, connecting the complexes to a polymeric chain. Hence, three whole counterions can be assigned to one molecule. These structural features demonstrate that the bridging tetra-aza ligand is triply negatively charged and therefore contains an unpaired electron.

The LDF-CAHF methodology was employed in combination with the SA-CASSCF and CASPT2 methods for the theoretical investigations in our publication on the complex, which is now also presented in this thesis.

3.1.5.4.1. Computational details

Multi-configurational LDF-CAHF/SA-CASSCF/CASPT2/SI-SO[37,69,86,97,158] ab initio calculations were performed for $[\{Co(H_2N_4SO_2Me)\}_2(N_4SO_2Me)](K\text{-}18\text{-}c\text{-}6)_3$ (**2**). The calculations were carried out with the Molpro[79,80] suite of ab initio programs using the measured crystal structure. Only the $[\{Co(H_2N_4SO_2Me)\}_2(N_4SO_2Me)]^{3-}$ anion was included in the calculations. One of the two Co^{2+} ions was substituted by diamagnetic Zn^{2+}. First, the radical ligand was reduced to the closed-shell form by adding one electron and then a LDF-CAHF calculation

was performed. The active space for LDF-CAHF included 7 electrons of Co^{2+} in five 3d-type orbitals (CAS(7,5)). In a second step, the additional electron was removed to obtain the radical form of the ligand. The LDF-CAHF orbitals were then used as starting guess for a subsequent SA-CASSCF calculation including two further closed-shell orbitals (corresponding to π-orbitals of the bridging ligand) a two further virtual orbitals (corresponding to π^*-orbitals of the bridging ligand) into the calculation, i.e. CAS(10,9), while the remaining closed-shell orbitals were kept frozen on LDF-CAHF level of theory. 10 quintet and 10 triplet states were calculated in these calculations. The SA-CASSCF wave functions were used as reference for multi-state internally contracted CASPT2 calculations[97,158] where only the active orbitals were correlated (correlating also the closed-shell orbitals with multi-state PNO-CASPT2[29] led to a change of the energy differences of ≤ 1 cm^{-1}). The spin-orbit matrix was built and diagonalized in the basis of the 10 quintet and 10 triplet roots obtained by SA-CASSCF. The multi-state CASPT2 energies were used to replace the diagonal elements of the spin-orbit matrix to correct them by inclusion of dynamical correlation. The Breit-Pauli SO-operator was used, employing the atomic mean field integral (AMFI) approximation, for the SO-coupling step[95,115]. The basis set employed for Co and Zn was def2-TZVPP[147] and the corresponding def2-TZVPP-JKFIT[149] basis set was used for the density fitting in LDF-CAHF. The directly coordinating N atoms in the close vicinity of Co and Zn were described by a cc-pVTZ[159] basis set and the corresponding auxiliary basis set for them were cc-pVTZ-JKFIT[76]. For the remaining elements, the cc-pVDZ[159] basis sets and the corresponding cc-pVDZ-JKFIT[76] basis sets for density fitting were used. Only the four most outer C atoms were given a def2-SVP[147] basis set and a def2-SVP-JKFIT[149] basis set for density fitting. Moreover, a minimal basis[81] (MINAO) was employed for H, but still the cc-pVDZ-JKFIT[76] basis sets for density fitting.

3.1.5.4.2. Results and discussion

To assess the strength and nature of the magnetic couplings of the cobalt(II)–radical–cobalt(II) system **2**, as well as to investigate its zero-field splitting, magnetic susceptibility measurements were carried out in our work[43] (Figure 3.1.11).

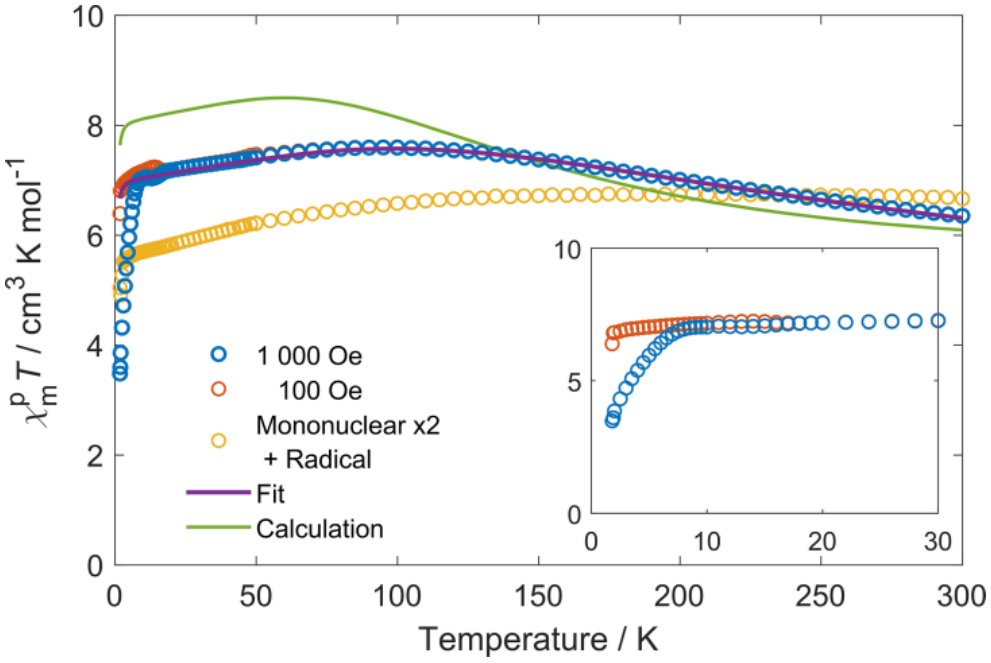

Figure 3.1.11. Susceptibility temperature product (χT) as a function of temperature for a pressed powder pellet sample of **2** in applied field of 0.1 T (blue symbols), as well as a fit using parameters given in the text (red line) and the ab initio-calculated susceptibility (green line). The yellow symbols indicate twice the χT value of **1**[154] plus a 0.375 cm^3 K mol^{-1} contribution for the radical. The inset magnifies the low-temperature region. Figure reproduced from *Angew. Chem. Int. Ed.*, DOI: 10.1002/anie.201904645 (2019)[43] (Figure 2).

The χT data could be very well fitted on the basis of the following spin Hamiltonian:

$$\hat{H} = \sum_{i=1}^{2} \left(J_{Co-Rad} \hat{\vec{S}}_{Co,i} \cdot \hat{\vec{S}}_{Rad} + D_{Co,i} \hat{S}_{z,i}^2 + \mu_B \vec{B} \bar{\bar{g}}_{Co,i} \hat{\vec{S}}_{Co,i} \right) + \mu_B \vec{B} g_{Rad} \hat{\vec{S}}_{Rad}. \qquad (3.31)$$

The first term in the bracket describes the (isotropic) exchange coupling between the corresponding cobalt site and the radical bridge, the second term the ZFS of corresponding cobalt site and the third term its Zeeman interaction with the external magnetic field. The last term described the Zeeman interaction of the radical bridge with the external magnetic field.

The best fit yielded the values J_{Co-Rad}= +440(40) cm^{-1}, D_{Co} = –115(15) cm^{-1}, $g_{Co,\parallel}$ = 2.85(3), $g_{Co,\perp}$ = 2.09(7) (g_{Rad} was fixed to 2). These values confirm both the antiferromagnetic nature of the exchange coupling and the ferrimagnetic high-spin ground state discussed in our publication.

To obtain more information on the values of D and J, we aimed to carry out multireference ab initio calculations. However, such methods currently cannot easily tackle a molecule of

the size of **2** with three open shell centers. Therefore, in a first step we replaced one of the cobalt ions by diamagnetic zinc(II). Furthermore, we forced the bridging ligand to be closed shell by adding one electron. The orbitals resulting from a LDF-CAHF-calculation[37] on this fictitious compound were used as a starting guess for a subsequent calculation, where one electron was again removed from the bridging ligand HOMO giving an open shell ligand. Using an active space consisting of the five cobalt d-orbitals, as well as the bridging ligand frontier orbitals (two π- and two π^*-orbitals), i.e. CAS(10,9)), we carried out a SA-CASSCF calculation of this system with two open shells, calculating 10 quintet and 10 triplet roots. Description of the zero-field splitting requires taking into account spin-orbit coupling, while superexchange interactions involve dynamical correlations. The former was dealt with by constructing the matrix of the Breit-Pauli spin-orbit operator (in the atomic mean-field approximation). Here, the energies of the diagonal elements were replaced by those calculated at the multi-state CASPT2 level, which takes into account dynamical correlations. Diagonalization of this matrix gave the final states. Table 3.1.17 shows the energies of the lowest eight states and to which spin-manifold they mainly correspond to (note that in case of moderate and especially strong spin-orbit coupling different spin-manifolds can mix).

Table 3.1.17. Energies and spin composition of the lowest eight states of $[\{CoZn(H_2N_4SO_2Me)_2(N_4SO_2Me)\}]^{3-}$ obtained by LDF-CAHF/SA-CASSCF/CASPT2/SI-SO calculations mixing 10 quintet and 10 triplet roots in the SI-SO step. T: Triplet. Q: Quintet. Energies are given in cm^{-1}.

State	Energy	Composition
1	0.00	T
2	1.89	T
3	184.34	T
4	312.57	Q
5	312.58	Q
6	495.46	Q
7	496.41	Q
8	512.44	mainly Q with some T

The lowest eight states were projected onto a (S = 3/2)–(S = 1/2) dimer spin Hamiltonian analogous to equation (3.31) (by fitting the ab initio energies and checking for the right spin composition of the corresponding states). This allowed extracting spin Hamiltonian parameter values as J_{Co-Rad} = +174 cm^{-1}, which confirms the antiferromagnetic coupling found experimentally, and D_{Co} = –110 cm^{-1}. The latter value is very close to the values obtained from fitting the susceptibility. The former is less than half of what is found in the

susceptibility fit, indicating an imperfect description of the magnetic coupling. Because the molecule contains an inversion center, the coupling to the other cobalt ion, as well as the latter's zero-field splitting must be equivalent and collinear. This then allows calculating the susceptibility (Figure 3.1.11), where g-values of **1** were used. The plot reveals that the maximum in the χT value is calculated at a lower temperature than that found in the experiment. This demonstrates that the interaction is underestimated in the calculation and shows that the description of spin-orbit coupling (leading to ZFS) is better than that of dynamical correlations (leading to J). This is partly due to the fact that only the diagonal elements of the spin-orbit matrix were calculated at perturbational CASPT2 level, and partly due to the diamagnetic substitution of one cobalt ion. For such strong exchange couplings, this diamagnetic substitution of one cobalt is a very rough approximation, because three-centre effects to the coupling might play an important role. However, a more accurate treatment of dynamical correlation by, e.g., MRCI is not possible because of the size of the system. Moreover, a calculation of the full system without diamagnetic substitution of one cobalt ion is not feasible because it requires a very large active space and the calculation of numerous roots for the SO-coupling step.

Again, the LDF-CAHF methodology could be successfully applied to a transition metal based compound with a very complicated electronic structure to calculate the exchange coupling in this molecule. It could be used as starting point for subsequent correlation methods to obtain a more sophisticated description of the system. Therefore, the LDF-CAHF method is an efficient method to obtain a reasonable first estimate of the electronic structure in short time which can be used to save time in subsequent (correlation) methods and improve the convergence of these methods to the right electronic state.

3.1.6. Conclusions

We have presented a new approach for the fast ab initio calculation of crystal-field splittings of lanthanide complexes applicable to very large molecules due to the combination of configuration-averaged Hartree-Fock with the techniques of local-density fitting (LDF-CAHF). This method allows for the calculation of orbitals averaged over all spin-manifolds and, in combination with CASCI, of energy splittings in such complexes with the same accuracy as state-averaged CASSCF, but is much more time-efficient. The low-order scaling allows computations for large molecules employing large basis sets within short time without the need of a high performance compute cluster. The superiority of the method to SA-CASSCF becomes more significant if one increases the system and basis set size. This is especially attractive if not only one single-point calculation is desired, but also the calculations of many different geometries constructed by, for instance, elongation along some normal coordinate to study, e.g., spin-phonon couplings. The method can also be extended to obtain orbitals which are only averaged for one specific M_S-value, which renders it also interesting for systems with weaker spin-orbit coupling**.** The remaining deviations from the experiment can be explained by the missing dynamical correlation in the calculations. Nevertheless, the averaged orbitals obtained by the method can be used in subsequent correlation methods like CASPT2 and MRCI to account for this effect and consequently substantially improve accuracy. Moreover, with slight modifications of the method, it is in principle possible to obtain orbitals for polynuclear systems containing more than one lanthanide ion because the scaling with respect to the size of the active/open space is the same as for a standard ROHF calculation. This is discussed at a later stage in this thesis (Chapter 3.3). We also applied the LDF-CAHF method to actinide and transition metal based systems. In SA-CASSCF calculations of these systems, a minimal active space (consisting out of seven 5f-orbitals for actinide systems and five d-orbitals for transition metal systems) is often not sufficient for an accurate description of the electronic structure and an extended active space is required. This is due to the larger spatial extension of the 5f- and d-orbitals and therefore the increased covalency of the metal-ligand interactions. However, extending the active space in the LDF-CAHF method leads to the inclusion of unwanted high-energy states in the averaging and leads to orbitals which are inappropriate for the description of the low-lying molecular states of interest. However, we could show that the LDF-CAHF method can be employed,

using a minimal active space, to efficiently generate a sophisticated initial orbital guess for subsequent SA-CASSCF (and (PNO-)CASPT2) calculations with an extended active space. In the SA-CASSCF calculations, the closed-shell orbitals can be kept frozen at the LDF-CAHF level of theory, to significantly decrease the computation time by circumventing the time-demanding SA-CASSCF-orbital-optimization for the closed-shell orbital space. We applied this strategy to a mononuclear uranium complex ($[U^{III}\{SiMe_2NPh\}_3$-tacn)$(OPPh_3)]$ (tacn=1,4,7,-triazacyclononane)), a mononuclear chromium complex ($[Cr(ddpd)_2](BF_4)_3$ (Figure 3.1.9, ddpd=*N,N'*-dimethyl-*N,N'*-dipyridine-2,6-diamine)) and a radical-bridged dinuclear cobalt complex ($(K\text{-}18\text{-}c\text{-}6)_3[\{(H_2L_B^{2-})Co^{II}\}_2(\mu\text{-}L_B^{3\bullet-})]$ (H_4L_B = 1,2,4,5-tetrakis(methanesulfonamido) benzene)), where we substituted one cobalt by diamagnetic zinc. For the transition metal based complexes, dynamical correlation was included by (PNO-)CASPT2. The ab initio results were compared with experimental findings. The LDF-CAHF/SA-CASSCF/SI-SO results for the uranium complex were in reasonable agreement with the experimental data, but seemed to be not fully converged with respect to the size of the active space, which consisted out of two sets of f-orbitals (double shell effect) and a further set of d-orbitals in the SA-CASSCF calculation. Moreover, the inclusion of dynamical correlation appears to be necessary to achieve accurate results. However, CASPT2 and MRCI calculations are not easily feasible for this large active space and a molecule of this size. Nevertheless, the LDF-CAHF method was shown to provide a good starting point for subsequent SA-CASSCF calculations with extended active space, where it can significantly reduce the required calculation time for SA-CASSCF. The LDF-CAHF/SA-CASSCF/(PNO-) CASPT2/SI-SO results for the chromium and cobalt complex were in good agreement with the experimental findings. Also for transition metal based systems, the LDF-CAHF method provides a good starting point for subsequent correlated calculations and drastically reduces the time requirements of the subsequent SA-CASSCF calculations with extended active space by freezing the closed-shell orbitals on LDF-CAHF level of theory. Therefore, the LDF-CAHF method is expected to be very helpful in future calculations of the magnetic and spectroscopic properties of not only lanthanide, but also actinide and transition metal based systems.

3.2. Increasing the accuracy of conventional calculations

Parts of this chapter have already been published in *J. Chem. Theory. Comput.* **14** (8), 3998–4009 (2018)[44] and have been used for the text/formulation of this thesis. In this publication, Dr. Alexander Mitrushchenkov helped to fix bugs in the MRCI and spin-orbit programs and provided technical support with the programs.

The (SA-)CASSCF/SI-SO and (LDF-)CAHF+CASCI/SI-SO methods cover only static correlation. In order to increase the accuracy of the (SA-)CASSCF/SI-SO or (LDF-)CAHF+CASCI/SI-SO calculations by including dynamical correlation, the multi-state complete active space perturbation theory of second order (CASPT2)[27–30] method can be employed to improve the diagonal elements of the spin-orbit matrix[31], but this method often suffers from problems if the minimal active space is chosen (e.g. *intruder state problems*, which can lead to convergence failures or the *overshooting effect*, which can lead to overestimation of crystal field splittings)[28,31,32] or is not feasible for large active spaces and large molecules. The multi-state MRCI method[33–36] is a method to variationally include dynamical correlation. It does not suffer from the standard problems (intruder state problems and overshooting effect) of multi-state CASPT2 and can be used to correct both diagonal and non-diagonal elements of the spin-orbit matrix by including dynamical correlation. The main problem of this method is that it is not feasible even for small lanthanide complexes, especially if the calculation of many states/roots is required.

Here, we present a solution to this problem in the form of a quasi-local projected internally contracted MRCI (qlp-icMRCI) approach. We make use of localized orbitals to only include the most important effects of dynamical correlation on the crystal-field splitting, in particular the effect of dynamical correlation on the interaction of the central lanthanide ion with the closest ligand groups. In addition, the required states are calculated sequentially instead of simultaneously by employing a projection operator technique, which is computationally much more efficient, due to the better (linear) scaling with respect to the number of states to be calculated and because of the reduced memory requirements (compared to conventional multi-state MRCI). We test this approach on two complexes for which extensive experimental data is available, namely the systems $[Er\{N(SiMe_3)_2\}_3]$ and $\{C(NH_2)_3\}_5[Er(CO_3)_4]\cdot 11H_2O$.

3.2.1. Problems of conventional multi-state icMRCI

Two problems arise when using conventional multi-state icMRCI (described in the theory section) to calculate crystal-field splittings in lanthanide complexes: the required time and random access memory (RAM) limitations. These problems arise for different reasons. For most of the lanthanide complexes, the number of closed-shell orbitals is very large and it is not feasible to correlate all of them, because the number of excited CSFs and ICCs grows rapidly with the number of closed-shell orbitals. Moreover, the calculation of crystal-field splittings in these complexes requires the calculation of a large number of states belonging to different spin-manifolds in order to account for the spin-orbit coupling. In conventional multi-state icMRCI calculations, one typically uses a basis which is the union of all contracted configurations generated from separate reference functions for each state up to and including the highest state of interest. Since the number of states of interest is usually large for lanthanide complexes, excitations out of many reference functions for different states have to be performed which further increases the size of the space of ICCs. This is likely the reason why MRCI calculations of crystal-field splittings of lanthanide complexes including spin-orbit coupling have not been carried out yet. In this work, we present a strategy to include dynamical correlation at the MRCI level of theory and still calculate sufficient states in order to account for the strong spin-orbit coupling. This is achieved by combining projection operator techniques with the exploitation of locality as explained in the following sections. The reference wave functions for this methodology can be efficiently obtained by our previously described LDF-CAHF+CASCI method[37].

3.2.2. Projection operator technique for excited states

A particular problem of conventional multi-state icMRCI is that, as already mentioned, if several excited states are computed, different contracted configurations are required for each state of interest. Therefore, the number of doubly external ICCs generated from these reference wave functions increases linearly with the number of states, as the calculation of k states requires the calculation of the first k eigenstates of the Hamiltonian matrix in this compound contracted basis[35]. This leads to a scaling behaviour as k^2 to k^3 of the whole calculation[35]. This becomes a serious problem for calculating the low-energy electronic structure of lanthanide complexes, as many roots have to be calculated to account for the strong spin-orbit coupling. A solution for this unfavorable scaling is found in the combined

use of a projection operator technique and the use of an ICC basis for state k which is generated only from the kth reference function. In this approach developed by Werner and Knowles[35], the desired kth state is obtained by calculating the ground state of a modified Hamiltonian matrix $\boldsymbol{H}^{(k)}$ iteratively by a direct CI procedure with the $(k-1)$ lower eigensolutions shifted away (their eigenvalues are shifted to zero). The modified or projected Hamiltonian matrix is given as

$$\boldsymbol{H}^{(k)} = \boldsymbol{P}^{(k)}\boldsymbol{H}\boldsymbol{P}^{(k)}, \tag{3.32}$$

with the projection matrix for state k defined as

$$\boldsymbol{P}^{(k)} = \mathbf{1} - \sum_{n=1}^{k-1} \boldsymbol{c}^{(n)}\boldsymbol{c}^{(n)\dagger}, \tag{3.33}$$

where $\boldsymbol{c}^{(n)}$ is the eigenvector for state n. Therefore, the methodology consists of a linear sequence of calculations, starting with the determination of the ground state of $\boldsymbol{H} \equiv \boldsymbol{H}^{(1)}$, using the solution to calculate $\boldsymbol{H}^{(2)}$ and subsequently finding the lowest root of $\boldsymbol{H}^{(2)}$ and then use the obtained eigenvectors to calculate $\boldsymbol{H}^{(3)}$ and so on, up to the desired state k. Thus, the computational effort scales linearly in the number of desired states k, because of the successive instead of simultaneous calculation of the desired states and the fact that the ICC basis for each state is generated only from its own reference function. Since the basis used for each state is different in contracted CI calculations, an approximate projector is constructed. Only those configurations are included in the vector $\boldsymbol{c}^{(n)}$, which are common for all states, i.e. the internal CSFs, which are the dominant part of the wave function and should be sufficient for shifting away the unwanted roots of the Hamiltonian matrix. This methodology can lead to problems such as non-orthogonal CI wave functions $\Psi^{(i)}$ for different states, because the basis used for each state is different and only an approximate projection operator is used. To account for these problems, a generalized eigenvalue problem in the basis of the already obtained n non-orthogonal CI wave functions

$$\mathbf{HC} = \mathbf{SCE} \tag{3.34}$$

is solved after calculating state n, where $\mathrm{H}_{mn} = \langle \Psi^{(n)} | \hat{H} | \Psi^{(m)} \rangle$ and $\mathrm{S}_{mn} = \langle \Psi^{(n)} | \Psi^{(m)} \rangle$.

Thus, the final states are linear combinations of the states calculated in the approximate projector calculation and the corresponding expansion coefficients and final eigenvalues are given by the column vectors of $\mathbf{C}$ and diagonal elements of $\mathbf{E}$. The calculations of excited states using this projection operator technique are faster and the memory requirements are smaller than for conventional multi-state MRCI calculations. This is due to the linear scaling in the number of states k and the use of an individual ICC basis for each state. This also makes it easier to parallelize the calculations (since each core needs less RAM). Nevertheless, the large number of closed orbitals to be correlated for most lanthanide complexes significantly slows down the calculation and inhibits the use of icMRCI. We present a remedy for this problem below, by combining projected icMRCI calculations with the exploitation of locality to include only the most important effects on the crystal field splittings.

3.2.3. Quasi-local projected internally contracted multireference configuration interaction

The exploitation of locality was previously used to determine the reference wave function in the LDF-CAHF+CASCI method[37]. In the last decade, there has also been a great deal of research in the field of local correlation methods including dynamical correlation, e.g. local coupled cluster or local CASPT2[29,160–170] or embedding approaches[171]. Nevertheless, these methods either do not go beyond the level of perturbation theory (local CASPT2), or are not yet applicable for multi-reference cases (local coupled cluster), or multi-state options have not yet been implemented/developed for the calculation of the large number of required states (local coupled cluster). A local multi-state icMRCI method would be highly desirable but has not been reported yet, to the best of our knowledge. Our approach is to use the icMRCI method in a quasi-local manner for the closed-shell orbital space. Our aim was to reduce the computation time and memory requirements to make icMRCI calculations of many states including dynamical correlation feasible. This allows increasing the accuracy of crystal field splitting calculations of lanthanide complexes compared to LDF-CAHF+CASCI in a non-perturbative way (beyond the usually used CASPT2 approach). Therefore we combined the projection operator technique for excited states with a physically reasonable subspace of closed orbitals to be correlated, which we identify by localization. It is expected, that the most important effects on the crystal field splitting are due to the interaction of the f-

orbitals of the central ion with the spatially closest ligand orbitals, e.g. the orbitals localized on the ligand atoms of the first coordination sphere of the lanthanide ion. Since the conventional canonical orbitals are normally delocalized over the whole molecule, we first perform a localization within the space of closed-shell orbitals, e.g. Foster-Boys[172] localization, and group the localized orbitals according to their distance (using the center of charge as measure) to the central ion. In the next step, we identify the space of localized closed-shell orbitals at or spatially closest to (e.g. the lone pairs of the directly coordinating atoms) the central ion, which we will call L in the following. Within this subspace L, we make the chosen closed-shell orbitals pseudocanonical again (for faster convergence in the icMRCI iterations), while leaving the remaining localized closed-shell orbitals unchanged, which are then treated as core (uncorrelated) orbitals in the subsequent icMRCI calculation. In our approach, the icMRCI wave function then has the following form

$$|\Psi_{\mathrm{icMRCI-loc}}\rangle = \sum_R C^R|\Phi_R\rangle + \sum_R \sum_{n\in\{L\},m\in\{A\}} C_m^{nR}\hat{E}_n^m|\Phi_R\rangle + \sum_R \sum_{n\in\{L\cup A\},a} C_a^{nR}\hat{E}_n^a|\Phi_R\rangle + \frac{1}{2}\sum_{mn\in\{L\cup A\},ab} C_{ab}^{mn}|\Phi_{mn}^{ab}\rangle, \tag{3.35}$$

where A is the space of active orbitals and where we suppose that the reference space is a CAS. Note that the internal configurations not contained in the reference space (second term on the right hand side (r.h.s.) of the equation) and the singly external configurations (third term in the r.h.s. of the equation) are uncontracted.

This means that all CSFs not contained in the reference space and all ICCs are generated by excitations from a restricted set of orbitals, i.e. the union of L and A ($\{L \cup A\}$), which means that only the active orbitals and the closed-shell orbitals in the vicinity of the central ion are correlated. This approach leads to a drastic reduction in the number of correlated closed-shell orbitals, but is still expected to cover the most important effects of dynamical correlation on the crystal field splitting, since the closed orbitals are selected in a physically reasonable way by a spatial distance criterion. Moreover, this approach can be systematically improved, as it is possible to increase the size of coordination spheres included in L. In combination with the projection operator technique and the efficiently obtained reference functions by LDF-CAHF+CASCI, this finally makes it feasible to include

dynamical correlation in a more accurate and variational way in calculations of crystal field splittings in lanthanide complexes and we will call this procedure quasi-local projected internally contracted MRCI (qlp-icMRCI).

3.2.4. Benchmark applications of qlp-icMRCI

This chapter focuses on Er containing systems as exemplary systems for our investigations, because the maximum number of roots to be calculated for the SO-coupling step is not too small and not too large for Er (35 S=3/2 roots and 112 S=1/2 assuming a minimal active space of seven 4f-orbitals). First, the effect of the inclusion of different numbers of states of different spin-manifolds on the first spin-orbit splitting (i.e. the energy of the first excited *J*-multiplet) is analyzed for the free Er^{3+} ion on SA-CASSCF/LDF-CAHF+CASCI level of theory to assess how many roots are needed to obtain a converged reference. Moreover, we will investigate the influence of correcting the non-diagonal elements of the SO-matrix for the free ion by dynamical correlation in section 3.2.4.2.1.2. We do this to analyze the difference between using correlated icMRCI wave functions to build up the SO-matrix and only correcting the diagonal elements by CASPT2 or icMRCI energies. In section 3.2.4.2.2, the effect of the number of included states on the crystal-field splitting of the ion surrounded by three singly negatively charged point charges is investigated at the SA-CASSCF/LDF-CAHF+CASCI level of theory. It is important to assess the minimum number of states needed to achieve converged energies for the reference wave functions for both the free ion and the ion surrounded by point charges and to identify the differences of both cases, because it is expected that fewer states are required to obtain converged crystal field energies of the ground multiplet than to obtain a converged energy of the (split) first excited multiplet. This analysis is important, because it is crucial to restrict the space of calculated states as much as possible, especially in view of the demanding icMRCI calculations of crystal field splittings for larger molecules. Moreover, the influence of dynamical correlation on the crystal field splitting employing the point charge model is investigated in section 3.2.4.2.2, using different levels of theory to assess the qualitative and quantitative differences of multi-state CASPT2 and multi-state icMRCI as well as the performance of the projected icMRCI method compared to multi-state icMRCI. Section 3.2.4.2.3 covers the application of the presented methodology to lanthanide complexes to demonstrate its applicability.

3.2.4.1. Computational details

In this section, the technical details of the calculations of the systems investigated in this work are presented, i.e. of the free Er(III) ion, the Er(III) surrounded by three singly negative point charges in C_{2v} symmetry and the lanthanide complexes $\{C(NH_2)_3\}_5[Er(CO_3)_4]\cdot 11H_2O$ and $[Er\{N(SiMe_3)_2\}_3]$. The structure of the Er(III) ion surrounded by point charges was obtained by placing the three point charges at a distance of 2.1914 Å (the N-Er distance in $[Er\{N(SiMe_3)_2\}_3]$[39]) around the central ion with one bond angle of 90° and two of 135°. All calculations were carried out with the Molpro[79,80] suite of ab initio programs. For the all-electron SA-CASSCF calculations (and all subsequent calculations including dynamical correlation) of the free Er(III) ion and the Er(III) surrounded by point charges, the ANO-RCC[118] basis set reduced to triple-zeta ([8s7p4d3f2g1h]) was used for erbium. Scalar-relativistic effects were accounted for by the second order Douglas-Kroll-Hess transformation, and the Breit-Pauli operator was used for the SO-coupling step. The LDF-CAHF calculations (and all subsequent calculations including dynamical correlation) were in all cases performed using the 28 electron pseudopotential/effective core potential (ECP) ECP28MWB[114] for erbium and an appropriate ECP-SO operator[114] was used for the SO-coupling step. In case of all LDF-CAHF calculations (and the subsequent correlated calculations) the def2-TZVPP/def2-ATZVPP basis sets and the corresponding def2-TZVPP/def2-ATZVPP-JKFIT auxiliary basis sets for density fitting were employed for erbium. For the molecular calculations, the cc-pVDZ/cc-pVTZ/aug-cc-pVTZ[120–122] basis sets were used for the remaining elements. In case of $[Er\{N(SiMe_3)_2\}_3]$, a minimal basis (MINAO[81]) was used for hydrogen, as no significant effect of these atoms on the crystal field splitting is expected for this molecule. The active space was always chosen to be CAS(11,7) for Er(III) and the corresponding erbium containing systems. The weighting factors in the all-electron SA-CASSCF calculations were chosen to be the same for each spin-manifold. In case of the CASPT2 calculations, only the diagonal elements of the spin-orbit matrix were replaced by CASPT2 energies, while the rest of the matrix was calculated using SA-CASSCF/LDF-CAHF+CASCI wave functions. The full spin-orbit matrix was calculated using icMRCI wave functions in case of the icMRCI calculations, if not mentioned otherwise. Although the Davidson correction can be employed to approximatively account for the size-consistency error of MRCI, the icMRCI energies used for the diagonal elements of the SO-matrix in this work were obtained without its use. This is because the deviation of the

energy differences obtained by calculations with and without Davidson correction is about 10^{-5} to 10^{-6} hartree for the systems investigated in this work and hence the Davidson correction has a negligible effect on the crystal field splitting. For the calculation of $\{C(NH_2)_3\}_5[Er(CO_3)_4]\cdot 11H_2O$, only the $[Er(CO_3)_4]^{5-}$ anion was explicitly treated quantum-chemically. The effects of the counter ions and the surrounding crystal were described by putting a +1-point charge at the crystallographic position[45] of the central C of the $[C(NH_2)_3]^+$ cation and a 5—-point charge at the position of the central Er of all $[Er(CO_3)_4]^{5-}$ anions, beside the one treated quantum-chemically. This was done for all ions within 4 crystallographic shells of unit cells in all directions of the crystal. The specific details for the different systems are shown in Table 3.2.1. For the LDF-CAHF+CASCI calculations of $\{C(NH_2)_3\}_5[Er(CO_3)_4]\cdot 11H_2O$ different basis sets were employed. In order to distinguish these basis sets, they are listed in Table 3.2.2 and numbered from 1 to 3.

Table 3.2.1. Computational details for the different systems.

	Free Er^{3+} ion	Er^{3+} + point charges	$[Er\{N(SiMe_3)_2\}_3]$	$[Er(CO_3)_4]^{5-}$
Basis set	def2-TZVPP	def2-TZVPP	Er: def2-TZVPP C,N,Si: cc-pVDZ H: MINAO	See Table 2
Auxiliary basis set	def2-TZVPP/ JKFIT	def2-TZVPP/ JKFIT	Er: def2-TZVPP/ JKFIT C,N,Si,H: cc-pVDZ/JKFIT	JKFIT basis sets corresponding to basis in Table 3.2.2
Pseudopotenial/all-electron calculation?	Pseudopotential + all-electron	Pseudopotential + all-electron	Pseudopotential	Pseudopotential
Pseudopotential for Er	ECP28MWB	ECP28MWB	ECP28MWB	ECP28MWB
Structure	-	See section "Computational details"	Crystallographic[b]	Crystallographic[a]
Energy convergence threshold (hartree)	10^{-9}	10^{-9}	10^{-7}	10^{-7}
Number of electrons	65	65	335	193

[a] From reference [45]

[b] From reference [39]

Table 3.2.2. Different basis sets used for the calculation of $[Er(CO_3)_4]^{5-}$. Close/distant refers to the distance to the central Er^{3+} ion.

	Basis 1	Basis 2	Basis 3
Er	def2-ATZVPP	def2-TZVPP	def2-TZVPP
O (close)	aug-cc-pVTZ	cc-pVTZ	cc-pVTZ
O (distant)	aug-cc-pVTZ	cc-pVTZ	cc-pVDZ
C	aug-cc-pVTZ	cc-pVTZ	cc-pVDZ

3.2.4.2. Results

3.2.4.2.1. Free Er^{3+} ion

3.2.4.2.1.1. Inclusion of different number of states/spin-manifolds

We performed state-averaged (all-electron) CASSCF and also LDF-CAHF+CASCI calculations with subsequent SI-SO calculations including different numbers of states for each spin-manifold. The number of states was always changed by at least one full degenerate set of scalar-relativistic states when assessing the number of states that must be included into the calculation to obtain reasonable results. For Er^{3+}, both quartets and doublets are relevant. In the SA-CASSCF calculations, the orbitals are optimized for the number of states to be mixed in the SI-SO step while the LDF-CAHF orbitals are equivalent to orbitals obtained from a SA-CASSCF calculation averaging over all possible states of all spin-manifolds within the chosen active space (35 quartets and 112 doublets for Er^{3+}), giving the roots of each spin-manifold a weighting factor corresponding to their relative M_S-degeneracy (4 for quartets, 2 for doublets, see Chapter 3.1.2). The results are displayed in Table 3.2.3. Note that the spin-state mixture 4 includes all possible states of all possible spin-manifolds within the chosen active space. The results of the CAHF and SA-CASSCF calculations are slightly different because of the different state-averaging, but also due to the fact that the LDF-CAHF calculations employ pseudopotentials for the scalar-relativistic part while the SA-CASSCF calculations are all-electron calculations and both types of calculations use a different SO-operator (pseudopotential vs. Breit-Pauli).

Table 3.2.3. Spin-orbit energies of first excited *J*-multiplet for Er^{3+} for different spin-state mixtures included in the SI-SO calculation using SA-CASSCF orbitals (optimized for the corresponding number of states) or LDF-CAHF orbitals. SA-CASSCF: All-electron calculations. LDF-CAHF: Pseudopotential calculations. Energies are given in cm^{-1}.

Mixture	# of S=3/2 states	# of S=1/2 states	SA-CASSCF	LDF-CAHF+CASCI
Pure spin 3/2	35	0	6208.05	5893.45
1	35	20	6196.26	5893.45
2	35	40	6700.38	6370.68
3	35	73	6675.40	6348.67
4	35	112	6670.10	6348.67

Table 3.2.3 shows a large gap of more than 500 cm^{-1} between spin-state mixture 1 and 2, while the difference between mixture 2 and 4 (the mixture including all possible states) is only about 30 cm^{-1} for SA-CASSCF and ~20 cm^{-1} for LDF-CAHF+CASCI. Therefore, it is necessary to include at least 35 quartets and 40 doublets (mixture 2) for the free Er^{3+}. We will investigate below if this large number of required states for the free ion to achieve converged SO-energies is also necessary to obtain converged results for the crystal-field splitting for the free ion surrounded by point charges or in molecules.

3.2.4.2.1.2. Influence of dynamical correlation on the SO-splitting

In the following we will consider the influence of dynamical correlation on the SO-splitting energy, i.e. the energy of the first excited *J*-multiplet, using all-electron SA-CASSCF wave functions as reference. This will be done using two methods: Multi-state CASPT2 and multi-state icMRCI. In case of the CASPT2 calculations, only the diagonal elements of the SO-matrix are replaced by the CASPT2 correlation energies and the reference CASSCF wave functions are used to calculate the non-diagonal elements. In the multi-state icMRCI calculations, it is possible to calculate the whole SO-matrix using correlated MRCI wave functions and therefore to investigate the effect of correcting also the non-diagonal elements by dynamical correlation. The energies of the first excited multiplet for CASSCF, CASPT2 and icMRCI correcting only the diagonal elements of the SO-matrix and for a calculation building the full SO-matrix using icMRCI wave functions are shown in Table 3.2.4.

Table 3.2.4. Effect of dynamical correlation on the energy of the first excited *J*-multiplet for the free Er^{3+} ion using SA-CASSCF wave functions as reference. CASSCF state-averaging SI-SO step: 35 quartets/40 doublets. Diag: Only the diagonal elements of the SO-matrix are corrected by dynamical calculation. Full: The whole SO-matrix is calculated using correlated wave functions. ms: multi-state. Energies are given in cm^{-1}.

Level of theory	Er^{3+} SO-splitting
SA-CASSCF	6700.38
ms-CASPT2	6692.44
ms-icMRCI diag	6725.41
ms-icMRCI full	6957.80

It is apparent that correcting the non-diagonal elements by dynamical correlation has an important effect (>200 cm^{-1}) on the SO-energies. The CASPT2 and icMRCI calculations replacing only the diagonal elements shift the SO-splitting energy approximately by 10 and 30 cm^{-1} respectively, while the calculation of the full SO-matrix using icMRCI wave functions leads to an energy change of more than 250 cm^{-1} compared to CASSCF. Therefore, the effect of dynamical correlation on the SO-splitting in the free ion is quite large and should be treated in a non-perturbative way and by correcting the full SO-matrix instead of the simple replacement of the diagonal elements.

3.2.4.2.2. Effect of dynamical correlation on the crystal field splitting using a point charge model

We performed SA-CASSCF, LDF-CAHF+CASCI, CASPT2 and icMRCI calculations of the crystal field splitting in an Er^{3+} surrounded by singly negatively charged point charges in C_{2v} symmetry (we did not use D_{3h} symmetry, because Molpro can exploit only Abelian point groups) as a model system. The effect of the spin-state mixture and the level of theory (CASPT2 vs. icMRCI) as well as the performance of the projected icMRCI method compared to multi-state icMRCI is discussed. First, the influence of the inclusion of different number of states of different spin-manifolds to build up the SO-matrix on the crystal field splitting is analyzed at the SA-CASSCF and LDF-CAHF+CASCI level of theory. This is done to assess how many states are required for each method to achieve a converged reference for the subsequent calculations including dynamical correlation where it is very important to reduce the number of states as much as possible to make the calculations feasible. In the SA-CASSCF calculations, the orbitals are again optimized for the number of states to be mixed in the SI-SO step while the LDF-CAHF orbitals are equivalent to orbitals obtained from a SA-CASSCF calculation averaging over all possible states of all spin-manifolds within the chosen active space (35 quartets and 112 doublets), giving the quartets a weighting factor of 4 and the

doublets a weighting factor of 2 (corresponding to their relative M_S-degeneracy). The results are displayed in Tables 3.2.5 and 3.2.6.

Table 3.2.5. Crystal-field splitting of the ground J-multiplet of Er^{3+} surrounded by three singly negative point charges in C_{2v} symmetry for different spin-state mixtures included in the SA-CASSCF/SI-SO calculation. Energies are given in cm^{-1}.

Doublet	13/0	35/20	35/40	35/73	35/112
1	0.00	0.00	0.00	0.00	0.00
2	127.11	121.52	135.12	130.28	122.21
3	226.35	216.52	241.36	233.02	218.61
4	306.82	293.73	327.00	316.26	297.24
5	391.56	376.33	417.13	403.07	379.80
6	503.15	485.01	535.96	517.51	488.67
7	640.72	618.76	682.27	658.81	623.08
8	811.17	784.61	862.29	833.46	789.27

Table 3.2.6. Crystal-field splitting of the ground J-multiplet of Er^{3+} surrounded by three singly negative point charges in C_{2v} symmetry for different spin-state mixtures included in the CASCI/SI-SO calculation using CAHF orbitals. Energies are given in cm^{-1}.

Doublet	13/0	35/20	35/40	35/73	35/112
1	0.00	0.00	0.00	0.00	0.00
2	118.51	118.22	122.20	122.48	122.48
3	212.76	212.26	219.95	220.46	220.46
4	288.86	287.97	298.79	299.48	299.47
5	367.27	366.75	379.70	380.49	380.49
6	470.72	470.61	486.53	487.45	487.45
7	598.63	598.73	618.60	619.72	619.72
8	756.59	756.90	781.10	782.56	782.57

Tables 3.2.5 and 3.2.6 clearly show that the crystal-field splitting is less sensitive to the spin-state mixture than the SO-splitting, i.e. the energy of the first excited J-multiplet. For the SA-CASSCF calculations, the mixture 35/20 and 35/112 (full averaging) yield very similar results (Table 3.2.5). In case of the LDF-CAHF+CASCI calculations, there is a slight gap between mixture 35/20 and mixture 35/40, but the average relative difference between 35/20 and the mixture 35/112 including all states is still only ~3.5 % (and the root mean square deviation of both mixtures only ~16 cm^{-1}). Therefore we will restrict the demanding MRCI calculations for molecules to a spin-state mixture of 35 quartets and 20 doublets in order to render them feasible. To investigate the effect of dynamical correlation in the point charge model, we performed multi-state icMRCI and CASPT2 calculations. We started with the spin-state mixture 13/0, due to the large required computational effort for the multi-state icMRCI

calculations, to assess which effect dynamical correlation has on the crystal-field splitting using different levels of theory. The results are displayed in Table 3.2.7.

Table 3.2.7. Influence of dynamical correlation on the crystal field splitting for Er^{3+} surrounded by three singly negative point charges in C_{2v} symmetry for different levels of theory calculating 13 quartet states using SA-CASSCF wave functions as reference and mixing them in the SI-SO-step. ms: multi-state. sym/no sym: Symmetry was employed/not employed in the calculations. Energies are given in cm^{-1}.

Doublet	13/0 CASSCF	13/0 ms-CASPT2 no sym	13/0 ms-icMRCI no sym	13/0 ms-icMRCI sym
1	0.00	0.00	0.00	0.00
2	127.11	137.12	128.63	131.98
3	226.35	240.57	226.94	229.55
4	306.82	325.04	306.98	309.32
5	391.56	417.81	394.31	397.92
6	503.15	540.47	509.16	512.67
7	640.72	691.98	650.18	654.03
8	811.17	882.66	825.38	825.48

Table 3.2.7 shows that dynamical correlation included by multi-state CASPT2 and multi-state icMRCI for the 13/0 mixture leads to a stretching of the crystal field splitting pattern to larger energies. The stretching is significantly smaller for icMRCI than for CASPT2. The CASPT2 method overestimates the crystal field splitting compared to icMRCI, which is much closer to CASSCF than to CASPT2. Moreover, we performed the multi-state icMRCI calculations employing symmetry. Table 3.2.7 shows that there are small differences between the calculations using and not using symmetry. This is due to the fact, that the configuration spaces for calculations with and without symmetry are different. This effect occurs because the wave function ansatz is constructed by applying excitations (see equation (4)) to the reference wave functions. If an excitation operator is applied to a reference wave function belonging to a certain irreducible representation, the resulting configuration or ICC is discarded if it does not belong to the same irreducible representation as the reference wave function, but the discarded configurations/ICCs can in principle contribute to the wave function of a state belonging to a different irreducible representation. In calculations without symmetry all configurations/ICCs are kept and therefore the configuration space is larger for all states. Multi-state icMRCI calculations for spin-state mixtures including more states (than for mixture 13/0) only converged when employing symmetry. The calculations employing symmetry can still be used to analyse the effect of dynamical correlation and to show the equivalence in terms of accuracy of the multi-state and projection methods, despite the small differences to the calculations not

employing symmetry. The molecular calculations will be all performed without the use of symmetry. We present the results for the spin-state mixture 35/20 in Table 3.2.8, where we also compare the icMRCI results using the multi-state method with the energies obtained by the projection method to justify the use of the latter.

Table 3.2.8. Influence of dynamical correlation on the crystal field splitting for Er^{3+} surrounded by three singly negative point charges in C_{2v} symmetry for different levels of theory calculating 35 quartet and 20 doublet states using SA-CASSCF wave functions as reference and mixing them in the SI-SO step. ms: multi-state. p: projection-method. sym/no sym: Symmetry was employed/not employed in the calculations. Energies are given in cm^{-1}.

Doublet	35/20 CASSCF	35/20 ms-CASPT2 no sym	35/20 ms-icMRCI sym	35/20 p-icMRCI sym
1	0.00	0.00	0.00	0.00
2	121.52	136.01	134.59	129.48
3	216.52	238.47	230.22	227.43
4	293.73	322.28	307.40	305.69
5	376.33	415.61	396.95	393.84
6	485.01	538.93	511.51	508.27
7	618.76	691.14	650.74	646.24
8	784.61	882.98	815.23	816.65

The CASPT2 method yields very similar results for both spin-state mixtures and overestimates the crystal field splitting (sometimes known as "overshooting effect"[31]) for both spin-state mixtures compared to MRCI. This is a well-known deficiency of the CASPT2 method and can, for example, be caused by intruder state problems[28,32]. These intruder state problems are defined by the existence of ICCs in the perturbation expansion which possess an energy comparable in magnitude to the energy associated to the zeroth order wavefunction. Due to the resulting nearly zero denominator in the expression of the perturbative correction, a divergent behavior or too large energy splittings can occur. Increasing the size of the active space by another set of seven metal-based f-orbitals in the SA-CASSCF calculations can reduce this effect, as some of the dynamical correlation is already included at the CASSCF level[31]. On the other hand, increasing the size of the active space often renders subsequent calculations including dynamical correlation unfeasible for larger systems. Table 3.2.8 shows that the stretching of the crystal field splitting pattern to larger energies by icMRCI is even increased for the 35/20 mixture (compared to the 13/0 mixture). This is consistent with the empirical use of scaling-factors[25] to match the experimental splitting and the energies obtained by the CASSCF/SI-SO approach which systematically neglects dynamical correlation. The projected icMRCI method yields results which differ at most by ~5 cm^{-1} from multi-state icMRCI which justifies its use for the

calculation of crystal-field splittings. The differences stem from the use of different ICC bases: While multi-state icMRCI employs a compound ICC basis generated from internally contracted double excitations applied to all reference functions for all states, projected icMRCI calculations employ an ICC basis for state k which is generated only from the kth reference function. This is an essential reason for the reduction of memory and computation time in the projected icMRCI method.

3.2.4.2.3. Application to molecules

3.2.4.2.3.1. Application to $Er[N(SiMe_3)_2]_3$

The first molecular system chosen was $Er\{N(SiMe_3)_2\}_3$[37–39] (Figure 3.1.1) because its low lying energy level structure is well-known from experiment[38] and it was already used as a benchmark system for the LDF-CAHF+CASCI methodology[37] (Chapter 3.1.4.2.1.2) which is used to generate the reference wave functions for the methodology described in this work. It was shown[37], that at the LDF-CAHF+CASCI/SI-SO level of theory energetically converged results are obtained, if one employs a def2-TZVPP[119] basis for erbium and a cc-pVDZ[120–122] basis for the remaining elements and that is it sufficient to calculate 35 quartet and 20 doublet states and mix them in the subsequent SI-SO step. The RMSD of the LDF-CAHF+CASCI/SI-SO calculation including only static correlation to the experimental energies obtained by luminescence[38] was shown[37] to be smaller than the RMSD of the CF fit[38] to these experimental energies and only 16 cm^{-1}. We employed the quasi-local projected icMRCI procedure and localized the LDF-CAHF orbitals and identified 7 closed-shell orbitals to be correlated, i.e. the 5s and 5p orbitals at the erbium site and the 3 lone pairs of the directly coordinating nitrogen atoms pointing towards the erbium ion, calculated 35 quartets and 20 doublets and mixed them in the SI-SO step. The corresponding crystal field energy levels of the LDF-CAHF+CASCI/SI-SO, SA-CASSCF/SI-SO and the LDF-CAHF+CASCI/qlp-icMRCI/SI-SO calculation, the full calculation time including the SI-SO step, as well as the experimental energies obtained by luminescence and the CF fit[45] are displayed in Table 3.2.9. We tried to perform multi-state CASPT2 calculations for this system employing the same basis, the same orbitals to be correlated and the same spin-state mixture, but these calculations failed to converge (we performed calculations both without level shift and with a level shift of 10 hartree[32]).

Table 3.2.9. Crystal-field splitting pattern of [Er{N(SiMe$_3$)$_2$}$_3$] for LDF-CAHF+CASCI/SI-SO, SA-CASSCF/SI-SO and LDF-CAHF+CASCI/quasi-local projected icMRCI (qlp-icMRCI)/SI-SO level of theory and their comparison with experimental values obtained by luminescence and the CF fit to magnetic data and the computation time for the full calculation including the SI-SO step. 7 closed (spatially closest to the central ion) + 7 active orbitals were correlated in the qlp-icMRCI calculation. 35 quartet and 20 doublet states were calculated in the ab initio calculations and mixed in the SI-SO step. RMSD: Root mean square deviation. Energies are given in cm^{-1}.

Doublet	LDF-CAHF	CASSCF	qlp-icMRCI	Exptl. CF energy[a]	CF fit energy[a]
1	0.00	0.00	0.00	0	0
2	107.53	111.98	129.89	110	111
3	191.11	199.12	212.72	190	173
4	262.11	272.83	278.21	245	228
5	320.74	333.26	338.42	327	280
6	424.35	439.86	464.70	455	450
7	480.97	497.96	530.26	-	495
8	517.94	535.95	572.95	-	528
RMSD Expt.	15.99	15.03	21.16	0.00	23.72
Full calculation time	1.98 h[b]	49.41 h[b]	396.97 h[b]	-	-

[a] From reference [38]

[b] Calculations were performed in a parallelized fashion on 8 CPU cores (AMD Opteron™ 6140, 2.6 GHz).

Inclusion of dynamical correlation by the qlp-icMRCI procedure leads to a stretching of the crystal field splitting pattern to larger energies as previously observed in the point charge model. For doublet 2, 3 and 4 this leads to a larger deviation from the experimental CF energy compared to LDF-CAHF+CASCI. For doublet 5 the deviation stays more or less the same and doublet 6 is closer to the experimental energy. We attribute the increased deviation of the lower doublets from the experimental energies (and therefore the resulting increased root mean square deviation/RMSD) to the effect of error compensation for LDF-CAHF+CASCI (and SA-CASSCF), that coincidentally leads to the exceptional agreement between experimental and ab initio values even though the method completely neglects dynamical correlation. The reason why the qlp-icMRCI method yields slightly worse results compared to the experiment is that dynamical correlation is probably not yet fully captured. This is due to the several restrictions in the wave function ansatz, e.g. the restriction to have at most double excitations, and limitations in the basis set size. In the full CI limit (if also relativistic effects, crystal environment effects etc. are treated properly and very large basis sets are used), this deviation should vanish. The increased deviation from the experiment is therefore a measure for the incompleteness of the correlation space and basis set.

The variational inclusion of dynamical correlation by qlp-icMRCI leads to a stretching of the energy level pattern with values that are in reasonable agreement with the experimental

values obtained by luminescence and no large overshooting occurs as it was observed for CASPT2 calculations of lanthanide complexes using small active spaces (seven $4f$-orbitals)[31]. We will investigate a second example where LDF-CAHF+CASCI or SA-CASSCF calculations fail to predict the energy levels properly, namely $\{C(NH_2)_3\}_5[Er(CO_3)_4]\cdot 11H_2O$, to assess if the qlp-icMRCI methodology can improve the results in cases where the neglect of dynamical correlation leads to large deviations from experimental data.

3.2.4.2.3.2. Application to $\{C(NH_2)_3\}_5[Er(CO_3)_4]\cdot 11H_2O$

We applied the described methodology to the single ion magnet (SIM) $\{C(NH_2)_3\}_5[Er(CO_3)_4]\cdot 11H_2O$[45] (Figure 3.2.1).

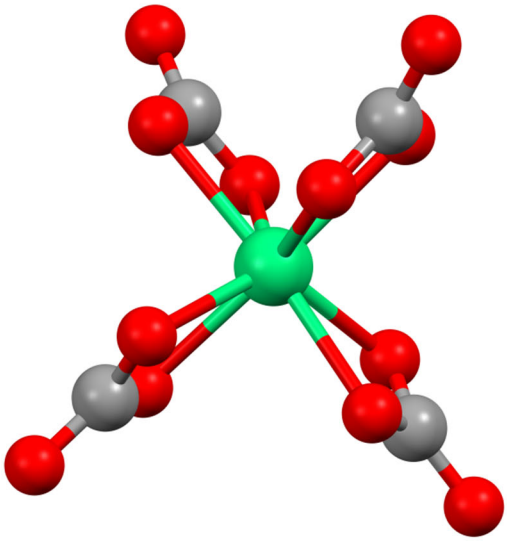

Figure 3.2.1. Crystal structure of the $[Er(CO_3)_4]^{5-}$ anion of $\{C(NH_2)_3\}_5[Er(CO_3)_4]\cdot 11H_2O$. Scheme: Er: green, O: red, C: gray.

We chose this system because of the highly negatively charged anion (-5) that increases the influence of dynamical correlation (because the electrons strongly need to avoid each other) on the crystal field energy levels and because of the availability of extensive experimental data of the crystal field splitting[45]. The high negative charge and large influence of dynamical correlation lead to a large deviation of ab initio calculations considering only static correlation from the experimental energies and makes the system interesting to assess the performance of the methodology described in this work to improve the results. We first performed LDF-CAHF+CASCI/SI-SO calculations to study the influence of the basis set size and the inclusion of different numbers of states of different spin-manifolds with the aim to

determine the smallest (regarding the basis set size and the number of included states) energetically converged LDF-CAHF+CASCI reference for our quasi-local projected icMRCI methodology. The results are shown in Table 3.2.10.

Table 3.2.10. Crystal-field splitting of $\{C(NH_2)_3\}_5[Er(CO_3)_4]\cdot 11H_2O$ for different basis sets and spin-state mixtures included in the CASCI/SI-SO calculation for LDF-CAHF+CASCI/SI-SO level of theory. Basis set numbers: See Table 3.2.2. Energies are given in cm^{-1}.

Doublet	35/112 Basis 1	35/112 Basis 2	35/112 Basis 3	35/20 Basis 3
1	0.00	0.00	0.00	0.00
2	42.49	43.72	44.04	45.07
3	67.61	66.98	68.49	66.68
4	151.42	149.35	153.78	149.93
5	205.41	206.95	208.15	209.55
6	233.36	234.38	236.16	236.93
7	283.07	285.02	285.80	288.39
8	366.04	365.82	370.10	371.34

Since the energy differences between basis 1 and mixture 35/112 and basis 3 and mixture 35/20 are at most approximately 5 cm^{-1}, it is sufficient to use the latter basis and number of states to obtain an energetically converged LDF-CAHF+CASCI reference for reasonable subsequent icMRCI calculations, for which it is crucial to restrict both the basis and the number of states to be calculated and mixed in the SI-SO step. Nevertheless, it should be noted that the convergence of icMRCI with respect to the basis set size is slower than the convergence of LDF-CAHF/CASCI. As a next step, we employed the previously described procedure and localized the LDF-CAHF orbitals obtained using basis 3 and identified 12 closed-shell orbitals to be correlated, i.e. the 5s and 5p orbitals at the erbium site and the 8 lone pairs of the directly coordinating oxygens pointing towards the erbium ion. After making the chosen closed-shell orbitals pseudocanonical within their subspace, a subsequent projected icMRCI calculation was performed for 35 quartet and 20 doublet states. The results, the full calculation time including the SI-SO step and the comparison with the LDF-CAHF+CASCI/SI-SO level of theory as well as the experimental energies obtained by far-infrared spectroscopy (FIR)[45] and the crystal-field fit to magnetic data[45] are shown in Table 3.2.11. We moreover performed SA-CASSCF calculations and also multi-state CASPT2 calculations (using the LDF-CAHF orbitals) for this system employing the same basis, the same orbitals to be correlated and the same spin-state mixture to assess the differences in accuracy and calculation time.

Table 3.2.11. Crystal-field splitting pattern of $\{C(NH_2)_3\}_5[Er(CO_3)_4]\cdot 11H_2O$ for LDF-CAHF+CASCI/SI-SO, SA-CASSCF/SI-SO, LDF-CAHF+CASCI/CASPT2/SI-SO and LDF-CAHF+CASCI/quasi-local projected icMRCI (qlp-icMRCI)/SI-SO level of theory and their comparison with experimental values from FIR-spectroscopy and the CF fit to magnetic data and the computation time for the full calculation including the SI-SO step. 12 closed (spatially closest to the central ion) + 7 active orbitals obtained by LDF-CAHF were correlated in the multi-state CASPT2 and qlp-icMRCI calculations. 35 quartet and 20 doublet states were calculated in the ab initio calculations and mixed in the SI-SO step and basis 3 (see Table 3.2.2) was employed. RMSD: Root mean square deviation. Energies are given in cm^{-1}.

Doublet	LDF-CAHF	CASSCF	CASPT2	qlp-icMRCI	FIR[a]	CF fit[a]
1	0.00	0.00	0.00	0.00	0	0
2	45.07	46.42	66.77	51.32	52	44
3	66.68	68.17	93.29	75.39	84	91
4	149.93	153.27	213.23	169.72	(105)[b]	112
5	209.55	214.20	313.04	249.02	-	280
6	236.93	241.20	354.05	280.97	-	325
7	288.39	294.43	436.01	341.61	-	437
8	371.34	380.27	549.20	435.15	-	462
RMSD FIR data to ab initio	13.19	11.87	12.34	6.11	-	-
Relative error FIR data to ab initio	20.7 %	17.6 %	16.0 %	6.4 %	-	-
RMSD CF fit to ab initio	80.23	76.15	53.87	48.33	-	-
Relative error CF fit to ab initio	30.1 %	28.7 %	17.0 %	18.7 %	-	-
Full calculation time	0.6 h[c]	5.16 h[c]	727.6 h[d]	520.8 h[c]	-	-

[a] From Ref. [45]

[b] Value in brackets because it was not clear if it is a real peak; it was included in the publication because the CF fit resulted in an energy level which is close to the uncertain band (doublet 4 at 112 cm^{-1} in the CF fit). Therefore this value is excluded in the determination of the RMSD and relative error.

[c] Calculations were performed in a parallelized fashion on 8 CPU cores (AMD Opteron™ 6140, 2.6 GHz).

[d] Calculations were performed in a parallelized fashion on 8 CPU cores (Intel® Xeon® CPU X5690, 3.47 GHz).

The inclusion of dynamical correlation by CASPT2 or qlp-icMRCI leads again to a stretching of the crystal field splitting pattern compared to LDF-CAHF+CASCI and SA-CASSCF. CASPT2 overestimates the total splitting and qlp-icMRCI slightly underestimates it compared to the CF fit. The first excited energy level obtained by qlp-icMRCI perfectly coincides with the FIR measurement and the deviation of the second excited state from the FIR measurement is also reduced to less than 9 cm^{-1}. The root mean square deviation (RMSD) and average relative error of the energy levels obtained by multi-state CASPT2 calculation is worse than for qlp-icMRCI for these lowest doublets, for which FIR data are available, and lies in the range of the RMSD and average relative error of the SA-CASSCF and LDF-CAHF calculations. The energy value of doublet 4 obtained by FIR spectroscopy deviates more from the MRCI and CASPT2 calculations including dynamical correlation than from the LDF-CAHF+CASCI or SA-CASSCF calculation including only static correlation, but it is not certain if this is actually a

real peak in the FIR spectrum or a measurement artefact. It was included in the publication by Rechkemmer et al.[45] because a quite close energy value resulted from the CF fit to the magnetic data. The RMSD to the CF fit is reduced by ~40% if dynamical correlation is included by the qlp-icMRCI methodology described in this work and the average relative error of the CF fit to the ab initio energies is also reduced from over 30% to less than 19 %. The CASPT2 calculation leads to similar results regarding the RMSD and relative error to the CF fit. It is expected that this RMSD/average relative error can be further decreased mainly by increasing the basis set size (due to the slow convergence of the dynamical correlation energy with respect to the size of the basis), but also by including more (groups of) closed-shell orbitals to be correlated (for comparison: correlating only 4 closed-shell orbitals at the erbium site resulted in a RMSD of ~55 cm^{-1} and an average relative error of ~21 %). Moreover, the results can be improved by calculating more states to be mixed in the SI-SO step, using a more sophisticated point charge lattice to describe the Madelung potential of the crystal environment and by increasing the quantum mechanically treated part of the system, e.g. by also treating the cation quantum mechanically, and finally by also including higher excitations than double excitations in the wave function ansatz. Furthermore, no overshooting effect, as often observed for CASPT2, occurs, where the (total) CF splitting is often significantly overestimated. The time required for the full calculation including the SI-SO step is significantly less than for multi-state CASPT2, even though the CASPT2 calculation was performed on a faster computer. The qlp-icMRCI method proves to be robust and is able to systematically improve the results in a case, where conventional SA-CASSCF or LDF-CAHF+CASCI calculations fail to reproduce the experiment and where multi-state CASPT2 calculations do not converge or are not feasible.

3.2.5. Conclusions

We have analyzed the influence of dynamical correlation beyond the second order perturbation theory on the energy levels of free lanthanide ions and lanthanide ions surrounded by point charges as model systems for single-molecule magnets. We showed that correcting the non-diagonal elements of the spin-orbit matrix by dynamical correlation for the free Er^{3+} has a large influence (over 250 cm^{-1}) on the energy levels. Moreover, we performed SA-CASSCF, LDF+CAHF+CASCI, multi-state CASPT2 and variational multi-state icMRCI calculations with subsequent spin-orbit coupling for an Er^{3+} ion surrounded by three

point charges. The results showed that the crystal-field splitting of the ground multiplet is significantly less sensitive to the spin-state mixture than the energy levels of the free ion on SA-CASSCF/LDF-CAHF+CASCI level of theory, i.e. less states are required to obtain converged results. Dynamical correlation included by CASPT2 and icMRCI stretched the crystal-field splitting pattern and replacing the diagonal elements of the spin-orbit matrix by CASPT2 energies overestimates the splitting compared to the calculation of the full spin-orbit matrix using icMRCI wave functions. We showed that projected icMRCI calculations can reliably reproduce the crystal field energies obtained by the multi-state MRCI method. Furthermore, we have presented a methodology for the inclusion of dynamical correlation effects beyond the second order perturbation theory in the calculation of crystal-field splittings of molecular lanthanide complexes consisting of the combination of techniques exploiting locality for the closed-shell/active orbital space with projected internally contracted MRCI (qlp-icMRCI). This method makes the variational inclusion of dynamical correlation feasible for molecules, even for large numbers of states to be mixed in the SI-SO step, and does not suffer from the well-known problems of multi-reference perturbation theory (as e.g. intruder state problems or "overshooting effect"). Moreover, it turned out to be more time-efficient than multi-state CASPT2 for the systems (and the chosen active space, basis set etc.) investigated in this work. As any other (MR)CI method, the method is systematically improvable by increasing the basis set size and the number of (groups of) correlated closed-shell orbitals while keeping the minimal size of the active space (seven $4f$-orbitals) . This is especially interesting for systems with large correlation effects, where conventional SA-CASSCF and LDF-CAHF+CASCI calculations, that neglect dynamical correlation, strongly deviate from the experiment. The reference wave functions for the qlp-icMRCI method can be time-efficiently constructed by the LDF-CAHF+CASCI method (Chapter 3.1.3.1). The qlp-icMRCI method is expected to enable a more efficient and accurate treatment of medium sized lanthanide complexes (~20-30 non-hydrogen atoms) than the multi-state CASPT2 method. In order to further increase the applicability to larger systems using large basis sets and large numbers of correlated orbitals, the local restrictions can in principle be extended from the closed space to the virtual space, i.e. restricting the excitations from the closed/active orbitals to localized virtual orbitals which are spatially close to the orbitals from which the electrons are excited. However, a fully local icMRCI method is a non-trivial task to implement but would be highly desirable.

3.3. Enabling fast and accurate ab initio calculation of magnetic exchange in polynuclear lanthanide complexes

Parts of this chapter have already been published in *Phys. Chem. Chem. Phys.,* **21**, 9769-9778 (2019)[46] and have been used for the text/formulation of this thesis. In this work, Prof. Dr. Hans-Joachim Werner helped to implement the local density-fitted multiple-open-shell configuration averaged Hartree-Fock method into Molpro, Dr. Daniel Kats developed the multi-state/many-state PNO-CASPT2 method and helped to fix technical problems regarding its application and Samuel Lenz helped to project the ab initio results onto a pseudospin Hamiltonian and to simulate the EPR spectra.

The development of polynuclear lanthanide complexes exhibiting strong exchange couplings is a promising approach to achieve true magnetic bistability in molecular nanomagnets[110]. Furthermore, magnetic exchange interactions between lanthanide ions have been suggested to allow the design of multiqubit gates in quantum information processing[6,47]. However, exchange interactions involving lanthanide ions are poorly understood. A minimal model is to consider such interactions as isotropic exchange interactions between Kramers doublets in a Lines model-like approach[3,173]. A more accurate and detailed description quickly leads to the necessity for many different parameters[174]. Experimentally, the magnetic coupling between lanthanide ions has been the subject of a number of investigations, where often the magnetic coupling was considered in terms of a highly anisotropic exchange tensor between $\tilde{S} = 1/2$ pseudospins corresponding to the ground Kramers doublets of the ions[47,175,176]. In those studies, supporting non-density-functional-theory (non-DFT) ab initio calculations were always carried out on structures where all paramagnetic lanthanides but one had been replaced with a diamagnetic ion. Only very recently non-DFT calculations on full polynuclear lanthanide complexes have been reported[111,112].

The SA-CASSCF/SI-SO and LDF-CAHF+CASCI/SI-SO methods presented in this thesis (Chapter 3.1.1 and 3.1.3.1) have been used for the calculation of crystal-field levels in mononuclear lanthanide complexes, i.e. complexes containing only one lanthanide ion. For polynuclear systems and the calculation of exchange couplings between the lanthanide ions in these complexes, the active space and therefore the number of CSFs becomes rapidly very large, which renders the CASSCF calculations extremely demanding and frequently impossible.

Moreover, the calculation of exchange couplings between the lanthanide ions often requires the inclusion of dynamical electron correlation by methods such as complete active space perturbation theory of second order (CASPT2)[96,97,158] or multi-reference configuration interaction (MRCI)[33,105], which are computationally even more demanding. Recently, ab initio investigations of the magnetic coupling in $Ce_2(COT)_2$ (COT=1,3,5-cyclooctatetraenide) including dynamical correlation by means of the (variational) difference dedicated configuration interaction (DDCI) method were presented[111,112] and by MRCI including only single excitations in the wave function ansatz (which is called MRCI+CIS by the authors)[112]. However, the resulting configuration space (i.e. the number of configurations used for the description of the wave function) for DDCI (DDCIn, n=2,3) and MRCI+CIS was smaller than the configuration space for CASPT2 assuming the same active space. Moreover, MRCI+CIS neglects two-electron correlations, which require at least double excitations for their description.

In this chapter, we present a complementary approach to calculating magnetic couplings in polynuclear lanthanide complexes, also including dynamical correlation. We present an extension of the LDF-CAHF method to systems with more than one group of open-shell orbitals and its combination with linear scaling *many-state* PNO-CASPT2[29,104] to render this type of calculations feasible.

3.3.1. Local density-fitted multiple-open-shell configuration-averaged Hartree-Fock + CASCI (RASCI) / PNO-CASPT2 / SI-SO

In the following we will define an open-shell as an orbital subset of the active space, e.g. the f-orbitals corresponding to one lanthanide ion. Accordingly, the active space is the union of all open-shells.

The active space for polynuclear systems and often also the number of closed-shell orbitals is very large, which renders the CASSCF orbital optimization and CASCI steps very demanding. In principle, the LDF-CAHF methodology can be applied to systems containing (a closed and) more than one open-shell, for example polynuclear lanthanide or transition metal complexes. However, using the conventional LDF-CAHF methodology to obtain the orbitals for these systems, with a composite active space consisting of the open-shell orbitals

of each ion, leads to inaccurate results for the low-lying states of the molecule. This is because the average energy functional would include “high-energy” ionic states with the paramagnetic ions being in different oxidation states, i.e. configuration state functions with active electrons being transferred from (e.g.) the f-/d-orbitals of one ion to the f-/d-orbitals of another ion. This leads to orbitals which are not appropriate for the description of the low-lying electronic states, where the contribution of charge-transfer between the ions to the wave functions is very small. Therefore we aim to implement an averaging procedure (over all M_S-states of all spin-manifolds) in which the orbitals are optimized with a constant number of active electrons in each shell, also considering the Coulomb and exchange interactions between different shells[51,177]. This is a good approximation for systems where direct “electron hopping” between different open shells is small, e.g. for systems where the paramagnetic ions are separated by bridging closed-shell ligands. We start from the energy functional defined by McWeeny[51]. We define the different open-shells K by the number m_K of spatial orbitals and the number of active electrons n_K in that shell. We furthermore define the (partial) occupation number of shell K as

$$a_K = \frac{n_K}{m_K}. \tag{3.36}$$

The energy functional then has the form (MOS=multiple open shells)

$$E_{av,MOS}^{all\ S/M_S} = 2H_c + 2G_{cc} + 2\sum_K a_K G_{cK} + \sum_K \left(a_K H_K + a_K \frac{(n_K - 1)}{(2m_K - 1)} G_{KK} \right) + \frac{1}{2} \sum_{K,L\ (K \neq L)} a_K a_L G_{KL} + E_{nuc}, \tag{3.37}$$

with

$$G_{cc} = \sum_{i,j} \left(J_{ij} - \frac{1}{2} K_{ij} \right), \tag{3.38}$$

$$G_{cK} = \sum_{t_K,i} \left(J_{t_K i} - \frac{1}{2} K_{t_K i} \right), \tag{3.39}$$

$$G_{KL} = \sum_{t_K,u_L} \left(J_{t_K u_L} - \frac{1}{2} K_{t_K u_L} \right), \tag{3.40}$$

where the index c refers to the closed-shell, $H_c = \sum_i \langle i|\hat{h}|i\rangle$ and $H_K = \sum_{t_K} \langle t_K|\hat{h}|t_K\rangle$ are the one-electron integrals and $J_{rs} = (rr|ss)$ and $K_{rs} = (rs|rs)$ the Coulomb and exchange integrals. The indices i, j run over the closed-shell orbitals, the indices t_K, u_L over the orbitals of open-shells K, L and E_{nuc} is the nuclear repulsion energy.

The first and second term in equation (3.37) represent the energy of the subset of closed-shell electrons in the field of the nuclei, the third term the Coulomb and exchange interactions of the closed-shell with the open shells, the argument of the sum of the fourth term represents the energy of the open shell K electrons alone in the field of the nuclei and the last double summation represents the Coulomb and exchange interactions between different open-shells.

In order to implement a LDF-CAHF code for systems containing more than one open-shell into Molpro[79,80], the energy functional has to be rewritten in a form compatible to the standard ROHF/CAHF equations implemented in Molpro. This form is (using the LCAO-approximation) given by

$$E_{av,MOS}^{all\ S/M_S} = \frac{1}{2}\mathrm{tr}[\mathbf{D}(\mathbf{H} + \mathbf{F}^c)] + \sum_K \frac{1}{2}\mathrm{tr}[\mathbf{D}_K^o \mathbf{F}_K^o] + E_{nuc}, \tag{3.41}$$

with the density and Fock matrices

$$D_{\mu\nu} = 2\sum_i^{n_c} C_{\mu i}\, C_{\nu i} + \sum_K D_{\mu\nu K}^o, \tag{3.42}$$

$$D_{\mu\nu K}^o = a_K \sum_{t_K}^{m_K} C_{\mu t_K}\, C_{\nu t_K}, \tag{3.43}$$

$$F_{\mu\nu}^c = H_{\mu\nu} + \sum_{\rho\sigma} D_{\rho\sigma}\left[(\mu\nu|\rho\sigma) - \frac{1}{2}(\mu\sigma|\rho\nu)\right], \tag{3.44}$$

$$F_{\mu\nu K}^o = \left(\frac{2(n_K - 1)}{a_K(2m_K - 1)} - 1\right)\sum_{\rho\sigma} D_{\rho\sigma K}^o\left[(\mu\nu|\rho\sigma) - \frac{1}{2}(\mu\sigma|\rho\nu)\right]. \tag{3.45}$$

Here, we define a total density $\mathbf{D}$, and a "total" Fock matrix $\mathbf{F}^c$ and in addition a density and Fock matrix for each open-shell. We can further split each of the last two equations into

expressions with separate Coulomb and exchange parts for the "total" and open-shell Fock matrices

$$F^c_{\mu\nu} = H_{\mu\nu} + 2J^c_{\mu\nu} - K^c_{\mu\nu}, \tag{3.46}$$

$$F^o_{\mu\nu K} = 2J^o_{\mu\nu K} - K^o_{\mu\nu K}. \tag{3.47}$$

The Coulomb part is calculated using the scaled density matrices and conventional density-fitting techniques. The more expensive exchange part is calculated using the same local-density fitting approximations as in conventional LDF-HF[69,78] or LDF-CAHF[37]

$$K^c_{\mu\nu} \approx \sum_i^{m_c} \left[\sum_{\bar{B}\in[i]_{fit}} (\bar{B}|\mu i)(\bar{B}|\nu i) \right] + \sum_K \frac{a_K}{2} \sum_{t_K}^{m_K} \left[\sum_{\bar{C}\in[t_K]_{fit}} (\bar{C}|\mu t_K)(\bar{C}|\nu t_K) \right] , \tag{3.48}$$

$$K^o_{\mu\nu K} \approx \left(\frac{(n_K - 1)}{(2m_K - 1)} - \frac{a_K}{2} \right) \sum_{t_K}^{m_K} \left[\sum_{\bar{C}\in[t_K]_{fit}} (\bar{C}|\mu t_K)(\bar{C}|\nu t_K) \right]. \tag{3.49}$$

The indices $\bar{B}$ and $\bar{C}$ denote the Cholesky decomposed local density fitting basis and the indices i/t_K run over localized molecular orbitals (LMOs) obtained by localization within the closed-/open-shell K only. This means we have to perform independent localizations for the closed space and each open-shell. As for the conventional LDF-CAHF method, the calculation of the different exchange matrices using local-density fitting is again the decisive factor which enables the high speed of the *local density-fitted multiple-open-shell configuration averaged Hartree-Fock (LDF-MOS-CAHF)* method. The calculation of the individual $K^o_{\mu\nu K}$ matrices requires negligible additional effort in the LDF implementation, since only contributions of different subsets of orbitals are scaled and stored separately.

The Lagrangian for the constrained minimization of the energy functional, including the appropriate intra- and intershell orthonormality conditions, is given as

$$L = E_{av,MOS}^{all\ S/M_S} - 2\sum_{i}^{m_c}\epsilon_i\left[\langle i|i\rangle - 1\right] - \sum_{K}\sum_{t_K}^{m_K}\epsilon_{t_K}[\langle t_K|t_K\rangle - 1] \\ - 2\sum_{K}\sum_{i}^{m_c}\sum_{t_K}^{m_K}\epsilon_{t_K i}\langle t_K|i\rangle - \sum_{K}\sum_{L\neq K}\sum_{t_K}^{m_K}\sum_{u_L}^{m_L}\epsilon_{t_K u_L}\langle t_K|u_L\rangle. \tag{3.50}$$

Here, we have assumed that the closed- and open-shell orbitals of all shells are canonical (the matrices of the Lagrangian multipliers are assumed to be diagonal).

Note that the scalar-product in the orthonormality constraints satisfies the following relation

$$\langle t_k|u_L\rangle = \langle u_L|t_K\rangle^*, \tag{3.51}$$

or, if real orbitals are used,

$$\langle t_k|u_L\rangle = \langle u_L|t_K\rangle, \tag{3.52}$$

which implies

$$\epsilon_{t_K u_L} = \epsilon_{u_L t_K}{}^*, \tag{3.53}$$

or, if real orbitals are used,

$$\epsilon_{t_K u_L} = \epsilon_{u_L t_K}. \tag{3.54}$$

Taking the derivatives with respect to the MO-coefficients of the closed and all open shells therefore (assuming real orbitals) leads to

$$\left(\frac{\partial L}{\partial C_{\mu i}}\right) = 4[\mathbf{F}^c\mathbf{C}]_{\mu i} - 4[\mathbf{SC}]_{\mu i}\epsilon_i - 2\sum_{K}\sum_{t}^{m_K}[\mathbf{SC}]_{\mu t_K}\epsilon_{t_K i}, \tag{3.55}$$

$$\left(\frac{\partial L}{\partial C_{\mu t_K}}\right) = 2a_K[(\mathbf{F}^c + \mathbf{F}_K^o)\mathbf{C}]_{\mu t_K} - 2[\mathbf{SC}]_{\mu t_K}\epsilon_{t_K} - 2\sum_{i}^{m_c}[\mathbf{SC}]_{\mu i}\epsilon_{t_K i} \\ - 2\sum_{L\neq K}\sum_{u_L}^{m_L}[\mathbf{SC}]_{\mu u_L}\epsilon_{t_K u_L}. \tag{3.56}$$

Setting these derivatives to zero, the variational conditions become:

$$2[\mathbf{F}^c\mathbf{C}]_{\mu i} = 2[\mathbf{SC}]_{\mu i}\epsilon_i + \sum_K \sum_t^{m_K} [\mathbf{SC}]_{\mu t_K}\epsilon_{t_K i}, \tag{3.57}$$

$$a_K[(\mathbf{F}^c + \mathbf{F}_K^o)\mathbf{C}]_{\mu t_K} = [\mathbf{SC}]_{\mu t_K}\epsilon_{t_K} + \sum_i^{m_c} [\mathbf{SC}]_{\mu i}\epsilon_{t_K i} + \sum_{L\neq K} \sum_{u_L}^{m_L} [\mathbf{SC}]_{\mu u_L}\epsilon_{t_K u_L}. \tag{3.58}$$

The Fock matrices in the MO basis are defined as

$$\mathbf{f}^c = \mathbf{C}^\dagger \mathbf{F}^c \mathbf{C}\,, \tag{3.59}$$

$$\mathbf{f}_K^o = \mathbf{C}^\dagger \mathbf{F}_K^o \mathbf{C}. \tag{3.60}$$

The variational conditions are now multiplied from the left with $\mathbf{C}^\dagger$ and become

$$f_{ij}^c = \epsilon_i \delta_{ij}, \tag{3.61}$$

$$2f_{t_K i}^c = \epsilon_{t_K i}, \tag{3.62}$$

$$f_{ai}^c = 0, \tag{3.63}$$

$$a_k(\mathbf{f}^c + \mathbf{f}_K^o)_{i t_K} = \epsilon_{t_K i}, \tag{3.64}$$

$$a_K(\mathbf{f}^c + \mathbf{f}_K^o)_{u_K t_K} = \epsilon_{t_K}\delta_{u_K t_K}, \tag{3.65}$$

$$a_K(\mathbf{f}^c + \mathbf{f}_K^o)_{u_L t_K} = \epsilon_{t_K u_L}, \tag{3.66}$$

$$a_K(\mathbf{f}^c + \mathbf{f}_K^o)_{a t_K} = 0. \tag{3.67}$$

There indices a, b refer to virtual orbitals. Equating the two expressions for $\epsilon_{t_K i}$ and exploiting that the matrices $\mathbf{f}^c$and $\mathbf{f}_K^o$ are symmetric yields

$$((2-a_K)\mathbf{f}^c - a_K\mathbf{f}_K^o)_{it_K} = 0. \tag{3.68}$$

Exchanging the indices for different open shells in the equation (3.66) yields

$$a_L(\mathbf{f}^c + \mathbf{f}_L^o)_{t_K u_L} = \epsilon_{u_L t_K}. \tag{3.69}$$

Using equation (3.54) implies

$$a_K(\mathbf{f}^c + \mathbf{f}_K^o)_{u_L t_K} = a_L(\mathbf{f}^c + \mathbf{f}_L^o)_{t_K u_L}. \tag{3.70}$$

Now, again, exploitation of the symmetry of the fock matrices yields

$$(a_K - a_L)\mathbf{f}^c + a_K\mathbf{f}_K^o - a_L\mathbf{f}_L^o = 0. \tag{3.71}$$

Furthermore, canonical virtual orbitals can be defined by imposing the condition

$$\left(\mathbf{f}^c + \sum_{\boldsymbol{N}} \mathbf{f}_N^o\right)_{ab} = \epsilon_a \delta_{ab}. \tag{3.72}$$

This set of variational conditions can be summarized in a large effective matrix eigenvalue equation

$$\begin{aligned}\bar{\mathbf{f}} &= \begin{pmatrix} \mathbf{f}^c & (2-a_K)\mathbf{f}^c - a_K\mathbf{f}_K^o & (2-a_L)\mathbf{f}^c - a_L\mathbf{f}_L^o & \cdots & \mathbf{f}^c \\ (2-a_K)\mathbf{f}^c - a_K\mathbf{f}_K^o & a_K(\mathbf{f}^c + \mathbf{f}_K^o) & (a_K - a_L)\mathbf{f}^c + a_K\mathbf{f}_K^o - a_L\mathbf{f}_L^o & \cdots & a_K(\mathbf{f}^c + \mathbf{f}_K^o) \\ (2-a_L)\mathbf{f}^c - a_L\mathbf{f}_L^o & (a_K - a_L)\mathbf{f}^c + a_K\mathbf{f}_K^o - a_L\mathbf{f}_L^o & a_L(\mathbf{f}^c + \mathbf{f}_L^o) & \cdots & a_L(\mathbf{f}^c + \mathbf{f}_L^o) \\ \vdots & \vdots & \vdots & \ddots & \vdots \\ \mathbf{f}^c & a_K(\mathbf{f}^c + \mathbf{f}_K^o) & a_L(\mathbf{f}^c + \mathbf{f}_L^o) & \cdots & \mathbf{f}^c + \sum_{\boldsymbol{N}} \mathbf{f}_N^o \end{pmatrix} \\ &= \begin{pmatrix} \mathbf{e}^c & \mathbf{0} & \mathbf{0} & \mathbf{0} & \mathbf{0} \\ \mathbf{0} & \mathbf{e}_K^o & \mathbf{0} & \mathbf{0} & \mathbf{0} \\ \mathbf{0} & \mathbf{0} & \mathbf{e}_L^o & \mathbf{0} & \mathbf{0} \\ \mathbf{0} & \mathbf{0} & \mathbf{0} & \ddots & \vdots \\ \mathbf{0} & \mathbf{0} & \mathbf{0} & \cdots & \mathbf{e}^v \end{pmatrix}. \end{aligned} \tag{3.73}$$

Comparing with conventional LDF-CAHF theory[37], we have an additional row/column for each additional open-shell. Furthermore, $\mathbf{e}^c$, $\mathbf{e}_K^o$, $\mathbf{e}_L^o$,… and $\mathbf{e}^v$ are diagonal Lagrangian multiplier matrices for the closed-shell, open-shell K,L,… and the virtual space. The effective Fock matrix $\bar{\mathbf{f}}$ is built and diagonalized in each iteration of the LDF-MOS-CAHF code until self-consistency is achieved. The resulting orbitals are equivalent to those from a state-averaged restricted active space self-consistent field (RASSCF) calculation with the same fixed number of electrons in the same orbital sets, averaging over as many states as there are possible

configuration-state functions and all possible total spins, giving the states weighting factors accounting for their corresponding M_S-degeneracy.

In the case of degeneracies or near-degeneracies some attention has to be paid, because the LDF-MOS-CAHF calculations might not converge if the Lagrange multipliers of different open shells $\mathbf{e}_K^o$,$\mathbf{e}_L^o$,… become (nearly) identical. As a simple example, one can consider the hydrogen molecule H_2 in the dissociation limit. The minimum energy for this case would be achieved if the two open-shells would be localized 1s-hydrogen orbitals at the two H-atoms. During the LDF-MOS-CAHF iterations, both active space Lagrange multipliers $\mathbf{e}_{1s}^o$ would be identical. This (near) equality allows the diagonalizer to randomly mix the corresponding localized orbitals. However, in contrast to conventional (CA)HF theory, this mixing of (near) degenerate orbitals (belonging to different open-shells) increases the energy und yields again non-zero off-diagonal-elements. Therefore, oscillations can occur and lead to convergence problems. A remedy for this problem is the use of level-shifts. If the diagonal elements of $\bar{\mathbf{f}}$ corresponding to different open-shells are shifted by different energies, the mixing of different (quasi-) degenerate solutions by the diagonalizer is inhibited without changing the converged orbitals or total energy. Therefore, level-shifts are a simple way to account for potential convergence problems. Moreover, as the electronic structure of the systems of interest is quite complicated, it is necessary to prepare a reasonable initial guess for the SCF iterations, which can be constructed out of separate calculations of the open-shell ions and ligands using the MERGE directive in Molpro as described in Chapter 3.1.3.2 or using the atomic valence active space (AVAS) technique[178].

The orbitals obtained by LDF-MOS-CAHF can be used in a single subsequent complete active space configuration interaction (CASCI) or restricted active space configuration interaction (RASCI) step to obtain many-electron wave functions, as well as in subsequent methods which account for dynamical electron correlation. In RASCI calculations, electron transfer between the different shells can be “activated” again, i.e. one can allow for a limited number of electrons to be transferred between the shells, although the orbitals are not optimized for this case. Nevertheless, the description of the exchange interaction between the shells can be improved by allowing this “electron hopping”. However, in many cases, a significant part of the exchange interaction between open-shell ions is mediated via a charge transfer

mechanism involving closed-shell orbitals of diamagnetic ligands between the ions, i.e. superexchange.

To account for this kind of superexchange in ab initio calculations of polynuclear complexes, configuration-state functions which are constructed by exciting electrons out of the bridging closed-shell ligand orbitals into the open-shell orbitals of the ions and into the virtual orbitals have to be included into the wave function. Technically speaking this means that the corresponding closed-shell orbitals have to be correlated in subsequent multireference (dynamical) correlation methods such as CASPT2 or MRCI. As the number of CSFs strongly increases with the number of closed-shell and active orbitals (i.e. the number of open-shells), this quickly becomes computationally demanding and is often not feasible.

In order to cope with large inactive spaces, local multi-reference correlation methods can be employed. In these methods, the number of CSFs is strongly reduced compared to non-local correlation methods. This is achieved by only including CSFs in the wave function which are constructed by excitations from localized closed-shell/active orbitals to spatially close localized active/virtual orbitals. A local multi-state PNO-CASPT2 (MS-PNO-CASPT2) version based on the PNO-CASPT2 implementation[29] (described in the theory section of this thesis) and the original multi-state CASPT2 method of Finley et. al.[27] has recently been implemented in Molpro[104]. However, for lanthanides the standard MS-CASPT2 method is known to introduce a substantial artificial splitting of exact degeneracies of free lanthanide ions[16] and therefore is not applicable for calculations of small crystal-field splittings. Instead, we use a *many-state* PNO-CASPT2 method, which neglects the state mixing and can be efficiently applied to hundreds of states of large molecules. In this method, many of the expensive integral transformations have to be done only once for all states of a given spin-manifold, since all the states share the same orbitals. More details on this method can be found elsewhere[104]. The individual state-specific PNO-CASPT2 energies are then used as diagonal elements in the spin-orbit matrix, which is finally diagonalized.

3.3.2. Benchmark applications of LDF-MOS-CAHF + CASCI (RASCI) / PNO-CASPT2 / SI-SO

In order to investigate the equivalence of the LDF-MOS-CAHF orbitals with orbitals obtained by RASSCF/CASSCF, we performed calculations of a Cu^{2+} dimer in the gas phase in the dissociation limit with a distance of 300 Å between the Cu^{2+} ions. Moreover, we chose the molecule $[hqH_2][Yb_2(hq)_4(NO_3)_3]\cdot MeOH$ (hqH=8-hydroxyquinoline, Figure 3.3.1) as test system for our method because the exchange coupling was recently investigated in a combined theoretical and experimental approach[47].

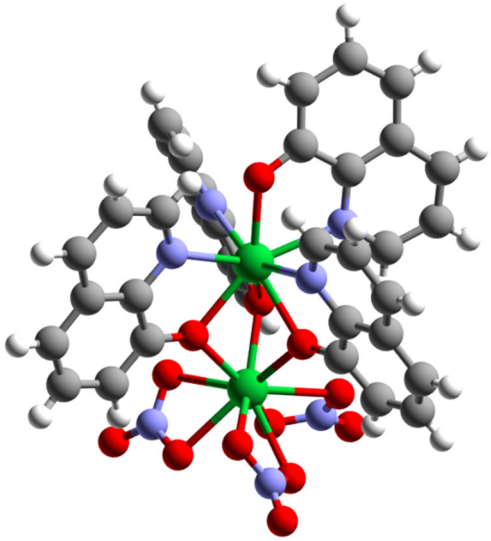

Figure 3.3.1. Crystal structure of $[Yb_2(hq)_4(NO_3)_3]^-$ with the two different coordination pockets. The lower metal site is the "NO_3 pocket" and the upper metal site is the "hq pocket". Scheme: Yb: green, O: red, N: blue, C: gray, H: white. Figure reproduced from *Phys. Chem. Chem. Phys.,* **21**, 9769-9778 (2019)[46] (Figure 1) with permission from The Royal Society of Chemistry.

In this work, the authors concluded that the superexchange is the dominant part of the magnetic interaction between the two Yb^{3+} ions and large compared to the magnetic dipolar interaction. The compound was investigated and characterized by magnetic (SQUID) measurements, electron paramagnetic resonance (EPR), inelastic neutron scattering (INS), far infrared (FIR) spectroscopy and CASSCF/SI-SO calculations using MOLCAS[127]. The authors used a pseudospin Hamiltonian $\widehat{H}$ to model the EPR spectra, written in the basis of the ground Kramers doublet of each ion, i.e. using a pseudospin $S = 1/2$ formalism. In this Hamiltonian, the anisotropic exchange interaction is described by a generalized exchange

tensor $\bar{\bar{J}}$ and the Zeeman interaction is described by effective g-tensors $\bar{\bar{g}}^{hq}$ and $\bar{\bar{g}}^{NO_3}$ for each coordination site (hq pocket and NO_3 pocket)

$$\widehat{H} = -2\vec{\hat{S}}_{hq}\bar{\bar{J}}\vec{\hat{S}}_{NO_3} + \mu_B\left(\vec{\hat{S}}_{hq}\bar{\bar{g}}^{hq} + \vec{\hat{S}}_{NO_3}\bar{\bar{g}}^{NO_3}\right)\vec{B}. \tag{3.74}$$

The CASSCF-SO calculations were performed with the method of diamagnetic substitution, i.e. one Yb^{3+} was replaced by diamagnetic Y^{3+}, either for the hq pocket or for the NO_3 pocket. The local g-tensors of each pocket were calculated and used to calculate the magnetic dipolar interaction tensor $\bar{\bar{J}}^{dip}$ for the exchange interaction of the lowest Kramers doublets of both Yb^{3+} by a point dipole approximation, assigning effective magnetic moments to each Yb^{3+} ion. The experimental EPR spectra could only be very poorly reproduced using only the magnetic dipolar tensor and it was concluded that the remaining part to the full coupling tensor $\bar{\bar{J}}$ must be of superexchange type. Fitting the superexchange part of the magnetic coupling to the experimental EPR spectra resulted in a good agreement.

3.1.3.2.1. Computational details

This section covers the technical details of the calculations of the systems investigated in this work, the Cu^{2+}-Cu^{2+} dimer and $[hqH_2][Yb_2(hq)_4(NO_3)_3]\cdot MeOH$. All calculations were carried out with the Molpro[79,80] suite of ab initio programs. For the calculation of the Cu^{2+}-Cu^{2+} dimer, the def2-TZVPP[147] basis set was employed and the corresponding def2-TZVPP-JKFIT[149] basis set for density fitting. The active space was chosen as 18 electrons in 10 (5 for each Cu^{2+}) 3d-type orbitals, i.e. CAS(18,10). The starting orbitals for both the LDF-MOS-CAHF and density-fitted CASSCF (DF-CASSCF) calculations were prepared from separate LDF-CAHF calculations of the single Cu^{2+} using the MERGE procedure. The active orbitals for each ion were assigned to different open-shells in LDF-MOS-CAHF and level shifts of -0.1 and -2.0 hartree were applied to the different open-shells. The energy was converged to 10^{-9} hartree. The full Breit-Pauli SO-operator[95] was used for the SO-coupling step. 25 triplet and 25 singlet roots were calculated in DF-CASSCF/CASCI and mixed in the SI-SO step. The calculations of $[hqH_2][Yb_2(hq)_4(NO_3)_3]\cdot MeOH$ were performed using the geometry of the isolated metal complex as reported from X-ray diffraction (XRD)[176], including only the $[Yb_2(hq)_4(NO_3)_3]^-$ anion in the ab initio calculation. The 28 electron pseudopotential ECP28MWB[114] was employed for Yb and the corresponding ECP-SO operator[114] for the SO-coupling step. The

def2-TZVPP[119] basis set was used for Yb and the def2-TZVPP-JKFIT/def2-AQZVPP-JKFIT[119] basis set for density fitting in LDF-(MOS-)CAHF/PNO-CASPT2. For Y (in the calculations using diamagnetic substitution), the pseudopotential ECP28MWB[130] and the def2-TZVPP[130] basis set were employed, and the def2-TZVPP-JKFIT[149] and def2-TZVPP-MP2FIT[148] basis sets for density fitting. For the remaining elements, the cc-pVDZ[120–122] basis set and the corresponding cc-pVDZ-JKFIT[76] and cc-pVDZ-MP2FIT[150] basis sets for density fitting were used. The active space was chosen as 26 electrons in 14 (7 for each Yb^{3+}) 4f-type orbitals for the full complex and 13 electrons in 7 4f-type orbitals for the calculations using diamagnetic substitution, i.e. CAS(26,14) and CAS(13,7). The starting orbitals for the LDF-(MOS-)CAHF calculations were prepared from separate LDF-CAHF calculations of the ligand and the Yb^{3+} ion(s) using the MERGE procedure. The active orbitals for each ion were assigned to different open-shells in LDF-MOS-CAHF and level shifts of -0.1 and -2.0 hartree were applied to the different open-shells and a level-shift of -4.0 hartree to the closed-shell space. To ensure that the same minimum is obtained for different level shifts, we tested different level shifts and exchanged the level shifts for the different open-shells. The results were identical in all cases. The energy was converged to 10^{-8} hartree.

For the calculations using the method of diamagnetic substitution, 7 doublet states of Yb were calculated and mixed in the SI-SO step. For the calculations of the full complex, 49 triplet and 49 singlet roots were calculated with CASCI and many-state PNO-CASPT2 and mixed in the SI-SO step and a level shift of 1.0 hartree was applied for many-state PNO-CASPT2. In the PNO-CASPT2 calculations Molpro's default local approximations[179] have been used, i.e., the PAO domains have been augmented by two shells of neighbouring atoms (IEXT=2 option in Molpro), and an occupation threshold of 10^{-8} together with a completeness criterion of 0.997 was used for PNOs. In all calculations employing the many-state PNO-CASPT2 method, the diagonal elements of the SO-matrix (in the LDF-(MOS-)CAHF+CASCI basis) are replaced by many-state PNO-CASPT2 energies. Stability tests were performed, i.e. the local approximations in LDF-MOS-CAHF were turned off and all possible roots (91 triplets and 105 singlets) were calculated and mixed in the LDF-MOS-CAHF+CASCI/SI-SO calculations of the full complex and the influence on the exchange spectrum of the lowest four states was investigated. The energies changed by less than 0.01 cm^{-1}, i.e. the energies of the lowest

four states are robust against these changes. The calculation of the g-tensors of the lowest Kramers doublets by projection onto a pseudospin were performed using SINGLE_ANISO[18].

3.3.2.2. Results for $(Cu^{2+})_2$

Cu^{2+} is a d^9 system with a spin of $S = 1/2$. The spins of the two ions can be coupled to a total spin of $S = 1$ (triplet) and $S = 0$ (singlet). We used the five 3d-orbitals of each ion in each active space for the LDF-MOS-CAHF method. The average energy resulting from this calculation must be compared with a DF-CASSCF calculation using the same active space consisting out of 5+5=10 3d-orbitals of the two ions, but without hopping of electrons between the two open-shells and an appropriate state-averaging. The large distance between the two ions makes the contribution of CSFs with electrons hopping from one Cu^{2+} to the other vanish in the CASSCF calculation, therefore no restrictions (i.e. RASSCF) are necessary. There are 5 possible CSFs for each Cu^{2+}. If no hopping between the two ions' open-shells is allowed, there are 5x5=25 CSFs for the triplet state and 5x5=25 CSFs for the singlet state of the dimer. Therefore we performed a DF-CASSCF calculation averaging over 25 triplet and 25 singlet states, giving the triplet states a weighting factor of 3 and the singlets a weighting factor of 1 to account for their M_S-degeneracy. The resulting orbitals from both calculations were used in subsequent CASCI calculations to calculate 25 triplet and 25 singlet states, build the spin-orbit matrix and diagonalize it. The spin-orbit energies are shown in Table 3.3.1. They are numerically identical, which proves the equivalence of the orbitals and thus validates the LDF-MOS-CAHF method.

Table 3.3.1. Spin-orbit energies of the Cu^{2+}-Cu^{2+} dimer at a distance of 300 Å for a CASCI/SI-SO calculation using state-averaged DF-CASSCF orbitals and LDF-MOS-CAHF orbitals. 25 triplet and 25 singlet roots were mixed in the SI-SO step. The states in each row are numerically degenerate. Energies are given in cm^{-1}.

Spin-orbit state	DF-CASSCF	LDF-MOS-CAHF
1-36	0.00	0.00
37-84	2060.69	2060.69
85-100	4121.38	4121.38

3.3.2.3. Results for $[hqH_2][Yb_2(hq)_4(NO_3)_3]\cdot MeOH$

Calculations using the method of diamagnetic substitution have certain drawbacks. On the one hand, replacing one Yb^{3+} by diamagnetic Y^{3+} changes the crystal field for the other Yb^{3+} to some (unknown) extent. On the other hand, no estimation of the exchange coupling from

an ab initio point of view can be given, as the method considers only one open-shell ion. Moreover, the method neglects the influence of dynamical correlation on the crystal field splitting on each Yb site. We wanted to overcome these drawbacks with our method. Therefore, we first performed conventional LDF-CAHF+CASCI(/PNO-CASPT2)/SI-SO calculations using the method of diamagnetic substitution on the system and then we used the LDF-MOS-CAHF+CASCI/(PNO-CASPT2/)SI-SO methodology to calculate the full molecule without replacing one of the two Yb^{3+} by Y^{3+} to investigate the influence of the substitution on the crystal field and moreover estimate the through-bond superexchange interaction between the two Yb^{3+} by correlating the closed-shell orbitals using many-state PNO-CASPT2. Table 3.3.2 and 3.3.3. show the crystal field energies for each coordination site for the method of diamagnetic substitution using conventional LDF-CAHF+CASCI/SI-SO without and with inclusion of dynamical correlation by many-state PNO-CASPT2.

Table 3.3.2. Crystal field energies of $[Yb_2(hq)_4(NO_3)_3]^-$ using the method of diamagnetic substitution obtained by LDF-CAHF+CASCI/SI-SO and their comparison with the CASSCF/SI-SO energies from *J. Am. Chem. Soc.* **140** (7), 2504–2513 (2018)[47]. Energies are given in cm^{-1}.

Kramers doublet	NO_3 pocket	hq pocket	NO_3 pocket ref. [47]	hq pocket ref. [47]
1	0.00	0.00	0.0	0.0
2	41.79	150.72	40.3	160.4
3	126.20	334.75	132.5	347.6
4	228.73	572.93	241.8	597.5

The energies (Table 3.3.2) are in good agreement with the energies obtained by CASSCF/SI-SO[47].

Table 3.3.3. Crystal field energies of $[Yb_2(hq)_4(NO_3)_3]^-$ using the method of diamagnetic substitution obtained by LDF-CAHF+CASCI/PNO-CASPT2/SI-SO. Energies are given in cm^{-1}.

Kramers doublet	NO_3 pocket	hq pocket
1	0.00	0.00
2	45.69	160.25
3	144.77	363.93
4	263.29	617.78

Inclusion of dynamical correlation by PNO-CASPT2 shifts the energies to values that are larger by about 10% (Table 3.3.3).

The energies for the full LDF-MOS-CAHF/SI-SO calculation without and with dynamical correlation, mixing 49 triplet and 49 singlet states in the SI-SO-step, are shown in Table 3.3.4.

Table 3.3.4. LDF-MOS-CAHF+CASCI/SI-SO energies (up to state 20) and calculation times for $[Yb_2(hq)_4(NO_3)_3]^-$ with and without dynamical correlation included by PNO-CASPT2. 49 triplet and 49 singlets were mixed in the SI-SO step. Energies are given in cm^{-1}.

State	LDF-MOS-CAHF+CASCI	+PNO-CASPT2
1	0.00	0.00
2	0.04	0.33
3	0.05	1.39
4	0.08	1.85
5	42.01	64.25
6	42.06	64.49
7	42.08	64.79
8	42.10	65.38
9	127.28	193.40
10	127.44	193.65
11	127.47	195.52
12	127.50	195.65
13	150.56	201.60
14	150.57	202.10
15	150.58	202.56
16	150.61	202.71
17	193.36	267.38
18	193.41	267.70
19	193.43	268.02
20	193.46	268.30
Calculation time		
LDF-MOS-CAHF	1.4 h [a]	
CASCI	0.7 h [b]	
PNO-CASPT2		82.9 h [b]

[a] Calculations were performed in a parallelized fashion on 26 CPU cores (Intel® Xeon® CPU E5-2690 v4, 2.60 GHz).
[b] Calculations were performed in a parallelized fashion on 4 CPU cores (Intel® Xeon® CPU E5-2690 v4, 2.60 GHz). The calculation time shown is the overall time for 49 triplet and 49 singlet states.

Table 3.3.4 shows that the energy spectrum obtained by LDF-MOS-CAHF+CASCI/SI-SO without dynamical correlation is approximately a combination of the energies resulting from the individual LDF-CAHF+CASCI/SI-SO calculations of each Yb site using the method of diamagnetic substitution. This results from the fact that both Yb^{3+} are only weakly coupled. The energy spectrum contains the excitation energies for each Yb site (states 5-12 correspond to the NO_3 pocket and states 13-16 to the hq pocket) as well as collective excitations, resulting from the crystal-field excitations of both Yb sites at the same time (states 17-20). The lowest four states are only very weakly split up to 0.08 cm^{-1}, i.e. the calculated exchange coupling of the lowest Kramers doublets of each Yb^{3+} ion is very small at LDF-MOS-CAHF+CASCI/SI-SO level of theory. This can be attributed to the fact that the

description of the superexchange interaction requires the correlation of the closed-shell orbitals of the bridging oxygens, which is achieved by PNO-CASPT2. Inclusion of dynamical correlation by PNO-CASPT2 significantly increases the exchange splitting of the lowest 4 states up to 1.85 cm^{-1}. Moreover, the higher crystal field states are also shifted to substantially higher energies compared to the LDF-MOS-CAHF+CASCI/SI-SO calculation without dynamical correlation and also compared to the LDF-CAHF+CASCI/PNO-CASPT2/SI-SO calculations using the method of diamagnetic substitution. Importantly, this finding indicates a non-negligible change of the crystal-field potential for each Yb site when the full complex is calculated including dynamical correlation, without replacing one Yb^{3+} by Y^{3+}. States 5-8 now perfectly fit to the experimental FIR transition[47] at 64 cm^{-1}. The calculation time is only ~2h for LDF-MOS-CAHF+CASCI and the inclusion of dynamical correlation requires approximately 1.7 days for each total spin-state manifold, i.e. 1.7 days for 49 triplet states and 1.7 days for 49 singlet states, which is very fast given the large active space and the large number of states. The PNO-CASPT2 calculations for each spin state manifold can be performed in parallel if needed to decrease the required computation time, when the calculation of more spin state manifolds is required, e.g. in complexes with lanthanide ions having a larger total spin.

Our ab initio calculations confirm[47] the existence of a significant superexchange interaction in $[hqH_2][Yb_2(hq)_4(NO_3)_3]\cdot$ MeOH. However, it has to be noted that the LDF-MOS-CAHF+CASCI/PNO-CASPT2/SI-SO calculations do not include the magnetic dipolar interaction between the two Yb^{3+} sites at this point. To include this interaction into the ab initio calculations, spin-spin integrals are required, which are computationally very demanding and which are currently not implemented in Molpro. In order to simulate the EPR spectra using the results obtained by ab initio methods, a projection onto a pseudospin Hamiltonian, i.e. a superexchange (se) coupling tensor $\bar{\bar{J}}^{se}$ is necessary. For this purpose, we fitted the elements $\bar{\bar{J}}^{se}$ of the pseudospin Hamiltonian

$$\hat{H} = -2\vec{\hat{S}}_{hq}\bar{\bar{J}}^{se}\vec{\hat{S}}_{NO_3}, \tag{3.75}$$

in its diagonal reference frame by reproducing the lowest four ab initio energies with the eigenvalues of this Hamiltonian (with a deviation of less than 0.01 cm^{-1}).

The tensor (in diagonal form) was found to be (in cm^{-1})

$$\bar{\bar{J}}^{se} = \begin{pmatrix} 0.065 & 0 & 0 \\ 0 & 0.395 & 0 \\ 0 & 0 & 1.455 \end{pmatrix}. \tag{3.76}$$

To estimate the magnitude of the magnetic dipolar interaction, we also used the point dipole approximation used by Giansiracusa et al.[47]. The dipolar coupling tensor used in a Hamiltonian of the type (3.75) is calculated by

$$\bar{\bar{J}}^{dip} = -\frac{1}{2}\frac{\mu_o \mu_B^2}{4\pi r^3}\left(\bar{\bar{g}}^{hq} \cdot \bar{\bar{g}}^{NO_3} - 3\left(\bar{\bar{g}}^{hq} \cdot \vec{R}\right) \cdot \left(\vec{R}^T \cdot \bar{\bar{g}}^{NO_3}\right)\right) \tag{3.77}$$

where r is the distance between the two Yb^{3+} ions and $\vec{R}$ is the directional unit vector between the two ions (and μ_o the magnetic constant of vacuum).

The dipolar coupling tensor in the coordinate frame of the xyz-file used for the ab initio calculations was calculated to be (in cm^{-1})

$$\bar{\bar{J}}^{dip} = \begin{pmatrix} -0.100 & 0.109 & 0.017 \\ 0.026 & -0.020 & 0.014 \\ 0.004 & -0.001 & -0.035 \end{pmatrix}. \tag{3.78}$$

To obtain the full exchange tensor $\bar{\bar{J}}$, $\bar{\bar{J}}^{dip}$ and $\bar{\bar{J}}^{se}$ have to be added. However, they are given in different reference frames. The only remaining unknown is the relative orientation of the diagonal reference frame of the superexchange tensor $\bar{\bar{J}}^{se}$ to the xyz-file frame. This lack of information results from projecting the energies of only the lowest four ab initio states onto the pseudospin Hamiltonian. To add the tensors to obtain $\bar{\bar{J}}$, we have to rotate one of the tensors to the reference frame of the other, e.g.

$$\bar{\bar{J}} = \bar{\bar{J}}^{dip} + \bar{\bar{R}}\bar{\bar{J}}^{se}\bar{\bar{R}}^T \tag{3.79}$$

with the rotation matrix $\bar{\bar{R}}$ given by

$$\begin{aligned}\bar{\bar{R}} &= \bar{\bar{R}}_1\bar{\bar{R}}_2\bar{\bar{R}}_3 \\ &= \begin{pmatrix} \cos(\gamma) & \sin(\gamma) & 0 \\ -\sin(\gamma) & \cos(\gamma) & 0 \\ 0 & 0 & 1 \end{pmatrix} \cdot \begin{pmatrix} \cos(\beta) & 0 & -\sin(\beta) \\ 0 & 1 & 0 \\ \sin(\beta) & 0 & \cos(\beta) \end{pmatrix} \begin{pmatrix} \cos(\alpha) & \sin(\alpha) & 0 \\ -\sin(\alpha) & \cos(\alpha) & 0 \\ 0 & 0 & 1 \end{pmatrix}, \end{aligned} \quad (3.80)$$

where α, β and γ are the unknown Euler angles for the rotation between the two reference frames.

In order to determine the three unknown Euler angles, we fitted the experimental Q-band EPR spectrum[47] employing Hamiltonian (3.74) with the exchange coupling tensor given by equation (3.79) using EasySpin[180]. The local g-tensors for each Yb site were obtained by LDF-CAHF+CASCI/PNO-CASPT2/SI-SO calculations using the method of diamagnetic substitution. They were calculated (in the reference frame of the xyz-file used for the ab initio calculations) to be

$$\bar{\bar{g}}^{hq} = \begin{pmatrix} 3.536 & -2.875 & -0.504 \\ -2.875 & 3.417 & -2.343 \\ -0.504 & -0.002 & 1.910 \end{pmatrix}, \quad (3.81)$$

$$\bar{\bar{g}}^{NO_3} = \begin{pmatrix} 4.269 & -0.304 & -0.617 \\ -0.304 & 2.037 & -1.435 \\ -0.617 & -1.435 & 3.234 \end{pmatrix}. \quad (3.82)$$

The best fit angles were determined to be $\alpha = 128.9°$, $\beta = 77.5°$ and $\gamma = 53.8°$. The resulting total exchange tensor in its diagonal form $\bar{\bar{J}}^{diag}$ is given as (in cm^{-1})

$$\bar{\bar{J}}^{diag} = \begin{pmatrix} 0.042 & 0 & 0 \\ 0 & 0.370 & 0 \\ 0 & 0 & 1.350 \end{pmatrix}. \quad (3.83)$$

Therefore, the inclusion of the magnetic dipolar coupling reduces the eigenvalues of $\bar{\bar{J}}$ compared to $\bar{\bar{J}}^{se}$ from equation (3.76).

Diagonalization of the Hamiltonian (3.75) using the g-tensors (3.81) and (3.82) and the $\bar{\bar{J}}$ resulting from equation (3.79) and the fitted Euler angles yields the exchange split energies for the system including both superexchange and magnetic dipolar interaction (in our effective tensor approximation (3.77)). The energy of state 3 and 4 are shifted to lower values (1.72 cm^{-1} and 1.31 cm^{-1}) when the magnetic dipolar coupling is included, while state 2 remains approximately at the same energy. This is shown in Figure 3.3.2.

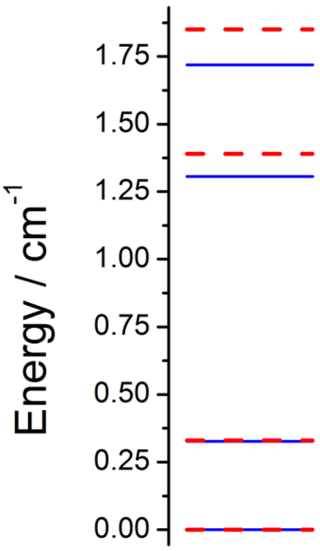

Figure 3.3.2. Calculated zero-field exchange spectrum without (red) and with (blue) the inclusion of magnetic dipolar coupling. Figure reproduced from *Phys. Chem. Chem. Phys.,* **21**, 9769-9778 (2019)[46] (Figure 2) with permission from the Royal Society of Chemistry.

The obtained full coupling tensor $\bar{\bar{J}}$ was then also used to simulate the X- and S-band spectra and compare them with the experimental spectra. Figures 3.3.3 and 3.3.4 show the simulated and measured Q-band and X-band spectra.

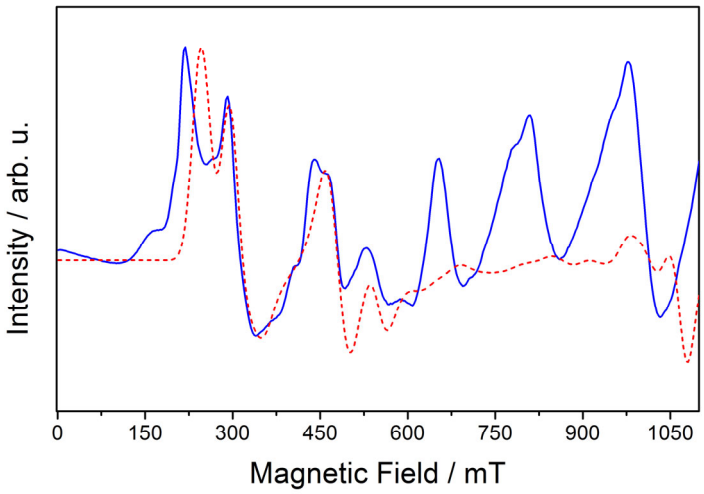

Figure 3.3.3. Simulated (red) and measured (blue) Q-band EPR spectrum using the exchange matrix (3.77) and the Euler angles fitted to the Q-band spectrum. Figure reproduced from *Phys. Chem. Chem. Phys.,* **21**, 9769-9778 (2019)[46] (Figure 3) with permission from The Royal Society of Chemistry.

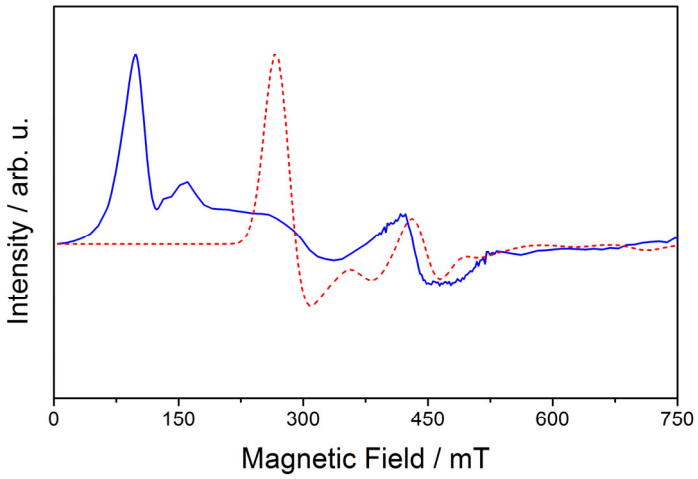

Figure 3.3.4. Simulated (red) and measured (blue) X-band EPR spectrum using the exchange matrix (3.77) and the Euler angles fitted to the Q-band spectrum. Figure reproduced from *Phys. Chem. Chem. Phys.,* **21**, 9769-9778 (2019)[46] (Figure 4) with permission from The Royal Society of Chemistry.

For the Q-band spectrum, the agreement of the measurement and the simulation is good and resonance lines are simulated at most positions where they occur in the experiment. The experimental and simulated X-band spectra show coinciding resonances for magnetic fields larger than ~375 mT, but the agreement for lower magnetic fields (< 375 mT) is worse than for Q-band. The first experimental X-band resonance in low-field is shifted by ~150 mT to high-field in the simulation.

The simulated S-band spectrum did not show any resonance peaks, in contrast to the experiment. This is most probably due to the fact that our calculations slightly overestimate

the exchange coupling. Therefore, the agreement of the spectra is better for Q-band than for X-band (and for S-band), as the measured energy differences decrease in this order. This demonstrates that the accuracy of the presented method is of the order of tenths of reciprocal centimeters. The accuracy of the method can be systematically improved using the general strategies of, e.g., improving the dynamical correlation description, increasing the basis set size, including the effect of the Madelung potential of the crystal environment by surrounding point charges and tightening the thresholds for the local approximations in the PNO-CASPT2 calculations.

3.3.3. Conclusions

We have presented a new method for the computationally efficient ab initio calculation of exchange couplings in polynuclear lanthanide complexes including dynamical correlation. The method is based on an extension of the local-density-fitted configuration-averaged Hartree-Fock (LDF-CAHF) method to systems with multiple open shells (LDF-MOS-CAHF) to determine the state-averaged orbitals for the polynuclear systems, which are then used in a subsequent CASCI or RASCI calculation to determine the multiconfigurational wave functions. Dynamical correlation is included by using the LDF-MOS-CAHF orbitals for a many-state PNO-CASPT2 calculation, where the exploitation of locality renders the calculation feasible and fast. We applied the method to the system $[hqH_2][Yb_2(hq)_4(NO_3)_3]\cdot MeOH$ and were able to reasonably reproduce the experimental EPR spectra by projecting the ab initio results onto a pseudospin Hamiltonian with anisotropic exchange coupling. The presented method can be used as a tool to guide the research in understanding the correlations between the exchange coupling and the chemical structure, with the long-term goal of chemically engineering the exchange coupling in molecular nanomagnets with improved magnetic properties. In the future, we plan to apply the method also to polynuclear lanthanide complexes with a higher total magnetic moment, e.g. complexes containing erbium and dysprosium, as well as to polynuclear transition metal complexes.

4. Summary and outlook

The aim of this thesis was to improve the speed and the accuracy of ab initio calculations of lanthanide based single-molecule magnets (SMMs) and also enable the efficient calculation of the electronic structure of polynuclear systems. Moreover, the developed methods should be applied to new systems, including transition metal and actinide based systems, to assess the performance of the new methods and to use electronic structure calculations of the chosen systems to enhance the understanding of these systems and to be able to rationally improve them for device applications.

In the first part of this thesis, the *local density-fitted configuration averaged Hartree-Fock (LDF-CAHF)* method[37] was developed, which represents an alternative to the time-consuming orbital optimization of the *state-averaged complete active space self-consistent field (SA-CASSCF)* method which is conventionally used in the field of single-molecule magnets. The LDF-CAHF method determines the SA-CASSCF-equivalent orbitals by solving restricted open-shell Hartee-Fock-(ROHF-)like equations and speeds up the calculations by employing local density-fitting approximations. It was shown to achieve a speedup factor of up to 26 compared to SA-CASSCF for the tested benchmark system $Er[N(SiMe_3)_2]_3$[37–39]. This speedup factor is expected to increase for larger systems, because of the near-linear scaling of the LDF-CAHF method with the molecular size, and it will also increase if more CPU cores are used, due to the efficiently parallelized implementation of the method. The accuracy of the energies using the orbitals obtained by this method is the same as for SA-CASSCF. In order to demonstrate the applicability of the method to different systems, it was furthermore applied to a dysprosium and a terbium complex ($[(HBpz_3)_2Ln(\mu\text{-}CA)Ln(HBpz_3)_2]\cdot 2CH_2Cl_2$ (Ln=Dy,Tb; $HBpz_3^-$=hydrotris(pyrazol-1-yl)borate, CA^{2-}=chloranilate))[40] as well as to a uranium complex ($[U^{III}\{SiMe_2NPh\}_3\text{-tacn})(OPPh_3)]$ (tacn=1,4,7,-triazacyclononane))[41]. While the results for the Dy and Tb complex agreed well with the experimental findings, the situation for the uranium complex was more involved. In this case, the LDF-CAHF orbitals were used as an initial guess for a subsequent SA-CASSCF calculation with a larger active space. Therefore, it could be shown, that the LDF-CAHF methodology can be efficiently applied in combination with other methods. However, the results for the uranium complex, even for the calculations with an increased size of the active space, were in worse agreement with the experiment than for the abovementioned

lanthanide complexes, which indicates, that more advanced ab initio methods including dynamical correlation should be applied to this system. In the next step, the LDF-CAHF method was applied to transition metal based systems, in particular to calculate the energy spectrum of a mononuclear chromium complex ($[Cr(ddpd)_2](BF_4)_3$ (ddpd=*N,N'*-dimethyl-*N,N'*-dipyridine-2,6-diamine))[42] and to calculate the exchange coupling in a dinuclear radical-bridged cobalt complex ($(K\text{-}18\text{-}c\text{-}6)_3[\{(H_2L_B^{2-})Co^{II}\}_2(\mu\text{-}L_B^{3\bullet-})]$ (H_4L_B = 1,2,4,5-tetrakis(methanesulfonamido)benzene))[43]. In case of the chromium complex, the LDF-CAHF orbitals were used as a starting point for a subsequent SA-CASSCF calculation with another set of more diffuse metal based d-orbitals included in the active space (double shell effect) and the closed-shell orbitals were kept frozen at the LDF-CAHF level of theory. The double shell effect cannot be properly accounted for in (LDF-)CAHF calculations, because increasing the active space by this additional (more diffuse) set of d-orbitals in a (LDF-)CAHF calculation would lead to the inclusion of *high-energy states* (see section 3.1.2), i.e. states, where the diffuse d-orbitals have large contributions to the wave function, into the state-averaging. This would yield state-averaged orbitals which are inappropriate for the description of the energetically low-lying molecular states of interest. Finally, dynamical correlation was included in the form of complete active space perturbation theory of second order using pair natural orbitals (PNO-CASPT2)[29]. The results, especially the zero-field splitting (ZFS) of the ground (spin) multiplet, were in good agreement with the experimental findings, demonstrating the efficient applicability of the LDF-CAHF methodology (in suitable combination with other methods) to transition metal based systems. The application of the methodology to the dinuclear radical-bridged cobalt complex employed the method of diamagnetic substitution, i.e., one cobalt was replaced by diamagnetic zinc and bridging ligand was reduced to its closed-shell form in the first step of the calculation. This is necessary, because the LDF-CAHF method would include "high-energy states" in the averaging where several electrons are transferred between the cobalt ions and also between the radical and the cobalt ions, which would yield inappropriate orbitals for the low-lying states of the molecule (an extension of the LDF-CAHF method was developed to solve this problem at a later stage of this thesis). The LDF-CAHF method was employed, with an active space consisting out of the five d-orbitals of the remaining cobalt, to obtain starting orbitals for a subsequent SA-CASSCF calculation, where the ligand was oxidized to its radical form again. In this calculation, the active space was extended by two π- and two π^*-orbitals of the

ligand and the closed-shell orbitals were kept frozen on LDF-CAHF level of theory. In the last step, dynamical correlation was included by CASPT2. Projection of the ab initio energy levels onto a pseudospin Hamiltonian including an isotropic exchange coupling term between the cobalt and the radical (and ZFS and Zeeman interaction terms) yielded an antiferromagnetic coupling, which is in agreement with the experimental findings. The magnitude of the ZFS term in this pseudospin Hamiltonian also agrees very well with the experimental value (ab initio D_{Co} = –110 cm^{-1}; experimental D_{Co} = –115 cm^{-1}). However, the exchange coupling constant obtained by ab initio calculations (J_{Co-Rad} = +174 cm^{-1}) was less than half of what was found experimentally (J_{Co-Rad} = +440 cm^{-1}). This is most probably partly due to an insufficient description of dynamical correlation and the crystal environment of the molecule, but also to a large amount attributed to the fact that diamagnetic substitution of one cobalt by zinc is a very rough approximation for such large exchange couplings, as the coupling of each cobalt to the radical might influence the coupling of the other cobalt to the radical. In order to cope with this problem, it is necessary to calculate the full molecule, which is a non-trivial task because of the large required active space and the numerous roots which need to be calculated for the SO-coupling step.

In conclusion, the LDF-CAHF method can be employed to efficiently calculate crystal-field splittings in lanthanide complexes with the same accuracy as the SA-CASSCF method, but with significantly reduced time requirements. Therefore, it would be interesting to extend the application of this method to fields, where the fast calculation of many geometries is necessary, e.g. in the calculation of spin-phonon couplings, or in the development of blueprints for molecular nanomagnets, where many different structures have to be tested/screened. Moreover, due to the high speed of the method for spatially extended systems, it could be applied to investigate the interaction of molecular nanomagnets with (closed-shell) surfaces, by cutting out a large finite part of the surface for the calculation. The method can also be applied to actinide containing and transition metal based systems. However, for these systems, it should be used in combination with other methods including static and dynamical correlation, to obtain accurate results. For example, it can be used as a starting point for an SA-CASSCF calculation with an extended active space and subsequent CASPT2 or multireference configuration interaction (MRCI) calculations. If the closed-shell orbitals in the SA-CASSCF calculations (with an extended active space) following the LDF-

CAHF calculations are kept frozen at the LDF-CAHF level of theory, the speedup factor (compared to SA-CASSCF without preceding LDF-CAHF) is similar to that for lanthanides, since only optimizing the active orbitals is usually very fast (unless very large active spaces are used).

In the second part of this thesis, the accuracy of conventional calculations of crystal-field splittings in lanthanide complexes was improved beyond CASPT2 level of theory by enabling MRCI calculations for these systems. This was achieved by developing the quasi-local projected internally contracted MRCI (qlp-icMRCI) method[44]. Conventional multi-state icMRCI calculations of lanthanide complexes are usually not feasible because of the enormous central processing unit (CPU) time and random access memory (RAM) requirements, which arise due to the large number of closed-shell orbitals to be correlated and the large number of states to be calculated simultaneously. The qlp-icMRCI method circumvents these problems by reducing the number of correlated closed-shell orbitals by localizing them and only correlating the local orbitals which are at or spatially closest to the central lanthanide ion and by using a projection operator technique to calculate the desired states sequentially instead of simultaneously. The method was applied to the single-ion magnet $\{C(NH_2)_3\}_5[Er(CO_3)_4]\cdot 11H_2O$[44,45]. The resulting energies were closer to the experimental values (obtained by far infrared spectroscopy) and the calculation time was significantly shorter than for the corresponding multi-state CASPT2 calculations of the system. The qlp-icMRCI method is expected to enable a more efficient and accurate treatment of medium sized (20-30 non-hydrogen atoms) complexes than multi-state CASPT2. To extend its applicability to larger systems, an extension of the local restrictions to the virtual space, to obtain a fully local (projected) icMRCI method, as well as the use of local density-fitting approximations to speed up the calculations, would be highly desirable. Moreover, it would be interesting to apply this method to actinide and transition metal based systems in the future.

The third and last part of the thesis dealt with the fast and accurate calculation of anisotropic exchange couplings in polynuclear lanthanide complexes. This is a very challenging task, due to the large active spaces, the large number of required states or the necessity to include dynamical correlation into the calculations. This problem was tackled by extending the LDF-CAHF method to systems with more than one group of open-shell orbitals

(e.g. at different metal atoms), yielding the LDF-MOS-CAHF (MOS: multiple open-shells) method, and combining it with linear-scaling many-state PNO-CASPT2 to efficiently include dynamical correlation into the calculations of polynuclear systems[46]. The new methodology was applied to the asymmetric dinuclear complex $[hqH_2][Yb_2(hq)_4(NO_3)_3]\cdot MeOH$ (hqH=8-hydroxyquinoline) which was intensively studied experimentally[47]. The ab initio calculations confirmed the existence of a significant superexchange interaction between the two Yb^{3+} ions and the results were projected onto a pseudospin Hamiltonian with anisotropic exchange coupling. The experimental electron paramagnetic resonance (EPR) spectra could be reasonably reproduced by employing this Hamiltonian. In the future, it would be interesting to apply this method to systems with more than two open-shell ions or to radical-bridged systems, as well as to polynuclear transition metal complexes. Moreover, the combination of the LDF-MOS-CAHF method with other subsequent (correlation) methods for systems with large active spaces, such as density matrix renormalization group (DMRG) and full configuration interaction quantum Monte Carlo (FCIQMC), would be an interesting topic to investigate, because this could speed up the (CAS)CI step after the orbitals have been determined by LDF-MOS-CAHF .

Concluding this thesis, new methodologies for the fast and accurate ab initio simulation of the energy spectrum and (magnetic) properties of mono- and polynuclear metal complexes were developed. They main idea of these methods was to circumvent the time-demanding orbital optimization of state-averaged CASSCF by implicitly including the state-averaging in the Hartree-Fock like equations of LDF-CAHF, which can be solved much faster than SA-CASSCF equations, for both systems with one (LDF-CAHF) or multiple (LDF-MOS-CAHF) open-shells. Moreover, (quasi-)local approximations and density fitting were exploited wherever possible, not only for the LDF-(MOS)-CAHF method, but also for the subsequent correlation methods (qlp-icMRCI and PNO-CASPT2). The memory requirements and the scaling of icMRCI with respect to the (large) number of states to be calculated could be reduced by employing a projection operator technique for the sequential instead of simultaneous calculation of the states (qlp-icMRCI). The methods were applied to well-known, as well as new systems and were able to improve both the speed and accuracy of conventional calculations, especially for large systems. Moreover, they were successfully combined with already existing approaches, i.e. the LDF-CAHF methodology was employed as basis for

subsequent SA-CASSCF calculations with an extended active space (and the closed-shell orbitals frozen at the LDF-CAHF level of theory) in order to avoid the time-demanding SA-CASSCF orbital optimization for the closed-shell orbitals. It was shown that there is no universal method for all tasks and that a reasonable combination of different methods and a sophisticated pre-analysis of the investigated systems are necessary to reduce the time requirements for the simulations and to achieve a high accuracy, especially for large systems. The efficient applicability of the LDF-(MOS-)CAHF methodology to spatially extended systems renders it interesting for the study of, e.g., single molecule magnets and molecular quantum bits on surfaces, in order to investigate the influence of the deposition on a surface (for device applications) on their properties. The methods are potentially interesting for all fields in which the calculation of the energy, the magnetic and spectroscopic (e.g. transition moments) properties of several (excited) states of materials based on open-shell transition metal, lanthanide and actinide ions are required. To further increase the accuracy of the calculations of the energy spectrum and other properties of mononuclear metal complexes beyond (qlp-ic)MRCI, the LDF-CAHF orbitals could be used for subsequent multireference coupled-cluster (MRCC) methods. Combining these MRCC methods with local approximations (i.e. local MRCC) could yield an efficient method for highly accurate electronic structure calculations. Furthermore, using the LDF-MOS-CAHF orbitals obtained for polynuclear open-shell systems in subsequent correlation methods suitable for the treatment of large active spaces, such as DMRG and FCIQMC, could replace SA-CASSCF calculations employing the method of diamagnetic substitution. To conclude, it can be said that due to the increasing computational power of modern computers and the efficient approximations in quantum chemical calculations, ab initio methods are expected to become an indispensable tool for the rational improvement of (even very large) metal complexes for device applications and to complement experimental investigations.

5. References

1. R. Sessoli, D. Gatteschi, A. Caneschi, and M. A. Novak, “Magnetic bistability in a metal-ion cluster,” Nature **365**, 141–143 (1993).
2. T. Lis, “Preparation, structure, and magnetic properties of a dodecanuclear mixed-valence manganese carboxylate,” Acta Crystallogr B Struct Sci **36**, 2042–2046 (1980).
3. R. Layfield and M. Murugesu, eds., *Lanthanides and actinides in molecular magnetism* (Wiley-VCH, Weinheim, op. 2015).
4. S. G. McAdams, A.-M. Ariciu, A. K. Kostopoulos, J. P.S. Walsh, and F. Tuna, “Molecular single-ion magnets based on lanthanides and actinides. Design considerations and new advances in the context of quantum technologies,” Coord. Chem. Rev. **346**, 216–239 (2017).
5. K. S. Pedersen, A.-M. Ariciu, S. McAdams, H. Weihe, J. Bendix, F. Tuna, and S. Piligkos, “Toward Molecular 4f Single-Ion Magnet Qubits,” J. Am. Chem. Soc. **138**, 5801–5804 (2016).
6. D. Aguilà, L. A. Barrios, V. Velasco, O. Roubeau, A. Repollés, P. J. Alonso, J. Sesé, S. J. Teat, F. Luis, and G. Aromí, “Heterodimetallic LnLn' lanthanide complexes. Toward a chemical design of two-qubit molecular spin quantum gates,” J. Am. Chem. Soc. **136**, 14215–14222 (2014).
7. N. Ishikawa, M. Sugita, T. Ishikawa, S.-Y. Koshihara, and Y. Kaizu, “Lanthanide double-decker complexes functioning as magnets at the single-molecular level,” J. Am. Chem. Soc. **125**, 8694–8695 (2003).
8. D. N. Woodruff, R. E. P. Winpenny, and R. A. Layfield, “Lanthanide single-molecule magnets,” Chem. Rev. **113**, 5110–5148 (2013).
9. R. Sessoli and A. K. Powell, “Strategies towards single molecule magnets based on lanthanide ions,” Coord. Chem. Rev. **253**, 2328–2341 (2009).
10. C. A. P. Goodwin, F. Ortu, D. Reta, N. F. Chilton, and D. P. Mills, “Molecular magnetic hysteresis at 60 kelvin in dysprosocenium,” Nature **548**, 439–442 (2017).
11. F.-S. Guo, B. M. Day, Y.-C. Chen, M.-L. Tong, A. Mansikkamäki, and R. A. Layfield, “Magnetic hysteresis up to 80 kelvin in a dysprosium metallocene single-molecule magnet,” Science **362**, 1400–1403 (2018).
12. M. Urdampilleta, S. Klyatskaya, J.-P. Cleuziou, M. Ruben, and W. Wernsdorfer, “Supramolecular spin valves,” Nat. Mater. **10**, 502–506 (2011).
13. K. Katoh, H. Isshiki, T. Komeda, and M. Yamashita, “Molecular spintronics based on single-molecule magnets composed of multiple-decker phthalocyaninato terbium(III) complex,” Chem. Asian J. **7**, 1154–1169 (2012).
14. R. Vincent, S. Klyatskaya, M. Ruben, W. Wernsdorfer, and F. Balestro, “Electronic read-out of a single nuclear spin using a molecular spin transistor,” Nature **488**, 357–360 (2012).
15. S. Thiele, F. Balestro, R. Ballou, S. Klyatskaya, M. Ruben, and W. Wernsdorfer, “Electrically driven nuclear spin resonance in single-molecule magnets,” Science **344**, 1135–1138 (2014).

16. L. Ungur, “Introduction to the electronic structure, luminescence, and magnetism of lanthanides,” in *Lanthanide-based multifunctional materials*. *From OLEDs to SIMs*, edited by M. Ramos-Silva and P. Martin-Ramos (Elsevier, Amsterdam, Netherlands, 2018), pp. 1–58.
17. F.-S. Guo, B. M. Day, Y.-C. Chen, M.-L. Tong, A. Mansikkamäki, and R. A. Layfield, “A Dysprosium Metallocene Single-Molecule Magnet Functioning at the Axial Limit,” Angew. Chem. Int. Ed. **56**, 11445–11449 (2017).
18. L. F. Chibotaru and L. Ungur, “Ab initio calculation of anisotropic magnetic properties of complexes. I. Unique definition of pseudospin Hamiltonians and their derivation,” J. Chem. Phys. **137**, 64112 (2012).
19. L. F. Chibotaru, L. Ungur, and A. Soncini, “The origin of nonmagnetic Kramers doublets in the ground state of dysprosium triangles: evidence for a toroidal magnetic moment,” Angew. Chem. Int. Ed. **47**, 4126–4129 (2008).
20. K. Bernot, J. Luzon, L. Bogani, M. Etienne, C. Sangregorio, M. Shanmugam, A. Caneschi, R. Sessoli, and D. Gatteschi, “Magnetic anisotropy of dysprosium(III) in a low-symmetry environment: a theoretical and experimental investigation,” J. Am. Chem. Soc. **131**, 5573–5579 (2009).
21. G. Cucinotta, M. Perfetti, J. Luzon, M. Etienne, P.-E. Car, A. Caneschi, G. Calvez, K. Bernot, and R. Sessoli, “Magnetic anisotropy in a dysprosium/DOTA single-molecule magnet: beyond simple magneto-structural correlations,” Angew. Chem. Int. Ed. **51**, 1606–1610 (2012).
22. M.-E. Boulon, G. Cucinotta, J. Luzon, C. Degl'Innocenti, M. Perfetti, K. Bernot, G. Calvez, A. Caneschi, and R. Sessoli, “Magnetic anisotropy and spin-parity effect along the series of lanthanide complexes with DOTA,” Angew. Chem. Int. Ed. **52**, 350–354 (2013).
23. M.-E. Boulon, G. Cucinotta, S.-S. Liu, S.-D. Jiang, L. Ungur, L. F. Chibotaru, S. Gao, and R. Sessoli, “Angular-resolved magnetometry beyond triclinic crystals: out-of-equilibrium studies of Cp*ErCOT single-molecule magnet,” Chem. Eur. J. **19**, 13726–13731 (2013).
24. J. Jung, O. Cador, K. Bernot, F. Pointillart, J. Luzon, and B. Le Guennic, “Influence of the supramolecular architecture on the magnetic properties of a Dy(III) single-molecule magnet: an ab initio investigation,” Beilstein J. Nanotechnol. **5**, 2267–2274 (2014).
25. R. Marx, F. Moro, M. Dörfel, L. Ungur, M. Waters, S. D. Jiang, M. Orlita, J. Taylor, W. Frey, L. F. Chibotaru, and J. van Slageren, “Spectroscopic determination of crystal field splittings in lanthanide double deckers,” Chem. Sci. **5**, 3287 (2014).
26. Y.-S. Ding, N. F. Chilton, R. E. P. Winpenny, and Y.-Z. Zheng, “On Approaching the Limit of Molecular Magnetic Anisotropy: A Near-Perfect Pentagonal Bipyramidal Dysprosium(III) Single-Molecule Magnet,” Angew. Chem. Int. Ed. **55**, 16071–16074 (2016).
27. J. Finley, P.-Å. Malmqvist, B. O. Roos, and L. Serrano-Andrés, “The multi-state CASPT2 method,” Chem. Phys. Lett. **288**, 299–306 (1998).
28. G. Ghigo, B. O. Roos, and P.-Å. Malmqvist, “A modified definition of the zeroth-order Hamiltonian in multiconfigurational perturbation theory (CASPT2),” Chem. Phys. Lett. **396**, 142–149 (2004).

29. F. Menezes, D. Kats, and H.-J. Werner, “Local complete active space second-order perturbation theory using pair natural orbitals (PNO-CASPT2),” J. Chem. Phys. **145**, 124115 (2016).
30. T. Shiozaki and H.-J. Werner, “Communication: Second-order multireference perturbation theory with explicit correlation: CASPT2-F12,” J. Chem. Phys. **133**, 141103 (2010).
31. L. Ungur and L. F. Chibotaru, “Ab Initio Crystal Field for Lanthanides,” Chem. Eur. J. **23**, 3708–3718 (2017).
32. B. O. Roos and K. Andersson, “Multiconfigurational perturbation theory with level shift — the Cr2 potential revisited,” Chem. Phys. Lett. **245**, 215–223 (1995).
33. H. -J. Werner and P. J. Knowles, “An Efficient Internally Contracted Multiconfiguration Reference CI Method,” J. Chem. Phys. **89**, 5803–5814 (1988).
34. H.-J. Werner and P. J. Knowles, “A comparison of variational and non-variational internally contracted multiconfiguration-reference configuration interaction calculations,” Theoret. Chim. Acta **78**, 175–187 (1991).
35. P. J. Knowles and H.-J. Werner, “Internally contracted multiconfiguration-reference configuration interaction calculations for excited states,” Theoret. Chim. Acta **84**, 95–103 (1992).
36. A. Mitrushchenkov and H.-J. Werner, “Calculation of transition moments between internally contracted MRCI wave functions with non-orthogonal orbitals,” Mol. Phys. **105**, 1239–1249 (2007).
37. P. P. Hallmen, C. Köppl, G. Rauhut, H. Stoll, and J. van Slageren, “Fast and reliable ab initio calculation of crystal field splittings in lanthanide complexes,” J. Chem. Phys. **147**, 164101 (2017).
38. S. Jank, H.-D. Amberger, and N.M. Edelstein, “Electronic structures of highly-symmetrical compounds of f elements,” Spectrochim. Acta Mol. Biomol. Spectrosc. **54**, 1645–1650 (1998).
39. P. Zhang, L. Zhang, C. Wang, S. Xue, S.-Y. Lin, and J. Tang, “Equatorially coordinated lanthanide single ion magnets,” J. Am. Chem. Soc. **136**, 4484–4487 (2014).
40. P. Zhang, M. Perfetti, M. Kern, P. P. Hallmen, L. Ungur, S. Lenz, M. R. Ringenberg, W. Frey, H. Stoll, G. Rauhut, and J. van Slageren, “Exchange coupling and single molecule magnetism in redox-active tetraoxolene-bridged dilanthanide complexes,” Chem. Sci. **9**, 1221–1230 (2018).
41. L. C. J. Pereira, J. T. Coutinho, M. Perfetti, J. J. Baldoví, M. A. Antunes, P. P. Hallmen, H. Bamberger, I. Crasse, M. Orlita, M. Almeida, and J. van Slageren, “Spectroscopic Determination of the Electronic Structure of a Uranium Single-Ion Magnet,” Chem. Eur. J. **25**, 1758–1766 (2018).
42. S. Lenz, H. Bamberger, P. P. Hallmen, Y. Thiebes, S. Otto, K. Heinze, and J. van Slageren, “Chromium(iii)-based potential molecular quantum bits with long coherence times,” Phys. Chem. Chem. Phys. **21**, 6976–6983 (2019).

43. U. Albold, H. Bamberger, P. P. Hallmen, J. van Slageren, and B. Sarkar, “Strong exchange couplings drastically slow down magnetization relaxation in an air-stable cobalt(II)-radical single-molecule magnet,” Angew. Chem. Int. Ed. (2019).
44. P. P. Hallmen, G. Rauhut, H. Stoll, A. O. Mitrushchenkov, and J. van Slageren, “Crystal Field Splittings in Lanthanide Complexes: Inclusion of Correlation Effects beyond Second Order Perturbation Theory,” J. Chem. Theory. Comput. **14**, 3998–4009 (2018).
45. Y. Rechkemmer, J. E. Fischer, R. Marx, M. Dörfel, P. Neugebauer, S. Horvath, M. Gysler, T. Brock-Nannestad, W. Frey, M. F. Reid, and J. van Slageren, “Comprehensive Spectroscopic Determination of the Crystal Field Splitting in an Erbium Single-Ion Magnet,” J. Am. Chem. Soc. **137**, 13114–13120 (2015).
46. P. P. Hallmen, H.-J. Werner, D. Kats, S. Lenz, G. Rauhut, H. Stoll, and J. van Slageren, “Toward fast and accurate ab initio calculation of magnetic exchange in polynuclear lanthanide complexes,” Phys. Chem. Chem. Phys. **125**, 8694 (2019).
47. M. J. Giansiracusa, E. Moreno-Pineda, R. Hussain, R. Marx, M. Martínez Prada, P. Neugebauer, S. Al-Badran, D. Collison, F. Tuna, J. van Slageren, S. Carretta, T. Guidi, E. J. L. McInnes, R. E. P. Winpenny, and N. F. Chilton, “Measurement of magnetic exchange in asymmetric lanthanide dimetallics. Towards a transferable theoretical framework,” J. Am. Chem. Soc. **140**, 2504–2513 (2018).
48. T. Helgaker, J. Olsen, and P. Jorgensen, *Molecular Electronic-Structure Theory* (Wiley-Blackwell, Chichester, 2013).
49. P. W. Atkins and R. Friedman, *Molecular quantum mechanics*, 5. ed. (Oxford Univ. Press, Oxford, 2011).
50. F. Jensen, *Introduction to computational chemistry*, 3rd edition (Wiley, Chichester, West Sussex, Hoboken, NJ, Oxford, 2017).
51. R. McWeeny, *Methods of molecular quantum mechanics*, 2. ed., 2. print (Academ. Press, London, 1996).
52. H. -J. Werner and A. Köhn, *Lecture Notes: Advanced Methods in Quantum Chemistry* (University of Stuttgart, 2014-2015).
53. M. Born and R. Oppenheimer, “Zur Quantentheorie der Molekeln,” Ann. Phys. **389**, 457–484 (1927).
54. M. Reiher and A. Wolf, *Relativistic quantum chemistry*. *The fundamental theory of molecular science*, 1. ed. (2009).
55. K. G. Dyall and K. Faegri, *Introduction to relativistic quantum chemistry* (Oxford Univ. Press, Oxford u.a., 2007).
56. M. Reiher, “Douglas–Kroll–Hess Theory. A relativistic electrons-only theory for chemistry,” Theor. Chem. Acc. **116**, 241–252 (2006).
57. M. Douglas and N. M. Kroll, “Quantum electrodynamical corrections to the fine structure of helium,” Annals of Physics **82**, 89–155 (1974).
58. L. L. Foldy and S. A. Wouthuysen, “On the Dirac Theory of Spin 1/2 Particles and Its Non-Relativistic Limit,” Phys. Rev. **78**, 29–36 (1950).

59. M. Reiher and A. Wolf, “Exact decoupling of the Dirac Hamiltonian. II. The generalized Douglas-Kroll-Hess transformation up to arbitrary order,” J. Chem. Phys. **121**, 10945–10956 (2004).
60. P. A. M. Dirac, “The Quantum Theory of the Electron,” Proceedings of the Royal Society A: Mathematical, Physical and Engineering Sciences **117**, 610–624 (1928).
61. Hess, “Applicability of the no-pair equation with free-particle projection operators to atomic and molecular structure calculations,” Physical review. A, General physics **32**, 756–763 (1985).
62. M. Dolg and X. Cao, “Relativistic pseudopotentials. Their development and scope of applications,” Chem. Rev. **112**, 403–480 (2012).
63. P. Schwerdtfeger, H. Stoll, and H. Preuss, “A study of potential curve crossing in X-Ar complexes (X=Mg, Ca, Sr, Ba),” J. Phys. B: At. Mol. Phys. **15**, 1061–1072 (1982).
64. W. H. E. Schwarz, “Das Kombinierte Näherungsverfahren,” Theoret. Chim. Acta **11**, 307–324 (1968).
65. L. R. Kahn and W. A. Goddard, “A direct test of the validity of the use of pseudopotentials in molecules,” Chem. Phys. Lett. **2**, 667–670 (1968).
66. L. R. Kahn and W. A. Goddard, “Ab Initio Effective Potentials for Use in Molecular Calculations,” J. Chem. Phys. **56**, 2685–2701 (1972).
67. W. C. Ermler, Y. S. Lee, P. A. Christiansen, and K. S. Pitzer, “Ab initio effective core potentials including relativistic effects. A procedure for the inclusion of spin-orbit coupling in molecular wavefunctions,” Chem. Phys. Lett. **81**, 70–74 (1981).
68. J. H. van Lenthe, R. Zwaans, H. J. J. van Dam, and M. F. Guest, “Starting SCF calculations by superposition of atomic densities,” J. Comput. Chem. **27**, 926–932 (2006).
69. C. Köppl and H.-J. Werner, “Parallel and Low-Order Scaling Implementation of Hartree-Fock Exchange Using Local Density Fitting,” J. Chem. Theory. Comput. **12**, 3122–3134 (2016).
70. P. Pulay, “Convergence acceleration of iterative sequences. the case of scf iteration,” Chem. Phys. Lett. **73**, 393–398 (1980).
71. P. Pulay, “Improved SCF convergence acceleration,” J. Comput. Chem. **3**, 556–560 (1982).
72. H.-J. Werner, F. R. Manby, and P. J. Knowles, “Fast linear scaling second-order Møller-Plesset perturbation theory (MP2) using local and density fitting approximations,” J. Chem. Phys. **118**, 8149–8160 (2003).
73. C. D. Sherrill, *Notes on density-fitting: Density-fitting approximations to the electron repulsion integrals* (School of Chemistry and Biochemistry, Georgia Institute of Technology, 2010).
74. J. L. Whitten, “Coulombic potential energy integrals and approximations,” J. Chem. Phys. **58**, 4496–4501 (1973).
75. B. I. Dunlap, J. W. D. Connolly, and J. R. Sabin, “On first-row diatomic molecules and local density models,” J. Chem. Phys. **71**, 4993 (1979).

76. F. Weigend, “A fully direct RI-HF algorithm. Implementation, optimised auxiliary basis sets, demonstration of accuracy and efficiency,” Phys. Chem. Chem. Phys. **4**, 4285–4291 (2002).
77. F. Weigend, A. Köhn, and C. Hättig, “Efficient use of the correlation consistent basis sets in resolution of the identity MP2 calculations,” J. Chem. Phys. **116**, 3175–3183 (2002).
78. R. Polly, H.-J. Werner, F. R. Manby, and P. J. Knowles, “Fast Hartree-Fock theory using local density fitting approximations,” Mol. Phys. **102**, 2311–2321 (2004).
79. H.-J. Werner, P. J. Knowles, G. Knizia, F. R. Manby, and M. Schütz, “Molpro. A general-purpose quantum chemistry program package,” WIREs Comput. Mol. Sci. **2**, 242–253 (2012).
80. H. -J. Werner, P. J. Knowles, G. Knizia, F. R. Manby, M. Schütz, P. Celani, W. Györffy, D. Kats, T. Korona, R. Lindh, A. Mitrushenkov, G. Rauhut, K. R. Shamasundar, T. B. Adler, R. D. Amos, A. Bernhardsson, A. Berning, D. L. Cooper, M. J. O. Deegan, A. J. Dobbyn, F. Eckert, E. Goll, C. Hampel, A. Hesselmann, G. Hetzer, T. Hrenar, G. Jansen, C. Köppl, Y. Liu, A. W. Lloyd, R. A. Mata, A. J. May, S. J. McNicholas, W. Meyer, M. E. Mura, A. Nicklass, D. P. O’Neill, P. Palmieri, D. Peng, K. Pflüger, R. Pitzer, M. Reiher, T. Shiozaki, H. Stoll, A. J. Stone, R. Tarroni, T. Thorsteinsson, and M. Wang, *MOLPRO, version 2015.1, a package of ab initio programs* (www.molpro.net, 2015).
81. G. Knizia, “Intrinsic Atomic Orbitals: An Unbiased Bridge between Quantum Theory and Chemical Concepts,” J. Chem. Theory. Comput. **9**, 4834–4843 (2013).
82. F. Weigend, “Accurate Coulomb-fitting basis sets for H to Rn,” Phys. Chem. Chem. Phys. **8**, 1057–1065 (2006).
83. K. Eichkorn, O. Treutler, H. Öhm, M. Häser, and R. Ahlrichs, “Auxiliary basis sets to approximate Coulomb potentials,” Chem. Phys. Lett. **242**, 652–660 (1995).
84. K. Eichkorn, F. Weigend, O. Treutler, and R. Ahlrichs, “Auxiliary basis sets for main row atoms and transition metals and their use to approximate Coulomb potentials,” Theor. Chem. Acc. **97**, 119–124 (1997).
85. K. P. Lawley, ed., *Advances in chemical physics*. Volume 69: Ab initio methods in quantum chemistry, Part 2, p. 1-62 (H.J.-Werner) (Wiley, Chichester West Sussex, New York, 1987).
86. H.-J. Werner and W. Meyer, “A quadratically convergent MCSCF method for the simultaneous optimization of several states,” J. Chem. Phys. **74**, 5794–5801 (1981).
87. H. -J. Werner and P. J. Knowles, “A Second Order MCSCF Method with Optimum Convergence,” J. Chem. Phys. **82**, 5053 (1985).
88. H.-J. Werner and W. Meyer, “A quadratically convergent multiconfiguration–self-consistent field method with simultaneous optimization of orbitals and CI coefficients,” J. Chem. Phys. **73**, 2342–2356 (1980).
89. P. J. Knowles and H. -J. Werner, “An Efficient Second Order MCSCF Method for Long Configuration Expansions,” Chem. Phys. Lett. **115**, 259–267 (1985).
90. B. O. Roos, “The complete active space SCF method in a fock-matrix-based super-CI formulation,” Int. J. Quantum Chem. **18**, 175–189 (1980).

91. B. O. Roos, P. R. Taylor, and P. E.M. Siegbahn, “A complete active space SCF method (CASSCF) using a density matrix formulated super-CI approach,” Chemical Physics **48**, 157–173 (1980).
92. J. Olsen, B. O. Roos, P. Jørgensen, and H. J. A. Jensen, “Determinant based configuration interaction algorithms for complete and restricted configuration interaction spaces,” J. Chem. Phys. **89**, 2185–2192 (1988).
93. P. A. Malmqvist, A. Rendell, and B. O. Roos, “The restricted active space self-consistent-field method, implemented with a split graph unitary group approach,” J. Phys. Chem. **94**, 5477–5482 (1990).
94. P.-Å. Malmqvist, B. O. Roos, and B. Schimmelpfennig, “The restricted active space (RAS) state interaction approach with spin-orbit coupling,” Chem. Phys. Lett. **357**, 230–240 (2002).
95. A. Berning, M. Schweizer, H.-J. Werner, P. J. Knowles, and P. Palmieri, “Spin-orbit matrix elements for internally contracted multireference configuration interaction wavefunctions,” Mol. Phys. **98**, 1823–1833 (2000).
96. K. Andersson, P.-Å. Malmqvist, and B. O. Roos, “Second-order perturbation theory with a complete active space self-consistent field reference function,” J. Chem. Phys. **96**, 1218–1226 (1992).
97. T. Shiozaki, W. Gyorffy, P. Celani, and H.-J. Werner, “Extended multi-state complete active space second-order perturbation theory: energy and nuclear gradients,” J. Chem. Phys. **135**, 81106 (2011).
98. C. Møller and M. S. Plesset, “Note on an Approximation Treatment for Many-Electron Systems,” Phys. Rev. **46**, 618–622 (1934).
99. C. Edmiston and M. Krauss, “Configuration-Interaction Calculation of H 3 and H 2,” J. Chem. Phys. **42**, 1119–1120 (1965).
100. W. Meyer, “Ionization energies of water from PNO-CI calculations,” Int. J. Quantum Chem. **5**, 341–348 (1971).
101. R. Fink and V. Staemmler, “A multi-configuration reference CEPA method based on pair natural orbitals,” Theoret. Chim. Acta **87**, 129–145 (1993).
102. P. Pulay, “Localizability of dynamic electron correlation,” Chem. Phys. Lett. **100**, 151–154 (1983).
103. Q. Ma and H.-J. Werner, “Scalable Electron Correlation Methods. 2. Parallel PNO-LMP2-F12 with Near Linear Scaling in the Molecular Size,” J. Chem. Theory. Comput. **11**, 5291–5304 (2015).
104. D. Kats and H.-J. Werner, “Multi-state local complete active space second-order perturbation theory using pair natural orbitals,” to be published.
105. K. R. Shamasundar, G. Knizia, and H.-J. Werner, “A new internally contracted multi-reference configuration interaction method,” J. Chem. Phys. **135**, 54101 (2011).
106. L. Ungur and L. F. Chibotaru, “Computational Modelling of the Magnetic Properties of Lanthanide Compounds,” in *Lanthanides and Actinides in Molecular Magnetism* , pp. 153–184.

107. A. Abragam and B. Bleaney, *Electron Paramagnetic Resonance of Transition Ions* (OUP Oxford, Oxford, 2012).
108. M. Vonci, M. J. Giansiracusa, R. W. Gable, W. van den Heuvel, K. Latham, B. Moubaraki, K. S. Murray, D. Yu, R. A. Mole, A. Soncini, and C. Boskovic, "Ab initio calculations as a quantitative tool in the inelastic neutron scattering study of a single-molecule magnet analogue," Chem. Commun. (Camb.) **52**, 2091–2094 (2016).
109. M. Ramos-Silva and P. Martin-Ramos, eds., *Lanthanide-based multifunctional materials*. From OLEDs to SIMs (Elsevier, Amsterdam, Netherlands, 2018).
110. J. D. Rinehart, M. Fang, W. J. Evans, and J. R. Long, "Strong exchange and magnetic blocking in N_2^{3-}-radical-bridged lanthanide complexes," Nat. Chem. **3**, 538-542 (2011).
111. F. Gendron, J. Autschbach, J.-P. Malrieu, and H. Bolvin, "Magnetic Coupling in the Ce(III) Dimer $Ce_2(COT)_3$," Inorg. Chem. **58**, 581–593 (2019).
112. E. Solis-Céspedes, N. Montenegro-Pohlhammer, and D. Páez-Hernández, "Theoretical insight into the superexchange mechanism of coupling in f^1-f^1 system. The case of study $Ce_2(COT)_3$ compound," Inorganica Chimica Acta **477**, 192–198 (2018).
113. A. Wolf, M. Reiher, and B. A. Hess, "The generalized Douglas–Kroll transformation," J. Chem. Phys. **117**, 9215–9226 (2002).
114. M. Dolg, H. Stoll, and H. Preuss, "Energy-adjusted ab initio pseudopotentials for the rare earth elements," J. Chem. Phys. **90**, 1730–1734 (1989).
115. B. A. Heß, C. M. Marian, U. Wahlgren, and O. Gropen, "A mean-field spin-orbit method applicable to correlated wavefunctions," Chem. Phys. Lett. **251**, 365–371 (1996).
116. R. McWeeny, "SCF theory for excited states," Mol. Phys. **28**, 1273–1282 (1974).
117. W. van den Heuvel, S. Calvello, and A. Soncini, "Configuration-averaged 4f orbitals in ab initio calculations of low-lying crystal field levels in lanthanide(iii) complexes," Phys. Chem. Chem. Phys. **18**, 15807–15814 (2016).
118. B. O. Roos, R. Lindh, P.-A. Malmqvist, V. Veryazov, P.-O. Widmark, and A. C. Borin, "New relativistic atomic natural orbital basis sets for lanthanide atoms with applications to the Ce diatom and LuF_3," J. Phys. Chem. A **112**, 11431–11435 (2008).
119. R. Gulde, P. Pollak, and F. Weigend, "Error-Balanced Segmented Contracted Basis Sets of Double-ζ to Quadruple-ζ Valence Quality for the Lanthanides," J. Chem. Theory. Comput. **8**, 4062–4068 (2012).
120. A. K. Wilson, D. E. Woon, K. A. Peterson, and T. H. Dunning, "Gaussian basis sets for use in correlated molecular calculations. IX. The atoms gallium through krypton," J. Chem. Phys. **110**, 7667–7676 (1999).
121. D. E. Woon and T. H. Dunning, "Gaussian basis sets for use in correlated molecular calculations. III. The atoms aluminum through argon," J. Chem. Phys. **98**, 1358–1371 (1993).
122. D. E. Woon and T. H. Dunning, "Gaussian basis sets for use in correlated molecular calculations. IV. Calculation of static electrical response properties," J. Chem. Phys. **100**, 2975–2988 (1994).

123. K. S. Pedersen, L. Ungur, M. Sigrist, A. Sundt, M. Schau-Magnussen, V. Vieru, H. Mutka, S. Rols, H. Weihe, O. Waldmann, L. F. Chibotaru, J. Bendix, and J. Dreiser, "Modifying the properties of 4f single-ion magnets by peripheral ligand functionalisation," Chem. Sci. **5**, 1650–1660 (2014).
124. B. M. Flanagan, P. V. Bernhardt, E. R. Krausz, S. R. Lüthi, and M. J. Riley, "Ligand-Field Analysis of an Er(III) Complex with a Heptadentate Tripodal N 4 O 3 Ligand," Inorg. Chem. **40**, 5401–5407 (2001).
125. E. Lucaccini, L. Sorace, M. Perfetti, J.-P. Costes, and R. Sessoli, "Beyond the anisotropy barrier: slow relaxation of the magnetization in both easy-axis and easy-plane Ln(trensal) complexes," Chem. Commun. (Camb.) **50**, 1648–1651 (2014).
126. M. Perfetti, E. Lucaccini, L. Sorace, J. P. Costes, and R. Sessoli, "Determination of magnetic anisotropy in the LnTRENSAL complexes (Ln = Tb, Dy, Er) by torque magnetometry," Inorg. Chem. **54**, 3090–3092 (2015).
127. F. Aquilante, J. Autschbach, R. K. Carlson, L. F. Chibotaru, M. G. Delcey, L. de Vico, I. Fdez Galván, N. Ferré, L. M. Frutos, L. Gagliardi, M. Garavelli, A. Giussani, C. E. Hoyer, G. Li Manni, H. Lischka, D. Ma, P. Å. Malmqvist, T. Müller, A. Nenov, M. Olivucci, T. B. Pedersen, D. Peng, F. Plasser, B. Pritchard, M. Reiher, I. Rivalta, I. Schapiro, J. Segarra-Martí, M. Stenrup, D. G. Truhlar, L. Ungur, A. Valentini, S. Vancoillie, V. Veryazov, V. P. Vysotskiy, O. Weingart, F. Zapata, and R. Lindh, "Molcas 8: New capabilities for multiconfigurational quantum chemical calculations across the periodic table," J. Comput. Chem. **37**, 506–541 (2016).
128. J. D. Rinehart, M. Fang, W. J. Evans, and J. R. Long, "A N_2^{3-} radical-bridged terbium complex exhibiting magnetic hysteresis at 14 K," J. Am. Chem. Soc. **133**, 14236–14239 (2011).
129. S. T. Liddle and J. van Slageren, "Improving f-element single molecule magnets," Chemical Society reviews **44**, 6655–6669 (2015).
130. D. Andrae, U. Häußermann, M. Dolg, H. Stoll, and H. Preuß, "Energy-adjusted ab initio pseudopotentials for the second and third row transition elements," Theoret. Chim. Acta **77**, 123–141 (1990).
131. S. A. Kozimor, B. M. Bartlett, J. D. Rinehart, and J. R. Long, "Magnetic exchange coupling in chloride-bridged 5f-3d heterometallic complexes generated via insertion into a uranium(IV) dimethylpyrazolate dimer," J. Am. Chem. Soc. **129**, 10672–10674 (2007).
132. L. Salmon, P. Thuéry, E. Rivière, J.-J. Girerd, and M. Ephritikhine, "Versatility of the nature of the magnetic Cu(ii)–U(iv) interaction. Syntheses, crystal structures and magnetic properties of Cu 2 U and CuU compounds," Dalton Trans **107**, 2872–2880 (2003).
133. L. Salmon, P. Thuéry, E. Rivière, and M. Ephritikhine, "Synthesis, structure, and magnetic behavior of a series of trinuclear Schiff base complexes of 5f (U^{IV}, Th^{IV}) and 3d (Cu^{II}, Zn^{II}) ions," Inorg. Chem. **45**, 83–93 (2006).

134. T. Le Borgne, E. Rivière, J. Marrot, P. Thuéry, J.-J. Girerd, and M. Ephritikhine, "Syntheses, X-ray crystal structures, and magnetic properties of novel linear $M_2^{II}U^{IV}$ complexes (M=Co, Ni, Cu, Zn)," Chem. Eur. J. **8**, 773–783 (2002).
135. K. R. Meihaus and J. R. Long, "Actinide-based single-molecule magnets," Dalton Trans. **44**, 2517–2528 (2015).
136. M. Dolg and X. Cao, "Accurate relativistic small-core pseudopotentials for actinides. energy adjustment for uranium and first applications to uranium hydride," J. Phys. Chem. A **113**, 12573–12581 (2009).
137. J. van Leusen, M. Speldrich, H. Schilder, and P. Kögerler, "Comprehensive insight into molecular magnetism via CONDON. Full vs. effective models," Coord. Chem. Rev. **289-290**, 137–148 (2015).
138. M. J. Graham, J. M. Zadrozny, M. S. Fataftah, and D. E. Freedman, "Forging Solid-State Qubit Design Principles in a Molecular Furnace," Chem. Mater. **29**, 1885–1897 (2017).
139. L. Escalera-Moreno, J. J. Baldoví, A. Gaita-Ariño, and E. Coronado, "Spin states, vibrations and spin relaxation in molecular nanomagnets and spin qubits. A critical perspective," Chem. Sci. **9**, 3265–3275 (2018).
140. M. S. Fataftah, J. M. Zadrozny, S. C. Coste, M. J. Graham, D. M. Rogers, and D. E. Freedman, "Employing Forbidden Transitions as Qubits in a Nuclear Spin-Free Chromium Complex," J. Am. Chem. Soc. **138**, 1344–1348 (2016).
141. S. Otto, M. Grabolle, C. Förster, C. Kreitner, U. Resch-Genger, and K. Heinze, "$Cr(ddpd)_2^{(3+)}$. A Molecular, Water-Soluble, Highly NIR-Emissive Ruby Analogue," Angew. Chem. Int. Ed. **54**, 11572–11576 (2015).
142. S. Otto, N. Scholz, T. Behnke, U. Resch-Genger, and K. Heinze, "Thermo-Chromium. A Contactless Optical Molecular Thermometer," Chemistry **23**, 12131–12135 (2017).
143. S. Otto, C. Förster, C. Wang, U. Resch-Genger, and K. Heinze, "A Strongly Luminescent Chromium(III) Complex Acid," Chemistry **24**, 12555–12563 (2018).
144. S. Otto, J. P. Harris, K. Heinze, and C. Reber, "Molecular Ruby under Pressure," Angew. Chem. Int. Ed. **57**, 11069–11073 (2018).
145. S. Otto, M. Dorn, C. Förster, M. Bauer, M. Seitz, and K. Heinze, "Understanding and exploiting long-lived near-infrared emission of a molecular ruby," Coord. Chem. Rev. **359**, 102–111 (2018).
146. C. Wang, S. Otto, M. Dorn, E. Kreidt, J. Lebon, L. Sršan, P. Di Martino-Fumo, M. Gerhards, U. Resch-Genger, M. Seitz, and K. Heinze, "Deuterated Molecular Ruby with Record Luminescence Quantum Yield," Angew. Chem. Int. Ed. **57**, 1112–1116 (2018).
147. F. Weigend and R. Ahlrichs, "Balanced basis sets of split valence, triple zeta valence and quadruple zeta valence quality for H to Rn. Design and assessment of accuracy," Phys. Chem. Chem. Phys. **7**, 3297–3305 (2005).
148. A. Hellweg, C. Hättig, S. Höfener, and W. Klopper, "Optimized accurate auxiliary basis sets for RI-MP2 and RI-CC2 calculations for the atoms Rb to Rn," Theor Chem Account **117**, 587–597 (2007).

149.F. Weigend, “Hartree-Fock exchange fitting basis sets for H to Rn,” J. Comput. Chem. **29**, 167–175 (2008).

150.C. Hättig, “Optimization of auxiliary basis sets for RI-MP2 and RI-CC2 calculations. Core–valence and quintuple-ζ basis sets for H to Ar and QZVPP basis sets for Li to Kr,” Phys. Chem. Chem. Phys. **7**, 59–66 (2005).

151.J. Krzystek, A. Ozarowksi, and J. Tesler, “Multi-frequency, high-field EPR as a powerful tool to accurately determine zero-field splitting in high-spin transition metal coordination complexes,” Coord. Chem. Rev. **250**, 2308–2324 (2006).

152.J. M. Zadrozny, D. J. Xiao, M. Atanasov, G. J. Long, F. Grandjean, F. Neese, and J. R. Long, “Magnetic blocking in a linear iron(I) complex,” Nat. Chem. **5**, 577–581 (2013).

153.X.-N. Yao, J.-Z. Du, Y.-Q. Zhang, X.-B. Leng, M.-W. Yang, S.-D. Jiang, Z.-X. Wang, Z.-W. Ouyang, L. Deng, B.-W. Wang, and S. Gao, “Two-Coordinate Co(II) Imido Complexes as Outstanding Single-Molecule Magnets,” J. Am. Chem. Soc. **139**, 373–380 (2017).

154.Y. Rechkemmer, F. D. Breitgoff, M. van der Meer, M. Atanasov, M. Hakl, M. Orlita, P. Neugebauer, F. Neese, B. Sarkar, and J. van Slageren, “A four-coordinate cobalt(II) single-ion magnet with coercivity and a very high energy barrier,” Nat. Commun. **7**, 10467 EP - (2016).

155.F. Liu, G. Velkos, D. S. Krylov, L. Spree, M. Zalibera, R. Ray, N. A. Samoylova, C.-H. Chen, M. Rosenkranz, S. Schiemenz, F. Ziegs, K. Nenkov, A. Kostanyan, T. Greber, A. U. B. Wolter, M. Richter, B. Büchner, S. M. Avdoshenko, and A. A. Popov, “Air-stable redox-active nanomagnets with lanthanide spins radical-bridged by a metal–metal bond,” Nat. Commun. **10**, 571 (2019).

156.J. A. DeGayner, I.-R. Jeon, and T. D. Harris, “A series of tetraazalene radical-bridged M_2 ($M = Cr^{III}$, Mn^{II} ,Fe^{II}, Co^{II}) complexes with strong magnetic exchange coupling,” Chem. Sci. **6**, 6639–6648 (2015).

157.S. Demir, I.-R. Jeon, J. R. Long, and T. D. Harris, “Radical ligand-containing single-molecule magnets,” Coord. Chem. Rev. **289-290**, 149–176 (2015).

158.P. Celani and H.-J. Werner, “Multireference perturbation theory for large restricted and selected active space reference wave functions,” J. Chem. Phys. **112**, 5546–5557 (2000).

159.T. H. Dunning, “Gaussian basis sets for use in correlated molecular calculations. I. The atoms boron through neon and hydrogen,” J. Chem. Phys. **90**, 1007–1023 (1989).

160.M. Schwilk, Q. Ma, C. Köppl, and H.-J. Werner, “Scalable Electron Correlation Methods. 3. Efficient and Accurate Parallel Local Coupled Cluster with Pair Natural Orbitals (PNO-LCCSD),” J. Chem. Theory. Comput. **13**, 3650–3675 (2017).

161.M. Schwilk, D. Usvyat, and H.-J. Werner, “Improved pair approximations in local coupled-cluster methods,” J. Chem. Phys. **142**, 121102 (2015).

162.H.-J. Werner, “Multipole approximations of distant pair energies in local correlation methods with pair natural orbitals,” J. Chem. Phys. **145**, 201101 (2016).

163.C. Krause and H.-J. Werner, “Comparison of explicitly correlated local coupled-cluster methods with various choices of virtual orbitals,” Phys. Chem. Chem. Phys. **14**, 7591–7604 (2012).

164.C. Riplinger and F. Neese, “An efficient and near linear scaling pair natural orbital based local coupled cluster method,” J. Chem. Phys. **138**, 34106 (2013).

165.M. Saitow, U. Becker, C. Riplinger, E. F. Valeev, and F. Neese, “A new near-linear scaling, efficient and accurate, open-shell domain-based local pair natural orbital coupled cluster singles and doubles theory,” J. Chem. Phys. **146**, 164105 (2017).

166.T. B. Adler and H.-J. Werner, “Local explicitly correlated coupled-cluster methods. Efficient removal of the basis set incompleteness and domain errors,” J. Chem. Phys. **130**, 241101 (2009).

167.T. B. Adler, H.-J. Werner, and F. R. Manby, “Local explicitly correlated second-order perturbation theory for the accurate treatment of large molecules,” J. Chem. Phys. **130**, 54106 (2009).

168.R. A. Mata and H.-J. Werner, “Calculation of smooth potential energy surfaces using local electron correlation methods,” J. Chem. Phys. **125**, 184110 (2006).

169.R. A. Mata and H.-J. Werner, “Local correlation methods with a natural localized molecular orbital basis,” Mol. Phys. **105**, 2753–2761 (2010).

170.E. Goll, T. Leininger, F. R. Manby, A. Mitrushchenkov, H.-J. Werner, and H. Stoll, “Local and density fitting approximations within the short-range/long-range hybrid scheme. Application to large non-bonded complexes,” Phys. Chem. Chem. Phys. **10**, 3353–3357 (2008).

171.D. J. Coughtrie, R. Giereth, D. Kats, H.-J. Werner, and A. Köhn, “Embedded Multireference Coupled Cluster Theory,” J. Chem. Theory. Comput. **14**, 693–709 (2018).

172.J. M. Foster and S. F. Boys, “Canonical Configurational Interaction Procedure,” Rev. Mod. Phys. **32**, 300–302 (1960).

173.L. F. Chibotaru, “Theoretical Understanding of Anisotropy in Molecular Nanomagnets,” in *Molecular Nanomagnets and Related Phenomena*, edited by S. Gao (Springer Berlin Heidelberg, Berlin, Heidelberg, s.l., 2015), Vol. 164, pp. 185–229.

174.N. Iwahara and L. F. Chibotaru, “Exchange interaction between J multiplets,” Phys. Rev. B **91**, 174438 (2015).

175.M. Gysler, F. El Hallak, L. Ungur, R. Marx, M. Hakl, P. Neugebauer, Y. Rechkemmer, Y. Lan, I. Sheikin, M. Orlita, C. E. Anson, A. K. Powell, R. Sessoli, L. F. Chibotaru, and J. van Slageren, “Multitechnique investigation of Dy_3 - implications for coupled lanthanide clusters,” Chem. Sci. **7**, 4347–4354 (2016).

176.E. Moreno Pineda, N. F. Chilton, R. Marx, M. Dörfel, D. O. Sells, P. Neugebauer, S.-D. Jiang, D. Collison, J. van Slageren, E. J.L. McInnes, and R. E.P. Winpenny, “Direct measurement of dysprosium(III)···dysprosium(III) interactions in a single-molecule magnet,” Nat. Commun. **5**, 5243 (2014).

177.J. Thyssen, *Development and Applications of Methods for Correlated Relativistic Calculations of Molecular Properties*, PhD thesis, Department of Chemistry - University of Southern Denmark - Odense University, http://dirac.chem.sdu.dk/thesis/thesis-jth2001.pdf, 2001.

178. E. R. Sayfutyarova, Q. Sun, G. K.-L. Chan, and G. Knizia, “Automated Construction of Molecular Active Spaces from Atomic Valence Orbitals,” J. Chem. Theory. Comput. **13**, 4063–4078 (2017).
179. Q. Ma and H.-J. Werner, “Explicitly correlated local coupled-cluster methods using pair natural orbitals,” WIREs Comput Mol Sci **8**, e1371 (2018).
180. S. Stoll and A. Schweiger, “EasySpin, a comprehensive software package for spectral simulation and analysis in EPR,” J. Magn. Reson. **178**, 42–55 (2006).